Scanning Probe Microscopy Studies of Spintronic Materials

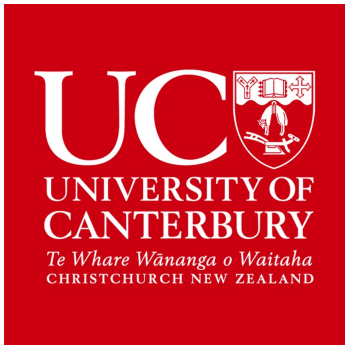

Maxime LE STER

School of Physical and Chemical Sciences

University of Canterbury

A thesis submitted in for the requirements for the degree of

Ph. D. in Physics

2019

Acknowledgements

Nothing in this thesis would exist without the bunch of brilliant people I had the chance to meet and interact with since early 2016, when I started my PhD studies. It feels like a long time ago.

Thanks to Prof. Simon Brown for taking me on board, for his guidance, patience and perspicacity throughout the last three or so years. I admire his consistency and the acuteness of his advice. The integrality of this thesis owes to the intelligence of his supervision.

Thanks to Dr. Franck Natali for the effort he has put into my work and for the knowledge he's allowed me to crystallize during my time in New Zealand (dating back from 2014 when I was a Master's student). One of the most memorable French accent in the crowd too, that almost made me under cover.

Thanks to Dr. Tobias Maerkl whose constant assistance was an absolute gift; the amount of knowledge in solid-state physics that he can store and deliver will not cease to impress me. And also for the company in the plains and summits of New Zealand - the topography of Canterbury has also helped a lot.

Thanks to Dr. Pawel Kowalczyk who taught me how to use the beautiful machine that is the STM; to Dr. Ben Ruck and Emeritus Prof. Joe Trodahl who gave me precious answers to my condensed-matter matters.

Thanks to the post-docs and PhD students at UC have been a constant dose of encouragement: Tobias (again), Saurabh, Susant, Ishan, Josh, Sara, Shota and Edo. They are a daily dose of humour. None of the rare-earth nitrides related work could have been achieved without the help of the whole REN team of PhD students; Jay, Felicia, Will, Jackson and Ali.

I dedicate this thesis to my parents, who always supported me in the pursuit of knowledge since day one. I am extremely grateful to my partner, Danielle, for proof-reading, but most importantly for her generosity, empathy and love. Also, thanks to her kindest parents who made my time in Christchurch serene.

Lastly, I want to pay tribute to those who tragically lost their lives on March 15th 2019 in Christchurch.

Abstract

Novel condensed-matter systems that host exotic electronic states provide many opportunities for new device technologies based on spintronics and topotronics. A wide variety of materials systems are under investigation internationally, each with its own advantages and disadvantages. Two promising families of materials are investigated via scanning probe microscopy (SPM) in this thesis. These materials are group-V elemental two dimensional (2D) materials which possess non-trivial topologies, and rare-earth nitrides (RENs) that are intrinsic ferromagnetic semiconductors. First, the geometry of the moiré patterns (MPs) in multi-layered 2D group-V materials are investigated by scanning tunneling microscopy (STM). The MPs arising from the superposition of various 2D allotropes of bismuth and antimony are characterised and accurately modelled with a simple superposition model. A general, analytical model for the predictions of MPs is also derived. Secondly, a method for overcoming the fast degradation of RENs in ambient atmosphere is developed using a removable samarium capping layer. The removal of the cap is performed through sputtering and thermal treatment, and characterised with atomic force microscopy, scanning electron microscopy, energy dispersive x-ray spectroscopy and other techniques. The removable cap enables further ex-situ surface characterisation of RENs. Lastly, a preliminary study of room temperature nitridation of gadolinium in ultra-high vacuum is also presented.

Contents

1 Materials for spintronics applications **1**

1.1 The future of Moore's law . . . 2

1.2 Spintronics . . . 3

1.2.1 Principle . . . 4

1.2.2 Ferromagnetic semiconductors . . . 6

1.2.3 Rare-earth nitrides (RENs) . . . 7

1.3 Topology and miniaturisation in 2D structures . . . 11

1.3.1 Early work . . . 11

1.3.2 3D topological insulators . . . 13

1.3.3 2D topological insulators . . . 14

1.3.4 Group-V 2D topological insulators . . . 15

1.3.5 Van der Waals heterostructures . . . 16

1.4 Scanning tunneling microscopy (STM) studies . . . 18

1.4.1 STM of REN surfaces . . . 18

1.4.2 STM of Bi nanostructures . . . 20

1.5 Motivation and plan of this thesis . . . 22

2 Experimental techniques **24**

2.1 Growth and treatment of the samples . . . 24

2.1.1 Combined system used in this thesis . . . 24

2.1.2 Growth of van der Waals heterostructures . . . 25

2.1.3 Molecular beam epitaxy of GdN . . . 26

2.1.4 Sputtering . . . 28

2.2 Sample characterisation . . . 30

2.2.1 Scanning tunneling microscopy . . . 30
2.2.2 Atomic force microscopy . . . 33
2.2.3 Scanning electron microscopy and energy dispersive spectroscopy . . . 34
2.2.4 Reflection high-energy electron diffraction . . . 36
2.2.5 X-ray diffraction . . . 37
2.2.6 Others . . . 37
2.3 Contribution to the work in this thesis . . . 38

3 Moiré patterns in van der Waals heterostructures 39
3.1 Introduction . . . 39
3.1.1 Concept . . . 41
3.1.2 Early MPs observations . . . 42
3.1.3 Moiré patterns as a method to control surface properties . . . 43
3.2 Characterisation and prediction . . . 43
3.2.1 Definitions and experimental procedure . . . 44
3.2.2 Predicting moiré patterns . . . 47
3.2.3 Summary . . . 51
3.3 Experimental results and modelling . . . 52
3.3.1 α–antimonene . . . 53
3.3.2 β–antimonene . . . 61
3.3.3 MBi . . . 66
3.3.4 α-Bi . . . 71
3.3.5 Conclusion . . . 75
3.4 Conclusions . . . 76
3.4.1 Achievements . . . 76
3.4.2 Limitations . . . 77
3.4.3 Further work . . . 79

4 Moiré patterns general solution 80
4.1 Concept . . . 81
4.1.1 Gratings . . . 82
4.1.2 Higher order reciprocal vectors . . . 84

4.1.3 Atomic lattices . . . 86
4.2 General method . . . 90
4.2.1 Reciprocal lattice of the layers . . . 90
4.2.2 MP vectors . . . 92
4.2.3 Function MP.m . . . 93
4.2.4 Function MPtheta.m . . . 94
4.2.5 Cut-off considerations . . . 96
4.3 Modeling group-V VDWHs . . . 97
4.3.1 α-Sb on α-Bi . . . 97
4.3.2 β-Sb on α-Bi . . . 100
4.3.3 MBi on α-Bi . . . 102
4.3.4 α-Bi on HOPG . . . 104
4.3.5 α-Bi on MoS_2 . . . 106
4.3.6 Summary . . . 108
4.4 Deeper understanding of the model . . . 109
4.4.1 Reciprocal space circles . . . 109
4.4.2 Commensurability . . . 111
4.5 Analytical solution . . . 114
4.6 Moiré Rosettes . . . 117
4.7 Discussion and conclusion . . . 118
4.7.1 Summary of the general model . . . 118
4.7.2 Discussion . . . 119
4.7.3 Future work . . . 121

5 Samarium capping layer for RENs **123**

5.1 Principle . . . 123
5.1.1 Removable capping layer . . . 123
5.1.2 Choice of samarium and samples . . . 125
5.2 Epitaxial Sm growth . . . 128
5.2.1 Stability of GdN . . . 128
5.2.2 Capping layer growth . . . 129
5.2.3 Capping layer morphology . . . 130

5.2.4 Electrical characterisation . . . 132
5.2.5 Magnetic characterisation . . . 133
5.3 In-situ sublimation . . . 134
5.3.1 During sublimation . . . 134
5.3.2 Post-sublimation characterisation . . . 136
5.4 Ex-situ sublimation . . . 138
5.4.1 RHEED . . . 138
5.4.2 XRD . . . 140
5.4.3 AFM . . . 141
5.4.4 SEM . . . 144
5.4.5 EDS . . . 146
5.5 Summary and discussion . . . 148

6 Capping layer removal with sputtering **150**
6.1 Principle . . . 150
6.2 Beam energy and current estimate . . . 152
6.2.1 Initial sputtering . . . 152
6.2.2 Summary . . . 155
6.3 Dependence on sputtering time . . . 155
6.3.1 Sputtering of thin Sm layers (A519) . . . 157
6.3.2 Sublimation of thin Sm layers (A519) . . . 161
6.3.3 Sputtering of thick Sm layer (A520) . . . 165
6.3.4 Sublimation of thick Sm layers (A520) . . . 168
6.4 Characterisation of the decapped samples . . . 171
6.4.1 GdN morphology . . . 171
6.4.2 Raman spectroscopy . . . 174
6.5 Conclusion and outlook . . . 175
6.5.1 Summary . . . 175
6.5.2 Future work . . . 176

7 Preliminary study of gadolinium nitridation **179**
7.1 Principle . . . 179

7.1.1 Catalytic breakdown of N_2 . . . 179
7.1.2 Nitridation . . . 181
7.1.3 Crystal structures . . . 182
7.1.4 Aim of this chapter . . . 182
7.2 Growth of Gd on AlN . . . 184
7.3 Nitridation results . . . 186
7.3.1 N_2 exposure . . . 186
7.3.2 Al capping . . . 187
7.4 Nitridation of air-exposed Gd layers . . . 189
7.4.1 After 8 h in air . . . 189
7.4.2 After 10 days in low vacuum . . . 191
7.5 X-Ray Diffraction . . . 192
7.6 Discussion and conclusion . . . 194

8 Conclusion, outlook and further work **197**
8.1 Topotronics and moiré patterns . . . 197
8.2 Spintronics and RENs . . . 199

Bibliography **201**

List of Figures

1.1 Spintronics: principles . . . 5
1.2 Rare-Earth Nitrides: FCC structure and relevant literature . . . 8
1.3 Topology in condensed-matter systems . . . 12
1.4 Three-dimensional topological insulators . . . 14
1.5 Two-dimensional topological insulators . . . 16
1.6 Van der Waals heterostructures . . . 17
1.7 Literature STM images of GdN and SmN . . . 19
1.8 Literature STM images of Bi nanostructures . . . 21

2.1 Omicron VT-AFM system overview . . . 25
2.2 Thermionics system overview . . . 27
2.3 Sputtering operation principle . . . 28
2.4 Scanning tunneling microscope principle . . . 32
2.5 Atomic force microscope principle . . . 34
2.6 Scanning electron microscopy principle . . . 35
2.7 Reflection high-energy electron diffraction . . . 37

3.1 Moiré pattern formation . . . 40
3.2 Moiré patterns: Fringes and moirons . . . 41
3.3 Early MPs observed via STM and TEM . . . 42
3.4 Moiré vectors and angle definitions . . . 45
3.5 FFT of a moiré pattern . . . 46
3.6 Simulated moiré pattern . . . 47
3.7 Beat pattern . . . 48

3.8 Analytical and simulated patterns comparison . . . 51
3.9 α-Sb observations . . . 54
3.10 α-Sb lattices and MPs agreement . . . 58
3.11 α-Sb rotation . . . 60
3.12 β-Sb observations . . . 61
3.13 β-Sb MPs simulations . . . 64
3.14 MBi observations . . . 67
3.15 MBi modeling . . . 69
3.16 α-Bi observations . . . 72
3.17 α-Bi MPs simulations . . . 73

4.1 Real space and reciprocal space gratings . . . 83
4.2 Grating superposition and higher order reciprocal vectors . . . 85
4.3 Atomic lattice superposition: real and reciprocal spaces . . . 88
4.4 Reciprocal lattices of twisted bilayer graphene . . . 92
4.5 MPtheta.m for twisted bilayer graphene . . . 95
4.6 The choice of k_r . . . 96
4.7 General model applied to α-Sb on 2ML-α-Bi (HOPG substrates) . . . 98
4.8 General model applied to β-Sb on 2ML-α-Bi . . . 101
4.9 General model applied to MBi on 2ML-α-Bi . . . 104
4.10 General model applied to α-Bi on HOPG . . . 105
4.11 General model applied to α-Bi on MoS_2 . . . 107
4.12 Reciprocal structures in a general superposition case . . . 110
4.13 Twisted bilayer graphene: commensurate and incommensurate cases . . . 113
4.14 Symmetry considerations of the analytical formulas . . . 116
4.15 Moiré rosettes for bilayer graphene and α-Bi on HOPG for various orders . . . 117

5.1 Schematics of the capping and decapping procedure . . . 124
5.2 Vapour pressure of various elements and sublimation rate . . . 126
5.3 Heterostructure schematics . . . 128
5.4 Thermal stability of GdN(111) . . . 129
5.5 Sm capping layer RHEED and XRD patterns . . . 129

5.6 AFM of untreated Sm caps . . . 131
5.7 Electrical characterisation of the cap . . . 133
5.8 Magnetic characterisation of the capped GdN . . . 134
5.9 RHEED patterns during in-situ decapping . . . 135
5.10 Structural and electrical characterisation of a decapped GdN sample . . . 136
5.11 Magnetic characterisation of a decapped GdN sample . . . 137
5.12 RHEED patterns of Sm-capped GdN samples exposed to air . . . 139
5.13 XRD $\theta - 2\theta$ patterns of air-exposed sublimated Sm/GdN samples . . . 140
5.14 AFM of air-exposed A314 (Sm/GdN) after sublimation . . . 142
5.15 SEM of air-exposed A314 (Sm/GdN) after sublimation . . . 145
5.16 EDS of air-exposed A314 (Sm/GdN) after sublimation . . . 147
5.17 Air-exposed samples sublimation schematics . . . 148

6.1 Air-exposed and sputtered sample schematics . . . 151
6.2 Morphology of sputtered R024 . . . 154
6.3 EDS of sputtered R024 . . . 155
6.4 AFM/SEM of sputtered A519 . . . 158
6.5 EDS spectra of sputtered A519 . . . 159
6.6 AFM/SEM of sputtered/sublimated A519 . . . 162
6.7 EDS spectra of sputtered/sublimated A519 . . . 163
6.8 AFM/SEM of sputtered A520 . . . 166
6.9 EDS spectra of sputtered A520 . . . 167
6.10 AFM/SEM of sputtered/sublimated A520 . . . 169
6.11 EDS spectra of sputtered/sublimated A520 . . . 170
6.12 GdN morphology and decapped samples . . . 172
6.13 Raman spectra of decapped samples . . . 175

7.1 Nitridation schematics . . . 181
7.2 Crystal structures of bulk AlN, Gd, GdN and Al . . . 182
7.3 Growth of Gd(0001) on AlN . . . 185
7.4 Nitrogen exposure of Gd(0001) . . . 186
7.5 Al capping of GdN_x . . . 188

7.6 N_2 exposure of Gd(0001) after 8 h in air 189
7.7 N_2 exposure of Gd(0001) after 5 min in air 191
7.8 XRD patterns of the samples 193

List of publications and conference talks

Peer-reviewed publications

M. Le Ster, T. Maerkl, P. J. Kowalczyk and S. A. Brown. Moiré patterns in van der Waals heterostructures. *Phys. Rev. B* **99**, 075422, 2019.

T. Maerkl, P. J, Kowalczyk, **M. Le Ster**, I. V. Mahajan, H. Pirie, Z. Ahmed, G. Bian, X. Wang, T.-C. Chiang and S. A. Brown. Engineering multiple topological phases in nanoscale Van der Waals heterostructures: realisation of α-antimonene. *2D Mater.* **5**, 011002, 2018.

P. J. Kowalczyk, O. Mahapatra, **M. Le Ster**, S. A. Brown, G. Bian, X. Wang and T.-C. Chiang. Single atomic layer allotrope of bismuth with rectangular symmetry. *Phys. Rev. B* **96**, 205434, 2017.

International conference talks and posters

M. Le Ster, T. Maerkl, P. J. Kowalczyk and S. A. Brown. Moiré patterns in van der Waals heterostructures (contributed talk). ACSIN-14/ICSPM26, Sendai, Japan, October 2018

M. Le Ster, J. Chan, S. Brown, B. J. Ruck, J. Trodahl and F. Natali. Ex-Situ surface studies of a challenging ferromagnet semiconductor: GdN (contributed talk). ACSIN-14/ICSPM26, Sendai, Japan, October 2018.

M. Le Ster, J. Chan, S. Brown, B. J. Ruck, J. Trodahl and F. Natali. Samarium capping layer for GdN (poster presentation). AMN8, Queenstown, New Zealand, February 2017.

Chapter 1

Materials for spintronics applications

Nanotechnology might possibly be one of the most profound technological revolutions that humankind has ever been facing. Feynman once said that "there is plenty of room at the bottom" [1], and that was a correct observation: the silicon era of the second part of the 20^{th} century has allowed us to compress information, and has contributed to make instantaneous telecommunication with high data volume universally accessible. Today, billions of transistors channel electrons in our very pockets making humans and the economy more interconnected than ever. However the many applications are more and more demanding in terms of computational power in particular in domains like big-data, artificial intelligence, climate modeling, etc.

The 'bottom' is however now a lot less empty than it was in the late 1950s: after decades of exponential increase in component density and processing frequency, Moore's law may be very close to saturation [2]. Transistor size is now plateauing at a few nanometres, with latest industrial plans aiming to release 7 nm or even 5 nm-node transistors on the market by 2020 [3]. Extreme miniaturisation however drops the device efficiency. For example, quantum tunneling through the gate layers is unavoidable [4] and heat management becomes a very difficult task [5]. To keep the pace with technological growth, novel pathways are being explored and different device designs are being researched, among which are *spintronics* and *topotronics*.

The modern challenges of reduction of energy consumption and greenhouse gas emissions in the context of global climate change are intertwined with the goal of developing new solid-

state devices. Internet traffic has soared by a factor 10 every 5 years since the 1990s [6], and its cost in terms of carbon emission and energy has also risen. Data centres currently use about 3% of the world's electricity [7] and a very large portion of that figure is used for cooling. If no progress in power efficiency is made, the energy cost of data centres will rise by a factor 3 by 2030 [8]. Development of dissipation-free electronics using novel building blocks and/or architectures is hence crucial.

This introductory chapter is organized as follows. Section 1.1 briefly reviews the various technological solutions that are being considered to overcome the limits of conventional silicon electronics, their advantages and remaining challenges. Section 1.2 brings the attention on spintronics and in particular focuses on the rare-earth nitrides (RENs) that are investigated later in this thesis. Section 1.3 explains the mechanisms behind the topological insulators (TIs) in particular focusing on group-V two-dimensional (2D) materials. Scanning tunneling microscopy (STM) studies on REN surfaces and on bismuth and antimony nanostructures will be reviewed in section 1.4. Finally section 1.5 presents the outline of this thesis.

1.1 The future of Moore's law

To meet ever increasing demands for computational power and to reduce its energy consumption, traditional complementary metal-oxide semiconductor (CMOS) transistors will have to be replaced or completed with other technologies that are currently at an early stage of development. This section reviews very briefly a handful of technologies that may lead to a paradigm shift in the coming decades.

Quantum computation Quantum computation, exploiting superposition and entanglement is expected to speed up a range of computational tasks [9]. Their advantage is to be able to process very large datasets and a lot of variables simultaneously. Commercially available products are still limited by decoherence management and error correction [10]. Typically very low temperatures are required for processing, which are not achievable in consumer electronics but could be considered for 'cloud'-based applications [11].

Superconducting electronics Superconducting devices that enable dissipation-free electronics have now been researched for several decades [12], and may also contribute to quantum computing [13]. The keystone devices are the Josephson junction [14] and the superconducting quantum interference device (SQUID). The primary advantage of exploiting the superconducting properties of materials over conventional CMOS is the absence of Joule heating, greatly improving the power efficiency. However, operation below the critical temperature (below which the material is superconducting) is a prerequisite for functioning.

Neuromorphic computing 'Brain-inspired' computing promises processing that is typically performed by neurobiological architectures, including associative memory, pattern recognition and complex systems prediction [15]. Deep-learning via neural networks is currently performed in software, but hardware realisation in integrated circuits may be a significant step for artificial intelligence development [16]. The other advantage it has over conventional silicon-based computing is to guarantee very low energy consumption [17].

Molecular/atomic electronics Single molecule devices were first demonstrated about 20 years ago [18]. The concept of molecular electronics was not new [19] but commercial devices are still not available [20]. The fabrication of the first single-atom transistors in 2012 [21] have created considerable hopes of miniaturisation beyond Moore's law, and materials other than silicon are also investigated [22]. The main challenge at this stage is in the difficulty of arranging molecular or single-atom transistors in a large-scale array, required to demonstrate their full potential [23].

Spintronics and Topotronics Classical electronics typically exploit the electron charge in their devices. Spintronics and topotronics conversely use the electron spin, respectively via magnetic coupling [24] and with exploiting the protected chiral boundary-modes in topological insulators (TIs) [25]. More details of the two are given in sections 1.2 and 1.3.

1.2 Spintronics

In this section, the principle of spintronics as well as the key materials necessary for their various functionalities will be briefly reviewed. A family of materials that is a candidate for

future spintronics applications known as the rare-earth nitrides (RENs) is also presented.

1.2.1 Principle

The basis of spintronics is the use and manipulation of the electron intrinsic spin in solid-state devices [26]. Being able to control both the charge (via electric fields as in conventional CMOS-based electronics) and the spin of the charge carriers may increase the information storage density, provide faster data processing, and reduce power consumption [27]. The manipulation of the spin is performed via magnetic fields or via the spontaneous magnetisation of the materials incorporated into the device. Spin-orbit coupling (SOC) is also at the centre of more recent devices [28], enabling spin manipulation without the use of magnets. Magnonics (using spin waves as information carrier [29]) and skyrmions (pseudo-particles of topological spin-textures [30]) are further branches of spintronics that lie beyond the scope of this thesis. Most of the phenomena discussed here are not directly investigated in this thesis and therefore this section briefly overviews the key aspects and challenges of spin-based electronics.

Spin-polarized currents Ferromagnetism is central in spintronics because it means that static magnetic fields can be generated spontaneously (avoiding cumbersome electromagnets which require large currents) and when the density of states (DOS) of spin-up and spin-down differ significantly at the Fermi level E_{F}, spin-polarized currents are enabled (below the Curie temperature T_C, above which spin up and down bands are degenerate). Typically magnetic materials rely on atomic d or f orbitals (in e.g. transition metals and rare-earths) where a higher number of unpaired electrons is possible as determined by Hund's rules [31]. Figure 1.1 shows a schematic band-structure of a ferromagnetic metal with a band spin splitting [26]. The conduction electrons in this simple model are 100% polarized, as there are no spin-up states at E_{F}.

Giant magnetoresistance and tunnel junctions The field of spintronics began with the discovery of the giant magnetoresitance (GMR) in metals [27, 32]. GMR originates from a strong dependence of the conductivity on the magnetisation alignment between two metallic layers that can be both ferromagnetic (F) with different coercivities, or F and antiferromag-

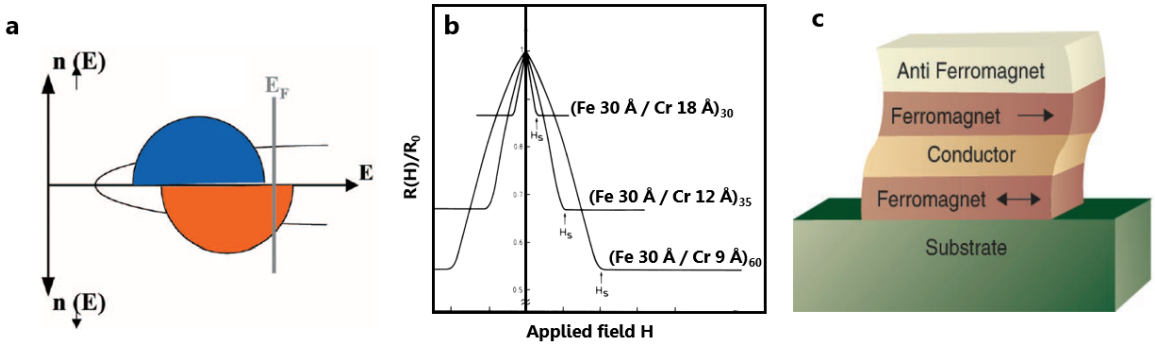

Figure 1.1: (a) Simplified model of the electronic band-structure of a ferromagnet, where spin up (blue) and spin down (orange) have different DOS at E_F (from [26]). (b) GMR in Fe/Cr superlattices. The resistance is strongly dependent on the applied field and the ratio $R(H)/R_0$ increases for increased ferro/antiferromagnetic (F/AF) coupling [32] (with R_0 the resistance without no applied field). (c) Spin-valve effect exploiting GMR. The top F (hard) and AF layers are coupled, and the bottom F layer (soft) magnetisation orientation modulates the resistance of the heterostructure, from [27].

netic (AF). Figure 1.1(b) shows the relative magnetoresistance as a function of the applied magnetic field in F/AF (Fe/Cr) superlattices [32]. This effect is exploited in the spin-valve shown in Fig. 1.1(c). The magnetisation alignment between the two F layers (parallel or antiparallel) is controlled via an external magnetic field. The top F layer is pinned via coupling with the AF layer, and the other is more sensitive to the external magnetic field ('free' layer). The two different states allow to switch between a high (antiparallel alignment) and low (parallel) resistances. When the two F layers are separated by an insulating layer (as opposed to metallic for the spin-valve) the device is known as a magnetic tunnel junction (MTJ). The principle of the MTJ is similar, but typically yields higher resistance ratios, labelled in the MTJ context as tunneling magnetoresistance (TMR) [33]. Spin valves and MTJs have been technologically successful and are already implemented in magnetic sensors (in hard disk read heads) and in magnetoresistive random-access memories (MRAMs) [26]. Beyond these magnetic storage purposes applications, future devices that use and manipulate spin currents in a transistor will require materials combining semiconducting and magnetic properties [34].

Towards spin processing A fundamental function in spintronics is the *spin injection* [35], which aims to induce a strongly spin-polarized current in a non-magnetic material using a F source. The spin extraction, the reciprocal effect, enables the spin-orientation read-out. Spin

injection was initially attempted in ohmic F/NF junctions (NF: non ferromagnetic) however spin accumulation at the interface leads to a rapid decrease of the spin polarisation [36]. In F/NF junctions using a NF semiconductor, the depolarisation is even more abrupt, which poses a challenge for information processing [24, 37]. This hurdle is partially overcome by introducing an insulating layer inside the junction (F/I/NF), where the mechanism of spin conduction is made possible through tunneling [26]. Today spin injection devices are still under intensive research and development as many obstacles remain, as spin lifetimes are relatively short and spin-injection efficiencies are still low [38]. Methods involving thermal gradients [39] and optical injection [40] have also been considered. A key device is the spin field effect transistor (FET) that could electrically modulate the spin-polarisation, enabling effective spin information processing [41]. The principle of the spin FET is to control the transmission of a spin-polarized channel between a drain and a source (both F materials) via gating of the channel. The conduction material must exhibit a strong SOC to operate [41]. Despite decades of efforts the spin FET is still not entirely successful [38, 42], partly due to the spin scattering processes in the ferromagnetic semiconductors (FS) used as the FET channel [42]. Superconductors have been proposed as a solution [43], yet there is still room for improvement of the FS as discussed below.

1.2.2 Ferromagnetic semiconductors

Ferromagnetic semiconductors (FSs) are key elements for effective spin-processing [34], as spin-dependent switching between two states (low and high resistance) is required to compete with standard CMOS electronics [27]. As for the F metals, the FSs possess spontaneous magnetisation below T_C, that ultimately determines the maximum device operation temperature.

Diluted magnetic semiconductors The chief FS material that has been considered is $Ga_{1-x}Mn_xAs$ and has been investigated for about 25 years [44]. It belongs to the family of the dilute magnetic semiconductors (DMS) where magnetic impurities (here Mn^{2+}) are introduced in the otherwise paramagnetic semiconductor (GaAs). Room temperature operation of alloys of $Ga_{1-x}Mn_xAs$ in the F phase has been theoretically predicted [45]. However the reported values of T_C rarely exceed 110 K (170 K for annealed $Ga_{1-x}Mn_xAs$ with x~0.08

[46]). The main technological issue in DMSs is that magnetic impurities also act as electronic p-type dopants, which prevents independent control of both carrier concentration and magnetism [35]. n-type doping is also challenging because Mn^{2+} substituting Ga^{3+} making the material p-type [47]. Furthermore, the high concentration of magnetic impurities required to make the material F can lead to phase segregation [48]. Lastly, integration of GaAs with Si-based electronics is not an easy task [49], and readily Si-compatible FS would be preferable for device applications.

Intrinsic ferromagnetic semiconductors The above drawbacks in DMSs might be counteracted with intrinsic FSs, whose main advantage over DMSs is to offer ferromagnetism without the presence of foreign magnetic ions. Intrinsic FSs are relatively uncommon [50], with the main examples being the europium chalcogenides and the rare-earth nitrides (RENs). Besides EuO [51] which is a FS with $T_C = 68$ K, little is known about EuS and EuSe besides their low Curie temperatures (respectively 18 and 8 K [52]). EuTe is on the contrary AF [53]. For these reasons, investigations of the rare-earth nitrides (RENs) occupy a central place in development of intrinsic FSs.

1.2.3 Rare-earth nitrides

Previous work on the rare-earth nitrides (RENs), investigated in this thesis, is reviewed here. This section's aim is not to give an extensive literature review, but rather to give an overview of their properties and in particular to show the potential of GdN, prototypical REN for spintronic applications.

Crystal structure The rare-earth (RE) (i.e. the lanthanide elements from La to Lu to which are often included Sc and Y) are for the most part trivalent (RE^{3+}) and combine with nitrogen ions N^{3-} to form the RENs. Figure 1.2(a) shows the face-centred cubic (FCC) 'rock-salt' structure of the RENs [50]. A (100) plane is indicated, as well as a (111) plane (yellow) showing 6-fold rotational symmetry.

Film growth There has been a growing interest in studying the REN due to their potential for spintronics applications in the last decade, and to that effect thin films have been stud-

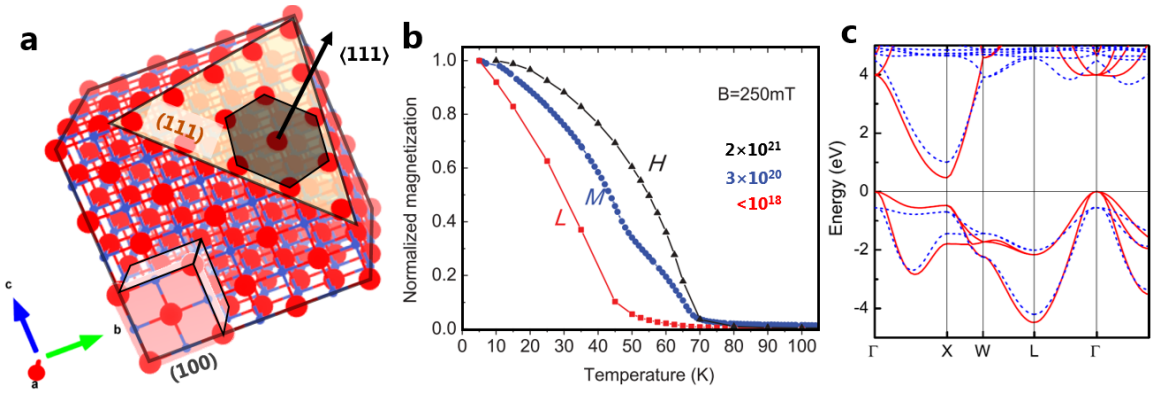

Figure 1.2: (a) Ball-and-stick model of FCC RENs (RE: red, N: blue). The cubic unit-cell is indicated with the (100) plane. A cut along the (111) plane is indicated (yellow) showing the hexagonal symmetry of the (111) plane. The ⟨111⟩ direction is indicated with an arrow. (b) Temperature-dependent normalized magnetisation of GdN for three carrier concentrations (L, M and H indicated with same colour) under a magnetic field $B = 250$ mT, adapted from [70]. (b) Calculated band-structure of GdN via DFT in the ferromagnetic phase (below T_C). The majority (solid) and minority (dashed) have different energies (adapted from [71]).

ied extensively [50]. Various deposition techniques for REN thin films have been reported, mostly grown in ultra-high vacuum (UHV) conditions e.g. molecular beam epitaxy (MBE) [54–56], pulsed-laser deposition (PLD) [57] and sputtering [58]. RE solid sources and gaseous nitrogen precursors (N_2 or ammonia NH_3) with pressures in the range 10^{-7} to 10^{-4} mbar are common [50]. Epitaxial REN(100) thin films have been achieved on MgO(100) [59, 60] and YSZ(100) [57, 61] substrates, and REN(111) oriented films have been obtained using (0001) oriented GaN [57, 62] and AlN [54, 57, 62, 63] substrates. The growth of RENs on Si wafers leads to the formation of undesired RE silicides [50, 64, 65] that can be avoided when deposited on an AlN buffer [54, 62, 66], promising integration with conventional Si electronics. The RENs oxidize rapidly in air and decompose into rare-earth oxides or hydroxides [66, 67], which means that the layers must be passivated with a capping layer for ex-situ measurements [50]. A very interesting aspect of the REN growth is the capacity of the RE elements (with the exception of the divalent Eu and Yb) to break the N_2 bond [68], which could have an impact beyond the field of spintronics, e.g. in catalysis and ammonia production [69]. The exposure of a Gd layer to N_2 in UHV is investigated in chapter 7.

Magnetic properties The RE elements have partially filled $4f$ orbitals which can lead to large spin and/or orbital momenta depending on the number of unpaired electrons. In the

RENs, the $4f$ shells are responsible for the magnetic properties [72], which started to be investigated about 40 years ago [73]. After several decades of conflicting results concerning the magnetic properties of the RENs, it was established that most are ferromagnets (NdN [74], SmN [75], GdN [58, 70], DyN [76], HoN [76], ErN [76]) as opposed to YbN that is antiferromagnetic [77]. GdN is the ferromagnet with the largest reported magnetic moment among the RENs series (7 μ_B per Gd^{3+} ion) with a small coercive field [56], whereas SmN has a near-zero magnetic moment with a large coercive field [75]. The magnetic ordering temperatures of the RENs are usually low, e.g. 27 K for SmN [75] [78] and $50-70$ K for GdN [56]. The T_C of GdN can be increased by a few dozens of Kelvins thanks to higher concentration of nitrogen vacancies V_N [55, 70] (see Fig. 1.2(b)).

Electronic properties The electronic properties of the RENs have also long been debated as e.g. GdN has been reported to be metallic [79], semimetallic [60, 80] and semiconducting [71]. Early experimental efforts were hindered by the rapid oxidation of REN films in air and by the varying stoichiometry in the samples [50]. With the advent of UHV deposition techniques, it was demonstrated that NdN [74], SmN [81], EuN [78], GdN [71, 82], DyN [83] and YbN [77] are semiconductors with band-gap energies in the vicinity of 1.0 eV, and shows a significant temperature dependence [61, 71, 84, 85]. Doping can be achieved with V_N (n-type), with concentrations depending directly on the nitrogen precursor partial pressure [55, 70]. Mg impurities (acceptors) have been demonstrated to decrease the carrier concentration (up to three orders of magnitude) without a noticeable change in the structural and magnetic properties [86, 87]. GdN has also been shown to have a strong magnetoresistance [88]. Recently, superconductivity has been observed in SmN [89]. Despite concentrated efforts on understanding the RENs electronic and magnetic properties over the last years, very little is known about their surface properties beyond what the diffraction techniques offer in-situ. Enabling ex-situ measurements of the surface (e.g. structural and chemical) properties with techniques that are not readily available in the growth chamber would be beneficial for further studies of the RENs.

Band-structure calculations Ab-initio methods such as density functional theory (DFT) are typically quite challenging for RENs due to the strongly correlated $4f$ electrons [50].

Recent band-structure calculations of GdN (involving correction parameters) [71, 80, 90] report an indirect band-gap of ~0.5 eV in the ferromagnetic regime, and ~1.0 eV above T_C. Figure 1.2 shows the DFT-calculated band-structure of GdN, where a spin-splitting of about 0.5 eV gap is predicted [71]. The spin-splitting has later been corroborated with optical measurements [84, 85]. Recently, LaN [91] and GdN [92, 93] have been predicted to possess non-trivial topologies. Several theoretical challenges remain in terms of understanding the band-structure, for example the position of the $4f$ electronic states in several RENs (including GdN and SmN) is unclear [50]. Direct observation of the electronic structure via e.g. scanning tunneling spectroscopy (STS) and angle-resolved photoemission spectroscopy (ARPES) would undoubtedly address these questions.

Devices including RENs The variety of ferromagnetic and electronic properties offered by the RENs means that these hold a strong potential for heterostructures on Si wafers (via AlN or GaN buffer layers). Combining RENs together is becoming a reality as GdN/SmN superlattices have been realized recently with high interface quality [94]. Applications in memory devices where GdN and SmN could act as soft and hard ferromagnets respectively are becoming possible [50]. To this effect, GdN-AlN-SmN magnetic tunnel junctions with a TMR as high as 200% have been successfully demonstrated for fields near 2 T [95]. The relatively strong spin-splitting in GdN below T_C makes it a good candidate for spin-injection [85, 96] (see also the calculated band-structure in Fig. 1.2(c)). Spin-filter Josephson junctions consisting of a GdN barrier between two layers of superconducting NbN layers have been demonstrated with 75% spin-filtering efficiency [97]. Further applications of GdN using TIs/magnetic heterostructures have been considered [98].

Relevance and challenges The intrinsic semiconducting and magnetic properties of the RENs might shape the next generation of spintronics. Their integration capability in Si-based spintronics is starting to leverage a significant interest for nanoscale devices. Proofs of concept junctions using RENs have been demonstrated, in particular for spin-filtering (with efficient Josephson junctions), magnetic memories (using magnetic tunnel junctions) and possibly topotronic applications [98]. It is clear that further developments will require a better control and understanding of their surfaces and interfaces, yet there is a clear gap in

the literature about the REN surface properties (see section 1.4). The possible surface measurements might also answer several theoretical questions that remain today open. Future surface-sensitive analyses are however prevented by the degradation that RENs undergo in air. The development of a method to overcome that issue is thus strongly desirable. In this thesis, this challenge is considered and a method involving a removable capping layer is investigated. Chapter 5 investigates the use of a Sm protective layer that is tentatively removed in a different vacuum system with thermal desorption techniques. The method is revisited in chapter 6 where the introduction of a sputtering step is investigated. Lastly, a novel epitaxial thin film growth method is examined in UHV involving nitridation of a pure Gd layer.

1.3 Topology and miniaturisation in 2D structures

Topological insulators (TIs) are a new class of materials that have emerged in the last decade [99–101] and are currently one of the most active areas of condensed matter physics. Beyond offering a platform for novel surface physics exploration, the potential of TIs in electronics is huge. The dissipation-free conduction that TIs promise via the boundary-states could have a significant impact in the device industry by reducing Joule heating [101]. This section gives a brief introduction to TIs and focuses on group-V two-dimensional (2D) TIs (Bi and Sb), which are investigated in this thesis.

1.3.1 Early work

Quantum Hall effect The importance of topology (the mathematics of space and shapes under continuous deformations) in condensed-matter systems was verified in the 1980s with the experimental discovery of the integer [102] and fractional [103] quantum Hall effect (QHE). The quantisation of the Hall conductivity in plateaus of quantum conductance e^2/h was observed for the first time in 2D electron gases in a metal-oxide semiconductor field effect transistor (MOSFET) structure in strong magnetic fields [102]. In the QHE electrons undergo cyclotron orbits [100, 104] in the interior of the device, and exhibit 'skipping' orbits along the edges of the sample, as shown in Fig. 1.3(a). Figure 1.3(b) shows a simplified band-structure of a QH insulator, where the empty conduction band is distinct from the fully

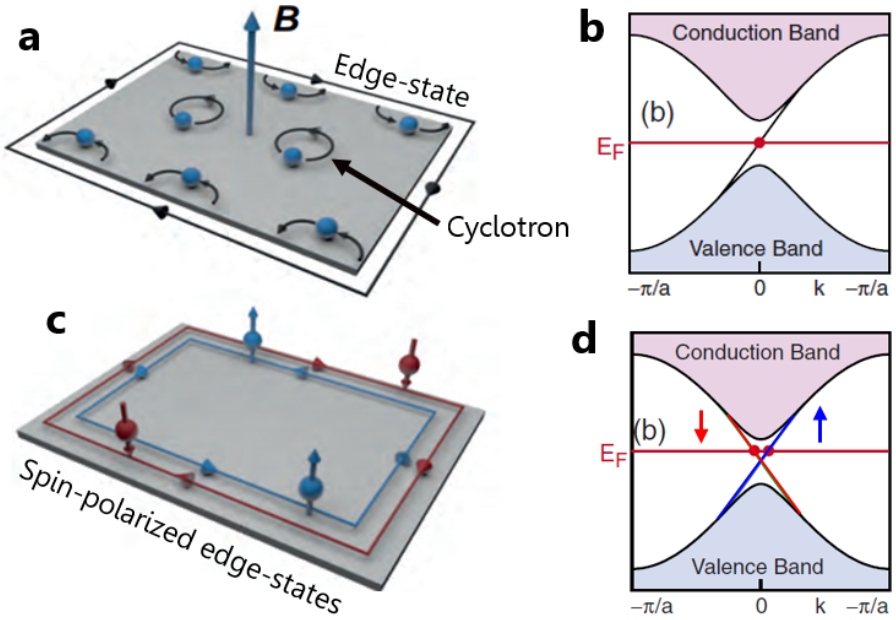

Figure 1.3: (a) Simplified model of the QHE. The magnetic field $\boldsymbol{B}$ leads to circular Landau orbits and edge-state perpendicular to $\boldsymbol{B}$ along the sample edges. (b) Band-model of the inside of the QHE material (coloured bands) and the single-mode edge-state crossing E_{F}. (c) QSHE model, with the spin-dependnt chiral edge modes. (d) Band-structure of a QSHE material with the gap corresponding to the 'bulk' of the material, and gapless states cone due to the edge modes. (a,c) are adapted from [104] and (b,d) from [100].

occupied valence bands with the Fermi level E_{F} in the band-gap. The single edge mode corresponding to the skipping orbits (crossing E_{F}) is indicated. Note that the edge modes propagate clockwise only.

Quantum spin Hall effect The quantum spin Hall effect (QSHE) is analogous to the QHE, with the fundamental difference that QSH insulators possess time-reversal symmetry [105] (and therefore the QSHE vanishes in presence of a magnetic field). Spin-orbit coupling (SOC) plays a major role in the QSHE by opening the energy band-gap [106, 107]. In a QSH insulator the 'bulk' of the material is insulating and the edges of the sample host chiral spin-polarized channels, as shown in Fig. 1.3(c). The spin up and down states propagate in opposite directions. The band-structure of a QSH insulator is shown in Fig. 1.3(d). The bulk bands are insulating and the two edge-states with opposite spin cross E_{F} [100].

Robustness The QHE and QSHE are not explained simply in terms *symmetry breaking*, but instead through the topological structure of the band-structure, in particular with the

Chern number and $\mathbb{Z}_2$ invariant [25, 108, 109]. The *bulk-boundary correspondence* is a crucial aspect of the QSH insulators [105]. When two insulators A and B (A or B can be vacuum) possess a different topology (characterized with different Chern numbers), no continuous deformation of the band-structure of A can be topologically identical to that of B. The phase transition observed at the interface between A and B is responsible for the edge-states. This is why the *topologically protected* edge-modes are distinguished from edge states in trivial gapped band-structures (e.g. via adsorption of other species [110]). The topology in QSH insulators protects the edge-states which are as a consequence more robust than trivial edge states. Variations in the edge geometry, or the presence of (non-magnetic) scattering impurities, mild deformations, structural defects do not change the topology in turn 'protecting' the edge modes. Elastic backscattering ($\mathbf{K}$ to $-\mathbf{K}$) in topological edge states is forbidden because this would require that the spin must also flip. This is referred to as *spin-momentum locking* [105] and topotronic devices thus reduce the dissipation energy [100].

1.3.2 3D topological insulators

The QSH insulators generalized in three dimensions (3D) [99] are the so called bulk or 3D TIs. Topologically protected states at the boundary are metallic surface states. The strong SOC in Bi is responsible for the topologically non-trivial band-structure in $Bi_{1-x}Sb_x$ alloy, which was the first 3D TI [111]. Other Bi-containing alloys have also been reported to be 3D TIs, including Bi_2Se_3 [112] and Bi_2Te_3 [113]. Bulk Bi was also reported to be a 3D TI [114], and very recently to possess an higher-order topology with 'hinge states' [115].

Bismuth antimonide The example of $Bi_{1-x}Sb_x$ is used here to show the importance of topology in the band-structure. Figures. 1.4(a), 1.4(b) and 1.4(c) show respectively the schematic band-structures of Bi_xSb_x for $x = 0$ (Bi), $0.07 < x < 0.22$, and $x = 1$ (Sb). The Bi valence and conduction bands at the L point (deriving from antisymmetric L_a and symmetric L_s orbitals) are separated by an energy gap. For antimony (Sb), despite sharing strong similarities in the band-structure (semimetallic and L-point also gapped) the bands at the L point are inverted with respect to Bi [100]. It is therefore impossible to find a continuous transformation between Bi and Sb without changing the topological property of the band-structure. Band-inversion occurs for $x = 0.04$ where the gap closes completely [111]. For $0.07 < x < 0.22$,

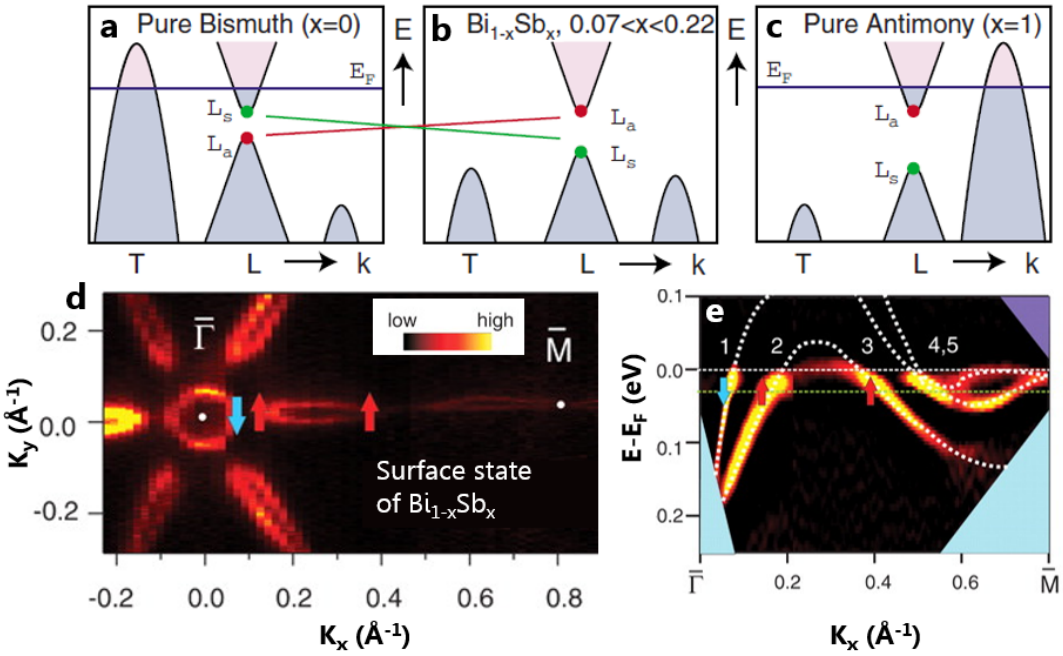

Figure 1.4: $Bi_{1-x}Sb_x$3D TIs. Simplified band-structures near the E_F for (a) $x = 0$ (pure Bi), (b) $0.07 < x < 0.22$ and (c) $x = 1$ (pure Sb). For an intermediate Sb concentration $0.07 < x < 0.22$, the alloy is a 3D TI (adapted from [100]). Spin-resolved ARPES of $Bi_{0.91}Sb_{0.09}$(111) at (d) E_F (Fermi surface) (e) and surface-states energies along the $\overline{\Gamma} - \overline{M}$ direction (from [116]).

the band-gap reopens but is inverted and the alloy becomes semiconductor, with topologically protected surface-states (note that pure Bi and pure Sb are semimetals). This has been experimentally verified [111, 116] via spin-resolved angle-resolved photoemission spectroscopy (ARPES). Figure 1.4(d) shows a cut through the band-structure of $Bi_{0.91}Sb_{0.09}$ at E_F. The spin-dependent (chiral) surface states are resolved, and their chirality indicated by different arrow directions. Their energy dispersion is shown in Fig. 1.4(e), displayed along the $\overline{\Gamma} - \overline{M}$ direction (respectively centre and one corner of the first Brillouin zone).

1.3.3 2D topological insulators

From 3D to 2D The first-observed TIs were in fact thin films confined within larger structures. Mercury and cadmium telluride (HgTe/CdTe) quantum wells were the first experimentally reported 2D TI [117], confirming an earlier prediction [118]. InAs/GaSb heterostructures with an inverted band-gap were also reported for its topotronics potential [105, 119]. Figure 1.5(a) shows the simplified band diagram of such heterostructure (top). Figure 1.5(b) (bottom) show the band-structure, with the helical edge modes [119]. The particularity of

that system is that it can be tuned between 2D insulating to 2D TI phase via an external electrical field, which could be used as a QSH field-effect transistor [105]. Beyond these quantum-well structures, a central question in the field of TIs is whether a bulk 3D TI becomes a 2D TI upon reduction of its dimensionality [120]. It is not a trivial question, as it is known that coupling of the surface states on either sides of the sample may destroy the topological states [121, 122].

Isolated 2D materials The isolation of graphene [123], group-IV 2D materials (Si [124], Ge [125], Sn [126]) and compounds like hexagonal boron nitride (hBN) [127], MoS_2 [128], etc. have drawn a considerable attention over the last 10-15 years [129–131]. A wide range of electronic properties are available, from zero band-gap semiconductor (graphene) to insulator (hBN, E_G~5 eV). Many of these 2D materials offer unprecedented mechanical, thermal and optical properties [132]. Graphene was expected to be a 2D TI and was the model used in the development of the QSHE model [106, 133]. However the gap-opening at the K and K' points is very limited due to its weak SOC (a few μeV [134]) which precludes experimental observation of its 2D TI properties. Today, several families of 2D materials are investigated for their non-trivial topological band-structures: WTe_2, [135], group-IV (silicene [136, 137], stanene [137, 138] and germanene [137]) and group-V atomically thin materials, as discussed below in section 1.3.4 (note the suffix -ene is used here to refer to the 2D form of an elemental crystal).

1.3.4 Group-V 2D topological insulators

Crystal structures The group-V elements (P, As, Sb and Bi) in 2D form can crystallize in two main allotropes. Figure 1.5(b) shows the α phase that consists of two paired layers with a rectangular symmetry (with an atom almost at the centre of the unit-cell), and the β phase that possesses hexagonal symmetry and is analogue to graphene but with a buckling. The existence of these allotropes distinguishes the group-V 2D materials from the vast majority of the other 2D materials, which exclusively display hexagonal symmetries [129–131]. To the best of our knowledge, the group-V 2D materials are the only ones that have been demonstrated to crystallize into a rectangular lattice, with the exception of WTe_2 [139]. The variety of crystalline structures that the group-V 2D materials can be synthesized is of crucial im-

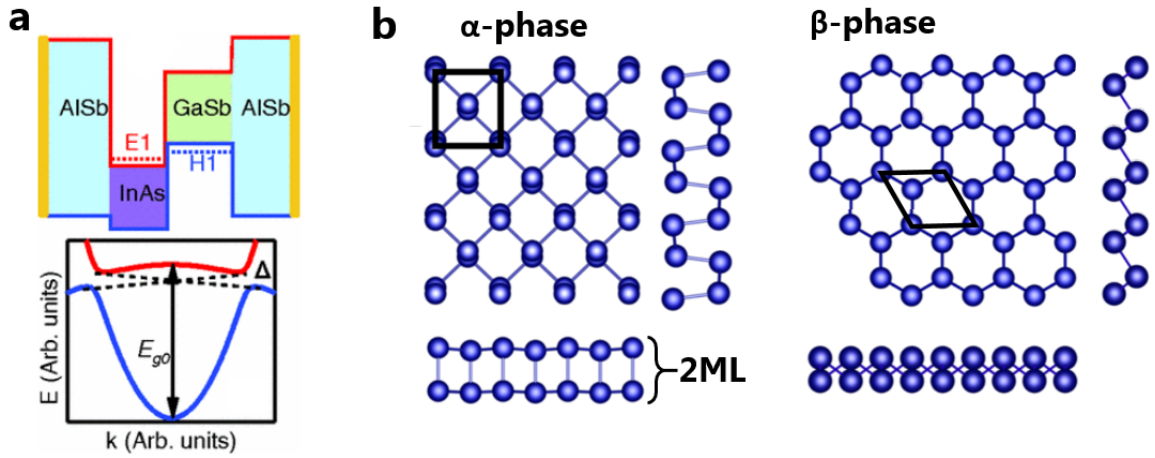

Figure 1.5: (a) Band-gap model of the InAs/GaSb heterostructure sandwiched between gated AlSb layers. The 2D TI band-structure is indicated below, with edge-states in dotted lines (from [119]). (b) Ball-and-stick models of the α and β phases, both from top and side views. Surface unit-cells are indicated.

portance in this thesis because the moiré patterns (see below that occur during superposition of different types of lattices are misunderstood.

Topological properties Several forms of bismuthene have been predicted to be topologically non-trivial: α-Bi [140], single-layer β-Bi [141, 142] and multi-layered β-Bi [143]. The most extensively studied of these is α-Bi, which has been investigated for more than 10 years, mostly as self-assembled islands on HOPG [144–151]. In this thesis, α-Bi is used as a layer onto which other group-V 2D allotropes are deposited. Antimonene (Sb) holds promise for topotronic devices too: β-Sb (under sufficient strain) [152] and multi-layered β-Sb [122] and predicted to have an non-trivial inverted band-structure. Recent calculations suggested that single-layered α-Sb is a topological semi-metal [153]. It is worth noting that nanostructures of 2D alloys $Bi_{1-x}Sb_x$ (its bulk form is known to be a 3D TI [111, 116]) have been recently investigated at UC, and the presence of brighter edges observed with tunneling spectroscopy suggests that these may potentially be 2D TIs [154].

1.3.5 Van der Waals heterostructures

Potential Multi-layered heterostructures comprised of 2D materials are known as van der Waals heterostructures. The intralayer bonding in a 2D crystal is typically covalent, whereas the cohesive order of a VDWH system is obtained via van der Waals interactions [130]. That

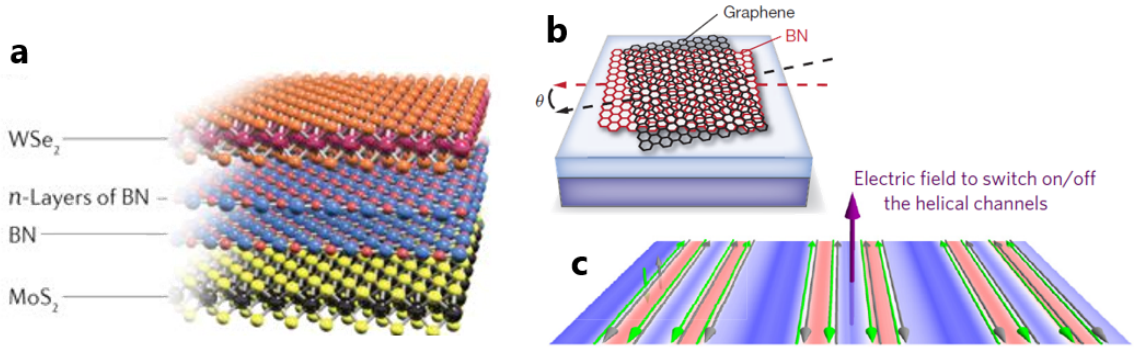

Figure 1.6: (a) Ball-and-stick model of a $MoS_2/(hBN)_n/WTe_2$ VDWHs device (from [155, 156]). (b) Moiré pattern in VDWHs (from [157]). (c) Topological order manipulation with moiré patterns (from [158]).

weak interlayer bonding permits to fabricate a VDWHs made of two or more 2D layers without the constraints of conventional interface engineering (e.g. diffusion length and lattice matching criteria). The VDWHs can be obtained via bottom-up (using successive deposition steps) or top-down approaches (fabrication of the individual layers and subsequent peel-off and assembly) [130, 132]. Figure 1.6(a) shows a model of a demonstrated VDWH made of $MoS_2/(hBN)_n/WTe_2$ has proposed as an optoelectronic device [155], where the number n of hBN layers modulates the energy band-gap of the structure. For more examples of VDWHs, refer to [156].

Moiré patterns One very interesting aspect of the VDWHs is that the rotation angle θ between two layers can drastically change the electronic properties of the heterostructure [157, 159–161]. Figure 1.6(b) shows the principle of the rotation of graphene layer with respect to an underlying hBN layer, leading to a moiré pattern (MP). It has been proposed [158] that MPs in VDWHs can locally modulate the topological order, which could lead to MP-engineered transistors. It is therefore relevant to focus the research and efforts into understanding the MPs in VDHWs, as MPs may open up new avenues in device design [162]. This thesis focuses on modeling the MPs observed in VDWHs made of group-V 2D materials, which possess topologically non-trivial band-structures as discussed previously in section 1.3.4. A more detailed literature overview on MPs is given in chapter 3.

Bi and Sb Samples comprised of multiple group-V 2D materials have not been investigated previously. Because this family of 2D materials hold promise in the development of future

topotronic devices, it is of primary importance to study their sequential assembly. Further theoretical and experimental investigations will almost certainly focus on the interaction and proximity effects between the topological orders of the various layers. To that effect, different superposition combinations of bismuthene and antimonene are investigated in this thesis (chapters 3 and 4) focusing primarily on the MPs that emerge in these heterostructures. Understanding the geometry of the MPs in experimentally observed structures and predicting it in other VDWHs is going to be vital in future topotronic device fabrication.

1.4 Scanning tunneling microscope studies

The challenges presented earlier both for the RENs and group-V VDWHs are likely to be addressed at least partially with scanning probe microscopy (SPM). SPM techniques, which includes scanning tunneling microscopy (STM) and atomic force microscopy (AFM), are ubiquitous in experimental nanoscience for their ability to image nanoscale features [163]. In this section, the literature of SPM on both RENs (and related materials) as well as on Bi nanostructures is briefly reviewed. For more details on the functioning principle of STM and AFM, refer to chapter 2.

1.4.1 STM of REN surfaces

Because the RENs decompose in air as discussed previously in section 1.2.3, it is not possible to grow a REN and image the surface unless STM or another technique is available in the vacuum system. REN samples have typically been passivated in the past with AlN or GaN capping layers, enabling optical and electrical characterisation [50], but not STM. GdN grown by chemical vapour deposition (CVD) has been imaged by AFM in air [164], but the resulting morphology was almost certainly the result of its rapid oxidation. RENs capped with a protective layers have been imaged via AFM in several works [58, 88, 165, 166] however these images reflect the morphology of the capping layer and not that of the underlying RENs and therefore these images will not be shown here. For details on the growth of RENs via molecular beam epitaxy (MBE), see chapter 2. A brief overview of the capping layers used previously is given in chapter 5.

Only a very limited number of publications have discussed the morphology of RENs im-

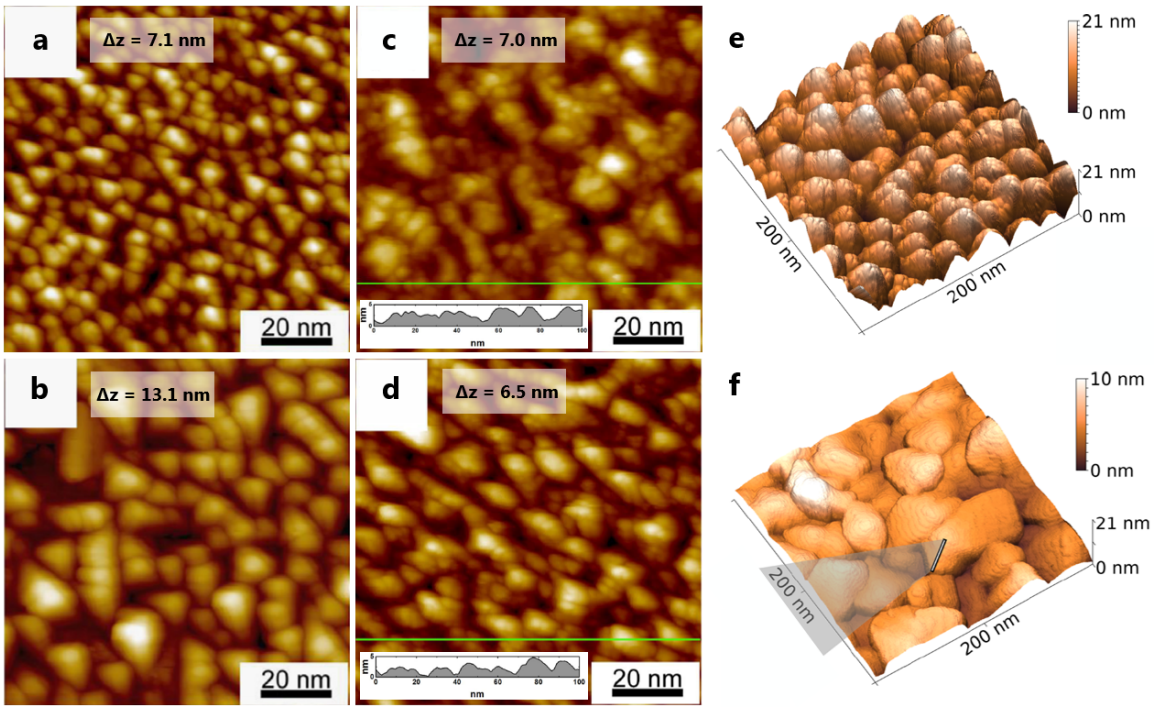

Figure 1.7: Published STM images of RENs adapted from [56, 62, 63]. STM image (V = +2 V, I = 0.1 nA) of a (a) 25 nm-thick and (b) 50 nm-thick epitaxial GdN(111) layer grown on AlN [56]. STM image (V = +2 V, I = 0.35 nA) of an epitaxial 13 nm-thick SmN grown on (c) GaN and on (d) AlN/GaN [62]. STM image of a 100 nm-thick SmN grown at (e) 700°C (V = +1.5 V, I = 1 nA) and (f) 800°C (V = +2.0 V, I = 1 nA) [63]. The line profile in (f) (not shown) reveals atomic steps of ~2.5 Å.

aged with scanning probe microscopy (SPM) [56, 62, 63]. Only one publication [56] reports STM measurements of an epitaxial GdN, investigating the surface morphology as a function of the layer thickness. Figures. 1.7(a) and 1.7(b) show STM images of GdN(111) thin films grown by MBE on AlN buffer layers. The grains are typically triangular as a result of the (111) orientation of the GdN films [56].

Two previous works report STM on SmN [62, 63]. Figures. 1.7(c) and 1.7(d) show STM images of SmN(111) thin films grown by MBE on GaN(0001) and AlN(0001) respectively [62]. No significant difference was observed via STM, however the crystalline quality of epitaxial SmN was improved significantly when grown using an AlN interlayer [62]. Figures. 1.7(e) and 1.7(f) show other STM images of SmN grown at different substrate temperatures (700°C and 800°C) which led to respectively (111) and (001) orientation [63].

It is important to note that the reported scanning probe images of GdN [56] and SmN [62, 63] shown in Fig. 1.7 were acquired at the *Centre de Recherche sur l'Hétéro-Epitaxie et*

ses Applications (CRHEA-CNRS) in Valbonne, France, using a combined MBE/STM system (thus imaging unoxidised REN surfaces). Such equipment is unfortunately no longer available in Valbonne, and similar system would be difficult to access elsewhere. Therefore, to pursue the investigation efforts of the REN surfaces via SPM, a reversible capping method must be developed. Such technique would permit to grow and to analyse via surface surface-sensitive techniques the REN samples in different chambers and different locations. This thesis focuses on such method (see chapters 5 and 6).

1.4.2 STM of Bi nanostructures

Bi islands Bi nanostructures have been studied with STM for several years [140, 146, 147, 149, 167]. When deposited on HOPG [149] or MoS_2 [153] with low coverages (less than a few nm) Bi grows as (110)-oriented Bi islands (rhombohedral notation [144, 168]) of α-Bi (considered in this thesis as two monolayers (2ML) thick Bi(110) layer as in Fig. 1.5). Because of the paired layer structure of α-Bi, the Bi(110) islands grow following 2ML, 4ML, 6ML thicknesses, adopting a 'wedding-cake' structure [146]. The island widths are governed by quantum size effects [149]. The presence of an underlying (~3 Å-thick) wetting layer below the bottom 2ML-α-Bi layer has been hypothesized based on the STM height measurements [146, 149]. For larger coverages (~10 nm and above), the Bi thin films reorient into the hexagonal Bi(111) phase [144].

Edge-states Figure 1.8(a) is a topography image of several Bi(110) islands grown on HOPG [140]. Both 2ML-thick and 4ML-thick Bi(110) islands are visible and their typical size is of the order of ~50 nm. The inset in Fig. 1.5(a) shows the atomic arrangement of the Bi(110) surface. Figure 1.8(b) shows scanning tunneling spectroscopy (STS) data obtained on a 4ML-thick Bi(110) island [140], where the DOS near E_F are resolved, here between -0.4 and $+0.4$ eV. A state near $E = 0.1$ eV is observed on the Bi(110) islands within ~2 nm of the edge [140]. This experiment is the first direct observation of an edge state on a 2D TI [170]. This result was essentially reproduced at UC also on different α-Bi thicknesses as shown in Fig. 1.8(c). The bottom-left corner of the image is a topographic STM image of a narrow 6ML-α-Bi stripe on a wider 4ML-α-Bi base. The top-right corner of the image is a DOS map (at $E = 100$ mV) obtained from dI/dV curves revealing the presence of the 1D edge-states.

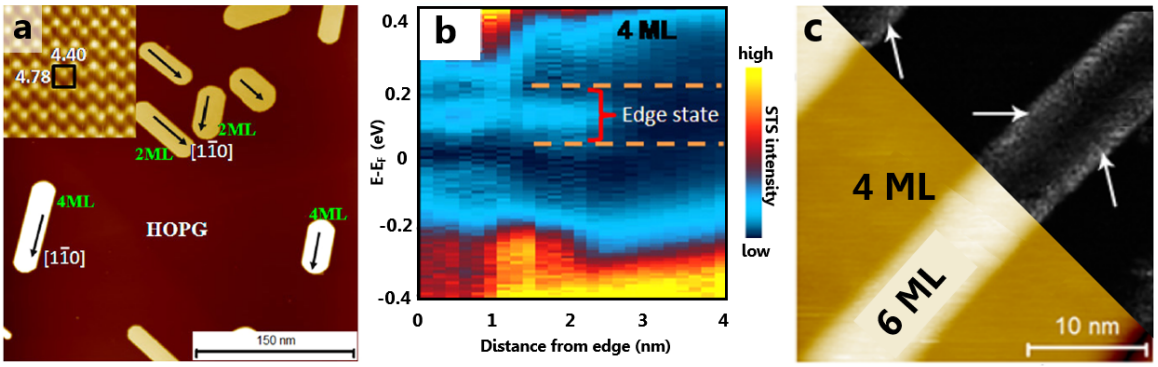

Figure 1.8: (a) STM image of Bi(110) islands (yellow/white) grown on HOPG (brown). The inset is a magnification obtained on Bi(110) revealing the atomic structure [140]. (b) STS signal recorded on a 4ML-Bi island as a function of the distance from the Bi[1$\bar{1}$0] edge. The high intensity indicates high DOS. An edge state at $E \sim +0.1$ eV is evidenced within ~2 nm from the Bi edge [140]. (c) Composite STM image of Bi(110) narrow stripe: topography (bottom left corner, in colour, $V = +1.0$ V, $I = 300$ pA) and STS mapping of the DOS for $E = 100$ mV (top right corner, grey-scale), adapted from [169]. The white arrows indicate the electronic edge states.

Antimonene Sb on the contrary does not form crystalline layers when deposited on HOPG [171]. Very little is known of antimonene to the exception of a very few experimental reports on β-Sb [172, 173]. Its structural properties in VDWHs and the MPs that emerge from superposition with other group-V 2D materials remain to be investigated.

Relevance The topological properties of Bi and Sb in their various allotropes have recently been demonstrated and research must now focus on pairing these layers together. It is expected, or at least possible, that the moiré patterns that arise from the various stacking combinations in VDWHs will modulate the electronical and topological properties. As discussed, the group-V 2D materials appear crucial in the development of future topotronic devices; it seems therefore essential to characterize and develop tools that model the MPs in these structures. The MPs on the surface of α-Bi grown on HOPG have been studied and explained previously using a commensurate model [151]. The variety of group-V 2D allotropes and the number of new combinations that can be designed can be viewed as a call for a more general model that do not require perfect atomic registry between the layers. Chapter 3 reviews the experimental characterisation of the MPs on the VDWHs. A ball-and-stick approach and an analytical model published earlier [174] are and used when possible to explain the MPs.

Chapter 4 presents a much more general approach for understanding the MPs using the reciprocal lattice.

1.5 Motivation and plan of this thesis

As reviewed in section 1.3, two dimensional topologically non-trivial materials promise a whole new physics in particular through the exotic edge states. Van der Waals heterostructures made of multiple 2D TIs will certainly be investigated and perhaps emerge as potential topotronic devices in the next few years. It is almost certain that the MPs will play a crucial role in the physics of these novel multilayered systems. Robust approaches for MP modeling are going to be necessary both for understanding of the experimentally observed MPs as well as for the prediction and design of future devices. Chapter 3 presents STM results of several group-V 2D materials that have established or potential topological properties (among which α-Bi, α-Sb, β-Sb and a new allotrope of bismuth, MBi) focusing precisely on characterizing the observed MPs. Two models for predictions are used, i.e. a ball-and-stick approach and an existing analytical model. Chapter 4 is an extension of the previous models, in which a universal approach is developed, potentially applicable for any VDWH. The agreement with the other modeling techniques is discussed and reciprocal space structures that this model includes described.

As discussed in section 1.2, the future of spintronics may well be depending upon further development of the intrinsic ferromagnetic semiconductors, among which the RENs (see section 1.2.3) are serious candidates. Despite being studied for several decades, the growth of RENs and their fundamental properties have only recently been formalised and the RENs are now open to more experimental characterisation. In particular, their surface properties for the most part are unknown. To address this, it seems essential to develop a method to enable ex-situ surface characterisation. Chapters 5 and 6 propose and investigate a method using a removable capping layer on GdN. Chapter 7 is a preliminary study on an curious phenomenon of the RE surfaces, i.e. the ease of reaction with molecular nitrogen N_2 thus forming a REN structure (nitridation), effect observed at room temperature at very low pressures. RE nitridation could be treated as an alternative growth method for RENs, but may also have a profound impact in catalysis and ammonia production industries.

An overview of the experimental methods used in this thesis is to be found in chapter 2. Finally, chapter 8 summarizes the key results of the different experimental investigations conducted for this PhD thesis, and critically discuss their limits. The last chapter also outlines the future work.

Chapter 2

Experimental techniques

This chapter overviews the various experimental methods that are used in this thesis. The aim is not to explain the detailed physics behind each technique, but rather to present their basic working principle and general methodology. Detailed descriptions are given in the standard references that are cited in the corresponding paragraphs. This chapter is divided as follows. Section 2.1 presents the methodology related to the growth and treatment of the samples, and section 2.2 reviews the various characterisation techniques used in this thesis. Finally, section 2.3 details the contribution of the people involved in the experiments. Note that the moiré pattern modeling is described in chapters 3 and 4 and the Sm capping/decapping experiments in chapters 5 and 6.

2.1 Growth and treatment of the samples

First, section 2.1.1 presents the STM/growth chamber system at University of Canterbury (UC). The deposition techniques used to achieve the van der Waals heterostructures (VDHWs) comprised of group-V 2D materials are described in section 2.1.2, and those required for rare-earth nitrides (RENs) in section 2.1.3. Sputtering is described in 2.1.4.

2.1.1 Combined system used in this thesis

The commercially available Scienta Omicron VT-AFM XA system [175] is shown in Fig. 2.1(a). Several main elements are indicated, including the ion and sublimation pumps. The samples are inserted via a load lock chamber located on the backside of the vacuum chamber isolated from the main chamber with a gate-valve (not visible in the figure). The wobblestick

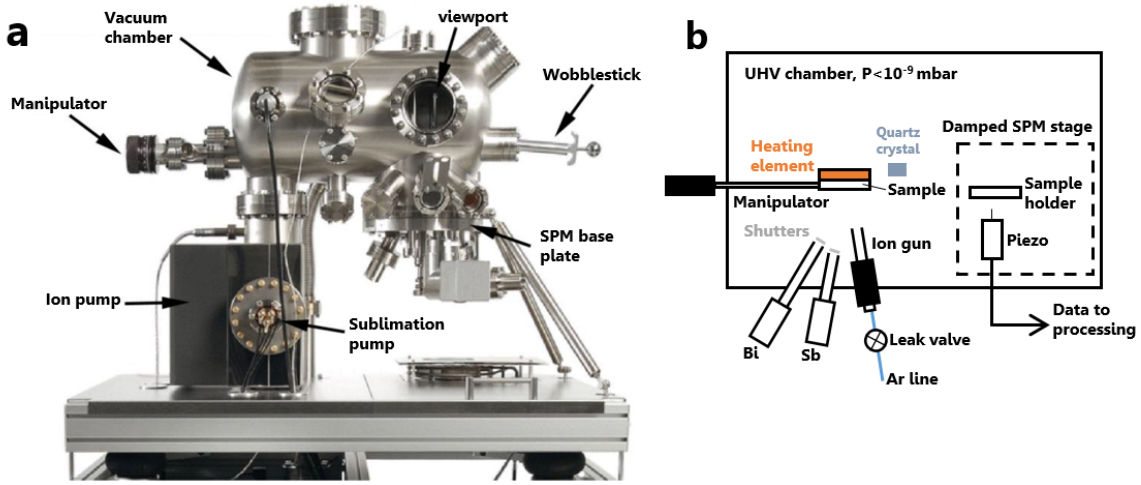

Figure 2.1: Overview of the Omicron VT-AFM XA system [175]. (a) Vacuum chamber with several elements indicated by arrows. The load-lock (not shown) is on the back-side of the chamber. (b) Schematic diagram of the UHV components important in this thesis. The manipulator allows critical positioning of the sample for Bi and Sb deposition (effusion cells indicated) and for Ar^+ sputtering. The heating element (orange) is used for Sm desorption and growth of VDWHs. The quartz crystal micro-balance is indicated. The ion gun is shown with the leak valve that allows fine control of the Ar^+ flow. The mechanically damped SPM stage consists of a sample holder and a piezo/motor unit that is used in the SPM experiments.

allows manipulation of the samples in the UHV chamber. A hot-filament ionisation gauge and a cold cathode gauge measure the pressure respectively in the vacuum chamber (base pressure $P < 10^{-9}$ mbar) and in the load lock (not shown). Figure 2.1(b) is a schematic representation of the sample growth, treatment and analysis components. The manipulator is used both for growth and treatment. The Bi and Sb effusion cells and their respective shutters are indicated. The heating element (orange) heats the sample through conduction on the back of the holder ($T < 700°C$). The temperature is measured via a thermocouple located in the sample holder. The ion gun, used for sputtering experiments is described in section 2.1.4.

2.1.2 Growth of van der Waals heterostructures

Substrates The VDWHs grown in this thesis are deposited on either highly-ordered pyrolytic graphite (HOPG) or molybdenum disulfide (MoS_2). The HOPG samples are commercially available ('SP1 grade' from SPI supplies [176]). The ~1×1 cm^2 HOPG crystals (~1 mm-thick) were mechanically cleaved in air using adhesive tape. The natural MoS_2 crystals used in the experiments in this thesis, provided by a collaborator (P. J. Kowalczyk, University of

Lodz, Poland) were cleaved using the same method. After mounting the substrates on sandard Omicron tantalum (Ta) transfer plates, they were loaded in the UHV system and heated for at least ~2 h at elevated temperatures (~500°C) to remove of the main contaminants. Scanning probe microscopy (SPM) of the substrates indicates atomic planes and terraces larger than $\sim 1 \times 1\ \mu m^2$. These are free of dangling bonds, enhancing the diffusion length of the adatoms [149]. This type of crystal deposition is often referred to as van der Waals epitaxy [177].

Deposition The VDWHs made of Bi and Sb are deposited on the substrates maintained at room-temperature. The solid sources (5N purity) are located in the refractory crucibles of effusion (or Knudsen) cells directly facing the substrate (see Fig. 2.1(b)). The operation is relatively simple and consists of heating the effusion cells sequentially as follows. First, the shutter of the Bi evaporator set to ~400°C was opened (flux ~0.1 Å/s, estimated from earlier calibration samples) to achieve a coverage ~1 nm. Bi growth on HOPG leads to the formation of self-assembled α-Bi 'wedding-cake' nanostructures [144, 146] (see also chapter 3). The shutter of the Sb effusion cell (set to ~300°C, i.e. flux ~0.01 Å/s) was then opened in order to decorate the α-Bi islands with about ~ 0.2 Å Sb. The coverage and deposition times were calibrated by previous students in the group [154]. The samples were imaged immediately after deposition with STM.

2.1.3 Molecular beam epitaxy of GdN

Figure 2.2 is a schematic diagram of the Thermionics growth system located in the crystal deposition lab in the School of Chemical and Physical Sciences, Victoria University of Wellington (VUW). The growth chamber consists of a series of evaporators, either electron-beam (for low vapour pressure elements, e.g. Gd) or thermal effusion cells (for high vapour pressure elements, e.g. Sm). The flux is monitored with a calibrated quartz crystal microbalance located near the sample holder. The base pressure of the deposition chamber is $P \sim 10^{-8}$ mbar.

Substrates The substrates used in this thesis are commercially available 2-inch n-doped Si(111) wafers, coated with epitaxial 100 nm-thick AlN(0001) layer (EasyGan [179]). The

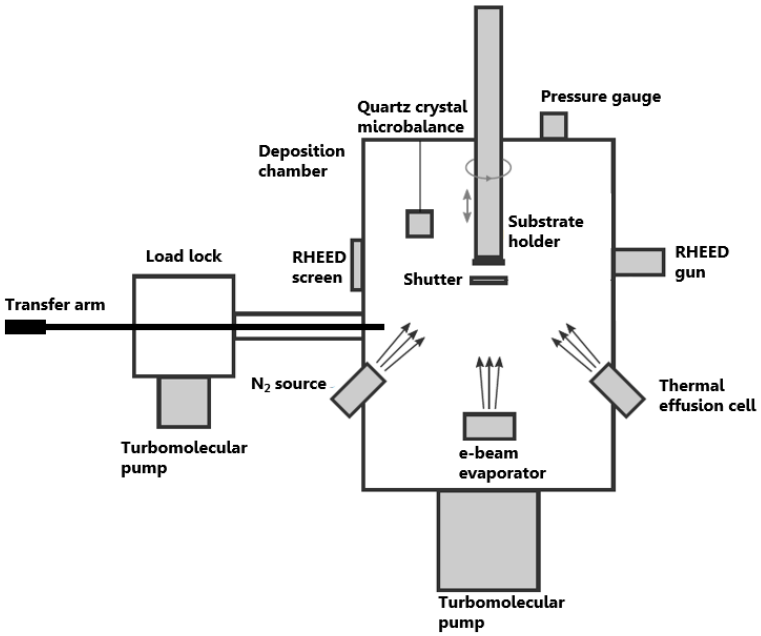

Figure 2.2: Thermionics growth system overview indicating the main growth and in-situ analysis components, adapted from [178].

substrates were loaded in the deposition chamber shown in Fig. 2.2 via the load lock. The substrates were heated to T~650°C (via the heating element located in the substrate holder) to get rid of the main contaminants.

Growth of GdN The GdN samples in this thesis were deposited via molecular beam epitaxy (MBE), at a growth temperature of T~650°C. Gd metal was evaporated using an electron beam in the presence of a molecular nitrogen (N_2) partial pressure of 1×10^{-4} mbar. It is important to point out that molecular nitrogen reacts spontaneously with Gd at the surface to form a GdN layer, even in the absence of activated N_2. The film deposition rate was ~ 0.1 nm/s and the film thicknesses where ~ 100 nm. After growth, the samples were left to cool down to room temperature. The growth of the Sm layer (either on bare AlN templates or on as-grown GdN) is detailed in section 5.2. The nitridation procedure is presented in detail in section 7.2.

Transport and storage of the REN samples The samples were taken out of the growth chamber and were immediately cleaved in air. The sample pieces were stored in a desiccator or in a vacuum-sealed bag for transport from VUW to UC (estimated pressure ~1 mbar). One

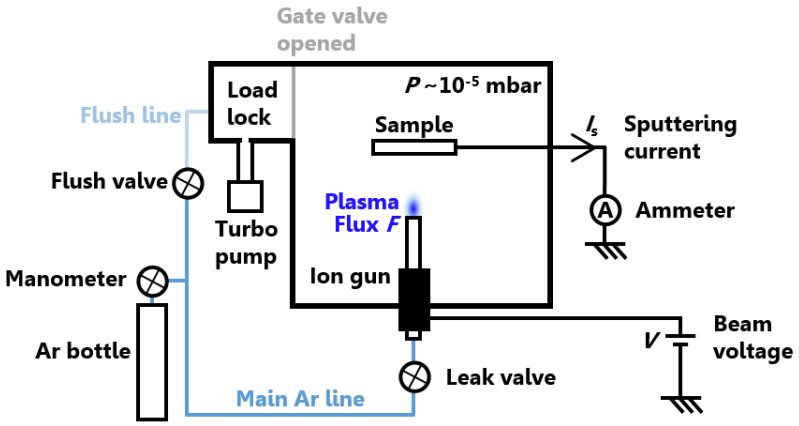

Figure 2.3: Sputtering operation during bombardment. Ar gas flows in the main line into the ion gun, where a built-in ionisation voltage generates a plasma. The main controls are the Ar flow via the leak valve and the ions kinetic energy via the beam voltage V. The sputter current I_s is read via an ammeter. Note the presence of the other valve for flushing.

of the sample pieces was subsequently transported to UC and the others were characterised at VUW or Robinson Research Institute (VUW), Lower Hutt. After transport to UC, the samples were mechanically cleaved into $\sim 1 \times 5$ mm^2 pieces, and mounted directly on a Ta plates for immediate insertion in the Omicron UHV system, or stored in a separate vacuum chamber (not shown, base pressure $P \sim 10^{-9}$ mbar) for later investigation. Between deposition at VUW and analysis at UC, the Sm/GdN and Sm/AlN samples were in ambient conditions ($P = 1$ atm) for an estimated time of 30 min and in vacuum in the sealed bags ($P \sim 1$ mbar) for about 2 days.

2.1.4 Sputtering

Sputtering is a technique used in chapter 6 for removing the oxide from the surface of the Sm samples exposed to air (in this thesis, 'sputtering' does *not* refer to a deposition technique). The sputtering experiments take place in the Omicron vacuum chamber at UC (Fig. 2.1) using a commercially available ISE-5 gun [180]. Essentially, argon (Ar) ions (5N purity Ar from BOC [181]) are accelerated in the vacuum chamber transferring their kinetic energy to the sample, in turn sputtering the surface. The experimental set-up is shown in Fig. 2.3 and is detailed as follows.

Operation principle After flushing the Ar line (via repeated pumping cycles using the turbo pump), the gate valve is opened. The ion and sublimation pump (see Fig. 2.1(a)), highly sensitive to Ar^+ ions, are therefore switched off. The beam voltage V or beam energy E [1] is set to the desired value ($V = 0.5 - 5.0$ keV). The sputtering conditions were always tested on a bare Ta sample plate first for fine tuning of the sputtering current I_s (typically a few μA) via the leak valve acting directly on the Ar^+ flux F and the pressure ($P \sim 10^{-5}$ mbar). The ion beam was focused on the sample (spot size ~0.5 cm), and a blue glow was typically visible at the gun extremity. When the pressure P and current I_s were stable, the sample was inserted in place of the Ta holder (after setting $V = 0$) and the sputtering starts after V is reset to the desired beam voltage. The sputtering conditions (P, V and I_s) were recorded during the entire bombardment. The samples were sputtered at fixed incidence angle $\theta = 45°$ (standard procedure [182]) and maintained at room temperature during the bombardment.

Sputtering yield A few important relationships between the different quantities are discussed here. The Ar^+ flux F directly impacts the sputtering current density J_s [182] as follows

$$J_s = \frac{F}{q} \tag{2.1}$$

assuming one electron per incident ion (which is expected from Ar^+ [182]). The sample holder is electrically grounded to allow the measurement of the sputtering current I_s. The sputtering density J_s could not be measured because the area is not directly measured (the estimated area participating to the charge transfer is estimated to ~1 cm^2). The yield Y is the amount of ejected atoms per incident ion, and is related to the sputtering rate $\frac{dz}{dt}$ as follows [182]

$$Y = \frac{q\rho}{J_s} \cdot \frac{dz}{dt} \tag{2.2}$$

where dz is the sputtered thickness during the time interval dt and ρ the atomic density of the sputtered material. The yield Y depends on various factors, including the beam energy E, the ion mass m, the binding energy at the surface of the material and the incident angle

[1] Note that the beam energy $E = qV$ is the kinetic energy of the ions with q the elementary charge.

θ [182]. Considering Ar^+ ions and a beam energy near ~1 keV, the reported values of the sputtering yield for a variety of materials in the literature fall typically between 0.4 and 20 [182]. These values can be used to estimate of the sputtering rate using equation (2.2) in chapter 6.

2.2 Sample characterisation

This section focuses on presenting the various characterisation techniques used in this thesis. The scanning probe microscopy (SPM) techniques are discussed first in sections 2.2.1 and 2.2.2 for scanning tunneling microscopy (STM) and atomic force microscopy (AFM) respectively. Scanning electron microscopy (SEM) and energy dispersive X-ray spectroscopy (EDS) analysis techniques are presented in section 2.2.3. Finally, the reflection high-energy electron diffraction (RHEED) and X-ray diffraction (XRD) are introduced in sections 2.2.4 and 2.2.5. Section 2.2.6 gives a few details about other techniques used very briefly in this thesis.

2.2.1 Scanning tunneling microscopy

Scanning tunneling microscopy (STM) was first demonstrated by IBM-Zürich researchers Binnig and Rohrer in the early 1980s [183–185] who were awarded the Nobel prize a few years later [186]. The principle is relatively simple and involves an atomically sharp metallic tip brought within a few Å of the conductive sample surface, and an applied potential between the sample and the tip that creates a tunneling current is measured as the tip scans the surface. This technique has revolutionised many fields of nanotechnology for its ability to image nanoscale features in real-space at atomic scale and to probe the electronic structure of materials [163]. For detailed literature on the general principles and applications of STM, refer to e.g. [187, 188].

Quantum tunneling Metal-insulating-metal tunneling has been thoroughly investigated in many standard references [189–192]. An important main result [189] is the tunneling

transmission probability T, approximated as

$$T(z,E,qV) \simeq \exp\Big[-2z\cdot\sqrt{\frac{2m}{\hbar^2}\big(\frac{\Phi_s+\Phi_t}{2}+\frac{qV}{2}-E\big)}\Big] \tag{2.3}$$

where z is the tunneling barrier width or tip-sample distance, Φ_s and Φ_t are the surface and tip work functions, m is the electron mass, $\hbar$ the reduced Planck's constant, V the bias voltage, and E the electron energy. One of the key aspects is the exponential dependence on z which is responsible for the sensitivity of STM. The tunneling current I_t (i.e. the rate of electrons flowing from tip to sample) depends on the density of states (DOS) of the sample D_s and of the tip D_t, and on the tunneling transmission probability T [191] as follows

$$I_t = \int_0^{qV} D_s(E)\cdot D_t(\pm qV \mp E)\cdot T(z,E,qV)\cdot dE. \tag{2.4}$$

Similarly, the tunneling current I_t depends exponentially on the tip-sample distance. Tunneling phenomenon is commonly illustrated with the idealised energy diagram in one dimension (1D) shown in Fig. 2.4(a). In this situation, a positive bias voltage V is applied such that the Fermi level of the tip is offset by qV. The tunneling current depends on the barrier height (Φ_t and Φ_s) and barrier width (z) and on both D_s and D_t (the latter approximated as independent of the energy). The local electronic structure near E_F has huge impact on I_t. For this reason the sample must have available conducting states in the region near $E_\mathrm{F}\pm qV$, which is typically not the case of insulators.

Operation principle The simplified working principle of the STM is shown in Fig. 2.4(b) and presented here. The sharp metallic tip (purple in Figure 2.4) is brought very close to the surface (green) until a set-point tunnel current I_s is detected (typically a few pA or nA) corresponding to a tip-sample distance $z \sim 1$Å. The position of the tip is handled with a piezoelectric system (simply referred as *piezo*, in yellow in the figure), controllable in all three spatial directions. The tunneling current I_t and the position z are recorded while the tip scans the surface of the sample. Essentially two imaging modes are available: (i) constant height mode, where z is constant and $I_t(x,y)$ forms the image and (ii) constant-current mode, where I_t is maintained constant forming a $z(x,y)$ image. In the constant-current mode, a feedback

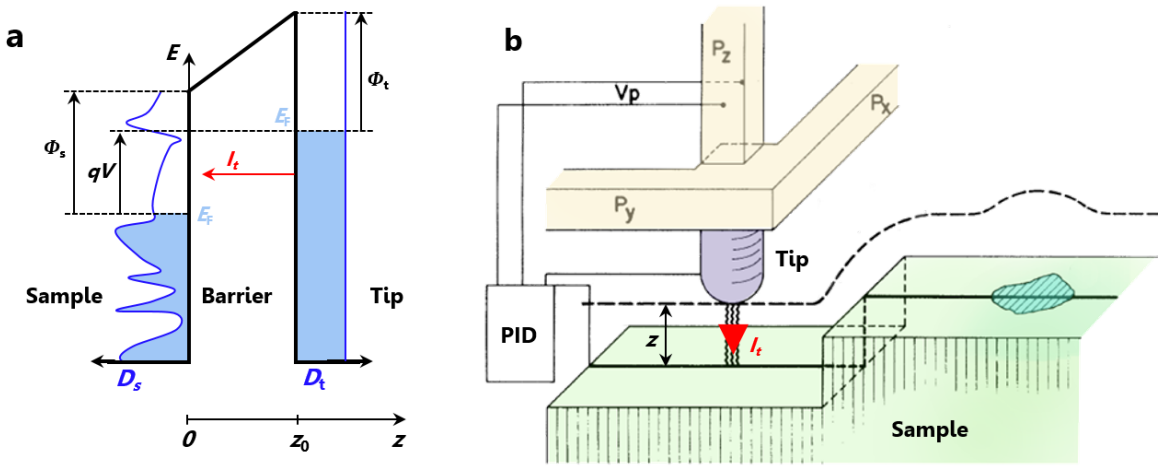

Figure 2.4: STM principle. (a) Simplified energy diagram of a tunnel junction. The density of states (D) of the sample (left) and tip (right) are indicated in blue. The states shown in light blue are occupied until E_{F}. Φ indicates the work function. The tip-sample distance is z_0 in this diagram. The tunneling current I_t is a consequence of the bias energy qV (that shifts the Fermi levels) and of the density of states between E_{F} and qV on the sample side. (b) Principle of operation of the STM, adapted from [184]. The piezo (yellow) controls the tip-position over the sample (green) and is sensitive to both topographic and electronic features. A PID controller monitors the tip-sample distance z in real-time.

loop monitored via a proportional-integral-derivative (PID) controller simultaneously measures I_t and controls the z-component of the piezo to maintain I_t as constant as possible. In Fig. 2.4(b) the dashed line represents the trajectory of the tip as it scans the sample. STM is sensitive to both topographic features and variations in the DOS (blue cross-hatched area). The apex of the STM tip must be atomically sharp in order to yield atomically-resolved images. Deviations from an ideal infinitely-sharp tip leads to artefacts in SPM images (e.g. blur, multiple imaging) as detailed in e.g. [193]. The STM stage (where the sample and probe are located in the device) is mechanically isolated from the environment by a damping system.

Experimental aspects In this thesis, the constant-current imaging technique is preferred in because this mode can image topographic features, thus avoiding tip 'crashing'. The STM stage is located in the Omicron VT-AFM XA UHV chamber, pictured in Fig. 2.1. The STM tips are made of manually cut platinum/iridium (Pt/Ir) alloys wires. The topographic data files are processed with Gwyddion [194]. To extract periodic information from the real-space STM images (e.g. lattice constant in atomically resolved images, or moiré patterns periods and fringe angles) the fast Fourier transform (FFT) is used [194, 195]. Unless mentioned

otherwise, the STM images shown in this thesis are acquired at room temperature ($T \simeq$ 293 K) in UHV conditions ($P < 10^{-9}$ mbar).

2.2.2 Atomic force microscopy

Atomic force microscopy (AFM) was invented by the same group at IBM-Zürich [196] that developed the STM. The general principle is very similar to STM: a probe is brought very close to the the sample and scans the surface. In AFM, the sharp tip mounted on an oscillating cantilever deflects as a result of van der Waals interactions between the tip and the sample. Two quantities are commonly used as a set-point in AFM (i) the force F between the tip and the sample (typically a few nN) or (ii) the frequency shift $\Delta f = f - f_0$ (in Hz) of the oscillation, where f_0 is the reference frequency at a large tip-sample distance z. The frequency shift Δf for $|\Delta f| \ll f_0$ is given by [197]:

$$\Delta f = -\frac{f_0}{kA^2}\langle F(t)z(t)\rangle \tag{2.5}$$

where A is the amplitude of oscillation (in nm), k the spring constant of the cantilever. The brackets indicate the mean value across one oscillation cycle. It has been shown [198, 199] that both $F(z)$ and $\Delta f(z)$ can be modeled by a Lennard-Jones potential as illustrated in Fig. 2.5(a). At large tip-sample distances, both F and Δf are zero. When the tip is brought closer to the surface, its oscillation is damped and the cantilever frequency decreases (typically a few Hz). The tip is attracted to the surface through van der Waals interactions, until at a certain tip-sample distance F rises sharply due to the Pauli exclusion principle. Both F and Δf are minimised for a value of z, typically the Δf minimum position is further away from the surface than the position of the F minimum ($z_{\text{min}} \sim 1$ nm).

Operation principle Figure 2.5(b) shows the measurement principle of the cantilever deflection. A laser source shines on the back of the cantilever and is reflected onto a photodetector, which can detect the frequency shift Δf or the force F.

Experimental aspects Similarly to STM described in section 2.2.1, two modes are available: constant set-point (here Δf) or constant height. In this thesis we use exclusively the

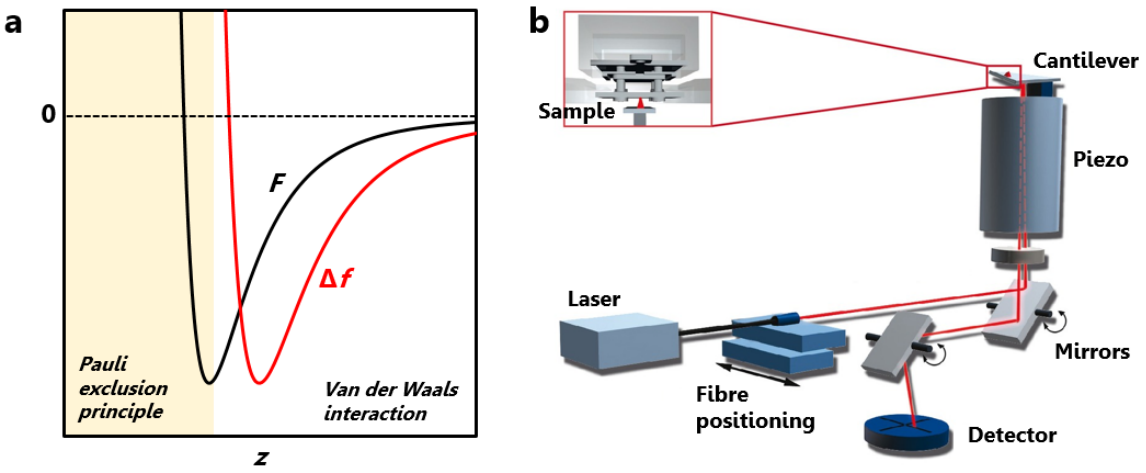

Figure 2.5: AFM principle. (a) Lennard-Jones model of the frequency shift Δf (red) and force F (black) as a function of the tip-sample distance z. (b) Principle of operation of the AFM. A laser (red line) is shun onto the back-side of the cantilever. The deflection impacts the reflected light, and is sensed on the photodetector.

constant Δf imaging in non-contact mode obtaining $z(x,y)$ images. All the AFM images in chapter 5 and 6 were recorded in UHV conditions with the Omicron VT-AFM and used a set-point in the range $\Delta f = -25$ to -10 Hz. The cantilevers (SuperSharpSilicon from Nano Sensors [200], typically $f_0 \sim 160$ kHz) and were glued on the Omicron cantilever transfer plates before insertion in the UHV chamber. The AFM image shown in Fig. 7.3 in chapter 7 was obtained with a NaioAFM device from Nanosurf [201] in air, located in the clean room Lab at VUW.

2.2.3 Scanning electron microscopy and energy dispersive spectroscopy

Scanning electron microscopy Scanning electron microscopy (SEM) is a very standard technique in material sciences and details can be found in reference literature [202]. It consists of a scanning electron beam focused on the sample, and a detector. The basic principle is shown in Fig. 2.6(a). Typically the secondary or backscattered electrons are used to create the image, typically allowing resolution of features larger than a few tens of nm. It is a relatively easy and fast technique, giving information about the surface topography of the sample. In this thesis the SEM is a commercial JEOL 7000F FE-SEM [203]. The images are acquired using secondary electron imaging mode (SEI) with an acceleration energy of $E = 15$ keV.

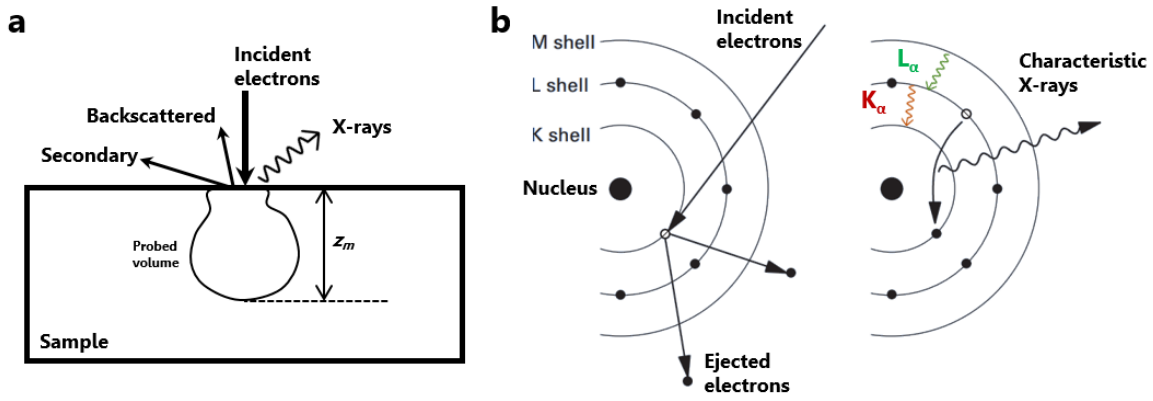

Figure 2.6: (a) SEM principle. The focused incident electrons hit the sample, creating backscattered and secondary electrons (as well as others, not described here). The emitted X-rays and electrons originate from the volume indicated with a characteristic depth z_m. (b) Schematics of X-ray emission, indicating the origin of the K_α and L_α photons.

Energy dispersive X-ray spectroscopy Energy dispersive X-ray spectroscopy (EDS) is an analytical technique for elemental characterisation. The incident electron beam ($E \sim 5-20$ keV) ejects core electrons, leading to radiative recombination in the X-ray range ($E_{\text{photon}} \sim 1-10$ keV). Figure 2.6(b) illustrates the emitted X-rays. Each element possesses it own characteristic signature. The X-ray photons are detected with a spectrometer yielding the EDS spectrum (typically the L_α and M_α for the elements of interest in this thesis). It is customary [202–204] to use the empirical Castaing formula to estimate the penetration depth z_m (in μm) of the electrons, given as follows

$$z_m = 0.033\ (E^{1.7} - E_c^{1.7})\frac{A}{\rho_m Z} \tag{2.6}$$

with E the acceleration energy (in keV), E_c the lowest X-ray emission energy of the element (in keV), A the atomic mass, ρ_m the density (in kg/m^3) and Z the atomic number of the considered element. For Sm one obtains $z_m \simeq 0.9$ μm with $E = 15$ keV. EDS, which is mostly sensitive to heavy elements, is used in this thesis to verify the removal of the Sm cap in chapters 5 and 6.

2.2.4 Reflection high-energy electron diffraction

Reflection high-energy electron diffraction (RHEED) is a surface-sensitive technique that uses the atomic lattice for scattering. It is a very common analysis technique, in particular for monitoring in-situ and in real time the crystal growth, i.e. the front growth profile [205]. Figure 2.7(a) shows the RHEED schematic set-up where the emitted from at grazing angles from the electron gun to the screen after reflection on the sample. The kinetic energy of the electrons this thesis is $E = 15$ keV. The diffraction patterns can be explained in terms of the Ewald sphere intersecting the reciprocal lattice of the sample [31, 206] as schematically shown in Fig. 2.7(a). Coherent interference of the electron wave is possible only if the surface is atomically well-ordered. Only the top half of the pattern is visible on the screen due to shadowing effect of the sample.

Surface analysis RHEED provides information on both the surface symmetry and the crystallographic orientation, and also provides information about the surface quality. Figure 2.7(b) shows in a schematic way, different surface structures and their corresponding RHEED patterns. Typically, if the surface of the sample is atomically flat (typically occuring during 2D growth mode) the RHEED pattern are comprised of vertical streaks. In the case of a surface reconstruction (not shown) the pattern is made of streaks as well as satellite peaks [206]. If the surface is rough (e.g. if the growth mode is 3D), the electrons will transmit through the islands and surface irregularities, and as a consequence a transmission pattern in the form of individual spots is formed. Figure 2.7(c) (top) is an experimental RHEED pattern from the literature of a GdN(111) surface grown by MBE [56]. The pattern is made up of spots indicating a 3D growth-mode. The presence of 'twin spots' (arrows) are due to the coexistence of twinned domains of fcc GdN(111) rotated by 180° [56, 166].

Experimental aspects RHEED patterns were acquired in-situ during the growth of the Sm/GdN samples in the VUW Thermionics UHV chamber (see Fig. 2.2). The RHEED patterns are acquired with a digital camera with a sampling rate of 1 image per second.In the experiments of chapter 7, the image files were analysed with a program designed by J. Chan [178], which measures the streak spacing. The streak spacing is directly related to the reciprocal lattice of the surface which allows to determine the (real-space) surface lattice con-

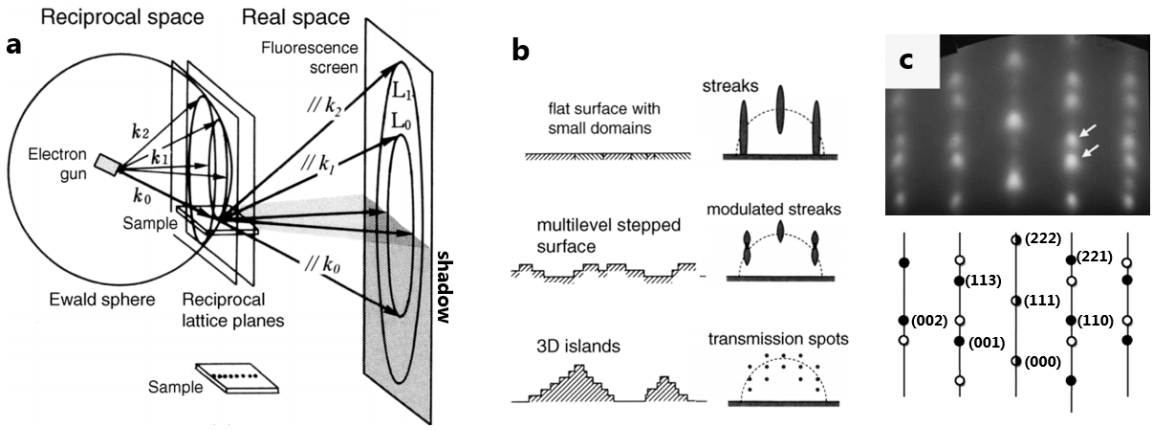

Figure 2.7: RHEED principle and GdN RHEED pattern. (a) Reciprocal lattice and real-space RHEED pattern, from [206]. (b) Schematics of realistic surface and their corresponding RHEED patterns. (c) Experimental RHEED pattern of a GdN(111) surface along the GdN $\langle 1\bar{1}0 \rangle$ direction (top) indicating two twin spots (white arrows), and geometric model of the RHEED for GdN (bottom), adapted from [56].

stants relatively to a known surface, usually the AlN template. For the other sample growth, RHEED was used mainly as a measure of the qualitative surface quality of the GdN and Sm crystals during deposition, and of the AlN templates.

2.2.5 X-ray diffraction

In X-ray diffraction (XRD) photons are scattered by the crystal lattice of the sample, forming characteristic patterns. XRD is a very standard crystallography technique and more details on the experimental set-up and applications can be found in the literature [207, 208]. Constructive interference is observed when the Bragg law [31]

$$n\lambda = 2d_{hkl}\sin\theta \tag{2.7}$$

is satisfied, where n is an integer, λ is the source wavelength (in the experiments we use the $Cu_{K\alpha}$ emission line λ = 1.5406 Å), d_{hkl} the distance between two (hkl) planes of the considered crystal, and θ the incidence angle relative to a plane. In this thesis $\theta - 2\theta$ were used to characterise the out-of-plane crystalline sturcture and texture of the films.

2.2.6 Others

Raman spectroscopy Raman spectroscopy is an optical characterisation technique, sensitive to the vibrational modes of the sampled material. Monochromatic photons from a laser

are absorbed and re-emitted via inelastic scattering, where the frequency shift σ (typically in cm^{-1}) corresponds the vibrational energy (phonons) of the lattice. For more details on that technique, refer to e.g. [209, 210]. In chapter 6, Raman spectroscopy was acquired with a Horiba Jobin-Yvon Raman spectrometer. The laser (λ = 514.5 nm, power ~ 1.8 mW) had a spot size of ~1.5 μm. The spectra were obtained at room temperature in ambient conditions.

Magnetisation measurements Magnetic measurements were carried out at Robinson Research Institute (VUW), Lower Hutt using a superconducting quantum interference device (SQUID) [211]. The commercial measurement system yields a magnetisation hysteresis loop $M(H)$ under magnetic fields up to 7 T at temperatures as low as 2 K. In chapter 5, the time-dependent saturation magnetisation $M_{sat}(T)$ were obtained from field-cooled curves.

Electrical characterisation Resistivity measurements in chapter 5 were performed using a four-terminal device using the van der Pauw geometry. The temperature-dependent resistivity data was acquired using a liquid helium cryostat with the temperature ranging from 4 K to room temperature.

2.3 Contribution to the work in this thesis

All the work in this thesis was done and written by the author, with the exception of the following significant contributions.

The group-V VDWHs samples in chapter 3 were grown conjointly with Dr. T. Maerkl, I. V. Mahajan and Dr. P. J. Kowalczyk. The STM data was jointly acquired with Dr. T. Maerkl, I. V. Mahajan and Dr. P. J. Kowalczyk.

The REN samples (chapters 5, 6 and 7) were grown with J. Chan and Dr. F. Natali (occasionally with help from F. Ullstad, W. Holmes-Hewett and J. Miller). The RHEED patterns were acquired in concert with J. Chan and F. Natali. The RHEED data in chapter 5 was analysed by J. Chan. The XRD characterisation was performed by J. Chan, J. Miller and W. Holmes-Hewitt. The magnetisation measurements were carried by J. Chan. Electrical characterisation was performed conjointly with J. Chan. Raman spectroscopy was undertaken and interpreted in collaboration with H. J. Trodahl.

Chapter 3

Moiré patterns in van der Waals heterostructures

3.1 Introduction

Moiré patterns (MPs) (from French *moire*, a type of fabric made of superposed silk layers, derived from English *mohair*) are, in the general sense, the interference patterns observed when two meshes are overlaid. Notably visible on the folds of silk or when walking past railing fences, MPs are due to similar but imperfect lattice matching, leading to large-scale fringes. They appear in a broad range of systems of different scales: in sampling they are related to aliasing issues, but can also be deliberately used for precision measurement in mechanical devices. In condensed matter physics they occur when an ultra-thin crystalline layer is superimposed on another crystalline structure [212]. The *overlayer* typically has a thickness of a few atomic layers, while the *underlayer* can either be a bulk material or another thin film. The crystallographies of the overlayer and that of the underlayer must be different in order to lead to a MP. This interference phenomenon appears as a periodic modulation on the surface of the overlayer.

Figure 3.1 shows schematically how MPs are generated. Panels (a) and (b) are respectively the underlayer and overlayer lattices (top view). The two layers exhibit a hexagonal symmetry, and possess a $\sim 10\%$ lattice mismatch. Their superposition (c) leads to a MP. The lighter spots on the image correspond to the local positions where the atoms from the underlayer and the overlayer are in registry. These spots are referred to as *moirons*. In contrast to the moirons, the areas in between (darker) are where the atomic positions are out of

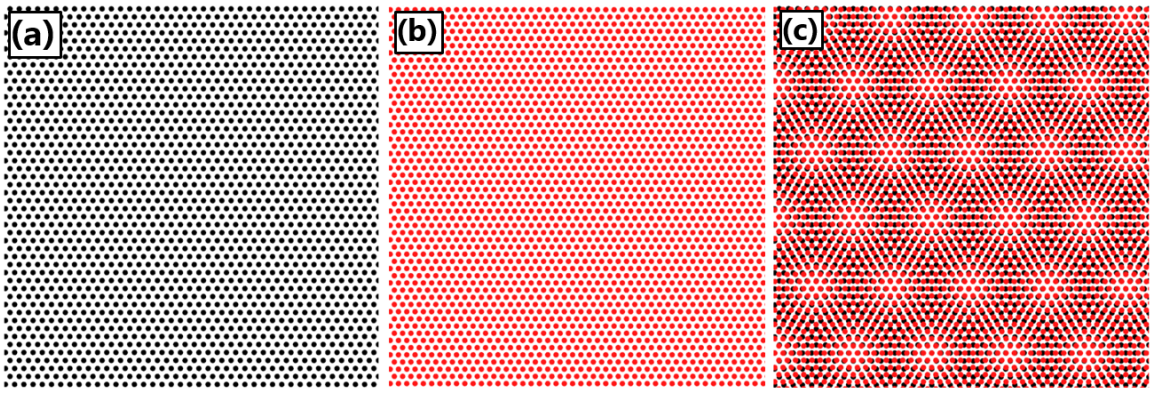

Figure 3.1: Moiré pattern formation: (a) and (b) are the under- and overlayer hexagonal lattices with dissimilar lattice constants ($k_b/k_a \simeq 1.1$). (c) Superposition of the atomic lattices in (a) and (b). A discrete MP is observed: light spots appear where atoms from layer (a) and (b) are in registry. All ball-and-stick simulations are generated with VESTA [213] and displayed to scale.

alignment.

Brown's group at University of Canterbury has focused their research on bismuth and antimony nanostructures for more than ten years [144, 146–151, 154, 169, 171], mainly using Scanning Probe Microscopy (SPM). The recent drive towards the fabrication and characterisation of van der Waals heterostructures [130, 132] (VDWHs) has led to the realisation of multiple systems in which MPs are observed with a high degree of reproducibility. As described in chapter 1, bismuthene and antimonene hold strong promise for novel topotronic devices. The study of the MPs on their surface is therefore important: for understanding the structures of the VDWHs, but also because the MPs can modulate the topological properties of the VDWHs [157–159, 214–216].

This chapter focuses on the MPs generated by the stacking of antimonene and bismuthene, onto either HOPG or MoS_2 substrates. The goal of this study is to successfully model the MPs observed by STM, and to derive critical information on the lattices. Section 3.1 introduces the necessary conditions for observing MPs via SPM as well as the early experimental observations. It also reviews some of the recent advances in theoretical and experimental work on MPs on VDWHs. Section 3.2 details the framework of the characterisation, and the analysis tools for the MPs. Finally, section 3.3 presents the results of characterisation and modeling (simulation and calculation) of the MPs observed at UC.

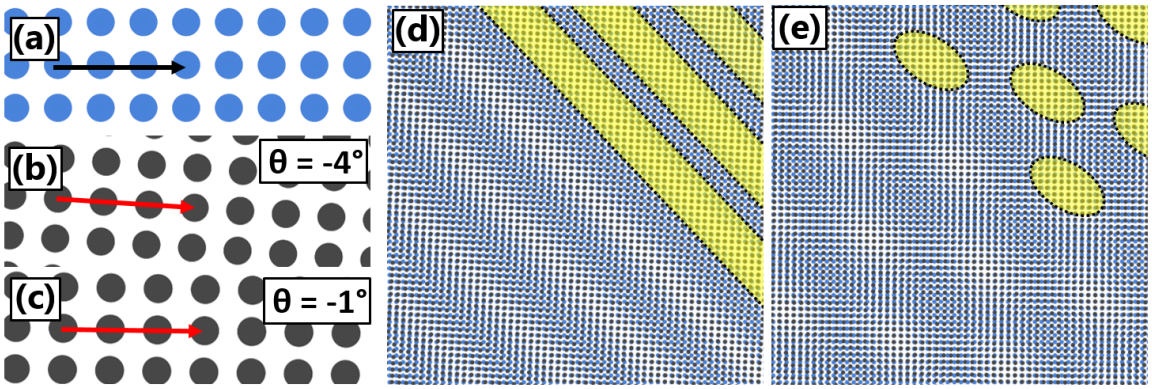

Figure 3.2: MPs simulations: (a) underlayer square lattice (4.5×4.5 Å^2). (b) Overlayer rectangular lattice (4.2×4.8 Å^2) rotated by $\theta = -4°$ with respect to the underlayer. (c) Same overlayer, rotated by $\theta = -1°$ (c). (d) Superposition of (a) and (b). The MP shows up as fringes. (e) Superposition of (a) and (c). The width of the simulated images is 400 Å. In this case, the MP shows up as moirons. The yellow zones identify the fringes in (d) and the moirons in (e). The arrows emphasize the crystalline directions in (a-c).

3.1.1 Concept

MPs are in this thesis only characterised through classical geometry, where the underlayer and the overlayer are described by non-interacting, rigid, 2D lattices and by the relative angle θ between the two. The resulting MPs can be described by a Bravais lattice whose lattice parameters are often much larger than the individual layers' unit vectors. The superposition of two lattices that are different or rotated breaks the unit cell translation symmetry. The new translation symmetry vectors of the system are given by the unit vectors of the MP super-lattice, that are not always commensurate with the underlayer or overlayer.

The prediction of the MPs based on the crystallography of the underlayer and that of the overlayer is not trivial. Minimal shift in the geometry of one of the layers can greatly impact the emerging interference patterns. This sensitivity is emphasised in Fig. 3.2. Ball-and-stick simulations are performed using a square lattice (a) overlapped with a rectangular lattice, tilted by $\theta = -4°$ in (b) and $\theta = -1°$ in (c). In (d) the superposition is performed with $\theta = -4°$, and MP fringes appear clearly. In (e) the superposition is such that the rotation angle is reduced to $\theta = -1°$. Clearly, this superposition leads to moirons instead of fringes. In both images, the MPs are highlighted in the top-right corner in yellow. This example illustrates that a small change, here a rotation of only 3° of the overlayer, can imply a huge change on the observed MPs. Similar examples can be constructed by varying the lattice constants or

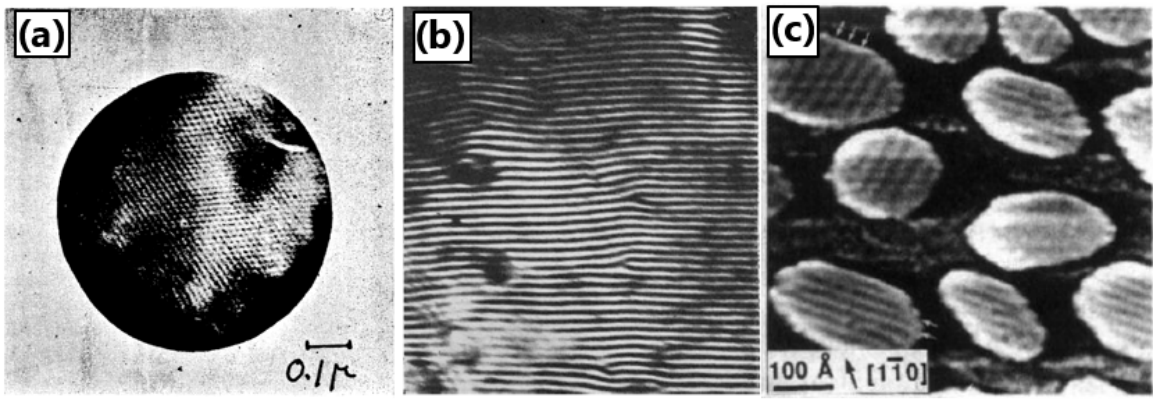

Figure 3.3: Early MPs observations. (a) First ever observation of MPs on a crystal, namely on graphite [217]. The electron micrograph shows a clearly visible hexagonal MP and manifests great ordering. (b) TEM image (magnification ×500000) of Pd film on Au(111) thin films [218]. The fringe-like MPs appear uneven where an edge dislocation is present. (c) STM image (75×75 nm^2) of 2-ML thick Bi(110) islands grown on GaAs(110) substrate [229].

the symmetry of a layer.

3.1.2 Early MPs observations

In solid-state systems, MPs have been first observed via electron microscopy on graphite [217]. Figure 3.3(a) reproduces one of the first micrographs of MPs. The MP are visible here as dark spots arranged in 3-fold symmetry. Research later focused on ultra-thin films deposited on metallic surfaces [218, 219], and on single crystals of polyethylene [220–222]. MPs were used to highlight the presence of dislocations [218, 219, 221–223] and to track structural changes during heat treatment [224]. Figure 3.3(b) shows a sample of an ultra-thin Pd film grown on Au(111) [218]. Despite a rather good ordering of the fringes, several fork-like fringes indicate the presence of edge-dislocations. With the advent of SPM allowing local surface sensitive measurements, MPs are routinely observed. Many reported MPs originate from graphite systems [225–228] or from ultra-thin films deposited onto a variety of flat surfaces: Bi on GaAs [229], Pb on Ag(111) [230] among others. Figure 3.3(c) displays an STM image of Bi(110) islands grown on GaAs(110) substrates. The mismatch between the under- and overlayer lattices gives rise to a MP in the form of fringes.

3.1.3 Moiré patterns as a method to control surface properties

Until the early 2000s, MPs are reported as essentially a method to monitor or confirm the structure of ultra-thin layers, e.g. lattice mismatch or defect presence.

More interestingly, the MPs can themselves possess interesting properties. The surface band structure of a crystal is sensitive to variations in the local strain: MPs can therefore modulate the electronic properties. They are seen as a perturbation that leads to the formation of 'minibands'. Localised, periodic surface states are revealed by STM spectroscopy [214], capacitance spectroscopy [231] and transport measurements [129, 157, 160].

This becomes more fascinating in some quantum-spin Hall insulators and semi-metals (see chapter 1). For example, the Dirac points of the graphene/hBN system in the first Brillouin zone (FBZ) can be shifted [214–216, 232] and may offer controllable Van Hove singularities via the rotation angle θ between the two lattices [159]. Very recently, graphene/graphene systems have been proven to exhibit superconductivity at specific rotation angles referred to as 'magic angles' superlattices [161].

These novel means of manipulation of the states of matter (in particular through a new degree of freedom in solid-state systems, the rotation angle θ) may allow control of the properties of future electronic devices. For example, the MPs fringes have been proposed to channel spin-polarised currents under sufficient strain at the correct rotation angle [158]. Moreover, MPs can give rise to fractal quantum Hall effect [129, 157, 160], confirming earlier theoretical works on 'Hofstadter Butterflies' [233].

There seems to have a fascinating coupling between MPs and electronic properties, in particular for materials hosting topological states. This obviously makes the study of MPs very relevant in the context of bismuthene and antimonene STM studies.

3.2 Characterisation and prediction

This section presents the tools that are available to us for characterizing MPs and for predicting them. First, we define the underlayer, overlayer, and MP superlattice. The experimental procedure for MP characterisation is briefly explained. Then the simulation technique based on simple superposition is presented as well as the analytical prediction model.

3.2.1 Definitions and experimental procedure

3.2.1.1 Vectors and angles

In order to characterize experimental MPs and to develop models for their prediction and simulation, geometrical definitions of (i) the underlayer lattice, (ii) the overlayer lattice and (iii) the MP superlattice are required. Since all three are 2D Bravais lattices, each is described by two independent 2D primitive vectors. Figure 3.4 shows the essential vectors and angles for the description of the MPs, adapted from [174]. The underlayer unit vectors are referred as $\mathbf{R_1}$ and $\mathbf{R_2}$, while the overlayer's are denoted as $\mathbf{R'_1}$ and $\mathbf{R'_2}$. The lattice parameters are R_1, R_2, R'_1 and R'_2. The relative rotation θ between the two layers is defined as the angle between $\mathbf{R'_1}$ and $\mathbf{R_1}$. The resulting MP superlattice, much larger than the individual lattices, is described by $\mathbf{R}_{\mathrm{M1}}$ and $\mathbf{R}_{\mathrm{M2}}$. Therefore the position of any moiron is given by an integer linear combination of $\mathbf{R}_{\mathrm{M1}}$ and $\mathbf{R}_{\mathrm{M2}}$. β is the angle between by $\mathbf{R}_{\mathrm{M1}}$ and $\mathbf{R}_{\mathrm{M2}}$. In Fig. 3.4, the moirons are located at the tip of the arrows $\mathbf{R}_{\mathrm{M1}}$ and $\mathbf{R}_{\mathrm{M2}}$. The equivalent fringes M1 and M2 are the lines connecting the moirons along the directions respectively given by $\mathbf{R}_{\mathrm{M2}}$ and $\mathbf{R}_{\mathrm{M1}}$. They are drawn with blurred lines in light blue (M1) and dark blue (M2).

It is more convenient in some cases to refer to periods λ_1 and λ_2, that may differ from the lengths R_{M1} and R_{M2}. For example, if the MPs appear as fringes, only one period can be directly observed. The moiré fringe angles δ_1 and δ_2 are, unless specified otherwise, defined with respect to $\mathbf{R_1}$, such that $0 < \delta < \pi/2$. This translates to

$$\lambda_i = R_{Mi} \sin\beta \tag{3.1}$$

$$\delta_1 + \delta_2 + \beta = \pi \tag{3.2}$$

3.2.1.2 Experimental moiré patterns

The simplest example of a VDWH, and the most reported, graphene-graphite, will be used to illustrate both the characterisation and the different methods of prediction throughout this section.

In the present experiments, the MPs are observed via STM, and they appear as a periodic modulation of the topography. STM imaging has long proven its capacity to measure the

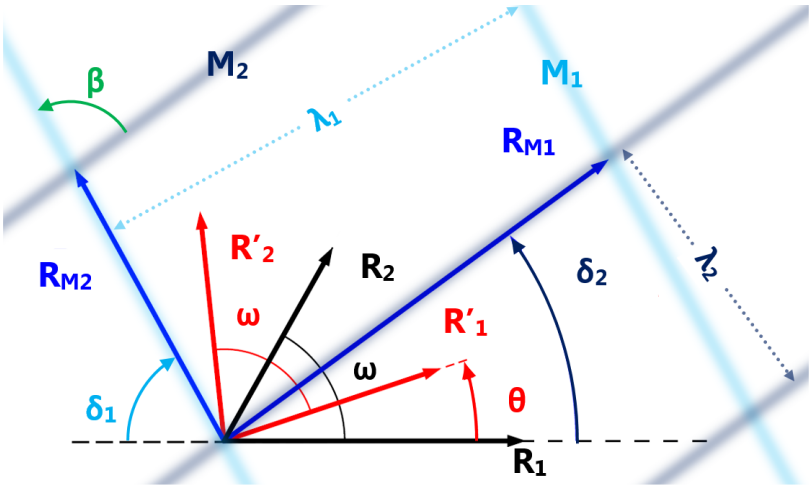

Figure 3.4: Vectorial and angular definitions for full description of a MP for an arbitrary oblique lattice symmetry (note that underlayer and overlayer share identical surface unit cell angle ω). $\mathbf{R_1}$ and $\mathbf{R_2}$ are the underlayer unit vectors (black), $\mathbf{R'_1}$ and $\mathbf{R'_2}$ are the overlayer unit vectors (red), misaligned to the underlayer's lattice by θ. The moiré lattice vectors, $\mathbf{R}_{M1}$ and $\mathbf{R}_{M2}$ are shown in blue. The equivalent moiré fringes (blurred lines) are depicted for M_1 (light blue) and for M_2 (dark blue). Moirons are located at the intersections of M_1 and M_2 fringes. δ_1 and δ_2 are the fringe angles (in reference to $\mathbf{R_1}$). The periods λ_1 and λ_2 are indicated, as well as the superlattice angle β. Adapted from ref. [174].

surface lattice constants of crystalline structures as reviewed in chapter 2. The method to characterize the superlattice is the same and equally relies on the 2D fast Fourier transforms (FFT) of the STM images. Fourier transform techniques have been previously used for the characterisation of MPs in graphene-graphite systems [234–236]. The MPs are characterised by a single fast Fourier transform (FFT) of one STM image (for the periods information), or two STM images: the MP-containing image and the atomically resolved image of the underlayer (for angular relationship with the underlayer δ determination).

To illustrate the process of experimental characterisation of the MPs, Fig. 3.5(a) displays an STM image of graphite from the literature [228] in which both the atomic structure and the MP are resolved. Here, the MP arises from the misalignment of the top monolayer (ML) of graphite (i.e. graphene) with respect to the bulk graphite underneath. The MP shows up as an hexagonal superlattice of moirons. The characterisation of both the crystal structure and the superlattice is illustrated with a single FFT of the image, shown in Fig. 3.5(b) (Note that this analysis was not done in the original publication [228]). The reciprocal spots corresponding to the atomic rows are indicated by the red arrows, and reveal an hexagonal

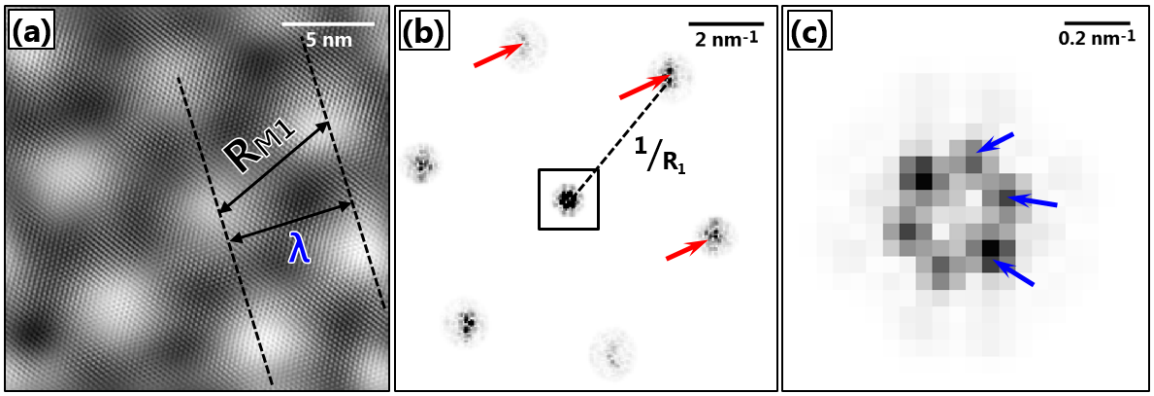

Figure 3.5: (a) Atomically resolved STM image (20×20 nm^2) of a graphite surface, in which both the atomic structure and the MP are resolved [228]. The superlattice period λ is highlighted as well as R_{M1}. (b) FFT of the STM image in (a), where the red arrows point out the 3-fold reciprocal spots corresponding to the atomic rows. (c) Cropped version of the FFT shown in (b): the blue arrows highlight the 3-fold reciprocal moiré spots.

structure, in agreement with the atomic structure of graphite. The distance between the rows of atoms R_1^* is different to the lattice constant R_1 by a factor $\sqrt{2}/3$, due to the hexagonal arrangement. Here one obtains $R_1 = 2.47 \pm 0.02$ Å, in very good agreement with the expected lattice parameter of graphite.

To determine the MP periods, one must focus on the information very close to $\mathbf{k} = 0$ since the distances are much larger than the crystal lattice constants. Figure 3.5(c) shows an expanded view of the black box shown in (b). Here too, the reciprocal spots reveal an hexagonal structure (indicated by blue arrows), reflecting the hexagonal arrangement of the moirons, as shown in (a). Analysis of the spots leads to the period of the MP, $\lambda_1 = \lambda_2 = 5.9 \pm 0.4$ nm. The angles δ_1 and δ_2 can not be extracted from this unique image because an atomically resolved image of the underlying graphite layer is missing. However, adequate modeling and/or simulation of the graphene-graphite stacking would allow the evaluation the underlayer orientation with respect to the overlayer θ. The value of the MP fringe angle δ_1 and δ_2 could subsequently be derived.

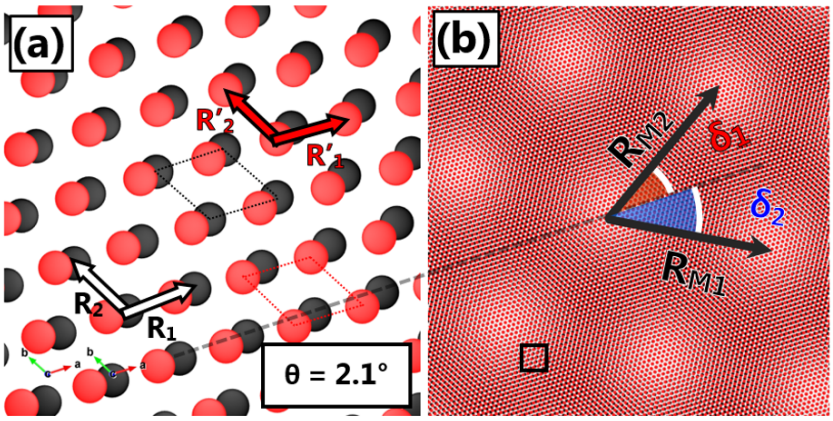

Figure 3.6: Simulated moiré pattern of the graphene-graphite system. (a) Hexagonal on hexagonal lattice (width: 1.5 nm) representing two individual layers of graphite ($R_1 = R'_1 = R_2 = R'_2 = 2.46$ Å), rotated by an angle of $\theta = 2.1°$. Underlayer vectors ($\mathbf{R_1}$,$\mathbf{R_2}$) and overlayer vectors ($\mathbf{R_1}$,$\mathbf{R_2}$) are indicated and the corresponding unit cells drawn in dotted lines. (b) Larger scale (width: 20 nm) of the simulation (the image in (a) is contained in the black box in (b)) where a clear hexagonal MP is observed in the image. $\mathbf{R}_{M1}$, $\mathbf{R}_{M2}$, δ_1 and δ_2 are recalled, dashed line is parallel to $\mathbf{R_1}$. The simulated pattern in (a,b) here agrees very well with the experimental image shown in Fig. 3.5(a).

3.2.2 Predicting moiré patterns

3.2.2.1 Simulated patterns

To predict the MPs arising from the superposition of any two 2D Bravais lattices, one can use a simple approach based on the crystal visualisation software, VESTA [213]. The software displays 2D arrays of points of desired lateral spacing and symmetries, and permits manipulation of the relative rotation θ between the layers. The MPs are then graphically identified by eye. This technique for MP prediction has been used successfully for a variety of systems [229, 230, 236, 237], including those containing point defects such as dislocations or wrinkles [215, 238] and grain boundaries [151].

The procedure for generating a simulated pattern works as follows. First, the underlayer is produced by setting the lattice constants R_1 and R_2 and the unit cell angle ω_1. The overlayer is then generated by setting R'_1, R'_2, and ω_2. The studied layers in the VDWHs are either hexagonal or rectangular, therefore $\omega = \pi/2$ or $2\pi/3$. The overlayer is afterwards rotated to the desired angle θ. Utilizing the in-built tool in VESTA , measuring the distance between two chosen positions, the MP periods λ_1, λ_2 are determined. The angles δ_1 and δ_2 are also estimated with the built-in tool giving the angle between three chosen atoms.

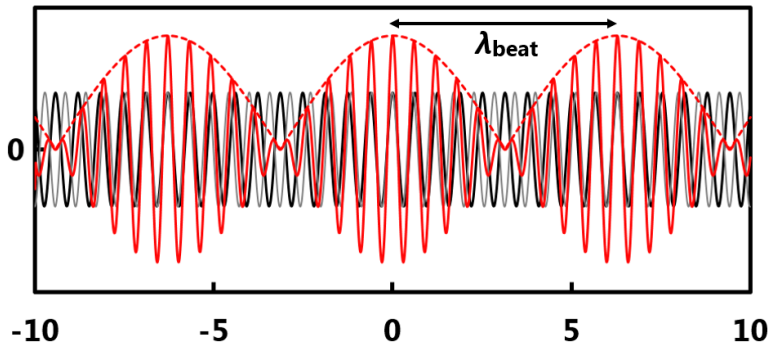

Figure 3.7: 1D MP analogy: the beat pattern. Two cosine functions of similar frequencies ($k_1/k_2 = 1.1$) are added (black and grey). The sum signal (red) can be seen as a modulation of a fast carrier signal ($k_+ = \frac{1}{2}(k_1 + k_2)$) by a slower oscillation ($k_- = \frac{1}{2}(k_1 - k_2)$). The envelope signal (dashed red), the equivalent of the MP in 1D, has a periodicity of λ_{beat}.

An example is shown in Fig. 3.6, where a MP is simulated using VESTA. Panel (a) shows the atomic arrangement of the layers (image dimensions: 15×15 Å^2), where the black atoms (underlayer) and red (overlayer) model the graphene-graphite system ($R_1 = R_2 = R'_1 = R'_2 =$ 2.46 Å). The rotation angle here is set to $\theta = 2.1°$. Figure 3.6(b) shows a different magnification (200×200 Å^2) where the MP is visible. The MP vectors $\mathbf{R}_{\text{M1}}$, $\mathbf{R}_{\text{M1}}$ and δ_1 and δ_2 are drawn on the figure. The pattern here ($\lambda_1 = \lambda_2 = 5.8$ nm) agrees very well with the experimental STM image of graphene-graphite shown in Fig. 3.5(a).

3.2.2.2 Analytical model

1D beat pattern Before delving into analytical 2D MP modeling, it is useful to consider the simpler case of the beat pattern. The beat is the interference from two temporal signals of very similar frequency. The resultant signal appears with the envelope modulated by a frequency lower than the individual signals. Spatial phenomena that are similar to the beat pattern are observed in the every day life, for instance when walking past an arrangement of two parallel railing fences. Due to parallax, the pitch of the fences appear slightly different, resulting in the observation of long range fringes. MPs can be understood as the 2D version of the beat pattern.

Assume a sum of two periodic signals with similar wavevectors $k_1 < k_2$ as shown as an example in Fig. 3.7 (black and grey) (in this thesis the crystallography convention holds, i.e.

$k = 1/\lambda$). The sum (shown in red) is written as a product as follows

$$\cos(k_1 x) + \cos(k_2 x) = 2\cos(k_+ x)\cos(k_- x) \tag{3.3}$$

where in the right-hand side the fast and slow oscillating wavevectors are respectively $k_+ = \frac{1}{2}(k_1 + k_2)$ and $k_- = \frac{1}{2}(k_2 - k_1)$. As observed on Fig. 3.7, the sum signals appears to possess a new large-scale periodicity. The beat period, λ_{beat}, corresponds to the distance between the maxima of the envelope signal (shown in dashed red), i.e of frequency $k_{\text{beat}} = 2k_-$. Therefore one obtains

$$\lambda_{\text{beat}} = \frac{\lambda_1 \lambda_2}{\lambda_1 - \lambda_2}. \tag{3.4}$$

The 1D beat period formula in Eq. (3.4) diverges if $k_1 = k_2$. When $\lambda_1 - \lambda_2 \ll \lambda_1 \lambda_2$, the resulting period λ_{beat} is sensitive to minute differences between λ_1 and λ_2.

2D model Analytical modeling of MPs is separated into two different approaches. If the layers are in perfect registry such that $a \times R_1 + b \times R_2 = c \times R'_1 + d \times R'_2$ where $a, b, c, d \in \mathbb{Z}$, the system is said commensurate. When this equality is not valid, the layers are incommensurate, and the MPs can be studied in principle for any rotation angle θ.

To date, there is no incommensurate model that successfully predicts the MPs arising from any two 2D crystals at any rotation angle (an update is provided in chapter 4). A commensurate model has been used to predict accurately the MPs emerging from α-Bi on HOPG, where both layers possess different symmetries [151]. However the prediction from this model is not straightforward as the periods λ_1 and λ_2 and the angles δ_1 and δ_2 cannot be analytically expressed as a function of the rotation angle θ. Instead, the procedure is painful and complicated.

A model for incommensurate layers has been published quite recently [174], however only applies to layers sharing identical symmetries (i.e. $\omega_1 = \omega_2$). Moreover, the model accurately models the MPs for small rotation angles only ($-10° < \theta < 10°$). The starting point of the model is to express the overlayer unit vectors as a function of the underlayer's:

$$\begin{pmatrix} \mathbf{R'_1} \\ \mathbf{R'_2} \end{pmatrix} = \overline{M} \cdot \begin{pmatrix} \mathbf{R_1} \\ \mathbf{R_2} \end{pmatrix} \tag{3.5}$$

where $\overline{M} = (p_1 \times p_2)\overline{R}_\theta$ where p_1 and p_2 are the scaling factors $p_i = R_i'/R_i$, and $\overline{R}_\theta$ the (2×2) rotation operator. The key is to express the under and overlayer by a infinite Fourier series describing the periodicities of the crystal layers:

$$f_u(r) = \sum_{j,k} c^u_{j,k} \exp[i(j\underline{G}_{u1} + k\underline{G}_{u2})r] \tag{3.6}$$

$$f_o(r) = \sum_{j,k} c^o_{j,k} \exp[i(j\underline{G}_{o1} + k\underline{G}_{o2})r] \tag{3.7}$$

where $j,k \in \mathbb{N}$, $c^u_{j,k}$ and $c^o_{j,k}$ are complex coefficients and $\underline{G}_{u1}$, $\underline{G}_{u2}$, $\underline{G}_{o1}$ and $\underline{G}_{o2}$ are the reciprocal lattice vectors of the underlayer and overlayer. The sum can be rearranged in a Fourier series:

$$f(r) = f_u(r) + f_o(r) = \sum_{j,k} c^u_{j,k} \exp[i(j\underline{G}_{u1} + k\underline{G}_{u2})r] a^M_{j,k}(r) \tag{3.8}$$

where the first term in the sum is deliberately set equal to the underlayer's Fourier series, and the other $a^M_{j,k}$ describes the moiré superlattice symmetry, given by two reciprocal lattice vectors $\overline{G}_{\mathrm{M1}}$ and $\overline{G}_{\mathrm{M2}}$. The solution is given by the following expression

$$\begin{pmatrix}\mathbf{R}_{\mathrm{M1}}\\ \mathbf{R}_{\mathrm{M2}}\end{pmatrix} = \overline{P}\cdot\begin{pmatrix}\mathbf{R_1}\\ \mathbf{R_2}\end{pmatrix} = (\mathbb{1}-\overline{M})^{-1}\overline{M}\cdot\begin{pmatrix}\mathbf{R_1}\\ \mathbf{R_2}\end{pmatrix} \tag{3.9}$$

with $\mathbb{1}$ the (2×2) unit matrix. $\overline{P}$ is the operator giving the MP vectors $\mathbf{R}_{\mathrm{M1}}$ and $\mathbf{R}_{\mathrm{M2}}$ in units of the underlayer unit vectors $\mathbf{R_0}$ and $\mathbf{R_1}$:

$$\overline{P} = \frac{1}{\Delta\sin\omega}\cdot\begin{pmatrix} p_1[\sin(\omega-\theta) - p_2\sin\omega] & q p_1\sin\theta \\ -\frac{1}{q}p_2\sin\theta & p_2[\sin(\theta+\omega) - p_1\sin\omega]\end{pmatrix} \tag{3.10}$$

with $q = R_1/R_2$. In the prefactor, Δ is

$$\Delta = 1 + p_1p_2 - (p_1+p_2)\cos\theta + (p_1-p_2)\cot\omega\sin\theta \tag{3.11}$$

All elements are now in hand for analytical prediction. From eq. (3.10) and (3.11) one can derive the MP lattice vectors in units of the underlayer vectors, for small rotation angles $|\theta| < 10°$.

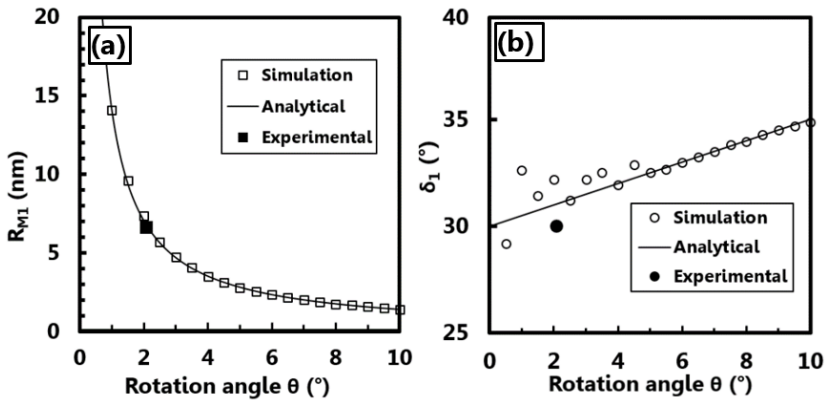

Figure 3.8: Analytical model for MP prediction. (a) Superlattice constant R_{M1} and (b) superlattice angle δ_1 as a function of the rotation angle θ for graphite-graphite system ($R_1 = R'_1 = R_2 = R'_2 = 2.46$ Å). The analytical prediction is represented in solid line and the results from VESTA simulations are represented with open symbols. Experimental values shown in Fig. 3.5(a) from [228] are represented in solid symbols.

Figure 3.8 illustrates the analytical model for graphene on graphite as θ is increased. The analytical model is using $\omega = 120°$ and $R_1 = R'_1 = R_2 = R'_2 = 2.46$ Å. R_{M1} and δ_1 are calculated for θ ranging between 0 and 10°, and plotted respectively in (a) and (b) with a solid line. The experimental values of R_{M1} and δ_1 from the STM image in Fig. 3.5(a), given in [228], are also plotted on the same graphs (solid symbols). Experimental values and analytical prediction agree very well.

Comparison with VESTA simulations The MPs are also simulated with VESTA by following the method previously described in subsection (3.2.2.1). The results are obtained by simulating two layers of graphene, and by successively measuring R_{M1} and δ_1 as θ is increased from 0 to 10°. The results are overlaid onto the analytical results in Fig. 3.8. Simulation and analytical predictions agree very well: the maximum errors for δ_1 and λ_1 are respectively 2° and 0.3 nm. The VESTA simulation in this case lacks precision for the low values of θ due to the very large simulated periods. Note that if the simulations are repeated and averaged, the agreement is improved.

3.2.3 Summary

The technique for characterizing experimental MPs is unambiguous and its principle is identical to that of the procedure for obtaining the surface lattice constant from STM images, both

Underlayer	Overlayer	Symmetry	Model	Section/Reference
α-Bi	α-Sb	R/R	Analytical	3.3.1, [153]
α-Bi	β-Sb	R/H	Simulation	3.3.2, [153]
α-Bi	MBi	R/R	Analytical	3.3.3, [239]
MoS_2	α-Bi	H/R	Simulation	3.3.4
HOPG	α-Bi	H/R	Simulation	3.3.4 [151]

Table 3.1: Studied VDWHs and their respective symmetries.

relying on FFT operations. To predict the MPs resulting from any two given incommensurate layers, two distinct methods exist:

- If the layers possess the same unit cell angle $\omega = \omega_1 = \omega_2$ and if the rotation angle between the two layers is known to be low $-10 < \theta < 10°$, the analytical model [174] can be used, since it is an immediate and accurate procedure.

- If the layers do not possess the same unit cell angle $\omega_1 \neq \omega_2$, or if the rotation angle from two similar layers have a large rotation angle, the approximate tool provided by simulating the two layers in VESTA can be used. Nonetheless, it is worth noting that the simulations do not permit exact determination of λ and δ and are rather slow to process as they rely on a point-and-click method. It is possible however to refine the results by repeating and averaging the measurements.

3.3 Experimental results and modelling

This section presents the experimental MPs that are observed via STM for the various stacking cases. The calculated and/or simulated models that agree with the observed crystal structures are detailed. Fidelity of agreements and their limits will be discussed.

As discussed in chapter 1, the VDWHs that are discussed in this thesis consists of 'wedding-cake' α-Bi islands grown on HOPG or MoS_2 via physical vapour deposition (PVD) in ultra-high vacuum (UHV). In some cases, Sb is subsequently deposited via PVD. A multitude of stacking combinations, in which MPs are visible, are then observed via STM. Table 3.1 summarizes the different studied stacking combinations, their unit cell symmetries (R: rectangle, H: hexagonal), the chosen model type and the section/reference to refer to. In most studied cases, α-Bi plays the role of the underlayer layer where α-Sb, β-Sb or MBi (see model struc-

tures in chapter 1) have the function of the overlayer. In the last case, the MP present for α-Bi when deposited onto MoS_2 are investigated. When α-Bi is grown on HOPG, MPs also appear on the surface of the 2ML bases. This was described earlier and modeled via a commensurate model [151].

A part of the work presented in this section, concerning α-Sb and β-Sb [153], and MBi [239] has been published in peer-reviewed journals.

3.3.1 α–antimonene

Antimony (Sb), which forms 3D amorphous islands on bare HOPG [171], grows very differently when α-Bi islands are already present. Indeed, the α-Bi nanostructures serve as a substrate for the subsequent deposition of crystalline Sb layers. Various crystalline forms of antimonene are observed, among them the rectangular α-Sb. Since this thesis focusses on the MPs, only a brief summary of the growth and of the detailed structures is given here. More information is given in chapter 2 or in references [144, 146–151, 153, 169, 171, 239].

3.3.1.1 Observations

There are subtle differences in the observed MPs whether the VDWHs are grown on MoS_2 or HOPG, hence the results are presented separately below.

HOPG substrates Figure 3.9(a) is an STM image of a typical island grown on HOPG. Bi is deposited first, forming wedding-cake structures (see chapter 1 for more details). On top of the 2ML-α-Bi base, several 4ML stripes are present, indicated with red arrows. Then, Sb is deposited, and the new, previously unobserved ultra-thin layers are therefore identified as antimonene. While the bottom part of the image is complex, the top part is clearer. Topography analysis and FFTs of atomically resolved STM images (not shown here) allow the identification of the observed layers, α-Sb (pink), and β-Sb (top-left part of the island) as in [153]. Figure 3.9(b) shows a different island, where α-Sb (pink) is identified on a 2ML-α-Bi base, between two narrow 4ML stripes. Figure 3.9(c) shows a thicker α-Bi base (4ML-α-Bi) in which a narrow 6ML-α-Bi stripe is present roughly in the middle (red arrow). The 4ML-α-Bi base here is entirely decorated with α-Sb, on both sides of the narrow stripe.

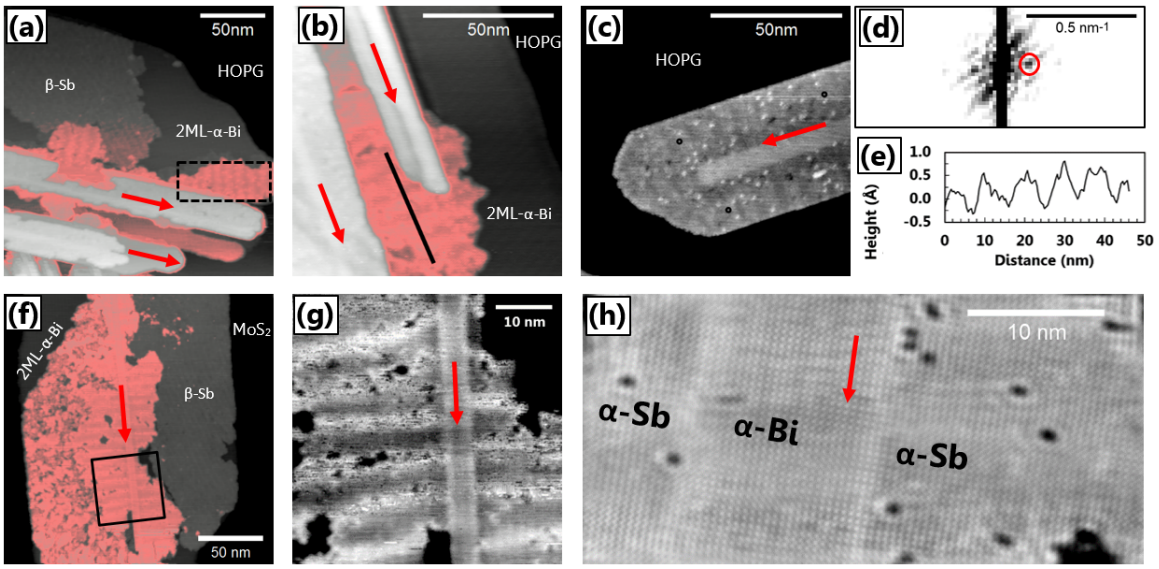

Figure 3.9: Experimental observations of α-Sb on α-Bi. (a,b) STM images ($V = +0.2$ V, $I = 10$ pA) of VDWHs grown on HOPG which bottom layer is a 2ML-α-Bi. Fringe-like MPs are clearly visible on the α-Sb layers (pink). (c) STM image ($V = +0.15$ V, $I = 50$ pA) of another island where α-Sb is covering the entire 4ML-α-Bi base. The 6ML-α-Bi stripe in the middle of the island (light grey) is visible, and a very faint MP (whose fringes are perpendicular to the α-Bi $\langle 1\bar{1}0\rangle$ direction) can be observed. (d) FFT of the region in the dashed rectangle present in (a). The reciprocal coordinates associated with the MP wave vector is circled in red. (e) Profile from the line drawn perpendicular to the fringes in (b) showing the MP amplitude of corrugation ~ 1 Å. (f) STM image ($V = +0.4$ V, $I = 10$ pA) of a typical VDWH grown on MoS_2, showing a relatively large flake of α-Sb (pink) grown on a 2ML-α-Bi base. (g) STM image ($V = +0.2$ V, $I = 50$ pA) of the region in the black box in (f). (h) Atomically resolved STM image ($V = 0.1$ V, $I = 50$ pA) showing α-Sb on both sides of the narrow 4ML-α-Bi stripe of an island similar to the ones shown in (f,g), also grown on MoS_2. This atomic resolution image confirms the alignment between the two crystals: $\theta = 0$. Red arrows in (a-c) and (f-h) indicate the direction of $\mathbf{R_1} \equiv \alpha$-Bi $\langle 1\bar{1}0\rangle$.

MoS_2 substrates Figure 3.9(f) shows a typical VDWH grown on MoS_2. The nanostructure is very similar to that observed in Fig. 3.9(a). A wide 2ML-α-Bi base is divided roughly at the middle by a narrow 4ML-α-Bi stripe (red arrow aligned with the stripe direction). Again, the two allotropes of antimonene are observed: α-Sb (pink) is crystallised next to the stripe, whereas β-Sb (grey) is located on the right-hand side of the island. Figure 3.9(g) is an expanded version of the region highlighted in Fig. 3.9(f), where the 4ML-α-Bi narrow stripe and the α-Sb are more visible. The horizontal fringes on the α-Sb region are the MPs. Figure 3.9(h) is an atomically resolved STM image of the region near the 4ML-α-Bi stripe (middle of the image), is elongated in the $\mathbf{R_1} \equiv \langle 1\bar{1}0\rangle$ direction (red arrow). α-Sb, present on both sides

Subst.	NA	NA	HOPG	HOPG	MoS_2
Under.	NA	NA	2ML-α-Bi	4ML-α-Bi	2ML-α-Bi
Over.	NA	NA	α-Sb	α-Sb	α-Sb
Type	bulk (110)	calc.	exp.	exp.	exp.
α-Bi R_1	4.54	4.54	4.54 ± 0.10	4.53 ± 0.10	4.53 ± 0.10
R_2	4.75	4.75	4.75 ± 0.10	4.87 ± 0.10	4.87 ± 0.04
α-Sb R'_1	4.31	4.28	4.26 ± 0.19	4.18 ± 0.09	4.29 ± 0.07
R'_2	4.54	4.64	4.76 ± 0.20	4.84 ± 0.10	4.86 ± 0.11

Table 3.2: Measured lattice constants for the α phases of Bi and Sb, calculated free-standing structures (from DFT calculations in [153]) and measured bulk values.

of the 4ML-α-Bi stripe, is in almost perfect registry with α-Bi, although the atomic spacing differ (see Table 3.2).

α-Sb structural properties α-Sb exhibits the black phosphorus (BP) structure, which is very similar to the structure adopted by α-Bi (see chapter 1 for more details on the BP structure). The lattice constants are measured via FFT of the atomically-resolved STM images, e.g. Figure 3.9(h). Results are given in Table 3.2. The measurements vary slightly whether HOPG or MoS_2 is the substrate onto which α-Bi is initially grown, and whether antimonene is deposited on 2ML- or 4ML-α-Bi. Nonetheless, the measured lattice constants are very similar within their uncertainties: the unit cell of α-Sb is roughly $R'_1 \times R'_2 = 4.2 \times 4.8$ Å^2. For the different substrates and underlayer thicknesses, atomically-resolved STM images of both α-Sb and α-Bi reveal the alignment of the unit cells: α-Bi $\langle 1\bar{1}0 \rangle$ || α-Sb $\langle 1\bar{1}0 \rangle$, as shown for example in Fig. 3.9(h). Since the MPs are very sensitive to minute variations of the crystal structure, the three cases are analysed separately: (1) 2ML-α-Bi/HOPG, (2), 4ML-α-Bi/HOPG, (3), 2ML-α-Bi/MoS_2.

Moiré patterns observations Figure 3.9(a-c,f-h) shows instances of α-Sb layers in which clear MPs are resolved, regardless of the sample substrate and of the thickness of α-Bi (2ML or 4ML). In all cases, the MPs appear as fringes, nearly perpendicular to $\mathbf{R_1} \equiv \langle 1\bar{1}0 \rangle$ (red arrows in the STM images in Fig. 3.9). The MPs are observed regardless of the substrate (HOPG or MoS_2) or the thickness (2ML or 4ML) of α-Bi bases. The observed amplitude of the MPs is of the order of 1 Å, as shown in Fig. 3.9(e), corresponding to the height profile of the black line in Fig. 3.9(b). MP periods (λ_1) and angles (δ_1) are gathered in Table 3.3. The

Substrate	No.	$\lambda_1 \pm d\lambda_1$ (nm)	$\delta_1 \pm d\delta_1$ (°)
HOPG/2ML-α-Bi	47	8.7 ± 0.9	78 ± 25
HOPG/4ML-α-Bi	7	6.8 ± 0.9	87 ± 17
MoS_2/2ML-α-Bi	22	7.2 ± 0.8	84 ± 7

Table 3.3: Experimental characterisation of the moiré patterns of α-Sb on different α-Bi thicknesses or sample substrates, also indicating the number of individual measurements.

measured periods are typically $\lambda_1 \sim 7-9$ nm with uncertainties slightly below 1 nm. The fringe angle δ_1, with respect to $\mathbf{R_1} = \alpha$-Bi $\langle 1\bar{1}0 \rangle$, is always very close to 90°. The relatively large error bars on the measurement are the result of three different factors:

- (i) The small lateral extension of the islands, and therefore of the number of fringes of the MPs that are visible. The direct consequence of this is, due to the properties of the FFT, is the low resolution of the reciprocal coordinates associated with the MP wavevector. Figure 3.9(d) shows the FFT of the area in the dashed box present in Fig. 3.9(a). The reciprocal spots here are very close to $\mathbf{k} = 0$. Uncertainties associated with coordinates close to the centre of the FFT are larger than those from more distant coordinates.

- (ii) The statistical spread of the data. Indeed, the period and/or the angle of the fringes on α-Sb seem to vary from island to island, sometimes even within the same island. For instance, in Fig. 3.9(a), the two visible domains of α-Sb (left and right of the image) show fringes that differ both in the measured λ_1 and in δ_1 (the fringes are misaligned by about 20°). Thermal drift and/or creep can also affect the MPs characterisation, as briefly discussed in chapter 2.

- (iii) The intrinsic disorder of the MPs, i.e. the deviation of the MPs from a perfectly ordered plane-wave. The STM image shown in Fig. 3.9(g) illustrates this: the fringes appear slightly bent, λ_1 and δ_1 vary locally. As a consequence, the FFT does not contain simple point-like patterns, expected from perfectly ordered fringes.

3.3.1.2 Analytical modeling of α-Sb on α-Bi

The substrate and the overlayer that lead to MPs here are α-Bi and α-Sb. The use of the analytical model (subsection 3.2.2.2) is permitted here, because the two layers are expected

to share an identical unit cell angle (rectangular symmetry, i.e. $\omega_1 = \omega_2 = \pi/2$) and because they are aligned ($\theta \simeq 0° < 10°$ as previously shown in Fig. 3.9(h)). In such case, the 2D model simplifies into beat patterns in each crystal direction ($\mathbf{R_1}$ and $\mathbf{R_2}$) described by Eq. (3.4).

Using the experimental lattice constants By simply computing the expected MP period based on the measured lattice constants of α-Bi and α-Sb for the different cases (as displayed in Table 3.2), one obtains the following expected periods: $\lambda_1 = 6.9 \pm 2.5$ nm for HOPG/2ML-α-Bi, $\lambda_1 = 5.4 \pm 0.8$ nm for HOPG/4ML-α-Bi, and $\lambda_1 = 8.1 \pm 0.8$ nm for MoS_2/2ML-α-Bi. All these predicted values are in rough agreement with the measured periods (see Table 3.3). The agreement can be improved by fine-tuning the lattice parameters within the observed uncertainties.

Refinement of the lattice constants To address the deviation between prediction and observation it is possible to rearrange Eq. (3.7):

$$R_1' = \frac{\lambda_1 \times R_1}{\lambda_1 + R_1} \tag{3.12}$$

where $R_1 > R_1'$. The corresponding plot $R_1' = f(R_1')$ is shown in Fig. 3.10(a) for α-Sb/2ML-α-Bi/MoS_2. The ensemble of possible values of (R_1, R_1') that leads to the observed period is shown ($\lambda_1 = 7.2 \pm 0.8$ nm, solid blue line). The uncertainty in the period measurement $d\lambda_1$ leads to the existence of a wider domain within which (R_1, R_1') agree with the observed period (dashed lines). The experimental lattice parameters (R_1, R_1') are added (black square). Clearly, the domain of possible lattice parameters that lead to a MP whose period agrees with the observation overlaps with the domain of the observed lattice constants. This space is where the atomically-resolved lattice constants R_1 and R_1' agree with the observed periods. The optimised values $R_1 = 4.544$ Å and $R_1' = 4.272$ Å(corrections well below the uncertainties) lead to a period of $\lambda = 7.14$ nm, in very good agreement with the measured λ_1.

The procedure is identical for the otherα-Sb/α-Bi cases (i.e. α-Sb/2ML-α-Bi/HOPG and α-Sb/4ML-α-Bi/HOPG, plots not displayed here). The results of the refined lattice constants are gathered in table 3.4. Altogether, the corrections on the lattice constants R_1 and R_1' are smaller than 4 pm, which is much smaller than the experimental uncertainties.

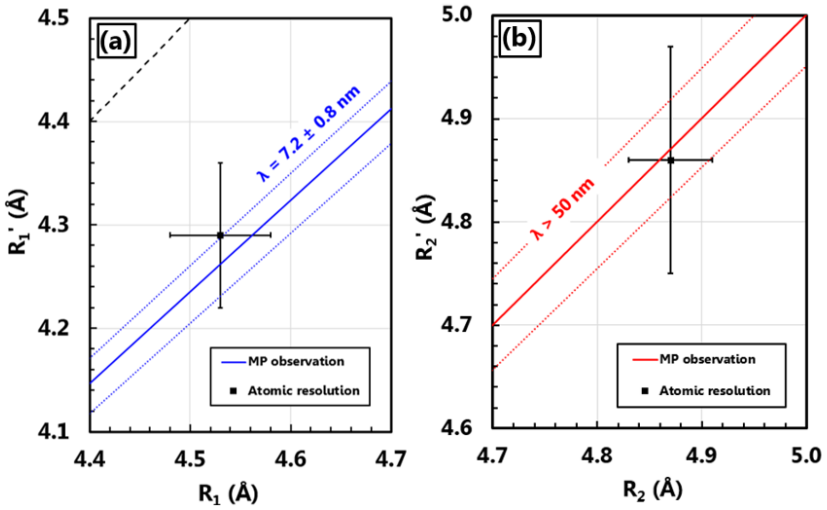

Figure 3.10: MPs and atomic resolution agreement for α-Sb on MoS_2/2ML-α-Bi. (a) R_1' (α-Sb) versus R_1 (α-Bi) based on the experimentally observed MP (solid blue line) and including the uncertainty of 0.8 nm (dotted blue lines). The dashed black line is the null mismatch $R_1' = R_1$ domain. (b) R_2' versus R_2, where $R_2' = R_2$ since no MP is observed in this direction (solid red line), yet the minimum period condition of 50 nm widens the domain of possible R_2, R_2' (dotted red lines). In both panels, the atomic resolution derived lattice constant measurement is shown with their experimental uncertainties.

Concerning the other direction of the unit cell $\mathbf{R_2}$ (i.e. α-Bi $\langle 001 \rangle$), in all studied cases the lattice mismatch $R_2' - R_2$ is below 0.2% (see table 3.2). This very small mismatch leads to a very large predicted period λ_2 (in all cases, $\lambda_2 > 75$ nm). The maximum width W of the α-Sb flakes ($W \simeq 50$ nm) does not allow the observation of the potential MP in this direction. For completeness, a study of the possible (R_2, R_2') values that agree with a period λ_2 larger than 50 nm is shown in Fig. 3.10(b). The observed (R_2, R_2') (black square) agrees with $\lambda_2 > 50$ nm (zone within the dotted red lines).

Rotated α-Sb on α-Bi In some rare cases the MPs appear with a different period and a different angle. Figure 3.11(a) shows a zoomed-in version of the island in Fig. 3.11(a). A and B indicate the two different flakes. Analysis of the individual regions yield for region A: $\lambda_1(A) = 9.1 \pm 0.8$ nm, $\delta_1(A) = 84 \pm 5°$ and for region B: $\lambda_1(B) = 7.9 \pm 0.4$ nm, $\delta_1(B) = 68 \pm 9°$. While the MP observed in region A can be considered perpendicular to $\mathbf{R_1}$ ($\delta_1(A) \simeq 90°$), the MP in region B is clearly different. The simple, 1D model used to describe the MPs in aligned α-Sb previously cannot be used because α-Sb is no longer aligned with α-Bi, but instead

Subs.	HOPG		HOPG		MoS_2	
Under.	2ML-α-Bi		4ML-α-Bi		2ML-α-Bi	
Type	Exp.	Sim.	Exp.	Sim.	Exp.	Sim.
α-Bi R_1	4.54 ± 0.10	4.513	4.53 ± 0.10	4.497	4.53 ± 0.05	4.544
R_2	4.75 ± 0.10	4.750	4.87 ± 0.10	4.860	4.87 ± 0.04	4.870
α-Sb R'_1	4.26 ± 0.10	4.290	4.18 ± 0.09	4.218	4.29 ± 0.07	4.274
R'_2	4.76 ± 0.10	4.760	4.84 ± 0.10	4.860	4.86 ± 0.11	4.870
λ_1	87 ± 9	86.8	68 ± 9	68.0	72 ± 8	71.9
λ_2	N/A	∞	N/A	∞	N/A	∞

Table 3.4: Experimental lattices constants obtained from FFTs of atomically resolved STM images '(exp.)' and optimised lattices constants utilizing the observed MPs on α-Sb '(sim)' for α-Sb on 4ML-α-Bi (HOPG substrate) and α-Sb on 2ML-α-Bi (HOPG and MoS_2 substrates). Optimised lattice parameters are within 4 picometers of the observations. The periods λ_1 induced from the optimised lattice constants agree very well with the observed periods. All values are in Å.

rotated by an angle $\theta \neq 0$. The fringe period λ and angle δ are now calculated using the 2D analytical model described in subsection 3.2.1, i.e. varying the rotation angle θ below 10°.

The calculation is performed using the experimentally observed lattice constants, as given in Table 3.2. α-Bi lattice is therefore set to $R_1 \times R_2 = (4.54 \times 4.75)$ Å^2, α-Sb $R'_1 \times R'_2 = (4.26 \times 4.76)$ Å^2. The results are shown in Fig. 3.11(b), where δ is plotted as a function of λ for $\theta = 0...10°$ (dashed line). The observed MPs (A and B) are shown respectively with blue and red symbols. There is no value of θ that can yield an agreement with the observed MP for A and B. Instead the calculated periods are $\lambda_1 < 7$ nm, whereas the observed periods are closer to $8-9$ nm. To match the observations, the mismatch between the two layers must be reduced in order to enlarge the predicted periods.

A new (λ_1, δ_1) curve is computed using a slightly expanded α-Sb unit cell: $R'_1 \times R'_2 = 4.318 \times 4.760$ Å^2. The resulting curve is shown in Fig. 3.11(b) (solid line). This time, the modeled (λ_1, δ_1) crosses the experimental values of both the MP in A and in B, for different values of $\theta_A = 0.3°$ and $\theta_B = 1.2°$. For visual comparison, the MPs are also simulated via VESTA for the two different values of rotation angle θ as shown in Fig. 3.11(c). Analytical modeling and simulations therefore agree with the experimentally observed MPs in both zones A and B. The MPs in A and B are hence explained by a slightly expanded α-Sb unit cell (less than 6 pm extension for R'_1, well below the experimental uncertainty of 20 pm obtained via atomic-resolution imaging), that is rotated respectively by $\theta_A = 0.3°$ and $\theta_B = 1.2°$ with

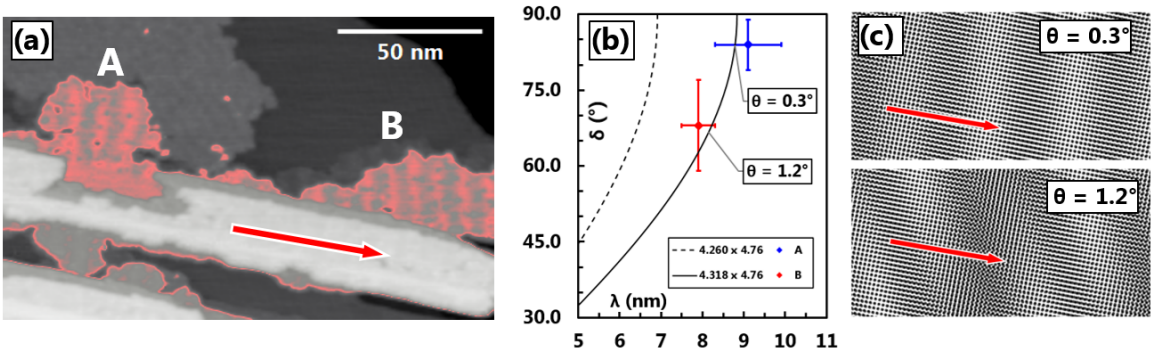

Figure 3.11: Rotation of α-Sb on 2ML-α-Bi (HOPG substrate). (a) Experimental STM image ($V = +0.2$ V, $I = 10$ pA) of an island where two distinct α-Sb zones (A and B) are sitting on 2ML-α-Bi bases (grown on HOPG). FFT analysis of the different zones yields $\lambda_1(A) = 9.1 \pm 0.8$ nm, $\delta_1(A) = 84 \pm 5°$ and $\lambda_1(B) = 7.9 \pm 0.4$ nm, $\delta_1(B) = 68 \pm 9°$). (b) Analytical predictions for the experimentally determined α-Sb ($R'_1 \times R_2 = 4.260 \times 4.76$ Å^2, in dashed line) and slightly expanded α-Sb ($R'_1 \times R'_2 = 4.318 \times 4.76$ Å^2, in solid line). The experimental MPs in A and B are also displayed here. (c) VESTA simulated MPs (4.318×4.76 on 4.54×4.75, widths of images are 30 nm) modeling zone A with $\theta = 0.3°$ (top part) and zone B with $\theta = 1.2°$ (bottom). For (a) and (c), $\mathbf{R_1} \equiv \langle 1\bar{1}0 \rangle$ is drawn in red.

respect to the α-Bi substrate layer.

3.3.1.3 Conclusion

The newly synthesised allotrope α-Sb shows moiré fringes, regardless of the underlying layer onto which it is grown (2ML-α-Bi or 4ML-α-Bi on HOPG, or 2ML-α-Bi on MoS_2). The measured periods, via FFT of the layers all range between $\sim 6-10$ nm, with a standard deviation below one nanometre The fringes are arranged perpendicular to the α-Bi $\langle 1\bar{1}0 \rangle$ direction. Because α-Bi and α-Sb have their unit cells aligned, the modeling of the MPs is therefore simplified to a beat pattern in each direction of the lattice. Agreement between the measured lattices with the MPs is always satisfactory, but can be improved upon minimal structural changes of the individual overlayer α-Sb (always smaller than 6 pm variation, i.e. strictly below the uncertainties in the measured lattice constants) with respect to the lattices initially observed with atomically-resolved STM. In the rare instances where the MPs appear slightly misaligned with the crystal directions, the observations are modeled with very good agreement, via introducing a very small rotation angle θ of $\sim 1°$.

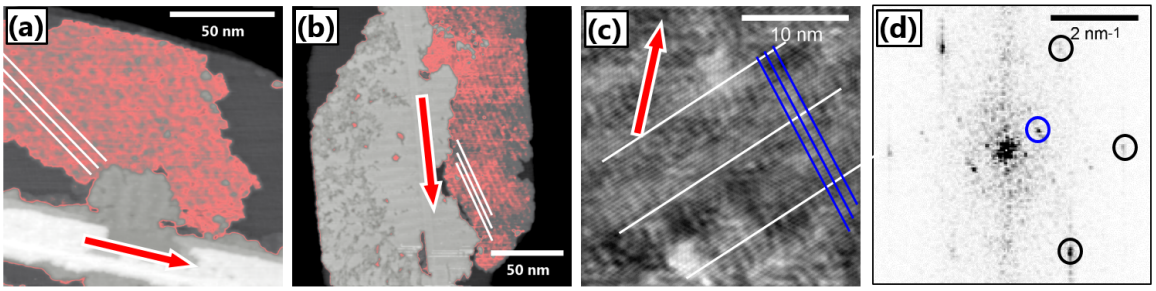

Figure 3.12: (a) STM image (V = +0.2 V, I = 10 pA) of a VDWH grown on HOPG. (b) STM image (V = +0.4 V, I = 10 pA) of a VDWH grown on MoS_2. In (a) and (b), β-Sb layer is coloured in pink, M1 fringes are indicated with white lines. (c) Atomically resolved STM image (V = +0.2 V, I = 50 pA) of β-Sb sitting on a 2ML-α-Bi base (grown on MoS_2) where two distinct MPs are observed, M1 ($\lambda_1 = 5.4 \pm 0.8$ nm, white lines) and M2, ($\lambda_2 = 1.07 \pm 0.04$ nm, blue lines). (d) FFT of the image in (c), evidencing an hexagonal atomic structure ($R'_1 = 4.04 \pm 0.04$ Å , reciprocal spots circled in black), and the fringe-like MP corresponding to $\lambda_2 = 1.07 \pm 0.04$ nm (reciprocal spot circled in blue). The reciprocal spot of the other MP (corresponding to $\lambda_1 = 5.4 \pm 0.8$ nm) is barely visible, in fact too close to $\mathbf{k} = 0$ to be distinguished here. In (a-c), the red arrow is aligned with $\mathbf{R_1} \equiv \alpha$-Bi $\langle 1\bar{1}0 \rangle$ direction.

3.3.2 β–antimonene

As discussed in subsection 3.3.1, another allotrope of antimonene, β-Sb, is observed via STM on the VDWHs.

3.3.2.1 Observations

β-Sb growth Similarly to α-Sb, β-Sb does not grow on bare substrates (whether HOPG or MoS_2). Figure 3.12(a) shows a typical STM image where a 2ML-α-Bi island is grown on HOPG (note this is a higher magnification of the island shown in Fig. 3.9(a)). A 4ML-α-Bi narrow stripe is present at the bottom of the image. The α-Bi nanostructure is decorated with the two allotropes of antimonene: α-Sb (grey) and β-Sb (pink). Figure 3.12(b) shows a typical VDWH grown on MoS_2. β-Sb layers cover larger areas than the α phase, and as shown in Fig. 3.12(a,b) often extends to the edges of the 2ML-α-Bi bases instead of existing only near the 4ML-α-Bi stripes. For both substrates, β-Sb (pink) is only observed on 2ML-α-Bi bases, never on the thicker 4ML-α-Bi bases, for a reason that is still unclear.

β-Sb structural properties β-Sb forms a 2D hexagonal lattice ($R'_1 = R'_2$, $\omega_2 = 2\pi/3$). The lattice constants are measured via FFTs of atomically resolved STM images. The unit cell of β-Sb is significantly smaller than the bulk Sb(111) lattice constant, but both agree with

	2ML-α-Bi ($R_1 \times R_2$) (Å^2)	β-Sb (R_1') (Å)
Experimental (HOPG sub.)	$(4.54 \pm 0.10) \times (4.75 \pm 0.10)$	4.02 ± 0.16
Experimental (MoS_2 sub.)	$(4.53 \pm 0.05) \times (4.87 \pm 0.04)$	4.04 ± 0.04
Calculated [153]	4.54×4.75	4.00
Bulk (110/111)	4.54×4.75	4.31

Table 3.5: Lattice parameters of experimental (for different substrates), free-standing calculation, and bulk Bi(110) and Sb(111).

the calculated free-standing β-Sb [153], as shown in Table 3.5. When atomically resolved STM images of both 2ML-α-Bi and β-Sb are available (not shown here), the rotation angle θ can estimated to be $\theta = 12 \pm 3°$, whether the nanostructures are grown on HOPG or MoS_2 substrates. Figure 3.12(c) shows an STM image that resolves the hexagonal atomic structure of β-Sb. The red arrow is aligned with $\mathbf{R_1}$ = α-Bi $\langle 1\bar{1}0 \rangle$. The FFT of the image present in Fig. 3.12(c) is displayed in Fig. 3.12(d), where the reciprocal spots of the atomic structure are circled in black.

MPs observations on β-Sb Wherever β-Sb is observed, MPs are clearly visible. The MPs show up in a very similar manner whether HOPG or MoS_2 are used as a substrate. In both cases, two distinct fringe-like MPs are observed; one with a large period (M1) and another with a short period (M2). In Fig. 3.12(a,b) M1 is clearly observed: the fringes are indicated by white lines on the images. To resolve M2, the magnification must be increased, as in Fig. 3.12(c) where both M1 (white lines) and M2 (blue lines) are visible. To characterize the MPs, the procedure is identical to that followed in subsection 3.2.1. Figure 3.12(d) is a FFT of the image present in Fig. 3.12(c). The reciprocal spots associated with the fringes of M2 (circled in blue) are very well resolved, leading to a small uncertainty on λ_2 and δ_2. Due to the limited number of M1 fringes in the image in Fig. 3.12(c), the reciprocal space coordinates of the M1 spot are very close to $\mathbf{k} = 0$ and cannot be resolved for this particular image. Larger images displaying a greater number of fringes (e.g. Figure 3.12(b)) are used for the measurement of M1.

The averaged results of the MP characterisation are given in Table 3.6. Despite obvious similarities in the MPs, the measured lattice constants of α-Bi and β-Sb seem to be substrate-dependent: M1 and M2 do not vary significantly whether β-Sb is deposited onto 2ML-α-Bi grown on HOPG or MoS_2. M1 has a period λ_1 typically $\sim 4.5-5.0$ nm, while $\delta_1 \sim 40°$. M2 has

Substrate	MoS_2		HOPG	
	exp.	sim.	exp.	sim.
α-Bi R_1 (Å)	4.53 ± 0.05	4.480	4.54 ± 0.10	4.540
α-Bi R_2 (Å)	4.87 ± 0.04	4.830	4.75 ± 0.10	4.750
β-Sb R'_1 (Å)	4.04 ± 0.04	4.08	4.02 ± 0.04	4.060
θ (°)	12 ± 3	12.2 ± 0.8	12 ± 3	13.0 ± 0.5
λ_1 (nm)	4.7 ± 0.4	4.7 ± 0.2	4.8 ± 0.5	4.8 ± 0.2
δ_1 (°)	39 ± 8	39 ± 2	34 ± 10	37 ± 3
λ_2 (nm)	1.06 ± 0.06	1.05 ± 0.05	1.06 ± 0.04	1.05 ± 0.05
δ_2 (°)	-37 ± 6	-40 ± 7	-42 ± 6	-40 ± 7

Table 3.6: Summary of the experimental lattice constants and MPs, as well as the optimised models for simulated MPs for β-Sb on 2ML-α-Bi (HOPG and MoS_2 substrates). Distances R_1, R_2, R'_1, λ_1 and λ_2 are expressed in Å, the angles θ, δ_1 and δ_2 are expressed in degrees (°). Periods and angles from simulations all agree with the observations.

a smaller period $\lambda_2 \sim 1.0 - 1.1$ nm, and the fringe angle $\delta_2 \sim -40°$. The uncertainties stem from the same reasons as for α-Sb, as detailed in subsection 3.3.1.The two following cases are therefore treated separately: (i) β-Sb on 2ML-α-Bi/MoS_2, and (ii) β-Sb on 2ML-α-Bi/HOPG.

3.3.2.2 Simulated moiré patterns of β-Sb on α-Bi

The individual layers that interfere here have different unit cell angles ($\omega_1 = \pi/2$ for α-Bi, $\omega_2 = 2\pi/3$ for β-Sb), and there is no mathematical model available for MPs prediction. VESTA simulations (subsection 3.2.1) are hence carried out. MPs are first simulated using the experimental lattice constants observed in the atomic-resolution images, and are then fine-tuned to optimize the model. The lattice constants and the MPs periods and angles M1 and M2, both those measured experimentally and those used for the optimised simulations are gathered in Table 3.6.

Using experimental lattice constants (MoS_2 substrates) The simulation using the experimental lattice constants of α-Bi and β-Sb (when grown on MoS_2 substrates) at the experimental rotation angle of $\theta = 12.0°$ is displayed in Fig. 3.13(a). Clearly, two MPs are present: M1 ($\lambda_1 = 5.5 \pm 0.2$ nm, $\delta_1 = 32 \pm 2°$, indicated with white lines), and M2 ($\lambda_2 = 1.06 \pm 0.05$ nm, $\delta_2 = -39 \pm 3°$, blue lines). Qualitatively, simulation and observation agree: the values of the periods and angles are comparable (refer to Table 3.6). Quantitatively, M2 is however successfully modeled with the experimental lattices and the angle $\theta = 12°$ while M1 appears

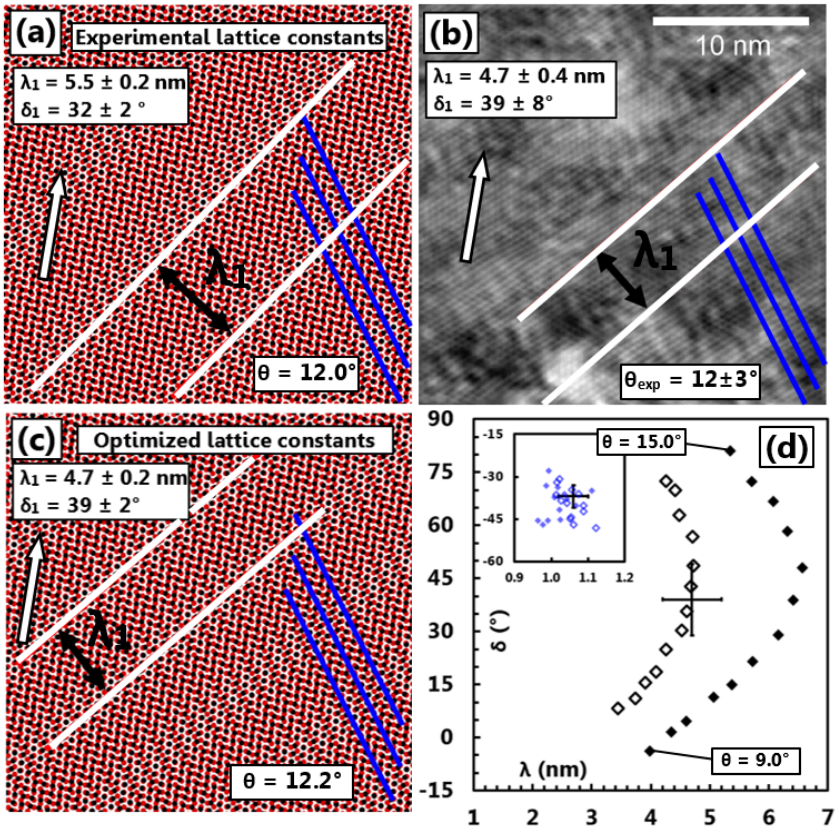

Figure 3.13: MPs simulations of β-Sb on α-Bi for the MoS_2/2ML-α-Bi case. (a) VESTA-Simulated MPs (width: 22.5 nm) using the experimentally observed lattice constants for α-Bi (black dots) and β-Sb (red dots) for the angle $\theta = 12.0°$. M1 and M2 fringes are shown in white and blue lines. The values of λ_1 and δ_1 are indicated. (b) Experimental STM image of β-Sb grown on MoS_2/2ML-α-Bi (width: 22.5 nm, V = +0.1 V, I = 50 pA) that resolves both atomic rows and the MPs M1 and M2, respectively indicated with red and blue lines. (c) VESTA-simulated MPs (width: 22.5 nm), obtained with optimised lattice constants such that the MPs M1 and M2 agree with the observation in (b). (e) $\delta_1 = f(\lambda_1)$ for the simulated patterns using the experimentally observed lattice constants for MoS_2 substrates ($R_1 \times R_2 = 4.53 \times 4.86$ Å^2 for α-Bi, $R'_1 = 4.04$ Å for β-Sb, black diamonds) and using corrected lattice constants ($R_1 \times R_2 = 4.48 \times 4.83$ Å^2, $R'_1 = 4.08$ Å , open diamonds). The inset shows the simulated $\delta_2 = f(\lambda_2)$. The experimentally observed MPs are plotted using a black cross with the measurement uncertainties. θ varies from 9° to 15° with a step of $\Delta\theta = 0.5°$. In (a-c), the white arrow indicates the α-Bi = $\langle 1\bar{1}0 \rangle$ direction.

with a larger period and smaller angle than expected (the experimental STM image from Fig. 3.12(c) is displayed in Fig. 3.13(b) to allow direct comparison).

The measurement uncertainty of $\pm 3°$ on the rotation angle θ allows to perform simulations as a function of θ. Figure 3.13(d) shows δ_1 plotted versus λ_1 when θ varies from 9° to 15° with an angle step of $\Delta\theta = 0.5°$, when using experimental lattice parameters of both 2ML-α-Bi and β-Sb (solid diamonds). The inset shows the plot for δ_2 versus λ_2. The experimentally characterised (λ_1, δ_1) and (λ_2, δ_2) are also plotted with a black cross representing the uncertainty of measurement. The simulated values of λ_1 and δ_1 do not agree with the observations, for any value of θ within that range. For M2 (see inset in Fig. 3.13(d)), the period λ_2 and angle δ_2 agree with the experimental observation. The large scatter in the simulated data for M2 originates from the difficulty in measuring accurate periods and angles, as the VESTA-simulated images can be visually ambiguous. Nonetheless, for $\theta = 12 \pm 3°$, the simulated M2 ($\lambda_2 = 1.05 \pm 0.10$ nm, $\delta_2 = -40 \pm 10°$) agrees with the observed M2 ($\lambda_{2\,\mathrm{exp}} = 1.06 \pm 0.06$ nm, $\delta_{2\,\mathrm{exp}} = -36 \pm 6°$).

Optimised lattice constants (MoS_2 substrates) The model can be improved in order to model the observed M1. The lattices constants are then fine-tuned within the respective uncertainties of the measured lattice parameters. New simulations were performed, varying by trial-and-error R_1, R_2, R_1' and R_2', until the simulated M1 agrees the observation. Figure 3.13(d) displays δ_1 versus λ_1 obtained with a slightly contracted unit cell for α-Bi: $R_1 \times R_2 = 4.48 \times 4.83$ Å^2, and a slightly expanded unit cell for β-Sb: $R_1' = 4.08$ Å(open diamonds). The simulated M1 ($\lambda_1 = 4.7 \pm 0.2$ nm, $\delta_1 = 39 \pm 2°$) now agrees with the experimental values, for rotation angles $\theta = 12.2 \pm 0.8°$. The inset of Fig. 3.13(d) displays the simulated M2. Despite being here also relatively scattered, M2 still agrees with the experimental values ($\lambda_2 = 1.05 \pm 0.10$ nm, $\delta_2 = -40 \pm 7°$).

Simulated moiré patterns for HOPG substrates An identical method is applied to simulation the MPs when β-Sb/2ML-α-Bi is grown on HOPG substrates. For $\theta = 12°$, simulated M1 (not displayed) has a period of $\lambda_1 = 5.2 \pm 0.2$ nm and an angle $\delta = 21 \pm 2°$, disagreeing with the observed M1 $\lambda_{1\,\mathrm{exp}} = 4.8 \pm 0.5°$, $\delta_{1\,\mathrm{exp}} = 34 \pm 10°$.

Simulations are therefore performed varying the rotation angle θ within the measurement uncertainty range, i.e. $\theta = 12 \pm 3°$. The simulations (not displayed) do not yield a good agreement: similarly, there is no unique rotation angle θ that achieves both λ_1 and δ_1 values that agree with the observations.

The lattice parameter of β-Sb is therefore fine-tuned. Maintaining the observed 2ML-α-Bi lattice parameters of $R_1 = 4.54 \times 4.75$ Å^2, with a slightly expanded unit cell for β-Sb $R_1' = 4.06$ Å, the simulation yields MPs with $\lambda_1 = 4.8 \pm 0.2°$ and $\delta_1 = 37 \pm 3°$, agreeing very well with the experimentally observed MPs. M2 also shows excellent agreement, as $\lambda_2 = 1.05 \pm 0.05°$ and $\delta_2 = -40 \pm 7°$, for the rotation angle $\theta = 13.0 \pm 0.5°$.

3.3.2.3 Conclusion

The β phase of antimonene is successfully grown on top of the 2ML-α-Bi bases (for both HOPG or MoS_2 substrates). In all the observed β-Sb layers, two moiré fringes are present: M1 is typically characterised with $\lambda_1 = 4.8 \pm 0.5$ nm, $\delta_1 = 40° \pm 15°$ and M2 with $\lambda_2 = 1.06 \pm 0.06$ nm, $\delta_2 = -40° \pm 10°$ (averaging the observations for HOPG and MoS_2 substrates). The MPs are first modeled using the experimentally observed lattices: VESTA-simulations are successful to model them qualitatively. Minimal changes in the lattice parameters used in the simulations are required (up to 5 pm, always within the experimental uncertainties) to model extremely well the observations.

3.3.3 MBi

3.3.3.1 Observations

MBi growth A new phase of bismuthene has recently been synthesised and observed via STM experiments, referred to as 'monolayer bismuthene' (MBi) [239]. MBi is present occasionally on pure α-Bi islands. To date, it has only been observed on the 2ML-α-Bi bases grown on HOPG, always identified between two narrow stripes of α-Bi, indicating the 4ML-α-Bi edges may play a crucial role in MBi growth. MBi is never observed in other regions of the islands, nor on the bare HOPG substrates. Figure 3.14(a) shows a typical MBi layer (pale blue) sitting on a 2ML-α-Bi base (dark blue), between two stripes of 4ML-α-Bi (orange).

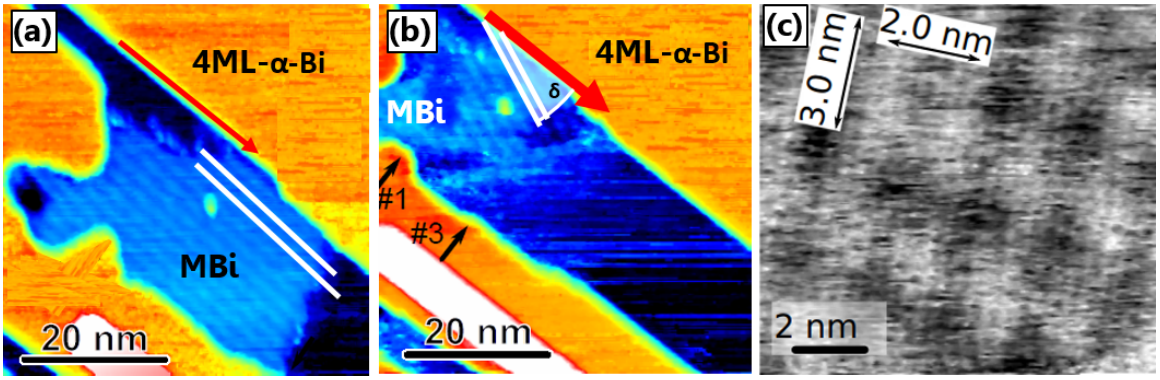

Figure 3.14: (a) STM image ($V = -0.8$ V, $I = 10$ pA) of a typical 2ML-α-Bi base (dark blue) decorated with MBi (pale blue), in between two 4ML-α-Bi stripes (orange). The white lines indicate the fringes of M1, the red arrow highlights the $\mathbf{R_1}$ direction. (b) STM image ($V = -0.8$ V, $I = 10$ pA) of the same area after a few scans at much higher set-point current ($I = 1$ nA). The fringes now appear at a different angle. (c) Atomically resolved STM image ($V = -0.8$ V, $I = 200$ pA) of MBi obtained at $T = 52$ K. Images adapted from [239].

	α-Bi ($R_1 \times R_2$) (Å^2)	MBi ($R'_1 \times R'_2$) (Å^2)
HOPG/2ML-α-Bi	$(4.5 \pm 0.1) \times (4.8 \pm 0.1)$	$(4.0 \pm 0.2) \times (4.1 \pm 0.3)$
Calculated	4.54×4.75	3.7×4.1 [a], 3.9×3.9 [b]
Bulk (110)	4.54×4.75	–

Table 3.7: MBi on α-Bi: experimentally observed lattices, DFT calculations and bulk values. [a] refers to the most stable configuration of MBi, [b] refers to the structure obtained when forcing the lattice into a square configuration. For more details, see [239].

MBi structural properties The MBi crystal structure is clearly different [239] from the previously synthesised α-Bi and β-Bi [240], with a significantly contracted surface unit cell compared to α-Bi. MBi differs also by its thickness: one atomic layer instead of two paired layers for α-Bi. Table 3.7 gives the results of the FFT analysis carried on atomically resolved STM images. MBi is characterised with $R'_1 \times R'_2 = (4.0 \pm 0.2) \times (4.1 \pm 0.2)$ Å^2, in agreement with the DFT prediction [239]. Height measurements indicate a thickness of about 2 Å. Figure 3.14(c) shows an STM image of MBi, where both the atomic structure and the MPs are resolved. Comparison between atomically resolved STM images and STM images of neighbouring α-Bi (shown in [239]) permits the determination of the rotation angle θ between the two layers. A small rotation angle is determined, as $\theta = 1 \pm 3°$.

MPs observations The differing crystal structures and orientation of α-Bi and MBi lead to the emergence of MPs. A clear MP is observed in Fig. 3.14(a), labelled M1, with fringes

	$\lambda_1 \pm d\lambda_1$ (nm)	$\delta_1 \pm d\delta_1$ (°)	$\lambda_2 \pm d\lambda_2$ (nm)	$\delta_2 \pm d\delta_2$ (°)
Before tip modification	1.9 ± 0.2	2.5 ± 2.1	3.1 ± 0.3	80 ± 10
After tip modification	1.9 ± 0.3	20 ± 4	–	–

Table 3.8: Experimental characterisation of the MPs of MBi on 2ML-α-Bi observed on HOPG, both before and after tip modification (TM).

running nearly parallel to $\mathbf{R_1}$ (i.e. α-Bi $\langle 1\bar{1}0 \rangle$). M1 fringes are indicated with white lines, $\mathbf{R_1}$ with a red arrow. M2 is observed in some images (e.g. in the atomically resolved STM image in Fig. 3.14(c)) but not in all of them (e.g. Fig. 3.14(a)). The results of the characterisation of M1 and M2 are given in the first row of Table 3.8. The large uncertainties on the measurement of the lattice constants and the periods is explained by the limited width of the layers ($\sim 20 \times 20$ nm^2, i.e. only a limited number of atomic rows and of MP fringes can be resolved), which in turns reduces the precision in the FFTs.

The STM image in Fig. 3.14(b) shows the same island that is present in Fig. 3.14(a), except acquired after a series of scans with a 100-fold higher set-point current (I = 1 nA), increasing tip-sample interactions. Note that both STM images in (a) and (b) have identical current set-points and bias voltages, but that the scans with an increased current set point (not shown) were recorded between the acquisition of the two STM images in Fig. 3.14(a) and in Fig. 3.14(b). Clearly, this treatment induced a change in the MBi layer. The area of the MBi flake reduced by roughly 50%, likely due to diffusion of the atoms that belong to the edge of MBi, as described in detail in [239]. More interestingly, the fringes that constitute the MP in Fig. 3.14(b) are completely different. Before and after tip modification, the periods λ_1 do not change within their uncertainties, however the fringe angle δ_1 has been altered drastically, as before tip modification $\delta_1 = 2.5 \pm 2.1°$, and after tip modification $\delta_1 = 20 \pm 4°$. Due to the lack of atomically-resolved STM images of the MBi flake after tip modification, it is hypothesised that scanning with increased tip-sample interactions induced a rotation of the MBi overlayer. In order to determine what is the new rotation angle θ after tip modification, the MPs are modeled as a function of θ.

3.3.3.2 Analytical modeling of MBi on α-Bi

The two layers α-Bi and MBi both exhibit rectangular lattices ($\omega_1 = \omega_2 = \pi/2$) which permit modelling of the MPs via the analytical model described in subsection 3.2.1. Using the same

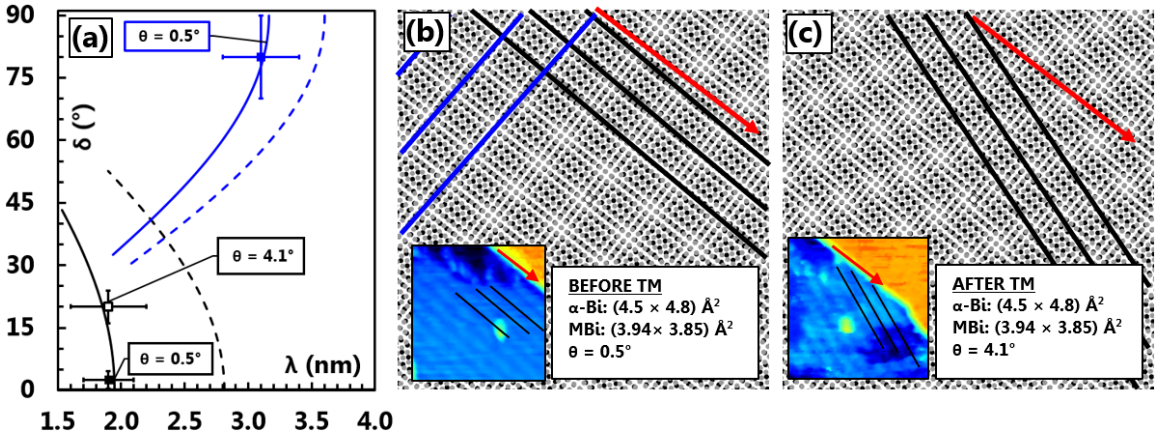

Figure 3.15: MBi analytical model. (a) (λ_1,δ_1) and (λ_2,δ_2) obtained using the analytical model, using the experimental lattice parameters ($R_1 \times R_2 = 4.5 \times 4.8$ Å^2, $R'_1 = 4.0 \times 4.1$ Å^2, dashed lines) and optimised lattice constants ($R_1 \times R_2 = 4.5 \times 4.8$ Å^2, $R'_1 = 3.94 \times 3.85$ Å^2, solid lines). The observed MPs are also plotted in the graph, both before tip modification (solid squares) and after tip modification (open square). M1 is represented in black, M2 in blue. (b) Simulated MPs obtained with optimised lattice constants for an angle of $\theta = 0.5°$ (inset: STM image of MBi before tip modification). (c) Simulated MPs obtained with optimised lattice constants for an angle of $\theta = 4.1°$ (inset: STM image of MBi after tip modification). In (b) and (c), $\mathbf{R_1}$ direction is highlighted with red arrows, M1 and M2 fringes are indicated respectively with black and blue lines. α-Bi atoms are represented in black, MBi in grey.

procedure as for previously studied systems (see subsections 3.3.1 and 3.3.2), the method consists of (i) calculating the MPs with the experimental unit cells obtained from atomically resolved STM images and (ii) correcting the model with optimised lattice constants to find better agreement with the observations.

Using the experimental lattice parameters First, the MPs are predicted using the experimental unit cells (i.e. $R_1 \times R_2 = 4.5 \times 4.8$ Å^2, $R'_1 \times R'_2 = 4.0 \times 4.1$ Å^2, see Table 3.7). Figure 3.15(a) displays the results of (λ_1,δ_1) (black dashed line) and (λ_2,δ_2) (blue dashed line) for $\theta = 0...10°$. For a null rotation angle $\theta = 0°$, $\lambda_1 = 2.8$ nm and $\lambda_2 = 3.6$ nm, and both reduce as θ increases. The fringe angles δ_1 and δ_2 are respectively parallel and perpendicular to the $\mathbf{R_1} \equiv \alpha$-Bi $\langle 1\bar{1}0 \rangle$ direction when $\theta = 0°$. The measured M1 (λ_1,δ_1) and M2 (λ_2,δ_2) before tip modification (in solid squares, respectively black and blue), and M1 after tip modification (open square) are overlaid onto Fig. 3.15(a). No agreement can be found for any value of θ, as the periods in the simulation are significantly larger than the observed ones. Therefore, the lattice mismatch between α-Bi and MBi must be increased.

Optimised lattice parameters The new MBi lattice is chosen such as R'_1 and R'_2 are still close to the observation (i.e. within the experimental uncertainties) as given in Table 3.7. A good agreement with the observed M1 and M2 both before and after tip modification is found when setting $R'_1 \times R'_2 = 3.94 \times 3.84$ Å^2 without modifying the α-Bi unit cell. The results are displayed in Fig. 3.15(a) with solid lines. This time, the simulated (λ_1, δ_1) and (λ_2, δ_2) cross through M1 and M2 before and after tip modification. It is found that the best agreement for M1 and M2 is obtained with $\theta = 0.5 \pm 0.5°$ (before tip modification), and $\theta = 4.1 \pm 0.8°$ (after tip modification). Figure 3.14(b) shows the VESTA simulations obtained using the optimised lattice parameters before tip modification ($\theta = 0.5°$). M1 fringes and $\mathbf{R_1}$ are highlighted respectively with black lines and a red arrow. The VESTA simulation shows a good agreement with the STM image in the inset. Figure 3.14(c) shows the simulated MPs this time for $\theta = 4.1°$ (i.e. after tip modification). Here too, simulation and experiment agree very well.

Note The previously studied α-Sb and β-Sb were modeled with an underlying α-Bi identical to the bulk Bi(110) i.e. $R_1 \times R_2 = 4.75 \times 4.54$ Å^2. For the MBi study here, less accurate characterisation of α-Bi yields $R_1 \times R_2 = 4.8 \times 4.5$ Å^2. In principle, there is no reason why α-Bi would possess a different unit cell when it is decorated by MBi. Analytical calculations show (not displayed here) that using bulk values for α-Bi leads to calculated MPs with a very good agreement with the observations if the MBi lattice constants are set to $R'_1 \times R'_2 = 3.97 \times 3.82$ Å^2. This minute difference is however insignificant and therefore not concerning.

3.3.3.3 Conclusion

The newly synthesised MBi is found on top of the 2ML-α-Bi bases, between two narrow 4ML-α-Bi stripes. STM experiments clearly reveal periodic surface modulations that can be successfully modeled using the MPs emerging from rigid layers. Analytical modeling of the MPs confirms the previously determined lattice constants (with minimal change in the lattice parameters of MBi, of 5 and 15 pm, below the uncertainties), as well as their relative orientation. Moreover, analytical modeling and VESTA-simulations explain the change in the observed MPs after tip modification, due to a rotation of the MBi layer with respect to

α-Bi by a few degrees. This shows that analysis of MPs (i) confirms the lattice parameters as well as the orientation between the layers, and (ii) offers a measurement of the structural changes that can be induced by tip-modifications or other phenomena.

3.3.4 α-Bi

The 2ML-α-Bi phase itself exhibits MPs. When grown on HOPG substrate, the MPs show up as stripes and have previously been studied with a model that assumes commensurability between the two crystals [151]. Since the lattice parameters of HOPG ($R_1 = R_2 = 2.46$ Å) and MoS_2 ($R_1 = R_2 = 3.16$ Å) differ, the MPs emerging from the stacking of α-Bi on MoS_2 are expected to differ as well. The growth and structural properties of α-Bi are discussed in subsection 3.3.1.

3.3.4.1 Moiré patterns observations

HOPG underlayer Figure 3.16(a) shows an STM image of an 2ML-α-Bi island grown on HOPG where a MP is resolved (adapted from [151]). The inset in (a) shows an STM image of the island at larger scale. The averaged periods are measured to be $\lambda = 4 \pm 1$ nm, with a mean fringe angle of $\delta = 52 \pm 9°$. The MPs are observed only in $\sim 20\%$ of the islands, when $\mathbf{R_1}$ is aligned with the armchair direction of HOPG [151]. Results of the characterisation are gathered in Table 3.9. In Fig. 3.16(a), $\lambda = 3.2 \pm 0.4$ nm and $\delta = 54 \pm 5°$.

MoS_2 underlayer Figure 3.16(b) shows an atomically resolved STM image of a 2ML-α-Bi island, grown on MoS_2. The MPs are different than those for Bi structures grown on HOPG. The fringes are nearly parallel to $\mathbf{R'_1}$ = 2ML-α-Bi $\langle 1\bar{1}0 \rangle$ direction (white arrow). The corresponding period and angle are $\lambda_0 = 2.22 \pm 0.07$ nm, $\delta_0 = 4 \pm 2°$. Comparison of atomically resolved STM images with the neighbouring MoS_2 substrate unit cell directions (not shown here) shows that $\theta = 0.3 \pm 0.6°$. Figure 3.16(c) shows the FFT of the STM image in (b). The reciprocal spots corresponding to 2ML-α-Bi are very well resolved. Closer to $k = 0$, the spots highlighted by the green arrow correspond to the main observed fringes. Two other pairs of spots $\mathbf{K_1}$ and $\mathbf{K_2}$ are visible and are indicated respectively with blue and red arrows. Their relative intensity is lower than that of the main spots $\mathbf{K_0}$, yet clearly resolved. Their corre-

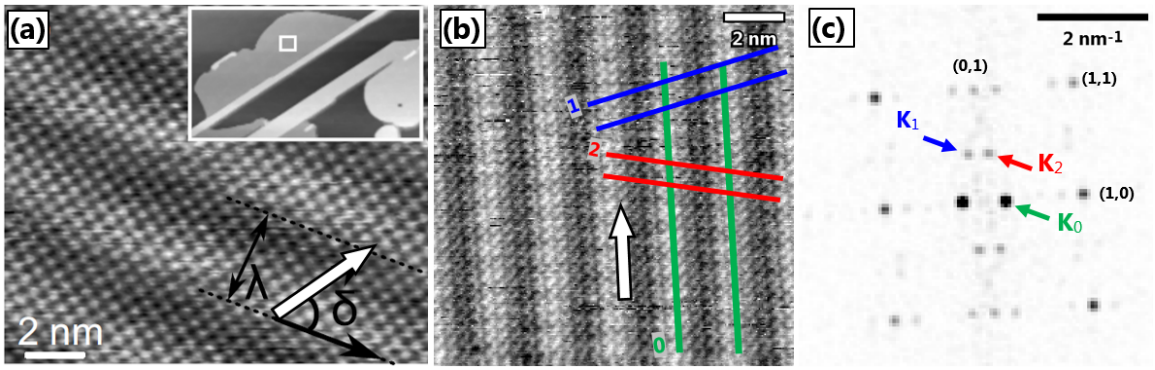

Figure 3.16: α-Bi on HOPG and MoS_2. (a) Atomically resolved STM image ($V = -2.0$ V, $I = 1.5$ nA) of α-Bi grown on HOPG, where a clear MP is observed (image from [151]). λ and δ are highlighted (inset: larger scale STM image in which the small white rectangle corresponds to (a)). All white arrows represent $\mathbf{R'_1}$ = α-Bi $\langle 1\bar{1}0 \rangle$. (b) Atomically resolved STM image ($V = +50$ mV, $I = 0.3$ nA) of a 2ML-α-Bi island grown on MoS_2. The main fringes (labelled "0") are highlighted in green lines, secondary fringes in blue ("1") and red ("2"). (c) FFT of the STM image in (b), where the reciprocal lattice spots of 2ML-α-Bi (1,0), (0,1) and (1,1) are resolved, as well as the MP reciprocal spots. The spot corresponding to the main fringes $\mathbf{K_0}$ is indicated with a green arrow. The faint secondary spots $\mathbf{K_1}$ and $\mathbf{K_2}$ are indicated with a blue and red arrow.

sponding periods are $\lambda_1 = 0.99 \pm 0.05$ nm and $\lambda_2 = 1.00 \pm 0.05$ nm, and their angles $\delta_1 = 79 \pm 2°$ and $\delta_2 = 75 \pm 2°$. The results from the characterisation of the MPs are gathered in Table 3.9. While the fringes are unambiguously resolved in the FFT, they appear very faintly in the STM image in (b), and are therefore highlighted with blue and red lines.

3.3.4.2 Simulation

The symmetries of the under- and overlayer are different (respectively hexagonal and rectangular), and so the MP simulations are performed using VESTA. Similar to the previously studied cases, the first step consists of modeling the two crystal lattices using the observed lattice constants. Then, a minimal correction of the lattice and/or their relative orientation may be necessary to improve the agreement.

HOPG underlayer The experimental lattice parameters (i.e. $R_1 = R_2 = 2.46$ Å, and $R'_1 \times R'_2 = (4.54 \times 4.75)$ Å^2) are firstly used for the simulations. The rotation angle is set as to the experimentally determined value of $\theta = 30°$. Starting with $\theta = 30°$ (not displayed), the simulated pattern agrees with the observation in terms of period, however the fringe angle

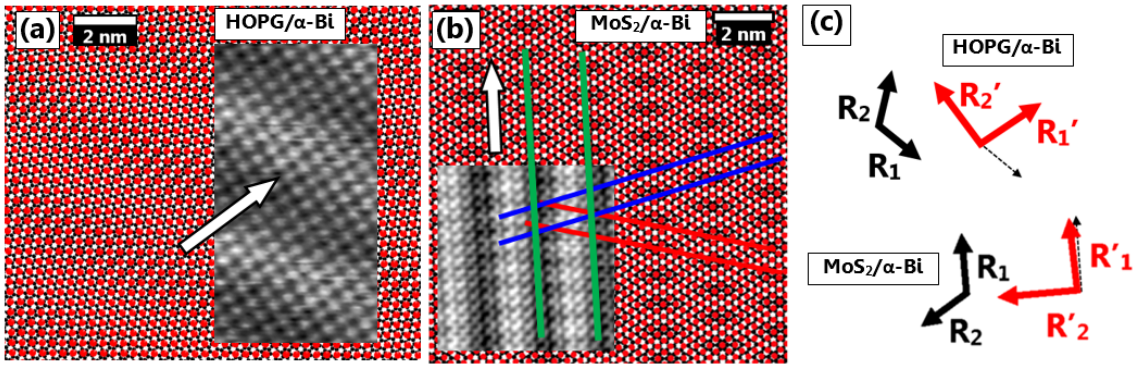

Figure 3.17: α-Bi on HOPG and MoS_2 simulations.(a) VESTA simulation (width: 13.5 nm) using the experimentally observed lattice constants and rotation angle ($R_1 = R_2 = 2.46$ Å, $R'_1 \times R'_2 = (4.54 \times 4.75)$ Å^2, for $\theta = 32.1°$). Inset: STM image scaled with the simulated image. (b) VESTA simulation (13.5×13.5 nm^2) using the experimentally observed lattice constants and rotation angle ($R_1 = R_2 = 3.16$ Å, $R'_1 \times R'_2 = 4.53 \times 4.87$ Å^2, $\theta = 0.3°$. Inset: STM image scaled with the simulated image. The main experimental fringes (green) align with the simulated ones. The secondary fringes (blue and red) align with a great agreement too. $\mathbf{R'_1}$ = α-Bi-$\langle 1\bar{1}0 \rangle$ direction is indicated with a white arrow. (c) Schematics of the under- (black) and overlayer (red) base vectors, for HOPG-α-Bi (top) and MoS_2-α-Bi (bottom). The underlayer base vector $\mathbf{R_1}$ is also drawn in dashed arrow to allow the visualisation of θ.

disagrees strongly ($\delta = 77°$, experimentally measured to be $54 \pm 5°$). An optimisation is therefore necessary. Due to the relative large uncertainty on the rotation angle θ (d$\theta = \pm 5°$) it is reasonable to vary θ until an agreement is found. Figure 3.17(a) shows the simulated MP obtained for $\theta = 32.1°$. The MPs show up as fringes and agree with the observations: there is a clear continuity between the simulated and the experimental fringes (a crop of the STM image is superposed to scale with the simulation). The simulated periods and angle in this optimised case are $\lambda_0 = 3.3 \pm 0.1$ nm and $\delta_0 = 58 \pm 2°$, which are in very good agreement with the observations.

MoS_2 underlayer The two lattices are set up in VESTA, i.e. $R_1 = R_2 = 3.16$ Å and $R'_1 \times R'_2 = (4.53 \times 4.87)$ Å^2. The rotation angle is also set to the experimental value, i.e. $\theta = 0.3°$. The produced image in shown in Fig. 3.17(b), with α-Bi lattice (red balls) superposed on MoS_2 (black balls). $\mathbf{R'_1}$ (i.e. α-Bi-$\langle 1\bar{1}0 \rangle$ direction) is indicated with a white arrow. A cropped, scaled STM image is superposed on the simulated image. The fringes arising from $\mathbf{K_0}$ (green), $\mathbf{K_1}$ (blue), and $\mathbf{K_2}$ (red) are shown. The unit cell vectors are also shown in (c). Unexpectedly, the simulated MPs appear as moirons instead of the experimentally observed

	Over. / Under. / Type	α-Bi HOPG exp.	sim.	α-Bi MoS_2 exp.	sim.
Under.	R_1 (Å)	2.46	2.46	3.16	3.16
α-Bi	R'_1 (Å)	4.54	4.54	4.53	4.53
	R'_2 (Å)	4.75	4.75	4.87	4.87
	θ (°)	30 ± 5	32.1	0.3 ± 0.6	0.3
M_0	λ_0 (nm)	3.2 ± 0.4	3.3 ± 0.1	2.22 ± 0.07	2.18 ± 0.02
	δ_0 (°)	54 ± 5	58 ± 2	4 ± 2	2.5 ± 0.7
M_1	λ_1 (nm)	N/A	N/A	0.99 ± 0.05	1.04 ± 0.01
	δ_1 (°)	N/A	N/A	79 ± 2	77.3 ± 0.9
M_2	λ_2 (nm)	N/A	N/A	1.00 ± 0.05	1.1 ± 0.2
	δ_2 (°)	N/A	N/A	-75 ± 2	74.6 ± 0.1

Table 3.9: Characterisation of the experimental and simulated MPs (using experimental lattice constants and rotation angle) for both HOPG and MoS_2 underlayers. In both cases, the simulation agrees very well with the observations.

fringes. However, the experimental 'secondary' fringes equivalent to $\mathbf{K_1}$ (blue lines) and $\mathbf{K_2}$ (red lines) are very well reproduced by the simulation. The quantitative characterisation of the simulated patterns is given in Table 3.9. The main fringes (λ_0, δ_0), agree very well, both for the period ($\lambda_0 = 2.18 \pm 0.02$ nm) and angle ($\delta_0 = 2.5 \pm 0.7$). The agreement is also very good for the secondary fringes: the observed values of $\lambda_1 = 1.04 \pm 0.05$, $\delta_1 = 77.3 \pm 0.9°$ and $\lambda_2 = 1.1 \pm 0.1$ nm, $\delta_2 = -76.6 \pm 0.1°$ are in very close agreement with the observed values.

3.3.4.3 Discussion: second-order moiré patterns in the MoS_2 case

The simulated MPs, obtained by modeling the lattices of MoS_2 and 2ML-α-Bi as observed, yield a very good agreement: the periods and angles corresponding to the three modulations fall within the observation uncertainties. No corrections on the modeled lattices are necessary to bring the agreement further. However, despite an extremely good agreement, the nature of the MPs here needs some discussion.

Experimentally, the MPs appear as a evident fringes displayed nearly vertically on the STM image. The FFT reveals the existence of faint fringes that run with an angle of approximately $\pm 75°$ with respect to the $\mathbf{R'_1}$ direction of α-Bi. The low intensities of these secondary reciprocal spots in the FFT indicates their relative muteness in the real space image. Interestingly, in the reciprocal space, the difference wave-vector $\mathbf{K_1} - \mathbf{K_2}$ equals to $\mathbf{K_0}$. In other words, the mainly observed fringes arise from a linear combination such that $\mathbf{K_0} = \mathbf{K_1} - \mathbf{K_2}$.

This is an effect that is commonly seen in Fourier analysis: for example the reciprocal lattice in Fig. 3.16(c) shows clearly the α-Bi (1,1) reciprocal lattice spots in the FFT, because the atomic arrangement of α-Bi cannot be described by a unique couple of sinusoidal oscillations, but rather by a Fourier series including integer linear combinations.

In the simulation, the MPs do not show up as fringes, but rather appear as a moiron super-lattice, characterised by two periodicities. These periods correspond to the 'secondary', faint fringes observed in the FFT ($\mathbf{K_1}$ and $\mathbf{K_2}$) with an unprecedented precision. The nearly vertical modulation visually appears upon 'squinting', in other words by mentally merging the ellipse-shaped moirons together.

The reason behind this is still unclear. While the simple superposition of the lattices lead to an emergent moiron super-lattice, the observation is that of a fringe-like MP that seem to appear from a linear combination of the wave-vectors evidenced by the simulation. This may indicate that the real VDWHs and the interference patterns described by MPs deviate from simple ball-and-stick simulations. The atomic arrangement of the under- or overlayer may be locally strained, leading to a fringe-dominant MP. Alternatively, one can not completely rule out imaging with a not perfectly sharp STM tip. To clarify this, further experiments should to be conducted, e.g. focusing on the local dI/dV curves to be compared with calculated LDOS of the VDWHs.

3.3.5 Conclusion

The two systems - HOPG/2ML-α-Bi and MoS_2/2ML-α-Bi - lead to the presence of MPs that are consistent from island to island. Due to the nature of the stacking symmetry (rectangular on hexagonal), VESTA simulations are performed to model and reproduce the observed MPs. Utilizing the experimentally observed lattice constants and rotation angles, very good agreement is found for the MoS_2 case. For HOPG, a minute correction of the rotation angle is required (+2.1°, below the measurement uncertainty of 5°) in order to obtain a suitable agreement, confirming results published earlier [151].

While the nature of the MPs in the HOPG/2ML-α-Bi is fringe-like, that of MoS_2/2ML-α-Bi is that of a moiron super-lattice, characterised by two MP vectors. The experiments are found to diverge from the VESTA simulations, where the observed MPs appear as an

ensemble of three periodic fringes. The mainly observed fringes are found emerge from a linear combination of the wavevectors of the two fainter ones, indicating that MPs can also interfere together.

3.4 Conclusions

3.4.1 Achievements

In this chapter, the VDWHs consisting of multiple layers of group-V elemental (Sb, Bi) 2D materials are successfully grown via PVD on either MoS_2 or HOPG, two van der Waals substrates. Despite the different electronic structure of the substrates, the VDWHs show very consistent structural properties, which is promising in terms of adaptability of the α-Bi/Sb nanostructures onto other VDW substrates. Low deposition coverage in UHV conditions and the nature of the substrates (i.e. lack of dangling bonds on the surface) leads to the formation of BP-like Bi islands. A large majority of the bases are identified as 2ML-α-Bi, occasionally containing a 4ML-α-Bi narrow stripe in the middle elongated along the α-Bi $\langle 1\bar{1}0\rangle$ axis. In some cases, thicker and narrower 4ML-α-Bi bases are observed. In rare occasions, 2ML-α-Bi bases are decorated with MBi, a completely different structure, which was previously unobserved nor predicted. Additional deposition of Sb onto the pre-existing α-Bi bases leads to the formation of two allotropes of antimonene, coexisting on top of the bases: β-Sb and α-Sb. On the thicker 4ML-α-Bi bases, only α-Sb is identified. While β-Sb was previously studied and successfully grown by other groups [241, 242], α-Sb had until then been the focus of theoretical works only [243–246]. MBi [239], α-Bi [140], and α-Sb [153] are predicted to be topologically non-trivial. While β-Sb is a classical semiconductor, it is possible that sufficient strain induces topological properties in its band-structure [247].

All the different superposition combinations that are studied in this thesis present more or less ordered fringes that modulate the apparent height of the layers (typically ~ 1 Å) in STM images. Those are in fact MPs, emerging from the differing unit cells of the individual layers. This phenomenon is expected from VDWHs, where structural properties of the 2D crystals remain relatively independent from its neighbouring layers. Therefore the layers are less expected to strain and adapt for lattice matching than for conventional heteroepitaxy. In the cases where the symmetries of the underlayer and overlayer were identical (i.e. α-Sb

on α-Bi (2ML or 4ML α-Bi bases), and MBi on α-Bi), analytical formulas developed earlier [174] permitted to model accurately the observed MPs. When the symmetries of the under- and overlayer unit cells are different (i.e. 2ML-α-Bi on HOPG, 2ML-α-Bi on MoS_2 and β-Sb on 2ML-α-Bi), the MPs are successfully modeled using VESTA simulations, where the two crystals are superposed in the software using the experimentally observed lattice parameters and rotation angle. Minute corrections, always within the experimental uncertainties of measurements on the lattice constants and/or the angle of rotation, can be required in order to obtain a very good agreement with the observations.

When the two crystals that lead to MPs possessed the same symmetry (α-Sb on α-Bi and MBi on α-Bi), the rotation angles were always very close to 0, confirmed by modeling of the MPs. In the rare cases where the rotation angle was non zero, the 2D crystal layers showed MP fringes ordered differently than those observed in most islands. Adequate analysis always explained the MPs in these particular cases. For the MBi on 2ML-α-Bi, it was shown that strongly increasing the tip-sample interactions during STM scans led to a rotation of the MBi with respect to α-Bi by a few degrees, paving the way for engineering nanostructures in which the MP fringes can be tuned.

3.4.2 Limitations

While one can successfully confirm all the observed MPs, there are fundamental limits with the developed methods for modeling MPs that need to be addressed. The models used here make the hypothesis that underlayer and overlayer are rigid, each described by a pair of 2D Bravais lattices. In other words, the models to not take into account any deviation from perfectly ordered crystals. It can be expected that the layers behave totally differently at the edges, where relaxation and surface reconstruction usually occurs (and paradoxically, where the topological properties are expected to manifest via the edge-states). If these structures happen to be used for devices in which the MPs play an important role, the edges of the nanostructures would need in-depth characterisation and modeling because it is likely that contacts with metallic electrodes would take place at the edges of the layers. Also, there is a possibility that the 2D layers grown in this thesis contain a certain density of point-defects (e.g. point dislocations), or 1D-defects (e.g. grain boundaries) within the crystal.

These phenomena have been partially studied in terms of geometry of the MPs emerging from such defect-containing crystals [151, 215], yet the influence on the band-structure is still totally unknown. Also, the topographic corrugations present on the surface of the MPs are inseparable from local strain, that strongly modify the local band-structure. All these phenomena that account for deviations from perfectly ordered crystals are not taken into consideration within the simulation and analytical modeling. In fact, preliminary results on aged α-Sb tend to show that a large number of dislocations or local relaxations are taking place within weeks after deposition.

VESTA is a convenient tool for visualisation and illustration of the MPs in most cases (i.e. fine-tuning the lattice constants or rotation angle θ), nonetheless the technique is relatively painful and slow (and by experience somewhat leading to eye-pain). The procedure is based on the identification of the fringes by eye, and subsequently, by clicking manually on two atomic positions that are *believed* to be part of the MP fringes. Because the MPs are incommensurate, it is possible that there is no atomic position belonging to any fringe. The final characterisations will therefore only yield an approximate simulated (θ, λ, δ), although the accuracy may be improved upon repetition of the simulations. Lastly, as seen in the case of the 2ML-α-Bi on MoS_2, the MPs can be difficult to visualize in the software.

The analytical model that is used in this thesis [174] is instantaneous, simpler to use and much more accurate than the VESTA simulations. However to be valid, two conditions must be fulfilled. First, the unit cells of the under- and overlayer must possess an identical angle ω, thus limiting the range of systems that can be analytically modeled (e.g. graphene on graphite: $\omega_1 = \omega_2 = 120°$, or α-Sb on α-Bi: $\omega_1 = \omega_2 = 90°$). The MPs originating from α-Bi on MoS_2 cannot be predicted through calculations ($\omega_1 = 120° \neq \omega_2 = 90°$). Secondly, the range in which the rotation angle θ can be varied is limited to $|\theta| < 10°$. A general, mathematical solution to the problem of the MPs hasn't yet been proposed.

As mentioned in detail in section 3.3.1 (this is true for the other studied cases), the experimental characterisation of the MPs often includes a relatively large uncertainty. The reason is multiple: intrinsic disorder of the fringes potentially due to local strain or defects, small number of fringes limiting the precision in the FFT and the lack of a very large sample size to obtain a sense of the statistical dispersion of the MPs for a given superposition case.

A more precise, lengthy characterisation would permit to study with more detail the subtle differences between the different islands in terms of e.g. lattice parameters or rotation angle.

3.4.3 Further work

To address the limits evoked in the previous paragraphs, further work can be done. To improve the experimental characterisations, additional depositions should be performed, focusing this time in growing larger bases of 2ML-α-Bi and larger bases of decorating antimonene (α-Sb and β-Sb, although it is not clear yet if both allotropes will be present on larger bases). The route is to deposit islands with increased coverage, both for Bi and Sb (e.g. twice the typical coverage used in this thesis).

An in-depth spectroscopy study focusing on the moiré fringes would be a requirement for the investigations into device engineering in which the MPs can be used for their local modulation of the electronic band-structure, e.g spin-polarised channels. Such devices are still highly speculative at the moment, as most studies cited in this thesis focused on theoretical predictions of various nanostructures electronic properties. To address this, dI/dV mapping at low temperatures, conducted on wider layers, resolving the fringes, are of prior interest. If possible, the results should be paired with DFT calculations of mismatched layers leading to MPs. However such predictions are difficult due to the incommensurability of the crystals in the VDWHs, where DFT calculation typically assumes periodic boundary conditions.

Finally, during the work on the MPs modeling it was noticed that deriving a general approach for any symmetries and any rotation angle θ would increase the efficiency in understanding the observed MPs. The precision of the modeling would benefit form having a unique, precise, and fast procedure. A general method was then developed, and is presented in chapter 4.

Chapter 4

Moiré patterns general solution

The moiré patterns (MPs) observed on the various group-V van der Waals heterostructures (VDWHs) in this thesis are accurately described by ball-and-stick superpositions (through VESTA simulations) or analytically when possible, as extensively detailed in chapter 3. However, both techniques have their limitations. The VESTA simulations require a manual approach and are therefore not always precise and are relatively slow (see section 3.2.2.1). Conversely, the analytical modelling is possible only for specific symmetries and a limited range of rotation angles (see section 3.2.2.2).

A general method, applicable for any set of crystalline symmetries and for any rotation angle θ is therefore highly desirable. Instantaneous and accurate evaluation of the MPs (the period λ and the fringe angle δ) would supersede previous modeling techniques, potentially benefiting VDWHs research where MPs have been proven to have a tremendous impact on the electronic properties [129, 157, 159–161, 214, 215, 231, 232, 248, 249] and the topological order [158]. A huge part of the literature has focused on hexagonal symmetries, but developments in group-V materials research and the discovery of novel allotropes necessitate consideration of more complex symmetries. A geometrical model for understanding the MPs observed on α-Bi/HOPG has been proposed [151], however that approach was complex and focused only on commensurate superposition (i.e. exact registry) in real-space only. A more general model is therefore desirable.

The general solution detailed in this chapter was developed following the work presented in chapter 3. An approach to understanding MP wave-vectors in the reciprocal space has been formalised previously for optical gratings [250–252], and the same principle is applied

here to the more complex case of atomic lattices. To our knowledge, a similar approach using the reciprocal space has never previously been used to describe the MPs observed in VDWHs, except for the case of hexagonal/hexagonal layers [253].

This chapter first focuses on the concept of a general solution based on Fourier theory, in section 4.1, focusing first on the simpler case of the superposition of gratings, and then generalised for two-dimensional (2D) lattices. In section 4.2, the calculation scheme is shown in detail, discussing the model parameters, illustrated with the simplest and most reported case of twisted bilayer graphene. Section 4.3 applies the new general model to the group-V VDWHs investigated in chapter 3 and agreement with previous modeling techniques is discussed. The model is then described in more depth and the assumptions from the early sections are revisited in section 4.4. The analytical solution of the problem is then presented in section 4.5. The concept of 'moiré rosettes' is introduced in section 4.6. Finally section 4.7 summarizes and discusses the general model. Future work is also outlined.

4.1 Concept

The geometry of the MPs in hexagonal 2D systems has been extensively studied [174, 228, 234, 236, 254] and therefore provides a test for comparison with the general method described in this chapter. In particular, a generalisation of the formula presented by Hermann [174] giving the distance between two moirons L would be desirable. Hermann's result for the hexagonal case is

$$L = \frac{pR}{\sqrt{1+p^2-2p\cos\theta}} \tag{4.1}$$

where p is the ratio between the lattice constants of the over- and underlayer and R the lattice constant of the underlayer. Hermann also proposes a similar formula for other symmetries, provided that both under- and overlayer share the same unit cell angle. Note that the range of application of Hermann's model is $-10 < \theta < 10°$ and $0.8 < p < 1.2$ [174].

The case of gratings (each grating is described by a unique vector $\mathbf{k}$) is first presented in sections 4.1.1 and 4.1.2, and the case of atomic lattices (where a pair of independent vectors $\mathbf{k_1}$ and $\mathbf{k_2}$ defines each lattice) is developed in section 4.1.3.

Conventions The Fourier transform ($\mathscr{F}$) is the operation used here to determine the reciprocal vectors from real-space information [31]. Only the modulus of $\mathscr{F}$ describes the periodicity (period and orientation), therefore the phase of the $\mathscr{F}$ is ignored. In other words, the analysis here is independent of the relative translation of the layers in the (x,y) plane. Only the *geometry*, i.e. the real-space period λ and the angular orientation δ of the MPs are considered here. In this chapter the crystallographic convention is used where $k = \frac{1}{\lambda}$ ($2\pi = 1$). The vectors are written in bold e.g. $\mathbf{R_1}$ and the scalars in italic e.g. $k = |\mathbf{k}|$. Linear combinations using a negative coefficient e.g. for $n = 1$ and $m = -1$ are written $\mathbf{K_{nm}} = \mathbf{K_{1\bar{1}}}$. Complex numbers are italicised and underlined e.g. $\underline{K}$.

4.1.1 Gratings

Real space The method is illustrated in this section with the simplified case of two gratings, which was formalised by Amidror [250, 252]. A grating g is defined by its *transmittance* $g(x,y)$ such that if the point (x,y) belongs to the grating, $g(x,y) = 0$ ('blue'). Elsewhere $g(x,y) = 1$ ('white'). Only binary gratings are considered, i.e. no intermediate value $0 < g(x,y) < 1$ can exist. The grating spacing is R.

Figure 4.1(a) shows a horizontal grating g_1. Another grating g_2, identical to g_1 but rotated by $\theta = +10°$ is shown in Fig. 4.1(b). The superposition g_{12} of the two gratings is displayed in Fig. 4.1(c). A moiré pattern (MP) appears clearly in the superposition. The MP fringes run nearly vertically with a spacing λ of about 6 times the grating periodicity. The superposition $g_{12}(x,y) = 0$ when (x,y) belongs to either g_1 or g_2 ($g_1(x,y) = 0$ *or* $g_2(x,y) = 0$). The superposition can then be described by a product function $g_{12}(x,y) = g_1(x,y) \times g_2(x,y)$ [250, 252].

Reciprocal space The Fourier transform $\mathscr{F}$ of the binary gratings yields their reciprocal vectors $\mathbf{k_n}$[1] (in inverse units of grating spacing). Figure 4.1(d) shows $\mathscr{F}(g_1)$. Because the grating in Fig. 4.1(a) is horizontal, the basis vector $\mathbf{k_1}$ is aligned with the $\hat{\mathbf{y}}$ axis and its norm is $k_1 = 1/R$. As a result of the binary nature of the grating, an infinite Fourier series is observed in reciprocal space with $\mathbf{k_n} = n \times \mathbf{k_1}$, where $n \in \mathbb{Z}$. Figure 4.1(e) shows $\mathscr{F}(g_2)$,

[1] Note that the need for $|n| > 1$ is discussed in 4.1.2.

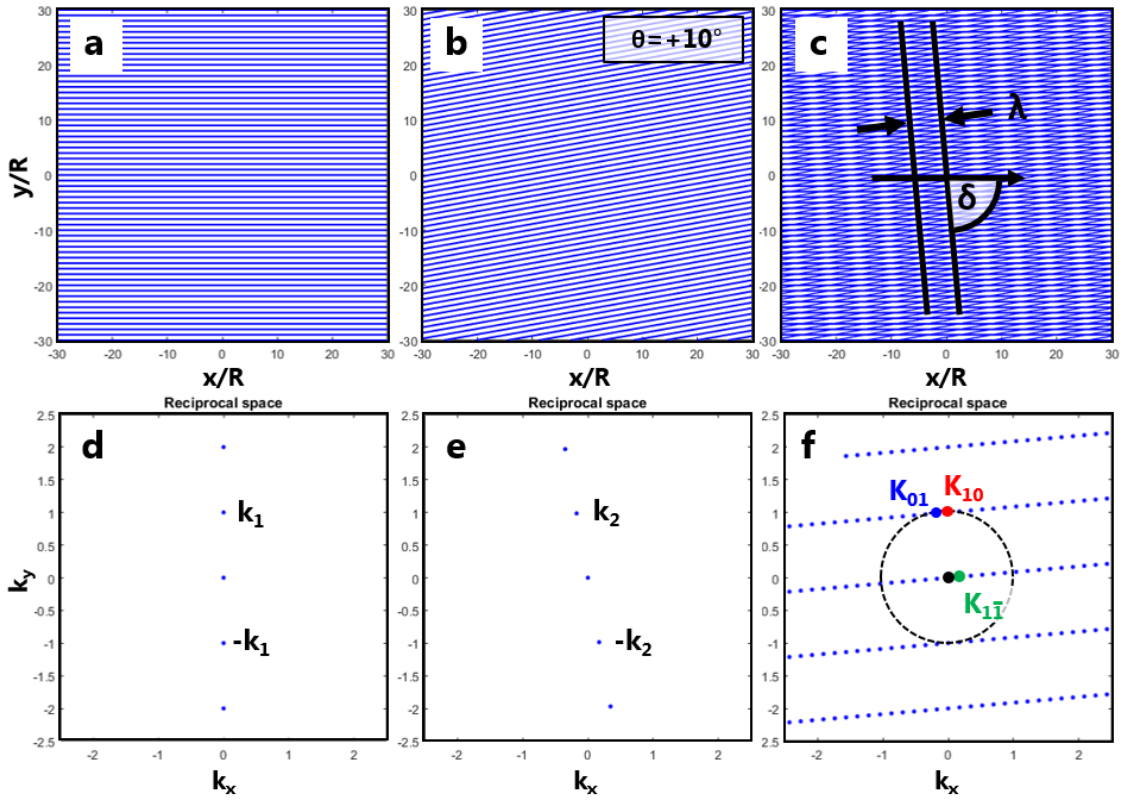

Figure 4.1: Grating superposition in real and in reciprocal space. (a) g_1 grating with horizontal ($\theta_1 = 0$) fringes with a spacing of R_1. (b) g_2 grating, identical to g_1 but rotated ($\theta_2 = +10°$). (c) Superposition of the gratings $g_{12} = g_1 \times g_2$. A MP appears upon superposition, two fringes, the period λ and angle δ are indicated. (d-f) Reciprocal space of the grating g_1 (d), g_2 (e), and g_{12} (f). The $\mathbf{K_{1\bar{1}}}$ and $\mathbf{K_{10}}$ reciprocal vectors of the superposition are indicated in green and red respectively. The dashed circle centred at origin in (f) has a radius of $1/R_1 = K_{01} = K_{10}$.

and is identical to $\mathscr{F}(g_1)$ except rotated by $\theta = +10°$. The convolution theorem [255] states that the Fourier transform $\mathscr{F}$ of a product is the *convolution* of the Fourier transforms of the individual functions i.e.

$$\mathscr{F}[g_{12}] = \mathscr{F}[g_1] * \mathscr{F}[g_2] \tag{4.2}$$

with $*$ the convolution operator. The Fourier transform of the product g_{12} shown in Fig. 4.1(c) is then a lattice in the reciprocal space, where the basis vectors are $\mathbf{k}_1$ and $\mathbf{k}_2$, as shown in Fig. 4.1(f), and

$$\mathbf{K_{nm}} = n \cdot \mathbf{k}_1 + m \cdot \mathbf{k}_2 \tag{4.3}$$

where $n, m \in \mathbb{Z}$. The vectors $\mathbf{K_{10}} = \mathbf{k_1}$ and $\mathbf{K_{01}} = \mathbf{k_2}$ are indicated (in blue and red respectively), as well as their linear combination $\mathbf{K_{1\bar{1}}} = \mathbf{k_1} - \mathbf{k_2}$ (in green).

Moiré pattern definition The MP in real-space is defined as the sets of fringes that emerge from the superposition of two gratings. An essential condition is that the MP period is larger than the spacing of the individual gratings. In the present context of gratings, we postulate that the MP is described by the unique $\mathbf{K_{nm}}$ vector that is the closest to origin and that it can be seen as the fundamental wave-vector of the MP. The other vectors that emerge from the convolution (corresponding to higher orders that are more distant to origin and therefore correspond to shorter real-space periods) are ignored. This will be revisited in section 4.4.

Moiré pattern period The period of a MP is defined as $\lambda = \frac{1}{|\mathbf{K_{nm}}|}$. In the example of Fig. 4.1, the wave vectors $\mathbf{K_{nm}}$ that are inside the dashed circle ($k < k_1 = k_2$) might possibly represent the MP. The actual MP vector here is the one closest to origin, i.e. $\mathbf{K_{1\bar{1}}}$ (note that the vector $-\mathbf{K_{1\bar{1}}} = \mathbf{K_{\bar{1}1}}$ represents the same information and is not discussed further). Its period is $\lambda_{1\bar{1}} = 1/K_{1\bar{1}} \simeq 5.74$ (units of grating spacing) which effectively corresponds to the distance between the two fringes of the MP indicated in Fig. 4.1(c). The other vectors within the circle do not correspond to the MP that is observed in real-space. For instance, the period corresponding to $K_{2\bar{2}}$ is a factor 2 smaller ($\lambda_{2\bar{2}} \simeq 2.87$), which does not correspond to a visible MP in the real-space image.

Moiré pattern angle As in chapter 3, the angle of the MP δ is defined as the angle between an arbitrary but fixed vector (here $\hat{\mathbf{x}}$) and the fringes of the MP. The fringes are perpendicular to the MP vector, i.e. $\delta = \arg(\mathbf{K}) + \pi/2$ (in rad). The fringe angle is restricted to the range $]-90°...90°]$ because the fringes do not have 'a direction'. In the example of Fig. 4.1, $\delta = -85°$.

4.1.2 Higher order reciprocal vectors

In the previous section, the MP fringes of Fig. 4.1 were described by the unique difference vector $\mathbf{K_{1\bar{1}}}$. It seems natural to understand the MP in general as the difference vectors obtained with $n = 1, m = -1$ and to discard all other higher reciprocal vectors. However in the

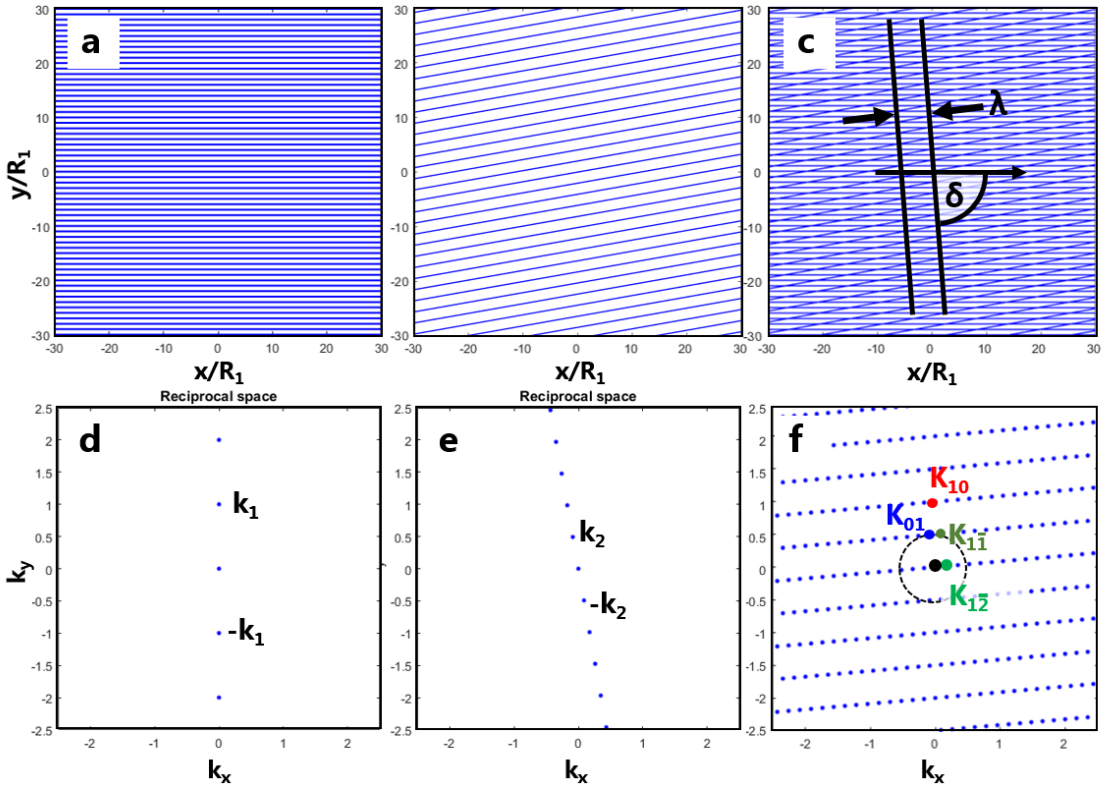

Figure 4.2: Grating superposition and higher order reciprocal vectors. (a) Horizontal grating g_1 with a spacing R_1. (b) Grating g_2 with $\theta = 10°$ and a spacing $R_2 = 2R_1$. (c) Superposition g_{12}. The fringes (two of them are indicated in black), albeit less clear than in Fig. 4.1 have the same period λ and angle δ. (d-f) Reciprocal space of g_1 (d), g_2 (e) and g_{12} (f). The $\mathbf{K_{10}}$, $\mathbf{K_{01}}$, $\mathbf{K_{1\bar{1}}}$ and $\mathbf{K_{1\bar{2}}}$ vectors are indicated. The dashed circle centred at origin has a radius equal to $\min\{K_{01}, K_{10}\} = K_{01}$.

general case, the higher order vectors of the gratings must be considered, as illustrated with the example below.

Real space Figure 4.2 considers the superposition of two gratings, where one of the gratings has a spacing two times larger than the other. The first grating g_1 of spacing R_1 is shown in Fig. 4.2(a), and is identical to the one in Fig. 4.1(a). The second grating g_2 is shown in Fig. 4.2(b). The grating g_2 differs to that of Fig. 4.1(b) because of its larger spacing, two times that of g_1 (i.e. $R_2 = 2R_1$). The superposition g_{12} is shown in Fig. 4.2(c). A MP is visible and two fringes are indicated in black. The period λ and the fringe angle δ are identical to those in Fig. 4.1.

Reciprocal space The observation of the gratings and their superposition in the reciprocal space is now discussed. Figure 4.2(d) shows the reciprocal vectors of g_1, unchanged from Fig. 4.1. Figure 4.2(e) shows the Fourier transform of g_2. The reciprocal vectors form an array that is two times denser than the Fourier transform of g_1 in Fig. 4.2(d) since the grating spacing is two times larger. The Fourier transform of the superposition (i.e. the convolution of the individual Fourier transforms) is shown in Fig. 4.2(f). It is a lattice of points in reciprocal space constructed from the base vectors $\mathbf{k_1}$ and $\mathbf{k_2}$, as previously obtained in Fig. 4.1. The vector that is the closest to origin is not $\mathbf{K_{1\bar{1}}}$ (indicated in dark green) as previously in Fig. 4.1. Instead, $\mathbf{K_{1\bar{2}}} = \mathbf{k_1} - 2\cdot\mathbf{k_2}$ is closer to origin. The inverse of its norm is $\lambda = 1/K_{1\bar{2}} \simeq 5.74$ (in units of R_1) corresponding to the MP observed in real-space in Fig. 4.2(c).

General case As is obvious from the preceding example, the MP is not necessarily described by the difference of the first order vectors $\mathbf{k_1}$ and $\mathbf{k_2}$ ($n = 1,\ m = -1$). Higher order reciprocal vectors seem to be required to account for significantly large spacing difference.

4.1.3 Atomic lattices

The case of two interfering 2D atomic lattices requires the definition of the under- and overlayer lattices using two real-space vectors per layer. The lattices are defined as in chapter 3, with $\mathbf{R_1}$, $\mathbf{R_2}$ and $\mathbf{R'_1}$, $\mathbf{R'_2}$ denoting the under- and overlayer unit vectors respectively (see Fig. 3.4 in chapter 3). The lattice constants of the underlayer are R_1, R_2 (typically in Å) and the unit cell angle is ω (R'_1, R'_2 and ω' for the overlayer). The underlayer is fixed ($\mathbf{R_1}$ aligned with $\hat{\mathbf{x}}$), and the overlayer is rotated by the angle θ. For illustration, the example of bilayer graphene [160, 235, 236] is used here.

Real space Figure 4.3(a) displays an atomic lattice representing the underlayer, where $R_1 = R_2 = 2.461$ Å and $\omega = 120°$. Figure 4.3(b) shows the overlayer graphene lattice, using the same lattice constants and unit cell angle, but rotated by $\theta = 6°$. The superposition of the two layers is shown in Fig. 4.3(c). The MP consists of 'moirons' arranged hexagonally. The MP period, i.e. the distance between the rows of moirons (indicated with dashed lines) λ is about 2 nm. λ_1 and δ_1 are indicated on the figure but since the MP possesses a sixfold

rotational symmetry λ_2, δ_2, λ_3 and δ_3 are not shown for clarity.

Reciprocal space The reciprocal lattice unit vectors are defined as follows [31].

$$\mathbf{k_1} = \frac{\mathbf{R_2} \times \mathbf{R_3}}{\mathbf{R_1} \cdot (\mathbf{R_2} \times \mathbf{R_3})} \tag{4.4}$$

$$\mathbf{k_2} = \frac{\mathbf{R_3} \times \mathbf{R_1}}{\mathbf{R_2} \cdot (\mathbf{R_3} \times \mathbf{R_1})} \tag{4.5}$$

where $\times$ and $\cdot$ indicate the vector and dot product, respectively. In 2D lattices, $\mathbf{R_3}$ can be taken as a unit vector perpendicular to the plane of the lattice, i.e. $\mathbf{R_3} = (0,0,1)$. Part of the reciprocal lattice of the underlayer is shown in Fig. 4.3(d). Each point is equidistant from the origin with $k_1 = k_2 = \frac{2}{R_1\sqrt{3}} \simeq 4.69$ nm^{-1}. The reciprocal lattice of the overlayer is represented in Fig. 4.3(e) and is identical to that of the underlayer rotated by $\theta = 6°$. The *difference* vectors (in blue) are present in 'clusters' near the positions of $n\mathbf{k_1} + m\mathbf{k_2}$ and $p\mathbf{k'_1} + q\mathbf{k'_2}$. These coordinates are

$$\mathbf{K_{nmpq}} = p \cdot \mathbf{k'_1} + q \cdot \mathbf{k'_2} - n \cdot \mathbf{k_1} - m \cdot \mathbf{k_2} \tag{4.6}$$

where $n, m, p, q \in \mathbb{Z}$ are the four indices needed to describe a vector that emerges from the convolution. The difference vector between e.g. $\mathbf{k_1}$ and $\mathbf{k'_1}$ is then written $\mathbf{K}_{1010}$. Note that $\mathbf{K_{\bar{n}\bar{m}\bar{p}\bar{q}}} = -\mathbf{K_{nmpq}}$. In general, there are an infinity of vectors $\mathbf{K_{nmpq}}$ that emerge from the convolution, whereas the MPs are generally described by up to three wave-vectors (as observed experimentally in chapter 3). A general method must then determine which of these are important, and this can be challenging as there can be an infinite number of them (assuming $n, m, p, q \in \mathbb{Z}$). To simplify the analysis we start by assuming that we need to consider only the n, m, p, q such that $|n\mathbf{k_1} + m\mathbf{k_2}|$ and $|p\mathbf{k'_1} + q\mathbf{k'_2}|$ are smaller than a cut-off k_r, typically only considering the first orders of the reciprocal lattices in the generation of the difference vectors $\mathbf{K_{nmpq}}$. This assumption is revisited and discussed explicitly in sections 4.2.5 and 4.4.1.

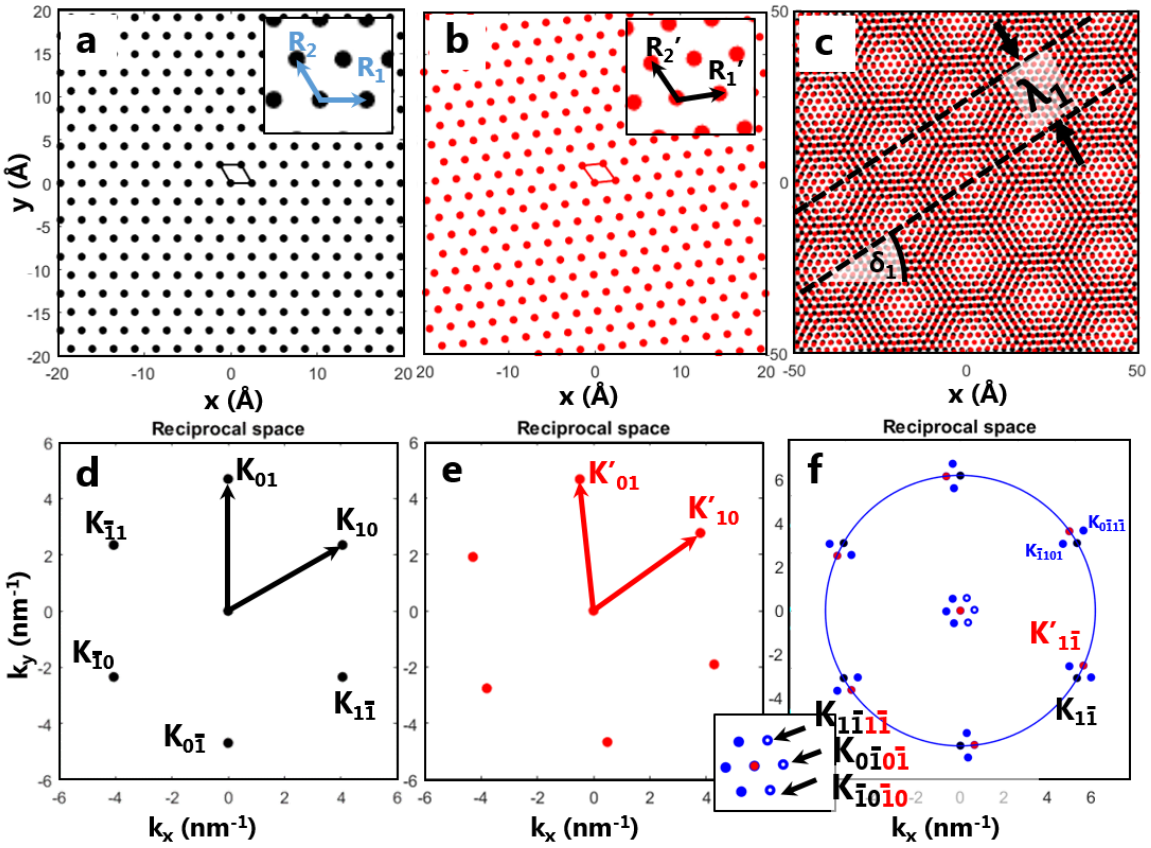

Figure 4.3: Atomic lattice superposition in real and reciprocal spaces using bilayer graphene. Real space representation of the graphene underlayer (a), overlayer (twisted by $\theta = 6°$) (b) and superposition (c). Reciprocal spaces of the underlayer (d), the overlayer (e) and the superposition (f). The lattice constants are $R_1 = R_2 = R_1' = R_2' = 2.461$ Å and $\omega = \omega' = 120°$. The unit cells are displayed in (a) and (b). The insets in (a) and (b) are magnifications indicating the unit vectors. In (c), the period λ_1 and the angle δ_1 are indicated. In (d) and (e) the reciprocal vectors of under- and overlayer are indicated. In (f), the black (red) spots indicate the underlayer (overlayer) reciprocal vectors. The blue spots are the reciprocal lattice obtained by convolution of the under- and overlayer reciprocal lattices. The inset in (f) is a magnification near the origin where the MP vectors $\mathbf{K}_{\bar{1}0\bar{1}0}$ and $\mathbf{K}_{0\bar{1}0\bar{1}}$ (as well as the redundant $\mathbf{K}_{1\bar{1}1\bar{1}}$) are indicated in white. The indices of $\mathbf{K}_{\mathbf{nmpq}}$ are explained in the main text.

Possible moiré pattern vectors In Fig. 4.3(f), the *possible MP vectors* are all the $\mathbf{K_{nmpq}}$ that are within a radius $k_1 \simeq 4.69$ nm^{-1} (indicated with a blue circle in the figure). The difference vectors $\mathbf{K_{nmpq}}$ outside the circle correspond to modulations with real-space periods shorter than the lattice constants ($R_1 = 2.461$ Å) which can not be MPs; these vectors are hence discarded. The two vectors $\mathbf{K_{0\bar{1}1\bar{1}}}$ and $\mathbf{K_{\bar{1}101}}$ are indicated in Fig. 4.3(f), where the former is outside the circle and the latter is a possible MP vector. In section 4.4, all the $\mathbf{K_{nmpq}}$ vectors (including those that are outside the blue circle defined by k_r) are discussed in a more general context.

Moiré pattern vectors The vectors that describe the real-space MP (visible in Fig. 4.3(c)) are two independent vectors that belong to the subset of $\mathbf{K_{nmpq}}$ that are the closest to the origin (note that $\mathbf{K_{0000}}$ is a null vector). In the bilayer graphene case shown in Fig. 4.3(f), the two[1] chosen MP vectors correspond to $\mathbf{K_{\bar{1}0\bar{1}0}}$ and $\mathbf{K_{0\bar{1}0\bar{1}}}$. In the specific case of hexagonal bilayers that lead to a MP that possesses a sixfold rotational symmetry, it can be convenient to define a third MP vector (not independent of the two others). Here, the third vector is $\mathbf{K_{1\bar{1}1\bar{1}}}$ (in the inset of Fig. 4.3(f) the MP vectors are indicated with open blue circles).

Moiré pattern period The periods λ_{nmpq} are defined as for the case of gratings

$$\lambda_{nmpq} = 1/|\mathbf{K_{nmpq}}|. \tag{4.7}$$

The difference (with the case of gratings) is that there are now two vectors that lead to two different sets of fringes. For the bilayer graphene case displayed in Fig. 4.3, the period is $\lambda_{1010} = \lambda_{0101} = 2.03$ nm. Note that $\lambda_{\bar{1}1\bar{1}1}$ also yields the same value. It is worth emphasizing that λ is *not* the inter-moiron distance but the period of the MP.

Moiré pattern angle The fringe angles δ_{nmpq} (in rad) are defined as for the gratings

$$\delta_{nmpq} = \arg(\mathbf{K_{nmpq}}) + \pi/2. \tag{4.8}$$

Again for atomic lattices due to the presence of multiple MP vectors, there are multiple sets of fringes. For the bilayer graphene case used for illustration in Fig. 4.3, the angles are

[1] Note that six $\mathbf{K_{nmpq}}$ vectors that are equidistant from the origin and could be used interchangeably provided that they form a complete basis.

$\delta_{1010} = 33°$ and $\delta_{0101} = -87°$. The redundant MP vector $\mathbf{K_{\bar{1}1\bar{1}1}}$ yields $\delta_{\bar{1}1\bar{1}1} = -27°$. The sixfold symmetry of the MP is verified as the three fringe angles are 60° apart.

4.2 General method

Given the results above it appears that the MP geometry can be obtained in an straightforward way using the independent reciprocal lattices of the under- and overlayer. This section overviews an algorithm that allows the calculation of the MPs for any rotation angle θ and for any combination of under- and overlayer symmetry. The functions that yield $\lambda(\theta)$ and $\delta(\theta)$ are detailed in section 4.2.4 and are tested against the case of twisted bilayer graphene .

4.2.1 Reciprocal lattice of the layers

The unit vectors of the underlayer ($\mathbf{R_1}$, $\mathbf{R_2}$) and the overlayer ($\mathbf{R'_1}$, $\mathbf{R'_2}$) are the input values. For convenience, complex notation is used in a Matlab script, the real part being along the x axis and imaginary part along the y axis. To rotate a lattice by θ, one can simply multiply the matrix by $\exp(i\theta)$. The complex scalars, equivalent to the unit vectors in section 4.3, are calculated as follows

$$\underline{R_1} = R_1 \tag{4.9}$$

$$\underline{R_2} = R_2 \cdot \exp(i\omega) \tag{4.10}$$

$$\underline{R'_1} = R'_1 \cdot \exp(i\theta) \tag{4.11}$$

$$\underline{R_2} = R'_2 \cdot \exp[i(\theta + \omega')]. \tag{4.12}$$

The complex reciprocal scalars are then obtained from equations (4.4) and (4.5)

$$\underline{K_1} = \frac{1}{R_1 \sin\omega} \cdot \exp i(\omega - \pi/2) = k_1 \cdot \exp[i(\omega - \pi/2)] \tag{4.13}$$

$$\underline{K_2} = \frac{i}{R_2 \sin\omega} = i \cdot k_2 \tag{4.14}$$

$$\underline{K_1'} = \frac{1}{R_1' \sin\omega'} \cdot \exp i(\theta + \omega' - \pi/2) = k_1' \cdot \exp[i(\theta + \omega' - \pi/2)] \tag{4.15}$$

$$\underline{K_2'} = \frac{1}{R_2' \sin\omega'} \cdot \exp i(\theta + \pi/2) = k_2' \cdot \exp[i(\theta + \pi/2)]. \tag{4.16}$$

The complex $(2N+1)\times(2N+1)$ matrices U (for the underlayer) and O (overlayer), containing the complex coordinates of the reciprocal lattices are calculated as follows

$$U_{nm} = n \cdot \underline{K_1} + m \cdot \underline{K_2} \tag{4.17}$$

$$O_{pq} = p \cdot \underline{K_1'} + q \cdot \underline{K_2'} \tag{4.18}$$

where $n, m, p, q = 0, \pm 1, \pm 2 ... \pm N$ with $N \in \mathbb{N}$. In other words, the complex number U_{nm} represents the vector $n\mathbf{k_1} + m\mathbf{k_2}$ and O_{pq} represents $p\mathbf{k_1'} + q\mathbf{k_2'}$. N is the maximum order of the reciprocal lattice (required for computational considerations). The expanded form of U is

$$U = \begin{bmatrix} U_{\bar{N}N} & \dots & U_{0N} & \dots & U_{NN} \\ \vdots & \ddots & \vdots & & \vdots \\ U_{\bar{N}0} & \dots & 0 & \dots & U_{N0} \\ \vdots & & \vdots & \ddots & \vdots \\ U_{\bar{N}\bar{N}} & \dots & U_{0\bar{N}} & \dots & U_{N\bar{N}} \end{bmatrix}.$$

Note that $U_{00} = O_{00} = 0$. The matrices $\overline{U}$ and $\overline{O}$ are identical to U and O, except that those exclude the values that extend beyond the cut-off value k_r. $\overline{U}_{nm}$ and $\overline{O}_{pq}$ are

$$\overline{U}_{nm} = \begin{cases} U_{nm}, & \text{if } |U_{nm}| < k_r \\ \text{NaN}, & \text{otherwise} \end{cases}$$

$$\overline{O}_{pq} = \begin{cases} O_{pq}, & \text{if } |O_{pq}| < k_r \\ \text{NaN}, & \text{otherwise} \end{cases}$$

with 'NaN' the undefined value. Using $\overline{U}$ and $\overline{O}$ as opposed to U and O for the model allows to discard high orders of the reciprocal lattices whose magnitudes are larger than the cut-off

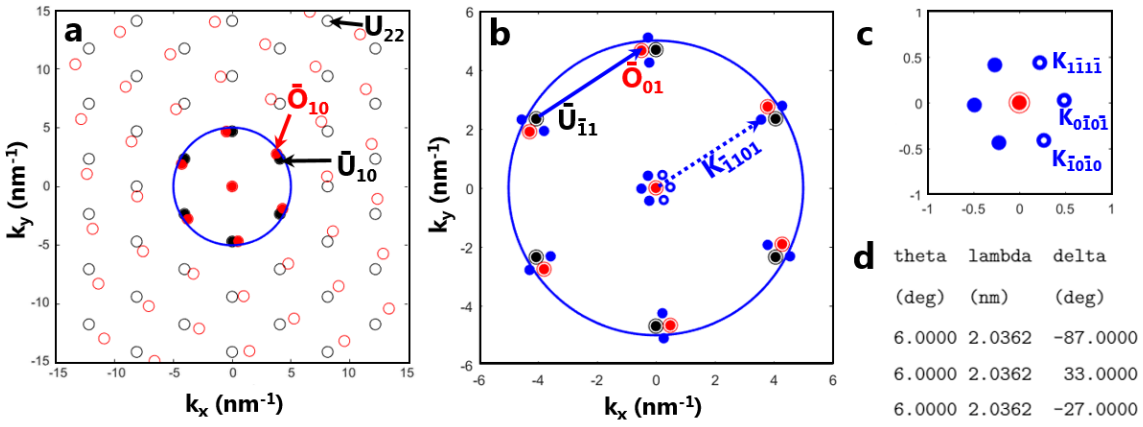

Figure 4.4: Reciprocal lattices for twisted bilayer-graphene where $\theta = 6°$. (a) Underlayer reciprocal lattice described by U (black circles) and overlayer lattice described by O (red circles). The points larger than $k_r = 5$ nm^{-1} (blue circle) are excluded from the matrices $\overline{U}$ (black solid dots) and $\overline{O}$ (red solid dots). U_{22}, $\overline{U}_{10}$ and $\overline{O}_{10}$ are indicated. (b) Reciprocal space showing the difference vectors $\mathbf{K_{nmpq}}$ (blue). As an example $\mathbf{K_{\bar{1}101}}$ is constructed from $\overline{O}_{01}$ and $\overline{U}_{\bar{1}1}$. (c) Expanded view from (b) where the MP vectors are indicated (blue circles). (d) 'MP.m' output for twisted bilayer-graphene for $\theta = 6°$ and $k_r = 5$ nm^{-1}.

k_r. In Fig. 4.4, using the twisted bilayer graphene example from above, the value of the cut-off is $k_r = 5$ nm^{-1}, i.e. just slightly larger than $k_1 = k_2 \simeq 4.69$ nm^{-1} (such that only the first orders of the reciprocal vectors are chosen).

4.2.2 MP vectors

K represents the ensemble of vectors that emerge from the difference of the under- and overlayer reciprocal lattices (from which the values beyond k_r are discarded). The values K_{nmpq} are defined as follows

$$K_{nmpq} = \overline{O}_{pq} - \overline{U}_{nm}. \tag{4.19}$$

K_{nmpq} can also be seen as the ensemble of all the difference vectors (written as complex numbers) between the under- and overlayer reciprocal lattices. In the example of the bilayer graphene in Fig. 4.4(b), the vectors described by K_{nmpq} are shown in blue. The vectors described by $K_{\bar{1}101}$ is drawn for illustration. The values that correspond to a possible MP are those that fulfil $|K_{nmpq}| < k_1 = k_2 \simeq 4.69$ nm^{-1} (specifically to the twisted bilayer graphene example). The K_{nmpq} values exhibit a sixfold rotational symmetry, as does the MP in real space in Fig. 4.3(c).

A consequence of the Fourier transform is that for each reciprocal vector **K**, the opposite vector −**K** also exists containing the same information about the geometry of the modulation (period and orientation). For this reason, to describe the MPs in this model, only the positive values $\mathrm{Re}(K_{nmpq}) \geq 0$ are considered. The 3 values of K_{nmpq} that are the closest to the origin are the MP vectors. Using such scheme is found to be sufficient to model accurately the MPs observed in real VDWHs (see section 4.3). In section 4.4 the model is generalised to all the K_{nmpq} complex values. In Fig. 4.4(c), these MP vectors are shown as blue circles.

Null vector of the reciprocal lattices If one of the two reciprocal vectors used in the difference vector is null ($n,m = 0$ or $p,q = 0$) the resulting K_{00pq} and K_{nm00} are

$$K_{00pq} = \overline{O}_{pq} - \overline{U}_{00} = \overline{O}_{pq} \tag{4.20}$$

$$K_{nm00} = \overline{O}_{00} - \overline{U}_{nm} = -\overline{U}_{nm} = \overline{U}_{\bar{n}\bar{m}} \tag{4.21}$$

describing the reciprocal lattices of the over- and the underlayer, respectively. This means that the periods corresponding to K_{00pq} and K_{nm00} are shorter (e.g. $n = 1$, $m = 2$) or equal (e.g. $n = 1$, $m = 0$) to the lattice constants, and so do not represent a MP. Note that the $K_{0000} = 0$, which represents a MP with an infinite period and undefined angle. The null vectors can therefore be excluded in the difference vector calculation.

4.2.3 Function MP.m

Practically, to apply these ideas to an arbitrary pair of under- and overlayers it is necessary to design an algorithm (implemented in MATLAB) that captures the essential features of the model. The inputs of the function are the following: R_1, R_2, ω, R'_1, R'_2, ω', θ and k_r. The function 'MP.m' was designed according to the following scheme:

1. The complex numbers acting as the unit-vectors of the reciprocal lattices $\underline{K_1}$, $\underline{K_2}$, $\underline{K'_1}$ and $\underline{K'_2}$ are computed with equations (4.13)-(4.16).

2. The matrices U and O are generated from $\underline{K_1}$, $\underline{K_2}$, $\underline{K'_1}$ and $\underline{K'_2}$, using equations (4.13)–(4.16).

3. The matrices $\overline{U}$ and $\overline{O}$, identical to U and O respectively, 'trimmed' from the values larger than k_r, are obtained.

4. The K_{nmpq} values are calculated for $|n,m,p,q| \leq N$ using equation (4.19).

5. The values of K that fulfil (i) $\mathrm{Re}(K_{nmpq}) > 0$ and (ii) $|K_{nmpq}| < \min(k_1, k_2, k'_1, k'_2)$ are sorted in a list, and the three values that are the closest to origin are selected. These values are the MP vectors. Note that there can be up to three MP vectors, and any other number of MP vectors below 3 is possible.

6. Finally, the values of the periods λ and angles δ are calculated using equations (4.7) and (4.8).

Figure 4.4(d) shows the output of MP.m using $R_1 = R_2 = R'_1 = R'_2 = 2.461$ (in Å) and $\omega = \omega' = 120$ (in degrees), $\theta = 6$ (in degrees) and $k_r = 5$ (in nm^{-1}). The values of the periods and fringe angles are given. The values of λ agree exactly with the periods given by the previous hexagonal analytical model [174, 254]. Note that $N = 1$ or 2 is usually sufficient to obtain the MPs modeling the observations (as will be discussed in section 4.3). When k_r is carefully chosen, the value of N can be set to an arbitrary large value (as high as the computation power reasonably allows), because the $\overline{U}$ and $\overline{O}$ obtained will discard points of the reciprocal lattices larger than the cut-off.

4.2.4 Function MPtheta.m

The next step is to generate the values of λ and δ for a range of rotation angle θ allowing $\lambda(\theta)$ and $\delta(\theta)$ to be plotted. The function 'MPtheta.m' is then designed which calculates the MPs using the 'MP.m' function, this time for a range of rotation angles specified by θ_0, θ_1 and $\Delta\theta$ (respectively initial, final, and step angles). The function MPtheta.m has the following inputs: $R_1, R_2, \omega, R'_1, R'_2, \omega'$, θ_1, θ_2, $\Delta\theta$ and k_r. The algorithm is:

1. The function MP.m is used for $R_1, R_2, \omega, R'_1, R'_2, \omega'$, θ_1, and k_r; the output ordered in a table with 3 columns for θ, λ and δ, respectively

2. Entries are added successively to the table by using the function MP.m with the same inputs except that the j^{th} iteration uses $\theta = \theta_1 + j\Delta\theta$ where $j \geq 1 \in \mathbb{N}$ until $\theta \geq \theta_2$.

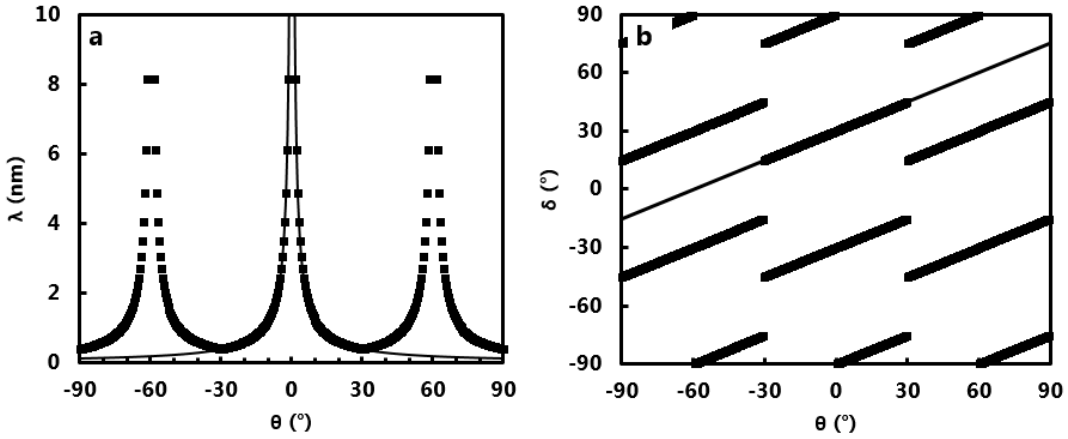

Figure 4.5: MPtheta.m output for twisted bilayer graphene, from $\theta_0 = -90°$ to $\theta_1 = 90°$ with a step of $\Delta\theta = 0.5°$ (squares). (a) Period $\lambda(\theta)$ and (b) fringe angle $\delta(\theta)$. The cut-off is $k_r = 5$ nm^{-1}. In (a) and (b) λ and δ are also obtained using Hermann's model [174] (black solid line).

3. $\lambda(\theta)$ and $\delta(\theta)$ are plotted. $\delta(\lambda)$ or the reciprocal vectors may also be obtained if required.

Example of bilayer graphene Figure 4.5 shows the output of MPtheta.m for the bilayer graphene case ($R_1 = R_2 = R'_1 = R'_2 = 2.461$ Å, $\omega = \omega' = 120°$ and $k_r = 5$ nm^{-1} for $\theta_1 = -90°$, $\theta_2 = 90°$ with a step angle of $\Delta\theta = 0.5°$). Figure 4.5(a) shows the period λ for an entire half revolution of the overlayer. For any θ, the three periods λ have the same value (because of the sixfold symmetry of the MPs in this case as shown in Fig. 4.3(c)). The periods diverge for $\theta = 0$ and $\pm 60°$. Because of the symmetry of the problem, $\lambda(\theta) = \lambda(-\theta)$ (not always true). The angles of the fringes $\delta(\theta)$ are shown in Fig. 4.5(b), and the three fringe angles δ are 60° apart for any θ. For any θ, there are three sets of fringes corresponding to the 3 MPs. From inspection of Fig. 4.5(a) and (b) it is clear that the MPs of the twisted bilayer graphene possess a sixfold rotational symmetry as $\lambda(\theta) = \lambda(\theta + 60°)$ and $\delta(\theta) = \delta(\theta + 60°)$. This model clearly reproduces the experimental MPs observed on bilayer graphene systems [228, 234, 236, 254]. On a side note, $\theta = 30°$ represents a special case of twisted bilayer graphene that has been studied for its quasi-crystalline properties [256, 257].

Hermann model comparison The analytical model developed by Hermann [174] (see section 3.2.2.2) can be used for the case of bilayer graphene because the two layers share the same unit cell angle $\omega = \omega' = 120°$. The calculated period and angle using Hermann's model are displayed with solid lines in Fig. 4.5(a) and (b). The general method and Hermann's

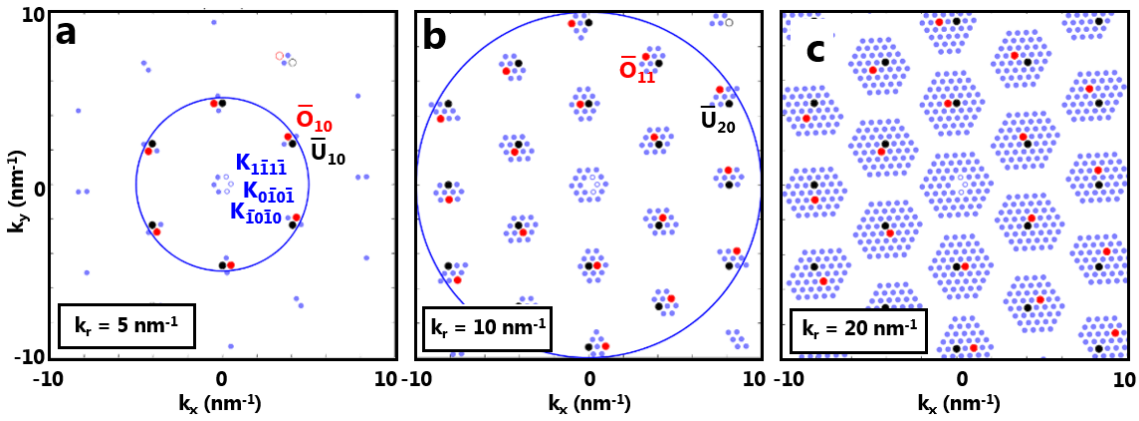

Figure 4.6: Effect of k_r on twisted bilayer graphene ($\theta = 6°$). Reciprocal space of underlayer (black), overlayer (red) and the ensemble of difference vectors (blue) obtained with $k_r = 5$ nm^{-1} (a), $k_r = 10$ nm^{-1} (b) and $k_r = 20$ nm^{-1} (c). The blue circles are centred on the origin and have a radius of k_r.

model agree exactly for $-30 < \theta < 30°$ (note this is beyond the range of application of Hermann's model as stated in [174]). Beyond that range, Hermann's model gives unrealistic values and clearly ignores the sixfold θ-symmetry of the bilayer. The advantage of the algorithm over Hermann's model here is that it reflects the symmetry of the problem, and is valid for all θ.

4.2.5 Cut-off considerations

The influence of k_r is now discussed[1] for the same example (twisted bilayer graphene). Figure 4.6(a) shows the reciprocal lattices of under- and overlayer graphene (black and red respectively) and the ensemble of difference vectors (blue), obtained using a k_r slightly above $k_1 \simeq 4.69$ nm^{-1} ($k_r = 5$ nm^{-1}). The difference vectors $\mathbf{K_{nmpq}}$ appear near the origin as a hexagon as seen in previous sections. Figure 4.6(b) shows the reciprocal space of the same superposition, except using a cut-off that is two times larger, $k_r = 10$ nm^{-1}. The difference vectors now include higher orders of the reciprocal lattices, e.g. $\overline{U}_{20}$ and $\overline{O}_{11}$. A direct consequence of this is that a larger number of difference vectors $\mathbf{K_{nmpq}}$ are generated. These are referred to as *satellites* and are also seen in diffraction experiments (e.g. RHEED). Interestingly, the satellites near the origin constitute now an outer 'ring' of vectors. Those that

[1]The trivial case of $k_r < k_1$ is not shown, where the ensemble of $\mathbf{K_{nmpq}}$ is empty with the exception of $\mathbf{K_{0000}}$ because no other points of the reciprocal lattices are taken into consideration in such case.

are the closest to origin for Re(k) > 0 (open blue circles) are still the same as in Fig. 4.6(a). Finally, the value of k_r is set to $k_r = 20$ nm^{-1} in Fig. 4.6(c). An even larger number of satellite vectors are generated, yet the obtained MP vectors are unchanged. For higher values of k_r, the satellite groups may start to overlap and this is discussed in more depth in section 4.4.2.

Summary The cut-off k_r can be selected just slightly larger than the reciprocal lattice constant ($k_r > \max\{k_1, k_2, k_1', k_2'\}$) in order to account for at least the first order of the reciprocal lattices. We find that this is sufficient to model the MPs observed in VDWHs (see section 4.3). The assumption that k_r can be chosen in this way is discussed in 4.4 and 4.6.

4.3 Modeling group-V VDWHs

In the previous sections, the general model was successfully tested on the well-known twisted bilayer graphene system. To verify its validity on a broader set of symmetries (e.g. rectangular/hexagonal), the method is tested for the experimentally observed MPs discussed in chapter 3. This section is presented as follows; α-Sb on α-Bi (section 4.3.1), β-Sb on α-Bi (section 4.3.2), MBi on α-Bi (section 4.3.3), α-Bi on HOPG (section 4.3.4), and α-Bi on MoS_2 (section 4.3.5). The approach is identical for all the studied systems. First the reciprocal lattices at the observed angle $\theta = \theta_{\text{exp}}$ are visualised and the difference vectors calculated with a k_r just slightly larger than the first order reciprocal vectors. The periods and angles are then calculated for a range of θ near the observed angle using MPtheta.m described above. The curves are then compared with either the Hermann model when applicable or the VESTA simulations, and to the experimental MPs. Finally, the results are summarised and discussed in section 4.3.6.

4.3.1 α-Sb on α-Bi

As discussed previously in chapter 3, MPs on α-Sb were observed for VDWHs involving α-Sb in three cases: (i) α-Sb on 2ML-α-Bi (on HOPG), (ii) α-Sb on 4ML-α-Bi (on HOPG) and (iii) α-Sb on 2ML-α-Bi (on MoS_2). These were independently analysed because of the slight differences in the measured lattice constants in the same layers for the different cases. The α-Sb crystals were highly aligned with the α-Bi underlayer lattice ($\theta = 0 \pm 2°$). The MPs

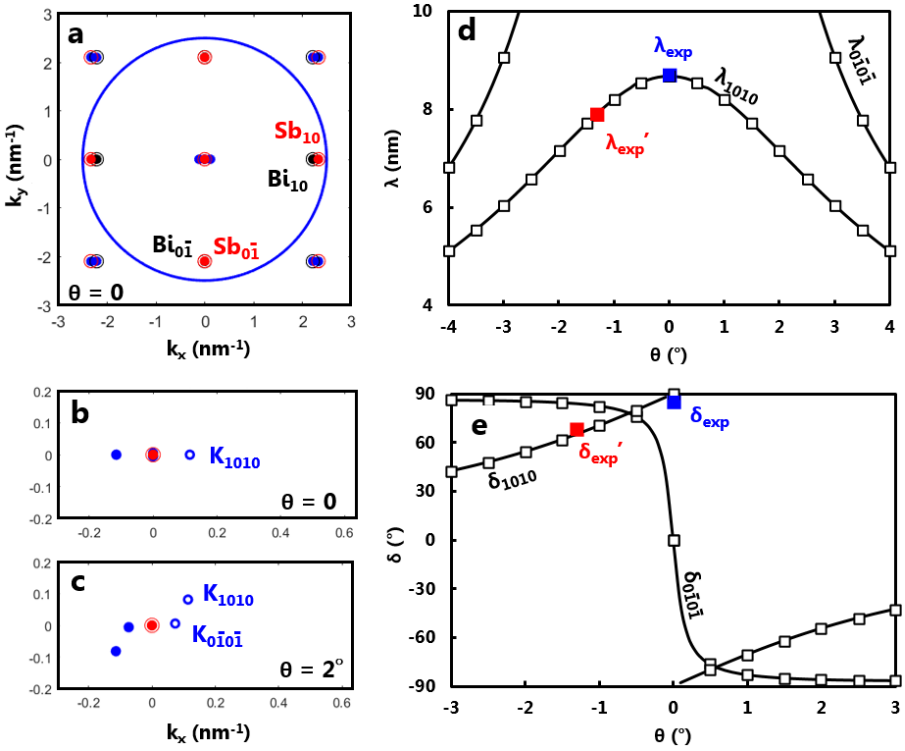

Figure 4.7: General model applied to α-Sb on 2ML-α-Bi (HOPG substrates). (a) Reciprocal lattice for $\theta = 0°$. $\mathbf{Bi_{nm}}$ are indicated in black and $\mathbf{Sb_{pq}}$ in red. The cut-off k_r is set to only keep the first order vectors of the reciprocal lattices ($k_r = 2.5$ nm^{-1}, blue circle). The difference vectors are shown in blue. (b) Magnification near the origin, showing $\mathbf{K_{10\bar{1}0}}$. (c) same reciprocal space for $\theta = 2°$, where $\mathbf{K_{0\bar{1}0\bar{1}}}$ is now visible. MPtheta.m outputs $\lambda(\theta)$ (d) and $\delta(\theta)$ (e) (white squares). In (d) and (e) two experimentally observed periods (λ_{exp}, λ'_{exp}) and fringe angles (δ_{exp}, δ'_{exp}) are displayed (blue and red), and λ and δ are also calculated using the Hermann model [174] (solid lines).

were very similar ($\lambda = 7-9$ nm and $\delta \sim 90°$) with fringes perpendicular to the preferred α-Bi island elongation axis (parallel to $\mathbf{R_1}$ referred to as Bi $\langle 1\bar{1}0 \rangle$ in previous literature [146–151, 239]). The MPs were successfully modelled with VESTA simulations and the analytical model (permitted here because $\omega = \omega' = 90°$). Here, we only focus on α-Sb on 2ML-α-Bi (grown on HOPG) for conciseness as the results are very similar for the other cases. Nonetheless all the lattice constants used in the model for different cases are given in Table 4.1 at the end of this subsection.

Reciprocal lattices and MP for $\theta = 0$ Figure 4.7(a) shows the reciprocal lattice of the two layers for $\theta = \theta_{\text{exp}} = 0°$ using the 'optimised' lattice constants from chapter 3 (see Table 4.1). Two pairs of reciprocal vectors are very close: $\mathbf{Bi_{10}}$ and $\mathbf{Sb_{10}}$, and $\mathbf{Bi_{0\bar{1}}}$ and $\mathbf{Sb_{0\bar{1}}}$ (the latter in

Underlayer	2ML-α-Bi	4ML-α-Bi	2ML-α-Bi
Substrate	HOPG	HOPG	MoS_2
R_1 (Å)	4.513	4.497	4.544
R_2 (Å)	4.760	4.860	4.870
R'_1 (Å)	4.290	4.218	4.274
R'_2 (Å)	4.760	4.860	4.870
θ_{exp} (°)	0 ± 2 (NA)	0 ± 2	0 ± 2
λ_{exp} (nm)	8.7 ± 0.9 (7.9 ± 0.4)	6.8 ± 0.9	7.2 ± 0.5
δ_{exp} (°)	87 ± 8 (68 ± 9)	87 ± 8	83 ± 5

Table 4.1: Lattices used in the models for α-Sb (copied from Table 3.4 from section 3.3.1) on various underlayers 2ML-α-Bi on HOPG, 4ML-α-Bi on HOPG and 2ML-α-Bi on MoS_2. θ_{exp}, λ_{exp} and δ_{exp} are indicated. The slightly rotated fringes/shorter period case observed in the α-Sb on 2ML-α-Bi on HOPG are indicated between brackets. Note the precision, required given the sensitivity on the simulated period.

fact almost superposed because $R_2 \simeq R'_2$). Higher order reciprocal vectors (e.g. $\mathbf{Bi_{11}}$ or $\mathbf{Sb_{02}}$) are excluded for the difference vector calculation by setting $k_r = 2.5$ nm^{-1}. The difference of the two reciprocal lattices vectors is shown in blue. Figure 4.7(b) is a magnification of the reciprocal space near the origin, where the difference vector $\mathbf{K_{10\bar{1}0}} = \mathbf{Sb_{10}} - \mathbf{Bi_{10}}$ is clearly visible. The inverse is $\lambda_{10\bar{1}0} = 1/|\mathbf{K_{10\bar{1}0}}| = 8.68$ nm, in agreement with λ_{exp}. The observed MP is therefore thought to arise from the difference vector $\mathbf{K_{10\bar{1}0}}$.

Rotation angle dependence For rotation angles $\theta \neq 0$, $\mathbf{Bi_{0\bar{1}}}$ and $\mathbf{Sb_{0\bar{1}}}$ are not superposed and $\mathbf{K_{0\bar{1}0\bar{1}}}$ is non-zero, as shown in Fig. 4.7(c) for $\theta = 2°$. The function MPtheta.m is used to plot $\lambda(\theta)$ and $\delta(\theta)$. Figure 4.7(d) shows the evolution of the period $\lambda_{10\bar{1}0}$ and $\lambda_{0\bar{1}0\bar{1}}$. The larger period $\lambda_{01\bar{1}0\bar{1}}$ was unobserved in the experiments. The observed period λ_{exp} is shown (blue square), and agrees with $\lambda_{10\bar{1}0}$ for $\theta = \theta_{exp} = 0°$. The case where the MP fringes were observed with a slight rotation and shorter period is also shown (red square) and is shown to correspond to $\theta = -1.2°$, consistent with section 3.3.1. The fringe angles $\delta_{10\bar{1}0}$ and $\delta_{0\bar{1}0\bar{1}}$ are shown in Fig. 4.7(e). Again, the observed δ_{exp} (blue square) agrees with $\delta_{10\bar{1}0}$ for $\theta = \theta_{exp} = 0°$. The rotated MP fringes that were occasionally observed (red square) also agree with $\delta_{10\bar{1}0}$ for $\theta = -1.2°$.

Hermann model and general model The Hermann model [174] is also applied with the same lattice constants (solid line). The periods $\lambda_{10\bar{1}0}$ and $\lambda_{0\bar{1}0\bar{1}}$ and the fringe angles $\delta_{10\bar{1}0}$ and

$\delta_{0\bar{1}0\bar{1}}$ from the general model agree exactly with the values obtained with Hermann's model. The algorithm developed in this chapter agrees with both Hermann's analytical model and the experimentally observed MPs. This is a good indication that the general model is valid for rectangular/rectangular symmetries.

4.3.2 β-Sb on α-Bi

The hexagonal allotrope of antimonene, β-Sb, was also observed on α-Bi underlayers. In section 3.3.2 the analysis was substrate-dependent, but the results were very similar and the two cases (HOPG and MoS_2 substrates) observed experimentally could be modeled very well using only slightly different lattice constants, always within the experimental uncertainties. Two distinct MPs were observed on β-Sb, $\lambda_{exp-1} = 4.7 \pm 0.5$ nm and $\lambda_{exp-2} = 1.06 \pm 0.06$ nm at respectively $\delta_{exp-1} = -39 \pm 8°$ and $\delta_{exp-2} = 37 \pm 7°$ (for the MoS_2 case). The general model here is illustrated for the α-Bi underlayers grown on MoS_2 substrate, but is also valid for HOPG. The lattice constants used for modeling, and the observed periods and angles in the β-Sb/α-Bi case are tabulated for the two different substrates (HOPG and MoS_2) in Table 4.2 at the end of this section.

Reciprocal lattices Figure 4.8(a) shows the reciprocal lattices of α-Bi and β-Sb (black and red respectively) for the observed angle of $\theta = \theta_{exp} = 12°$. Several reciprocal lattice vectors are close to each other: $\mathbf{Bi_{0\bar{1}}}/\mathbf{Sb_{0\bar{1}}}$, $\mathbf{Bi_{10}}/\mathbf{Sb_{1\bar{1}}}$ and in particular the pair $\mathbf{Bi_{\bar{1}\bar{1}}}/\mathbf{Sb_{\bar{1}0}}$ where the vectors have nearly the same coordinates. The difference vectors are obtained by discarding the points of the two reciprocal lattices that are outside the cut-off $k_r = 3.5$ nm$^{-1} > |\mathbf{Sb_{01}}|$. The difference vectors indicated in blue and several candidate vectors near the origin are obtained, corresponding to possible MPs. Figure 4.8(b) is a magnification of the region of the reciprocal space near $k = 0$ and the three spots that are the closest to the origin are indicated with their corresponding indices. One vector is particularly close to $k = 0$ and arises from the difference vector $\mathbf{K_{\bar{1}\bar{1}\bar{1}0}}$.

Rotation angle dependence The period related to $\mathbf{K_{\bar{1}\bar{1}\bar{1}0}}$ is $\lambda_{\bar{1}\bar{1}\bar{1}0} = 4.57$ nm and is in very good agreement with the observed $\lambda_{exp-1} = 4.7 \pm 0.5$ nm. The two other MP vectors lead to

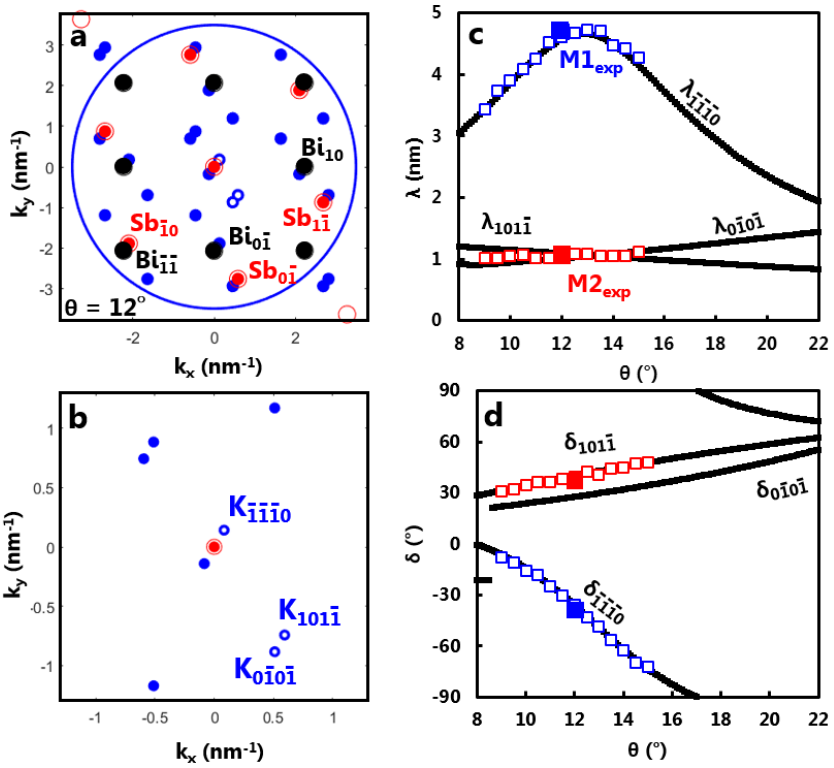

Figure 4.8: MPs of β-Sb/α-Bi using the general model. (a) Reciprocal lattices for $\theta = 12°$ using the optimised lattice constants in the MoS_2 substrate case. The α-Bi and β-Sb reciprocal vectors that are close to another are indicated (black and red respectively). The lattice arising from the difference of the under- and overlayer reciprocal vectors is shown in blue. (b) Magnification near the origin, where the MP vectors are indicated. MPtheta.m output $\lambda(\theta)$ (c) and $\delta(\theta)$ (d) (black). The observed MPs are also displayed in (b) and (c) in solid blue and red squares. The results of the VESTA simulations presented in chapter 3 are also added (open blue and red squares).

smaller periods and are relatively close to each other: $\lambda_{101\bar{1}} = 1.09$ nm and $\lambda_{0101} = 1.01$ nm, and it is not clear which of the two corresponding MPs was observed experimentally as both agree with $\lambda_{exp-2} = 1.06 \pm 0.06$ nm. The function MPtheta.m is used to generate λ and δ for $\theta = [8...22°]$ with a step angle $\Delta\theta = 0.1°$. Figure 4.8(c) shows the angular dependence of $\lambda_{\bar{1}\bar{1}\bar{1}0}$, $\lambda_{101\bar{1}}$ and $\lambda_{0\bar{1}0\bar{1}}$. $\lambda_{\bar{1}\bar{1}\bar{1}0}$ is the largest period for most of the range used here and peaks at $\theta = 12.8°$, which interestingly is in very good agreement with the observed $\theta_{exp} = 12 \pm 3°$. The calculated fringe angles are shown in Fig. 4.8(d). The observed δ_{exp-1} agrees very well with $\delta_{\bar{1}\bar{1}\bar{1}0}$ for $\theta = \theta_{exp} = 12°$. Likewise, the other observed fringe angle (δ_{exp-2}) agrees with $\delta_{101\bar{1}}$, and it is now clear that the experimentally observed M2 originates from $\mathbf{K_{101\bar{1}}}$.

Underlayer	2ML-α-Bi	2ML-α-Bi
Substrate	MoS_2	HOPG
R_1 (Å)	4.480	4.540
R_2 (Å)	4.830	4.750
R'_1 (Å)	4.080	4.060
θ_{exp} (°)	12 ± 3	12 ± 3
λ_{exp-1} (nm)	4.7 ± 0.5	4.8 ± 0.5
δ_{exp-1} (°)	-39 ± 8	-34 ± 10
λ_{exp-2} (nm)	1.06 ± 0.06	1.06 ± 0.04
δ_{exp-2} (°)	37 ± 6	42 ± 6

Table 4.2: Summary table for β-Sb overlayers, copied from Table 3.6 in section 3.3.2. The optimised lattice constants and rotation angles θ for the two substrates (MoS_2 and HOPG) and the experimentally observed periods λ_1 and λ_2 as well as the angles δ_1 and δ_2 are indicated.

VESTA simulations and general model The results of the VESTA simulations from chapter 3 are also displayed in Fig. 4.8(c) and Fig. 4.8(d). The simulations of M1 (open blue squares) and M2 (open red squares) agree very well with $\mathbf{K_{\bar{1}\bar{1}\bar{1}0}}$ and $\mathbf{K_{101\bar{1}}}$ respectively. The small deviations are attributed to the manual approach of the VESTA simulations. The case of β-Sb/α-Bi here is an indication that the general method is accurate not only for hexagonal/hexagonal and rectangular/rectangular symmetries as discussed in sections 4.2.4 and 4.3.1, but also for mixed symmetry cases.

4.3.3 MBi on α-Bi

The monolayer bismuthene (MBi) is a 2D allotrope of Bi with a rectangular unit cell [239] and was observed on 2ML-α-Bi initially deposited on HOPG substrates as discussed in section 3.3.3. The experimental lattice parameters were $R_1 = 4.0 \pm 0.2$ Å and $R_2 = 4.1 \pm 0.3$ Å, significantly contracted with respect to the α-Bi structure. The MP was characterised with $\lambda_{exp-1} = 1.9 \pm 0.2$ nm and $\lambda_{exp-2} = 3.1 \pm 0.3$ nm. The two fringes were nearly perpendicular to each other, with $\delta_{exp-1} = 2.5 \pm 2.1°$ and $\delta_{exp-2} = -80 \pm 10°$. The rotation angle was directly measured via STM ($\theta = 1 \pm 3°$) based on the atomically resolved STM images. After tip modification of the MBi layer the fringes of M1 appeared rotated ($\delta_{1_{TM}} = 20 \pm 4°$) with a similar period ($\lambda_{1_{TM}} = 1.9 \pm 0.3$ nm). After tip modification, the other fringes M2 and the atomic information could not be resolved.

Using both the analytical model developed by Hermann [174] and the VESTA simulations

the MPs were modelled with very good agreement using a slightly contracted MBi unit cell where $R_1 \times R_2 = 3.97 \times 3.82$ Å^2 and $\theta = 0.5°$. The MPs after tip modification were successfully modelled with a rotation of the MBi layer, where $\theta_{TM} = 4.1°$. Here, the general model is tested on the MBi/α-Bi case.

Reciprocal lattices Figure 4.9(a) shows the reciprocal lattices of α-Bi and MBi at the observed angle of $\theta = 1°$. Because of the shared symmetry $\omega = \omega'$, comparable lattice constants and small rotation angle, the reciprocal vectors $\mathbf{Bi_{10}}$ and $\mathbf{Bi_{0\bar{1}}}$ are very close to $\mathbf{MBi_{10}}$ and $\mathbf{MBi_{0\bar{1}}}$ respectively. The cut-off is set to account for the first orders of the reciprocal vectors only ($k_r = 3.0$ nm^{-1}). The difference vectors are shown in blue. Figure 4.9(b) is an expanded view of the reciprocal space near the origin and the two distinct MP vectors are clearly visible, $\mathbf{K_{1010}}$ and $\mathbf{K_{0101}}$. Their corresponding periods are $\lambda_{0101} = 1.95$ nm and $\lambda_{1010} = 3.14$ nm in good agreement with λ_{exp-1} and λ_{exp-2} respectively. The agreement justifies the use of k_r and the exclusion of reciprocal lattice higher orders (e.g. $\mathbf{Bi_{11}}$/$\mathbf{MBi_{11}}$) for the difference vector calculation.

Rotation angle dependence The MPs are then calculated with the MPtheta.m function for rotation angles $\theta = [-5 \ldots + 10°]$, with $\Delta\theta = 0.5°$ and $k_r = 3.0$ nm^{-1}. Figure 4.9(c) shows the calculated periods λ_{1010} and $\lambda_{0\bar{1}0\bar{1}}$. The two periods peak at $\theta = 0$ and $\lambda_{0\bar{1}0\bar{1}}$ is relatively constant for the considered range. The observed M1 and M2 before tip modification are indicated in Fig. 4.9(c) and agree well with the calculation for $\theta = \theta_{exp} = 1.0°$. Figure 4.9(d) shows the calculated fringe angles and again the agreement with the observations is valid. The experimental MPs M1 and M2 prior to tip modification correspond respectively to $\mathbf{K_{0\bar{1}0\bar{1}}}$ and $\mathbf{K_{1010}}$ for the rotation angle $\theta = \theta_{exp} = 1.0°$. The period and angle of the MP after tip modification ($M1_{TM}$) are indicated in Fig. 4.9(c) and (d) and agree with $\mathbf{K_{0\bar{1}0\bar{1}}}$ for the rotation angle $\theta = 4.1°$.

Hermann model and general model Periods and fringe angle were also calculated via the Hermann model [174] and displayed in Fig. 4.9(c) and (d) (solid lines). The general model and Hermann's model are in exact agreement both for λ and δ. Again, the general model is valid for rectangular/rectangular crystalline symmetries.

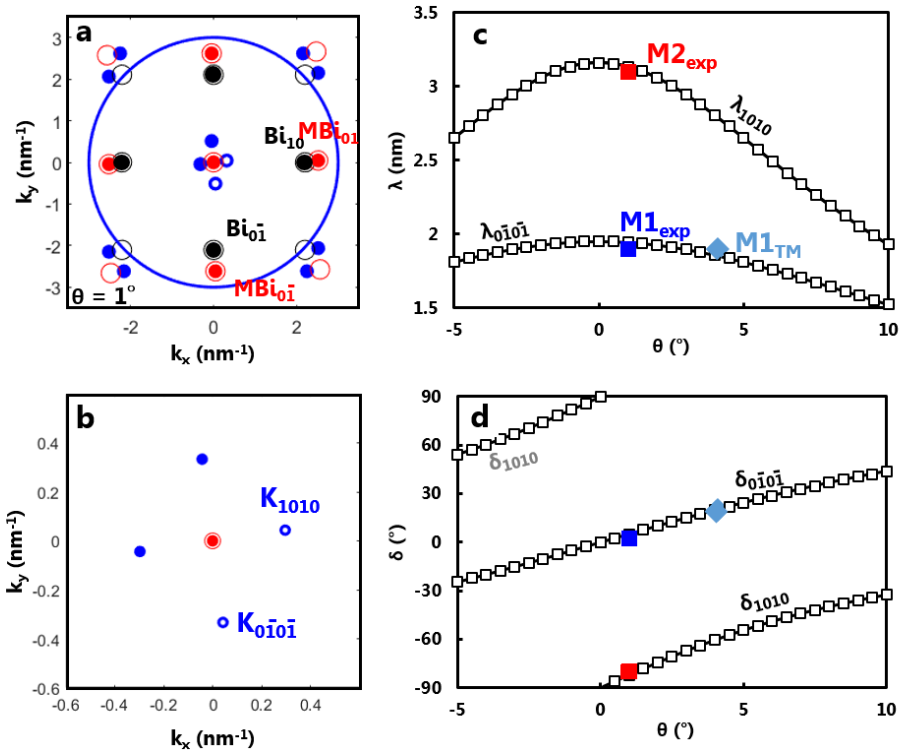

Figure 4.9: MPs on MBi/α-Bi using the general model. (a) Reciprocal lattices of the α-Bi underlayer (black) and MBi overlayer (red) using the optimised lattice constants from chapter 3. The first order reciprocal spots are indicated on the figure, and the difference vectors are in blue. (b) Magnification near the origin, the MP vectors $\mathbf{K_{10\bar{1}0}}$ and $\mathbf{K_{0\bar{1}0\bar{1}}}$ are indicated. MPtheta.m outputs for $\lambda(\theta)$ (c) and $\delta(\theta)$ (d). The observed MPs (M1, M2 and M1 after tip modification) are plotted and indicated in (c) and (d) (white squares). The period and fringe angles are also calculated using Hermann's model [174] (solid lines).

4.3.4 α-Bi on HOPG

As discussed in section 3.3.4, α-Bi layers also have clear MPs visible in STM images, both if grown on HOPG or MoS_2. For the α-Bi/HOPG case, the unique experimental MP was characterised with $\lambda_{exp} = 3.2 \pm 0.4$ nm and $\delta_{exp} = -54 \pm 5°$. Modeling was successfully achieved with VESTA simulations for $\theta = 29.6°$ which is in very good agreement with the observed rotation angle $\theta_{exp} = 30 \pm 5°$. The lattice parameters of α-Bi had to be expanded very slightly in the simulations with respect to the observations, in order to yield a simulated period that agrees perfectly with λ_{exp}. The values of the lattice parameters of both α-Bi/HOPG and α-Bi/MoS_2 systems are given in Table 4.3.

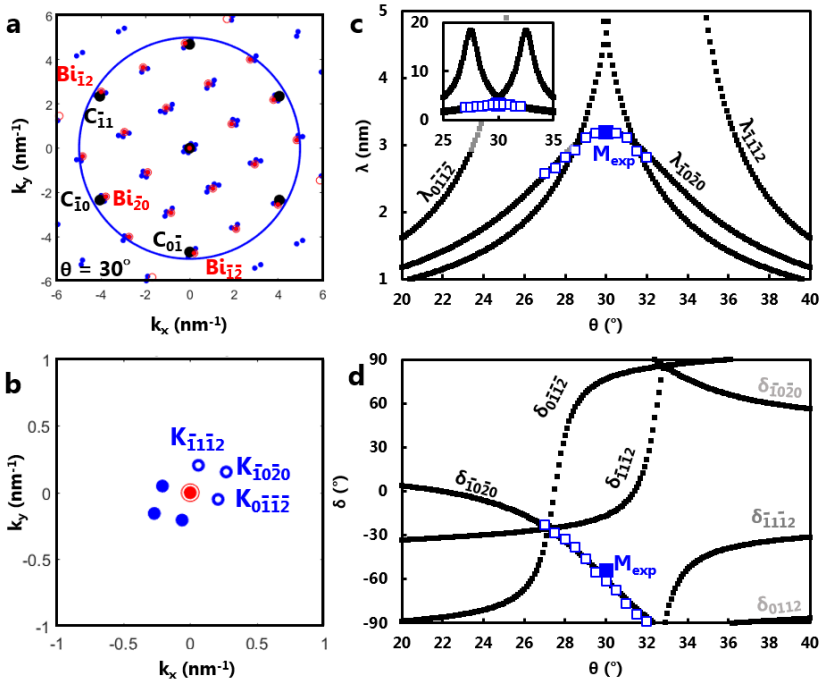

Figure 4.10: MPs on α-Bi/HOPG using the general model. (a) Reciprocal lattices of HOPG (black) and α-Bi (red) using the optimised lattice constants from chapter 3. The reciprocal lattice vectors that have similar coordinates are indicated. The difference vectors ($k_r = 5$ nm^{-1}) is shown in blue. (b) Magnification of (a) near the origin. MPtheta output $\lambda(\theta)$ (c) and $\delta(\theta)$ (d) (black squares). In (c) and (d) the observed MP is shown (solid blue square) and VESTA-simulated values are plotted too (open squares). The inset in (c) shows the same plot with a different scale.

Reciprocal lattices The reciprocal lattices of HOPG ($\mathbf{C_{nm}}$) and α-Bi ($\mathbf{Bi_{pq}}$) are shown in Fig. 4.10(a), using the optimised lattice constants from chapter 3 and the observed rotation angle of $\theta = \theta_{\text{exp}} = 30°$. Because the lattice constants of HOPG ($R_1 = R_2 = 2.461$ Å) are significantly smaller than α-Bi (experimentally $R_1 \times R_2 = 4.54 \times 4.75$ Å^2), there is a large difference in coordinates between e.g. $\mathbf{C_{10}}$ and $\mathbf{Bi_{10}}$. However the vector pairs $\mathbf{C_{\bar{1}0}}$/$\mathbf{Bi_{\bar{2}0}}$, $\mathbf{C_{0\bar{1}}}$/$\mathbf{Bi_{\bar{1}\bar{2}}}$ and $\mathbf{C_{\bar{1}1}}$/$\mathbf{Bi_{\bar{1}2}}$ are very close together. The difference vectors $\mathbf{K_{nmpq}}$ (using a cut-off just slightly larger than k_1, i.e $k_r = 5$ nm^{-1}) are shown in blue. Figure 4.10(b) is an expanded view near the origin, where three reciprocal coordinates of the candidate MP are observed. The three difference vectors $\mathbf{K_{\bar{1}0\bar{2}0}}$, $\mathbf{K_{0\bar{1}\bar{1}\bar{2}}}$, and $\mathbf{K_{\bar{1}1\bar{1}2}}$, corresponding to the vector pairs just mentioned, are indicated in the figure. Of these, only $\mathbf{K_{\bar{1}0\bar{2}0}}$ is a serious candidate to model the observations, as $\lambda_{\bar{1}0\bar{2}0} = 1/|\mathbf{K_{\bar{1}0\bar{2}0}}| = 3.22$ nm. The two other periods are $\lambda_{0\bar{1}\bar{1}\bar{2}} = \lambda_{\bar{1}112} = 4.67$ nm, significantly larger than $\lambda_{\text{exp}} = 3.2$ nm.

Rotation angle dependence The MPs originating from the difference vectors of the three pairs of reciprocal vectors described in the previous paragraph are investigated for a range of values near θ_{exp}. Figure 4.10(c) shows the evolution of the three periods. Interestingly, the periods $\lambda_{0\bar{1}\bar{1}\bar{2}}$ and $\lambda_{\bar{1}1\bar{1}2}$ peak at a value of λ = 18.4 nm respectively at $\theta = 27.5°$ and $\theta = 32.5°$ (see inset in Fig. 4.10). $\lambda_{10\bar{2}0}$ is maximised for $\theta = \theta_{exp} = 30°$. Figure 4.10(d) shows the evolution of the fringe angles δ for the three considered MP vectors. The calculated $\delta_{\bar{1}0\bar{2}0}$ agrees very well with the observation for $\theta = \theta_{exp} = 30°$. The observed MP is therefore attributed to $\mathbf{K_{\bar{1}0\bar{2}0}}$.

VESTA simulations and general model The VESTA simulations were undertaken for $\theta = [27...32°]$ and the results in terms of λ and δ are also plotted respectively in Fig. 4.10(c) and (d). The agreement with $\lambda_{\bar{1}0\bar{2}0}$ and $\delta_{\bar{1}0\bar{2}0}$ is very good. Again the deviation of the VESTA periods and angles from their calculated counterparts is due to the manual measurement during the simulations. This further confirms the validity of the general model developed in this chapter for rectangular/hexagonal symmetries.

4.3.5 α-Bi on MoS_2

The α-Bi lattice constants do not change significantly whether deposited on HOPG or MoS_2 substrates. However the lattice parameter of MoS_2 is about 28% larger than HOPG, and therefore the MPs are expected to differ significantly. The α-Bi was found to be nearly aligned with the zig-zag direction of MoS_2 (the measured rotation angle was $\theta_{exp} = 0.3 \pm 0.6$). The experimentally observed MPs differed significantly from the α-Bi/HOPG case, as three clear MPs were observed. The fringes of M1 ($\lambda_{exp-1} = 2.22 \pm 0.07$ nm) were nearly parallel to the α-Bi $\mathbf{R'_1}$ direction ($\delta_{exp-1} = 4 \pm 2°$) and two shorter but identical periods ($\lambda_{exp-2} = 0.99 \pm 0.05$ nm, $\lambda_{exp-3} = 1.00 \pm 0.05$ nm) were observed with different orientations ($\delta_{exp-2} = -79 \pm 2°$, $\delta_{exp-3} = 75 \pm 2°$). These values are tabulated in Table 4.3.

The observations were modelled with great precision using the experimental lattice constants in VESTA simulations. The rotation angle of $\theta = 2.7°$ was found to simulate MPs that were nearly identical to the experimentally observed ones, both in terms of periods and angles. However for consistency the general method is tested for the α-Bi/MoS_2 case below.

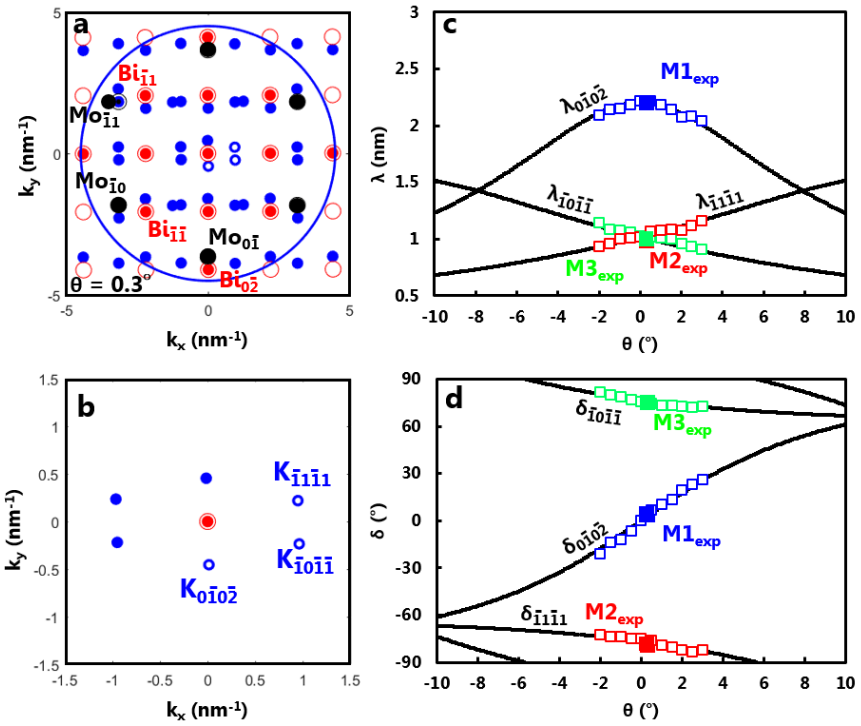

Figure 4.11: MPs on α-Bi/MoS_2 using the general model. (a) Reciprocal lattices of MoS_2 (black) and α-Bi (red) using the measured lattice constants. The reciprocal lattice vectors that have similar coordinates are indicated. The difference vectors (k_r = 4.5 nm^{-1}, blue circle) is shown (blue dots). (b) Magnification of (a) near the origin. MPtheta outputs $\lambda(\theta)$ (c) and $\delta(\theta)$ (d) (black). In (c) and (d) the observed MPs are shown (solid blue, red and green squares) and VESTA-simulated values are plotted (open squares).

Reciprocal lattices Fig. 4.11(a) shows the reciprocal lattices of MoS_2 (black) and α-Bi (red), using the experimentally observed lattice constants and rotation angle $\theta = 0.3°$. Here again the very large mismatch between the layers (~ 50 %) is such that the first order points of the reciprocal lattices are far apart. However linear combinations of α-Bi reciprocal vectors such as $\mathbf{Bi_{0\bar{2}}}$,$\mathbf{Bi_{\bar{1}\bar{1}}}$ and $\mathbf{Bi_{\bar{1}1}}$ are close to $\mathbf{Mo_{0\bar{1}}}$, $\mathbf{Mo_{\bar{1}0}}$ and $\mathbf{Mo_{0\bar{1}}}$, respectively. To avoid taking into account higher order reciprocal vectors, the cut-off value is set to $k_r = 4.5$ nm^{-1}. Figure 4.11(b) is a magnification of (a) near the origin where the three MP vectors $\mathbf{K_{0\bar{1}0\bar{2}}}$, $\mathbf{K_{\bar{1}0\bar{1}\bar{1}}}$ and $\mathbf{K_{\bar{1}1\bar{1}1}}$ are indicated. The periods are $\lambda_{0\bar{1}0\bar{2}} = 2.20$ nm, $\lambda_{\bar{1}0\bar{1}\bar{1}} = 1.00$ nm and $\lambda_{\bar{1}1\bar{1}1} = 1.03$ nm, consistent with the observations.

Rotation angle dependence The agreement with the observed periods is established but for consistency with the other treated VDWHs the values of λ_{0102}, λ_{1011} and $\lambda_{1\bar{1}1\bar{1}}$ are calculated for $\theta = [-10...+10°]$ with a step angle $\Delta\theta = 0.1°$. λ_{0102} is the largest of the three periods

Underlayer.	HOPG	MoS_2
R_1 (Å)	2.461	3.161
R'_1 (Å)	4.565	4.53
R'_2 (Å)	4.750	4.87
θ_{exp} (°)	30 ± 5	0.3 ± 0.6
λ_{exp-1} (nm)	3.2 ± 0.4	2.22 ± 0.07
δ_{exp-1} (°)	-54 ± 5	4 ± 2
λ_{exp-2} (nm)	NA	0.99 ± 0.05
δ_{exp-2} (°)	NA	-79 ± 2
λ_{exp-3} (nm)	NA	1.00 ± 0.05
δ_{exp-3} (°)	NA	75 ± 2

Table 4.3: Summary table for α-Bi both on HOPG and MoS_2 (copied from Table 3.9 in section 3.3.4). The optimised lattice constants used in the model and the experimentally observed periods λ and angles δ are indicated.

and is maximised for $\theta = 0$. This is not very surprising given that $\mathbf{Mo_{0\bar{1}}}$ and $\mathbf{Bi_{0\bar{2}}}$ are aligned (along the y axis) for $\theta = 0$, and for $\theta \neq 0$ the difference vector $\mathbf{K_{0\bar{1}0\bar{2}}} = \mathbf{Bi_{0\bar{2}}} - \mathbf{Mo_{0\bar{1}}}$ is longer. The two other periods remain in the range $0.5 - 1.5$ nm for the considered rotation angles. Figure 4.11(d) shows the evolution of the three calculated fringe angles. δ_{exp-1}, δ_{exp-2} and δ_{exp-3} are also in excellent agreement with respectively $\delta_{0\bar{1}0\bar{2}}$, $\delta_{\bar{1}1\bar{1}1}$ and $\delta_{\bar{1}0\bar{1}\bar{1}}$ for $\theta = 0°$.

Agreement with the VESTA simulations To verify the agreement with the VESTA simulations λ and δ are simulated for $\theta = [-2...2°]$ as shown in Figs. 4.11(c) and 4.11(d), respectively. The simulated MPs M1, M2 and M3 clearly agree with the calculated $\mathbf{K_{0\bar{1}0\bar{1}}}$, $\mathbf{K_{\bar{1}1\bar{1}1}}$ and $\mathbf{K_{\bar{1}0\bar{1}\bar{1}}}$. The unambiguous correspondence with the general model once again confirms the algorithm validity for understanding the MPs in rectangular/hexagonal heterobilayers.

4.3.6 Summary

The general method described in this chapter models the MPs observed in the experiments. When possible, the $\lambda(\theta)$ and $\delta(\theta)$ obtained from Hermann's model were found to agree with those calculated with the general model. The method relying on the reciprocal lattices encompasses Hermann's analytical model for it does not require restrictive conditions. The MPs emerging from (i) mixed symmetry stacking, (ii) for any arbitrary rotation angle and (iii) for scaling ratios R'/R larger than 1.2 (~ 2 in section 4.3.4) can be successfully modelled. The algorithm also largely supersedes the real-space ball-and-stick simulations using VESTA, in

particular in terms of rapidity and precision. The origin of the observed MPs (again in terms of geometry only) can now be understood with a pair of reciprocal vectors, each belonging to the under- and overlayer.

4.4 Deeper understanding of the model

4.4.1 Reciprocal space circles

The introductory sections 4.1 and 4.2 were illustrated with the twisted bilayer graphene case. Here, a more general example is used to understand the structure of the difference vectors in the reciprocal space.

Tracing the difference vectors for a general case The difference vectors $\mathbf{K_{nmpq}}$ for a fixed n,m,p,q (using the complex notation of equations (4.13-4.16) and (4.19)) is given by

$$K_{nmpq} = p \cdot K'_1 e^{i(\theta+\omega'+\pi/2)} + q \cdot K'_2 e^{i(\theta+\pi/2)} - n \cdot K_1 e^{i(\omega-\pi/2)} - m \cdot K_2 e^{(i\pi/2)}. \tag{4.22}$$

As θ is changed, the $\mathbf{K_{nmpq}}$ vector describes a circle centred at the $-n\mathbf{k_1} - m\mathbf{k_2}$ coordinates with a radius $|p\mathbf{k'_1} + q\mathbf{k'_2}|$. We illustrate this below with an example.

Case of β-Sb on α-Bi The case of β-Sb on α-Bi is discussed here because it is a general case (mixed symmetry and different lattice constants). Figure 4.12(a) shows the points of the reciprocal lattice of the underlayer (squares) and the overlayer (red diamonds) for $\theta = 0$. The difference vectors are calculated using a cut-off $k_r = 3.5$ nm^{-1}, just slightly above $|\mathbf{Sb_{01}}|$ (same value used in section 4.3). The construction of the difference vector $\mathbf{K_{\bar{1}\bar{1}0\bar{1}}}$ and is shown as an example. We now focus on the behaviour of all the $\mathbf{K_{nmpq}}$ vectors as θ is varied (shown in light grey in Fig. 4.12(a)). These can in principle be calculated for an entire $\theta = [0...360°]$ rotation, however, because the overlayer possesses a sixfold rotational symmetry, a rotation in $[0...60°]$ is sufficient. As expected from equation (4.22), eight circles are generated, centred at the coordinates of the eight points of the α-Bi reciprocal lattice $\mathbf{Bi_{nm}}$ (without including the null vector[1]). Their radii are identical and are equal to $|\mathbf{Sb_{01}}| = |\mathbf{Sb_{10}}| = |\mathbf{Sb_{1\bar{1}}}| \simeq 2.83$ nm^{-1}.

[1]It has been shown in section 4.2.2 that including the null vectors in the calculation of the difference vectors is not essential to understanding the MPs because it adds to the ensemble of difference vectors $\mathbf{K_{nmpq}}$ several

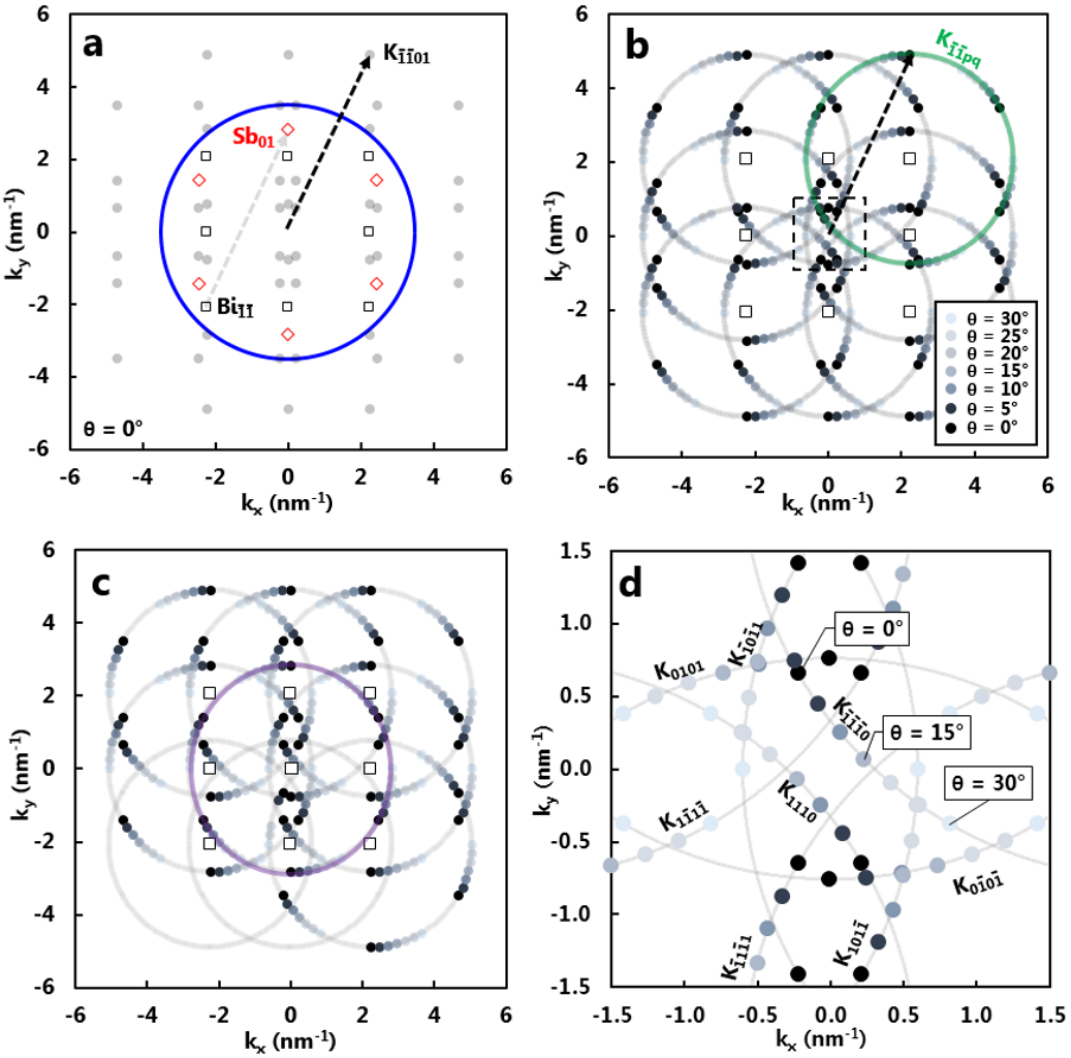

Figure 4.12: Reciprocal structures in a general superposition case. (a) Reciprocal vectors of α-Bi (squares) and and β-Sb (red diamonds). An example difference vector $K_{\bar{1}\bar{1}01}$ (dashed arrows) is indicated among all the other $\mathbf{K_{nmpq}}$ (light grey), obtained with a cut-off $k_r = 3.5$ nm^{-1} (blue circle). (b) Trace of all the difference vectors $\mathbf{K_{nmpq}}$ as θ rotates within [0...60°] (light grey), and some $\mathbf{K_{nmpq}}$ vectors are displayed for some angles (coloured dots, see legend). The null vectors $\mathbf{Bi_{00}}$ and $\mathbf{Sb_{00}}$ were not included in the calculation. The $K_{\bar{1}\bar{1}pq}$ circle is indicated in green. (c) Trace of all the difference vectors $\mathbf{K_{nmpq}}$ for the exact same under- and overlayer and k_r, except this time using the null vectors $\mathbf{Bi_{00}}$ and $\mathbf{Sb_{00}}$. The new circle K_{00pq} is indicated in purple. (d) Magnification from the dashed box in (b). Each $\mathbf{K_{nmpq}}$ arc is identified and uses the same colour scheme as in (b) and (c).

Several values of $\mathbf{K_{nmpq}}$ are highlighted for specific angles from $\theta = 0$ to $\theta = 30°$ (see legend). We focus on one circle, the $\mathbf{K_{\bar{1}\bar{1}pq}}$ (indicated in light green), i.e. the one centred at the coordinates $\mathbf{Bi_{11}}$ in Fig. 4.12(b). The six $\mathbf{K_{\bar{1}\bar{1}pq}}$ values for $\theta = 0$ are shown with black dots and are each 60° apart, which includes the example $\mathbf{K_{\bar{1}\bar{1}01}}$ from Fig. 4.12(a) (black arrow). The six difference vectors for $\theta = 0$ are a copy of the β-Sb reciprocal vectors $\mathbf{Sb_{pq}}$ for $\theta = 0$, translated by $\mathbf{Bi_{11}}$, i.e. to which are added the coordinates of $\mathbf{Bi_{11}}$ (or subtracted by $\mathbf{Bi_{\bar{1}\bar{1}}}$), as per equation (4.22). For a different rotation angle, e.g. $\theta = 5°$, the 6 values of $\mathbf{K_{\bar{1}\bar{1}pq}}$ remain on the same circle, but are rotated by $\theta = 5°$.

Realistic moiré patterns The MPs that are observes experimentally are located in the reciprocal space near the origin, as discussed in sections 4.1 and 4.3, and so the region in the dashed box in Fig. 4.12(b) is expanded in Fig. 4.12(d). The visible arcs of circles are labelled. Four $\mathbf{K_{nmpq}}$ arcs ($\mathbf{K_{\bar{1}\bar{1}\bar{1}0}}$, $\mathbf{K_{1110}}$, $\mathbf{K_{\bar{1}1\bar{1}1}}$ and $\mathbf{K_{1\bar{1}1\bar{1}}}$) pass near the origin and represent the MPs with the largest periods in the model (for the cut-off k_r considered) and also experimentally ($\lambda_1 \simeq 4.8$ nm, see section 4.3.2). The four other circles ($\mathbf{K_{101\bar{1}}}$, $\mathbf{K_{\bar{1}0\bar{1}1}}$, $\mathbf{K_{0101}}$ and $\mathbf{K_{0\bar{1}0\bar{1}}}$) are further from the origin compared to the ones just described ($\mathbf{K_{\bar{1}\bar{1}\bar{1}0}}$, $\mathbf{K_{1110}}$, $\mathbf{K_{\bar{1}1\bar{1}1}}$ and $\mathbf{K_{1\bar{1}1\bar{1}}}$). In section 4.3.2, the observed MP ($\lambda_2 = 1.06$ nm) was understood as emerging from the difference vector $\mathbf{K_{101\bar{1}}}$, located on the arc described by $\mathbf{K_{10pq}}$ in Fig. 4.12(d).

Summary In summary, the concept of $\mathbf{K_{nmpq}}$ arcs have been introduced. They correspond to the vectors $\mathbf{K_{nmpq}}$ observed as θ varies, shown to describe a circle centred at the underlayer $\mathbf{k_{\bar{n}\bar{m}}}$ position with a radius $\mathbf{k'_{pq}}$.

4.4.2 Commensurability

The general model developed here does not require the physical layers to be either commensurate or incommensurate in real space. In fact the model ignores commensurability. The

irrelevant quantities ($\mathbf{K_{0000}}$ which is a null vector, and the reciprocal lattice vectors $\mathbf{k_{nm}}$ and $\mathbf{k'_{pq}}$, which correspond to periods smaller or equal to the lattice constants). This is illustrated in Fig. 4.12(c) where the null vectors have been included in the calculation of the $\mathbf{K_{nmpq}}$ vectors. A new circle (centred at origin or radius $\mathbf{Sb_{10}} = \mathbf{Sb_{10}} = \mathbf{Sb_{1\bar{1}}} \simeq 2.83$ nm^{-1}, shown in purple) is generated and corresponds to the $\mathbf{K_{00pq}}$ vectors. The $\mathbf{K_{nm00}}$ vectors are also obtained, and are the fixed underlayer reciprocal vectors (white squares). Again, these added $\mathbf{K_{nmpq}}$ vectors do not represent a physical MP, consistent with the discussion in section 4.2.2.

positions of the $\mathbf{K_{nmpq}}$ vectors continuously vary as the overlayer rotates, even if within the considered rotation angle range, there is discrete set of angles that lead to a commensurate superposition. However, we believe that commensurability is crucial in the model and it is the reason why the cut-off k_r must be chosen carefully. Here, we review the implications of commensurability in reciprocal space, which emphasize the necessity of calculating the difference vectors $\mathbf{K_{nmpq}}$ with an adequate cut-off k_r. Note that this does not relate directly to our experiments where commensurability is not important.

One dimension The superposition of two Dirac combs (spacing R_1 and R_2) is commensurate if it is possible to find $u, v \in \mathbb{Z}$ such that

$$uR_1 = vR_2. \tag{4.23}$$

If the two combs are commensurate, the Fourier transform of the superposition is another comb with a spacing $K = \frac{1}{uR_1} = \frac{1}{vR_2}$ with u, v coprime integers. The MP period in this case is $\lambda = \frac{1}{K} = uR_1 = vR_2$. If the layers are incommensurate, the Fourier transform of the superposition contains an infinite number of discrete Dirac distributions for any compact interval considered.

Two dimensions In 2D, the two lattices are commensurate if it is possible to find $a, b, c, d \in \mathbb{Z}$ such that

$$a\mathbf{R_1} + b\mathbf{R_2} = c\mathbf{R'_1} + d\mathbf{R'_2}. \tag{4.24}$$

The comparison of a commensurate and incommensurate superposition is undertaken here using the simple illustrative example of twisted bilayer graphene. It is known that $\theta \simeq 9.43°$ leads to a commensurate bilayer, whereas for example $\theta = 10.00°$ is incommensurate [258]. Figs. 4.13(a) and 4.13(b) show the real-space model of twisted bilayer graphene for $\theta = 9.43°$ and $\theta = 10.00°$ respectively. Each moiron occurs at a coincidence position where the atom of the under- and overlayer atoms meet at the exact same (x, y) location in the case of the commensurate superposition (see inset in Fig. 4.13(a)). In the incommensurate case displayed in Fig. 4.13(b), with the exception of $(x, y) = (0, 0)$ there is no coincidence position.

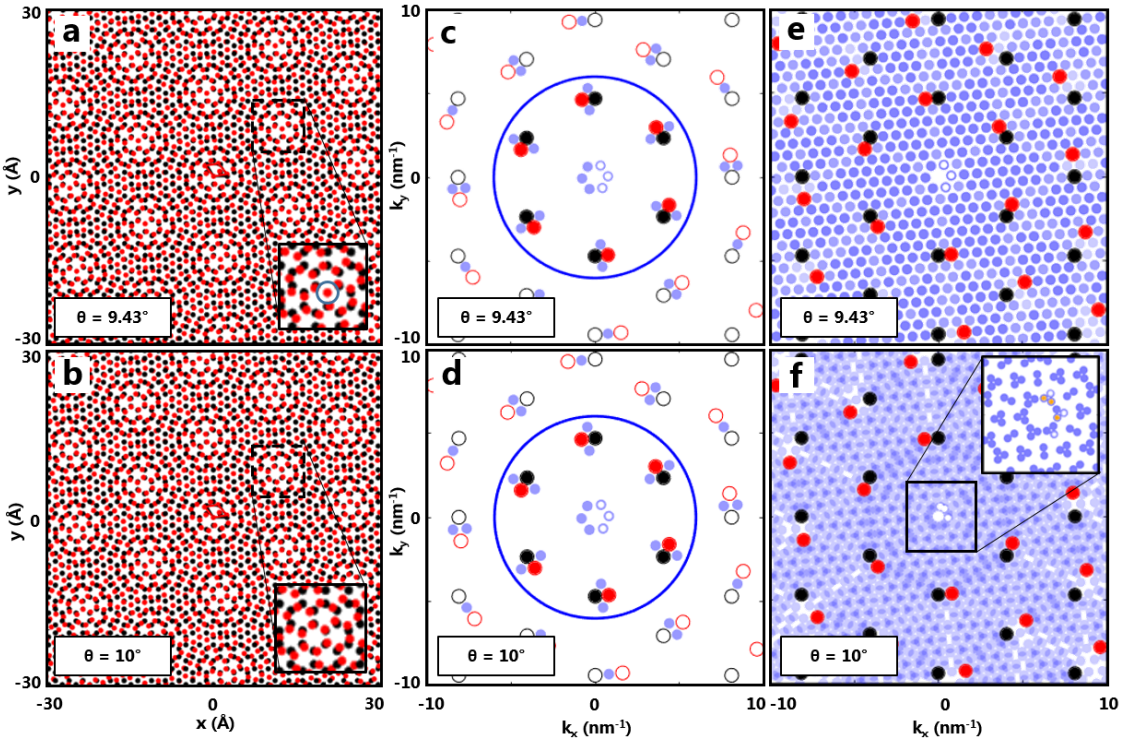

Figure 4.13: Twisted bilayer graphene: commensurate ($\theta = 9.43°$) and incommensurate ($\theta = 10.00°$) cases. Real-space ball-and-stick models (a,b), reciprocal spaces using $k_r = 5$ nm^{-1} (c,d) and $k_r = 25$ nm^{-1} (e,f). The rotation angles are displayed on the corresponding panels. The insets in (a) and (b) are magnified views near a moiron, showing respectively coincidence (circle) and mismatching of the layers. The inset in (f) is a magnification taken from the black square (width: 2 nm^{-1}). The open blue circles are the $\mathbf{K_{nmpq}}$ selected by the program as the MP vectors values that are the closest to $k = 0$. In the inset in (f) for $k_r = 25$ nm^{-1}, the $\mathbf{K_{nmpq}}$ values corresponding to the real-space MPs are shown in open circles, the ones obtained with an overestimated k_r are shown in orange.

The corresponding reciprocal lattices and the ensemble of difference vectors using a cut-off that is slightly above the initial reciprocal vectors ($k_r = 5$ nm^{-1}) are shown in Figs. 4.13(c) and (d). The difference vectors only differ minutely. The MP periods are respectively $\lambda_{9.43°} = 1.29$ nm and $\lambda_{10.00°} = 1.22$ nm, in agreement with the real-space periods visible in Fig. 4.13(a) and 4.13(b).

Now the calculation of all the difference vectors $\mathbf{K_{nmpq}}$ is performed using a cut-off that is ~ 5 times larger than $k_1 = k_2 \simeq 4.69$ nm^{-1} ($k_r = 25$ nm^{-1}). Figure 4.13(e) shows the reciprocal space for the commensurate case. Interestingly, the ensemble of $\mathbf{K_{nmpq}}$ is now an ordered lattice with the basis vectors $\mathbf{K_{0101}}$ and $\mathbf{K_{1010}}$ which are unchanged with respect to Fig. 4.13(c). The groups of $\mathbf{K_{nmpq}}$ satellite vectors near the individual U_{nm} and O_{pq} overlap, meaning

that many $\mathbf{K_{nmpq}}$ vectors reach the same positions in reciprocal space. The incommensurate case for a large cut-off ($k_r = 25$ nm^{-1}) is fundamentally different as shown in Fig. 4.13(f). The structure of all the $\mathbf{K_{nmpq}}$ vectors in that case is not that of an ordered lattice, instead it is a rather complicated structure. Importantly, there are now several difference vectors $\mathbf{K_{nmpq}}$ that are closer to the origin than the $\mathbf{K_{nmpq}}$ vectors in Fig. 4.13(d). In the inset of Fig. 4.13(f) the $\mathbf{K_{nmpq}}$ vectors obtained with $k_r = 5$ nm^{-1} are shown in white and those that are the closest to origin are indicated in orange. These additional vectors yield $\lambda = 1.69$ nm (about 40% larger than for $k_r = 5$ nm^{-1}), which does not correspond to the real-space period of the MPs.

Summary In the incommensurate cases it is necessary to keep a small value of k_r to model the MPs correctly. It is always possible to find a pair of arbitrary large reciprocal vectors of the under- and overlayer that are close enough to yield any arbitrary small $\mathbf{K_{nmpq}}$. In the case of commensurate layers (not experimentally realised in this thesis), the value of k_r can be set to any arbitrary larger value because the ensemble of difference vectors $\mathbf{K_{nmpq}}$ constitute a lattice where the values closest to $k = 0$ can be seen as base vectors.

4.5 Analytical solution

During the work on the general model it was realised that the problem of finding the reciprocal coordinates (or wave-vector) of the MPs could be generalised analytically under the conditions that orders (n,m) and (p,q) of the overlayer and underlayer reciprocal vectors that lead to the MP of interest are known. It can be demonstrated (using $\lambda_{nmpq} = \frac{1}{|\mathbf{K_{nmpq}}|}$ and equation 4.6) that the period (for any rotation angle θ, any indices n,m,p,q and lattice parameters and unit cell angles ω_1 and ω_2) is given by

$$\lambda_{nmpq} = \frac{1}{\sqrt{\kappa_1^2 + \kappa_2^2 + \kappa_1'^2 + \kappa_2'^2 - 2\Delta}} \tag{4.25}$$

where

$$\begin{aligned}\Delta = &\ \kappa_1\ \kappa_2 \cos(\omega) + \kappa_1\ \kappa_1' \cos(\theta+\omega) \\ &+\kappa_2\ \kappa_2' \cos(\theta) + \kappa_1'\ \kappa_2' \cos(\omega') \\ &-\kappa_1\ \kappa_2' \cos(\theta-\omega') - \kappa_2\ \kappa_1' \cos(\theta+\omega')\end{aligned} \tag{4.26}$$

and κ_1,κ_2,κ_1' and κ_2' are given by

$$\kappa_1 = nK_1 = \frac{n}{R_1 \sin\omega} \tag{4.27}$$

$$\kappa_2 = mK_2 = \frac{m}{R_2 \sin\omega} \tag{4.28}$$

$$\kappa_1' = pK_1' = \frac{p}{R_1' \sin\omega'} \tag{4.29}$$

$$\kappa_2' = qK_2' = \frac{q}{R_2' \sin\omega'}. \tag{4.30}$$

The fringe angle (in rad) is given by

$$\delta_{nmpq} = \tan^{-1}\left(\frac{\kappa_1\cos\omega - \kappa_2 - \kappa_1'\cos(\theta+\omega') + \kappa_2'\cos\theta}{-\kappa_1\sin\omega + \kappa_1'\sin(\theta+\omega') - \kappa_2'\sin\theta}\right) + \frac{\pi}{2}. \tag{4.31}$$

Note that the expression for λ_{nmpq} is equivalent to Hermann's equation (4.1) when $\omega = 120°$ and $n = 1$, $m = 0$, $p = 1$, $q = 0$.

Symmetry The real-space lattice definitions in this thesis implies that the overlayer rotated by 180° is identical to the non-rotated overlayer ($\mathbf{R_1'}$ becomes $-\mathbf{R_1'}$ and $\mathbf{R_2'}$ becomes $-\mathbf{R_2'}$). This implies that the MPs are invariant upon a half-rotation symmetry, and this is not visible in equation (4.25) and (4.31), as the two equations are 2π periodic only. It is necessary to consider both the $\mathbf{K_{nmpq}}$ and $\mathbf{K_{nm\bar{p}\bar{q}}}$ simultaneously (both existing together in the reciprocal space) in order to model the MPs as the overlayer rotates.

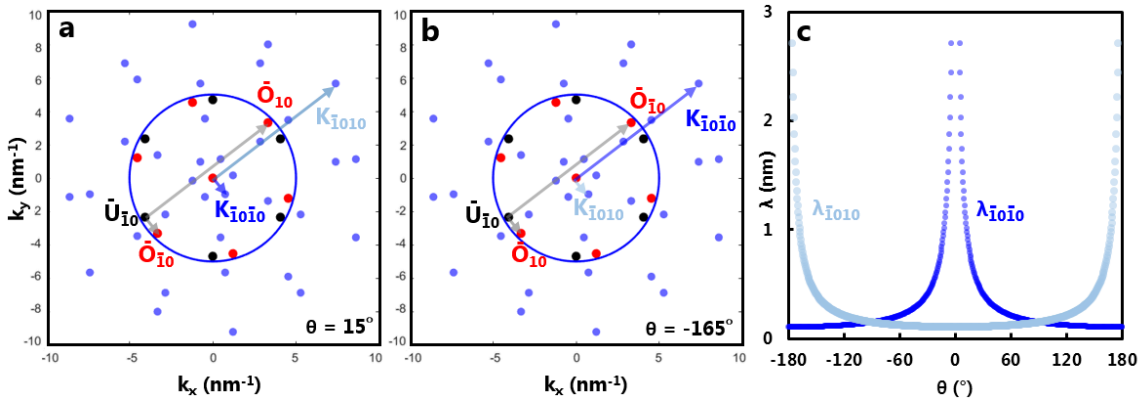

Figure 4.14: Half-revolution symmetry. (a) Reciprocal lattices of the underlayer (black) and overlayer (red) for the twisted bilayer graphene case for $\theta = 15°$. The two vectors $\mathbf{K_{\bar{1}0\bar{1}0}}$ and $\mathbf{K_{\bar{1}010}}$ are constructed as an example (dark and light blue). (b) Reciprocal lattices of the same system for $\theta = -165°$, i.e. for a half rotation of the overlayer. The two difference vectors are swapped from (a). The cut-off circle is shown in both panels with $k_r = 5$ nm^{-1}. (c) Calculated $\lambda_{\bar{1}0\bar{1}0}$ (dark blue) and $\lambda_{\bar{1}010}$ (light blue).

Example Figure 4.14 illustrates this idea for the case of bilayer graphene, for two rotation angles separated by 180°. Figure 4.14(a) shows the reciprocal lattices displayed for $\theta = 15°$, and two vectors $\mathbf{K_{\bar{1}0\bar{1}0}}$ and $\mathbf{K_{\bar{1}010}}$ are constructed (arrows) as an example. The difference vector $\mathbf{K_{\bar{1}0\bar{1}0}}$ is one of the three MP vectors, but $\mathbf{K_{\bar{1}010}}$ is not and in fact corresponds to a period that is smaller than the real-space lattice constants as it extends beyond $k_r = 5$ nm^{-1}. Figure 4.14(b) represents the two reciprocal lattices for $\theta = -165°$, i.e. after a half-revolution. The overlayer reciprocal lattice is unchanged because of the symmetry, however the MP vector is now $\mathbf{K_{\bar{1}010}}$ as it is very close to origin, and $\mathbf{K_{\bar{1}0\bar{1}0}}$ extends beyond the cut-off circle. The two difference vectors are in fact swapped upon a half-revolution of the overlayer, as discussed in the previous paragraph. The calculated periods that corresponds to the two $\mathbf{K_{nmpq}}$ discussed here are shown as a function of θ for the entire 360° rotation in Fig. 4.14(c). As discussed previously, λ_{nmpq} for one set of n,m,p,q indices is not 180°-periodic. Here, $\lambda_{\bar{1}0\bar{1}0}$ diverges for $\theta = 0$ but has a very small value for $\theta = 180°$. The other period $\lambda_{\bar{1}010}$ is equal to $\lambda_{\bar{1}0\bar{1}0}$ shifted by 180°. To obtain the sixfold symmetry of the MP that occurs in bilayer graphene, the other reciprocal vectors described by O_{01}, $O_{1\bar{1}}$, etc. must be taken into account.

Summary In order model the half-revolution symmetry of the superposition, it is important to compute the periods and angles associated with both $\mathbf{K_{nmpq}}$ and $\mathbf{K_{nm\bar{p}\bar{q}}}$.

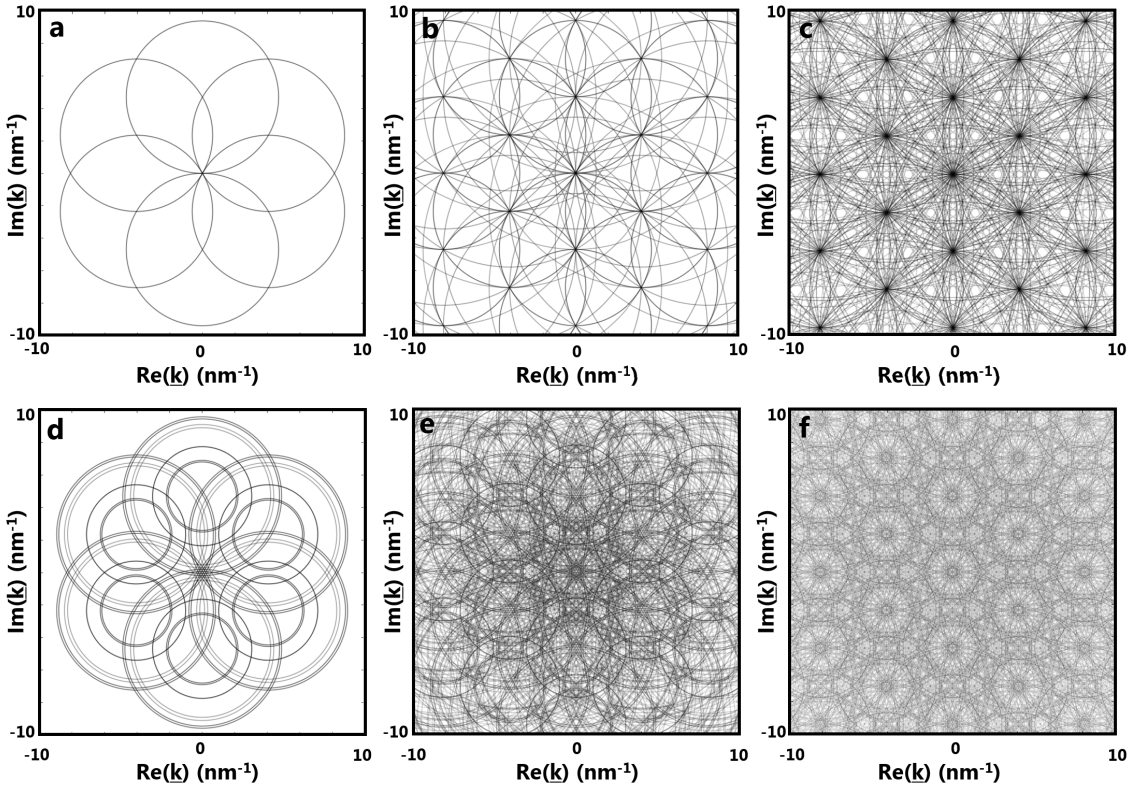

Figure 4.15: (a) Moiré roses for bilayer graphene for (a) $k_r = 6$ nm^{-1}, (b) $k_r = 12$ nm^{-1} and (c) $k_r = 18$ nm^{-1}. Moiré roses for α-Bi on HOPG for (d) $k_r = 6$ nm^{-1}, (e) $k_r = 12$ nm^{-1} and (f) $k_r = 18$ nm^{-1}.

4.6 Moiré Rosettes

We conclude by describing curious patterns observed in the reciprocal space by choosing cut-off values k_r that are much larger than those required to model the MPs observed in the experiments. These structures relate to the reciprocal circles that have been described earlier in section 4.4 for the example of β-Sb on α-Bi. Here, we illustrate a few examples of such resulting patterns, designated in this thesis as *moiré rosettes* (for their accidental resemblance to Islamic and Christian rosettes). The moiré rosettes are defined as the traces of all the $\mathbf{K_{nmpq}}(\theta)$ for $k_r \gg k_1, k_2, k_1', k_2'$.

The circles generated by all the difference vectors in a 360°-rotation of the overlayer for the case of twisted bilayer graphene are displayed in Fig. 4.15(a) using a cut-off value of $k_r = 6$ nm^{-1} (i.e. only considering the first order reciprocal vectors) and without the inclusion of the null vectors. It is made up of 6 circles of radii $k = k_1 \simeq 4.69$ nm^{-1} and centred at $\mathbf{K_{nm}}$

coordinates. The circles cross the origin indicating that λ_{nmpq} diverges for several values of θ. Increasing the value of k_r (i.e. using higher order vectors in the calculation of $\mathbf{K_{nmpq}}$) dramatically increases the level of complexity of these reciprocal structures becoming moiré rosettes, as shown in Figs. 4.15(b) and 4.15(c), for respectively $k_r = 12$ nm^{-1} (second orders included) and $k_r = 18$ nm^{-1} (third orders included).

Figure 4.15(d) shows the moiré rosette obtained for α-Bi/HOPG (using the first orders of HOPG only, $k_r = 6$ nm^{-1}). Again, the complexity of the traces increases dramatically with increasing the cut-off k_r as shown for $k_r = 12$ nm^{-1} and $k_r = 18$ nm^{-1} in Figs. 4.15(e) and 4.15(f).

It is important to note that the appearance of the moiré rosettes is also dependent upon the display properties on the screen, in particular the size and opacity of the markers (or line). However at this stage these mathematical objects and must be treated as a curiosity, their properties are unknown and extend beyond the scope of this thesis. Studying the moiré rosettes as a function of the symmetry of the layers considered would be a first focus of interest, and the study of these objects by varying the lattice constants could also be fruitful as it was found that the moiré rosettes are very sensitive upon slight variations of the lattice parameters (not shown). Their potential fractal properties could be investigated as well.

4.7 Discussion and conclusion

4.7.1 Summary of the general model

In this chapter, a general approach was developed to determine the geometry (period λ and angle of the fringes δ) of the MPs generated by the superposition of any pair of 2D lattices. The model does not require the layers to be commensurate or incommensurate. The concept is similar to that developed in previous work for optical gratings [250–252], but was adapted for the case of 2D lattices. The possible MPs are understood as difference vectors of the under- and overlayer reciprocal lattices. The MPs that are visible at a given rotation angle are the difference vectors that are the closest to origin.

An algorithm was developed to yield λ and δ from the lattice constants of both under- and overlayer, their respective unit cell angles and the cut-off k_r for a chosen rotation angle

θ. The value of k_r is obtained after inspection of the reciprocal lattices and requires critical assessment to represent the MPs that are visualised via either STM or in ball-and-stick simulations using VESTA. The algorithm yields the curves $\lambda(\theta)$ and $\delta(\theta)$, and were tested against the well-established model developed by Hermann [174]. The results were found to agree exactly for both hexagonal/hexagonal (in particular twisted bilayer graphene) and rectangular/rectangular (using the α-Sb/α-Bi and MBi/α-Bi examples) systems within the range of validation of the Hermann's model. The algorithm outperforms Hermann's model because it does not require a specific pair of lattice symmetry, and no limits on either θ or the scaling factors were necessary.

The agreement with the previous VESTA simulations (for β-Sb/α-Bi, α-Bi/HOPG and α-Bi/MoS_2) in the case of mixed symmetry stacking (hexagonal/rectangular and vice versa) was also clear. The improvement from the VESTA simulations is also clear, as the algorithm is faster and more accurate because no human interpretation of the real-space ball-and-stick models are required. The modeling methods presented in chapter 3 are clearly superseded with the universal model discussed in this chapter.

The general model can be expressed in analytical form, which makes it possible for anyone to predict the geometry of the MPs that may arise from the superposition of any 2D crystals at a given rotation angle θ. It is required in that case to know which pair of reciprocal vectors may interfere leading to the MP of interest (i.e. the n,m,p,q indices). The concept of 'moiré rosettes' was finally presented, and are today only mere aesthetic curiosities. Further work may indicate whether these objects can be interesting or functional in any way.

4.7.2 Discussion

Rotation angle at the periods maxima The MPs observed in this thesis are consistent across multiple islands and samples indicating preferred orientations of the overlayers with respect to the underlayer in VDWHs. The observed overlayers seem to be oriented so as to maximize the period of their MP. Indeed for all cases shown in this chapter (α-Sb/α-Bi in Fig. 4.7, β-Sb/α-Bi in Fig. 4.8, MBi/α-Bi in Fig. 4.9, α-Bi/HOPG in Fig. 4.10 and lastly α-Bi/MoS_2 in Fig. 4.11), the observed rotation angle is nearly exactly at the position of a

maximum of $\lambda(\theta)$. Only very rarely a deviation of a few degrees (up to $\sim 4°$) was observed, either 'naturally' (e.g. slightly misaligned α-Sb layer on α-Bi where the MP fringes appeared slightly rotated, see Fig. 3.11 in section 3.3.4), or via deliberate attempts to test the 2D crystal stability (rotated MBi by a few degrees after increasing the tip-sample interactions during STM imaging, see Fig. 3.15 in chapter 3.3.3). To explain this phenomenon it is hypothesised that the elastic deformation energy of the overlayer is minimised when the period of the MP is maximised (therefore providing higher stability). This preferred orientation is presumably determined during the initial growth of the islands, so as to minimise strain. A good example is the comparison of α-Bi/HOPG and α-Bi/MoS_2, where θ in the two cases clearly differs and α-Bi is in both cases rotated to maximize the period of the MPs.

Second order reciprocal vectors When using the general model, the cut-off k_r was always chosen just above the largest first order reciprocal vector the under- and overlayer ($k_r > \max\{k_1, k_2, k_1', k_2'\}$). While in most of the cases the MPs were successfully modelled from the vector difference between the first orders (e.g. $\mathbf{K_{10\bar{1}0}}$ for MBi/α-Bi), in several cases it was necessary to use higher orders (e.g. $\mathbf{K_{01\bar{0}2}}$ or $\mathbf{K_{1\bar{1}1\bar{1}}}$ for α-Bi/MoS_2). The reason for this is not fully clear, but a possible explanation is given as follows. When the MPs are modelled from the first orders of the reciprocal lattices, the MPs can be seen as an interference between two neighbouring atomic rows, as is the case e.g. for MBi on α-Bi (see real-space images of the modeling in Fig. 3.15). In the cases where the lattice mismatch is significantly larger it is hypothesised that the MPs emerge from the interference between every row of atoms with every second row of the other layer. When this happens, it is necessary to account for the second orders of the reciprocal lattices (as observed for the simple case of gratings in Fig. 4.2).

Physical corrugation and rigid lattice approximation The question of whether the observed MPs are the consequence of a physical corrugation in the atomic lattice (i.e. distortion of the overlayer) or arise purely from electronic effects (e.g. modulation of the electron density of states) still remains, and is not explicitly addressed in this thesis. Preliminary results (not shown) indicate that the MPs are observed in AFM (and are identical in terms of period and orientation), which is typically less sensitive to the surface electronic structure

than STM and more sensitive to the topographic features only. This suggests that the MPs observed in this thesis are at least partially a physical corrugation. However it is expected that such a physical deformation must impact the electronic structure of an initially flat, non-corrugated 2D layer, and so it is not possible to be certain at this point. It is worth clarifying that the present model assumes perfectly rigid layers and it is expected that in reality the lattice constants and possibly the unit cell angle depend subtly on θ and on the exact (x, y) position. Further experimental work could focus on obtaining high-precision lattice constant determination as a function of the rotation angle. It is also possible that the layers experience an in-plane strain. Experimental characterisation via STM is however challenging, with effects that limit the precision of the measurements, e.g. thermal drift and the limited size of the images.

4.7.3 Future work

A further confirmation of the validity of the general model, applied to a broader set of experimentally observed VDWHs would be desirable. Recent efforts in the UC research group have focused on what appears to be a new hexagonal allotrope of antimonene with a very large lattice parameter (~ 8 Å), which may be the result of a surface reconstruction. A modulation was observed on the surface of the new allotrope of antimonene, and it may be identified in the future as a MP, arising from the lattice mismatch with its substrate. Testing the various MP models (Hermann, VESTA-simulations, and the general model) with such case, where the lattice mismatch is significantly larger and in which a potential surface reconstruction is present would certainly stimulate and develop the understanding of the MPs.

More generally, focusing efforts on the MPs observed on a variety of VDWHs would be of a great interest in order to understand their potential for device engineering. Scanning tunneling spectroscopy experiments should be undertaken to measure the electronic band structure, and observe if and how the MP modulates the surface density of states near the Fermi level. Obtaining 2D materials with larger coherence length (i.e. wider areas) will enable other methods of characterisation of MPs; one can imagine θ-dependent ARPES or Raman spectroscopy experiments. Junctions and devices with different rotational configurations within the VDWH could be engineered and tested independently. Transport measurements at low

temperature would certainly be a tool of choice to probe the influence on the electronic (and topological) structure caused by the MPs.

This general method for prediction of the geometry of the MPs in VDWHs is beneficial for understanding the symmetry of a under- and overlayer system. The MPs possibly act as a periodic potential over a range typically of a few nanometres (larger than the lattice constants of the individual layers). It is clear that such general model could be helpful for band-structure calculation where boundary conditions play a fundamental role.

Chapter 5

Samarium capping layer for RENs

5.1 Principle

As reviewed in chapter 1, the rare-earth nitrides (RENs) are a class of materials that are potential candidates for a variety of spintronics applications, due to their coexisting intrinsic ferromagnetic and semiconducting properties. As pointed out, early investigations of different RENs in the 1960s were hindered by oxygen contamination and by the difficulty of obtaining stoichiometric samples, problems that were mostly resolved with the continuous development of high-purity thin film deposition techniques in ultra-high vacuum (UHV) such as molecular beam epitaxy (MBE) since the late twentieth century [50].

Because of the rapid oxidation that the RENs undergo [50, 67], it is not possible to study the films properties after exposure to air. Unless analysis techniques are readily available in the same chamber or without breaking the vacuum, it is necessary to passivate the RENs films with a capping layer (or simply *cap*). Typically, III-V nitrides (AlN [54, 58, 59], GaN [56, 60, 71, 166, 259]) have been chosen in the past due to their chemical stability, relative uniformity and ease of growth on REN surfaces, high resistivity permitting electrical characterisation, and transparency allowing for optical characterisation of the underlying RENs [56]. Metallic (W [260], Cr [260], Cu [67], TaN [165] NbN [96, 261]) and Gd [95]) and insulating (YSZ [88], MgF_2 [259], III-V compounds) caps have also been successfully tried.

5.1.1 Removable capping layer

While the use of a capping layer can still permit measurements of the bulk properties (SQUID, optical and transport measurements), no surface-sensitive technique (e.g. ARPES, XPS,

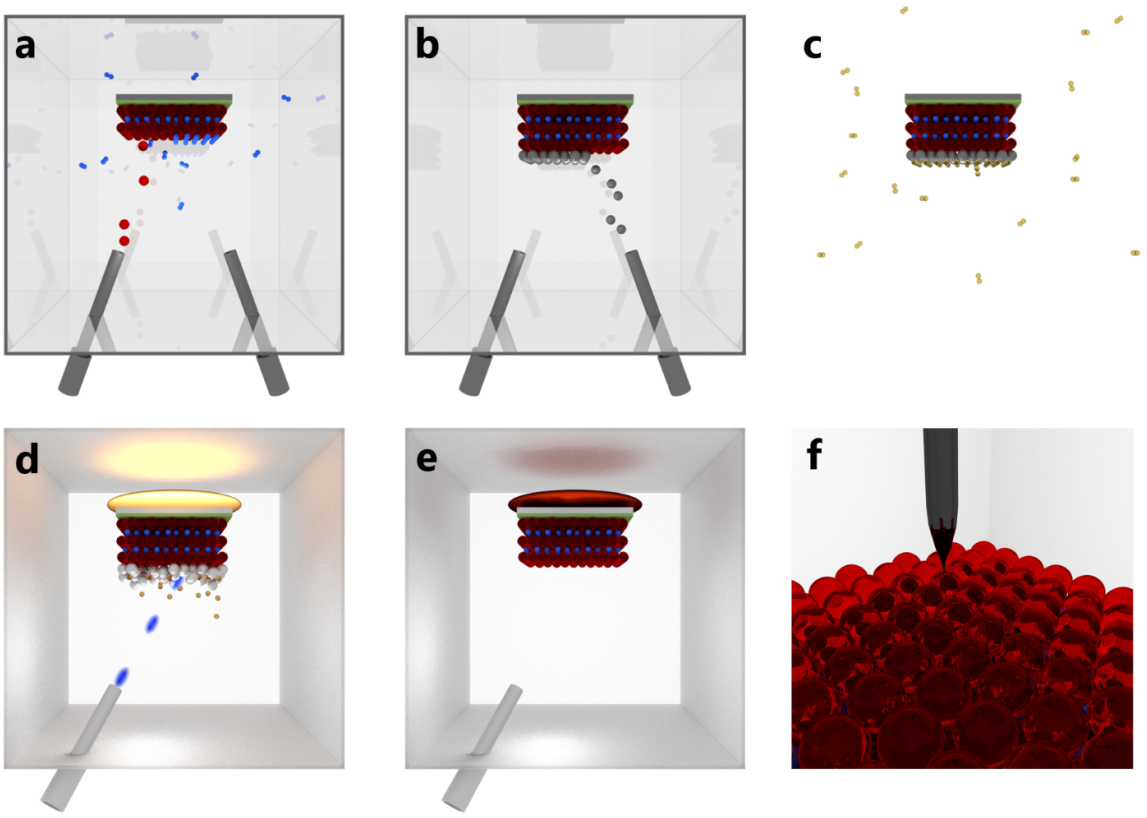

Figure 5.1: Schematics of the capping and decapping procedure. (a) REN growth (red: RE, blue: N) in the MBE growth chamber under a N_2 pressure. (b) Capping layer deposition (grey) via MBE. (c) Transport of the heterostructure in air (Yellow: impurities). (d) Treatment of the heterostructure in a different chamber for cap removal, using Ar ion bombardment (hazy blue) and/or heating (glowing element). (e) Successfully decapped sample. (f) Decapped REN(111) surface under a STM tip (black).

STM, ...) can be applied to study RENs in the presence of a cap. Surface characterisation is of particular relevance because RENs surfaces are relatively unknown in terms of morphology, surface reconstruction and electronic structure [50], with only a very few reports focusing on STM [56, 62] and one on XPS [62]. Further surface studies would be desirable.

It is therefore sensible to design a removable capping layer to enable ex-situ surface studies of RENs. The principle of the capping/decapping procedure is detailed schematically in Fig. 5.1. First, the REN layer is deposited in the growth chamber by MBE (a). The removable capping layer is then grown immediately (b). The heterostructure can then be transported in ambient conditions (c), where impurities from the air may be adsorbed on the cap surface. In a different analysis chamber (d), the cap is removed through sputtering and/or thermal desorption. In (e,f), the REN surface is recovered and is ready for surface-senstive

measurements, e.g. STM.

Removable capping layers using a similar principle have been applied successfully in the past for a variety of different materials that degrade in ambient air: epitaxial As on GaAs [262–264] and InAs [264], Se on $CuInSe_2$ [265], on ZnSe(100) [266], on Bi_2Se_3 [267, 268], P on InP and GaP [264]. To the best of our knowledge, a successful capping/decapping procedure has not yet been reported for RENs.

It should be noted that any decapping procedure may induce undesired effects, e.g. alloying of the cap material with the protected layer, as reported for As capping on GaSb crystals [269] or Se on Bi_2Te_3 [267]. The top few nanometres of the recovered surface may be contaminated through substitution with the cap material [267]. For As-capped GaSb layer, Sb is thought to diffuse to the cap surface during the capping deposition [269, 270].

5.1.2 Choice of samarium and samples

The approach considered here is to use samarium (Sm) to cap gadolinium nitride (GdN) samples. The reasons for focusing on GdN are the following:

- It is the most reported REN in the literature [50, 56, 94] yet suffers from a lack of surface data.
- It is one of the REN grown epitaxially with remarkable structural quality [50, 56].
- Possesses a high magnetic moment (of 7 μ_B per Gd^{3+} ion) [55, 56].
- It the highest reported Curie temperature among the RENs [50] with a report suggesting an increase of T_C from ~50 K to ~70 K through magnetic polarons [70].
- A series of devices using GdN have already been demonstrated [95, 96, 98] relevant for potential future applications.

The GdN samples were grown by MBE as detailed in chapter 1 in the UHV lab at Victoria University of Wellington (VUW). A suitable material for fulfilling the function of a removable capping layer should ideally possesses the following properties:

- Volatility, the cap must sublimate under moderate applied heat in the analysis chamber.

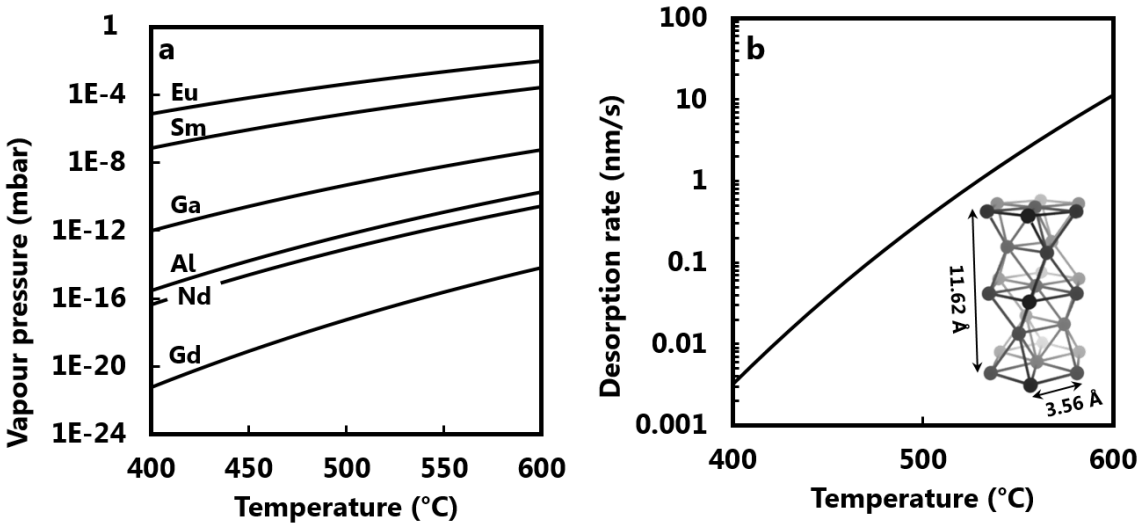

Figure 5.2: (a) Temperature dependent vapour pressure of elements that are available in the growth chamber (empirical data obtained from [271, 272]). (b) Sublimation rate of bulk Sm for the same temperature range using the Hertz-Knudsen equation. The inset in (b) is a ball-and-stick representation of dhcp Sm with lattice parameters indicated.

- Low reactivity with the underlying REN layer, the REN properties should not be affected by the capping and decapping procedure.
- Low reactivity with air, the transport of the capped sample in ambient condition should not interfere significantly with the decapping procedure (e.g. rapid oxidation, delamination).
- Homogeneity of growth when deposited on the REN, the cap should be continuous to offer effective protection against ambient conditions.
- Compatibility with the analysis vacuum chamber, it is desirable to avoid contamination of the instruments and/or vacuum environment.
- Availability because the cap source must be present in one of the effusion cell in the growth chamber.

The temperature-dependent vapour pressure of the various elements typically available in the growth chamber are displayed in Fig. 5.2(a). Several rare-earth sources (Eu, Sm, and Gd), Al and Ga are available in either Knudsen cells or electron-beam evaporators. As mentioned above, a cap made with an high vapour-pressure element is preferred to minimise the

desorption temperature required for future decapping. While Eu is very volatile it is known to oxidize very rapidly in air [273]. Sm therefore appears as a valid candidate. Although it is known to oxidize in presence of moist air [274], the oxidation rate of thin Sm films is typically a few nanometres per day in normal ambient conditions [275]. All other available elements have vapour pressures many orders of magnitude below that of Sm.

The desorption rate is determined from the vapour pressure, given by the Hertz-Knudsen equation [276] (assuming no re-adsorption of the sublimated atom) as follows:

$$\frac{1}{A}\frac{\mathrm{d}N}{\mathrm{d}t} = (2\pi m k_B T)^{-\frac{1}{2}} P \tag{5.1}$$

where A is the surface area, $\mathrm{d}N/\mathrm{d}t$ is the number of sublimated atoms per unit time, m the mass of the atom, k_B the Boltzmann constant and P the equilibrium vapour pressure of the material at temperature T. Figure 5.2(b) shows the equation (5.1) applied to bulk Sm. The surface density of atoms $N_s = 9.1 \times 10^{14}$ cm^{-2} and volume density $N_v = 3.0 \times 10^{-22}$ cm^{-3} used for the calculation of the desorption rate are calculated based on the crystalline structure of double hexagonal close-packed (dhcp) Sm [277] shown in the inset of Fig. 5.2(b). The calculated desorption rate increases by an order of magnitude every 57°C, indicating that a temperature of 500°C for 3 minutes will sublimate 60 nm of Sm. It is important to keep in mind that these values are derived from bulk Sm properties and the desorption behaviour of thin films may vary. Nonetheless, these values offer a reasonable estimate and serve as a reference.

Table 5.1 lists the samples grown and studied for this chapter and for chapter 6. Others were grown unsuccessfully and were not included in the analysis. Nominally identical templates consisting of 100 nm-thick AlN(0001) on 2 inch n-doped Si(111) wafers were used to grow all samples. Two typical sample types are fabricated: (1) cap only, i.e. ~100 nm-thick Sm, and (2) ~100 nm-thick GdN capped with ~100 nm-thick Sm, with an exception for A520 consisting of a 300 nm Sm capping layer on 100 nm GdN. An uncapped GdN sample (A517) was made as a reference sample. All samples were grown at VUW using either a Thermionics (A* samples) or Riber (R* samples) UHV system. For more details concerning the GdN growth itself, refer to chapter 1. A cartoon of the typical heterostructure is represented in Fig. 5.3.

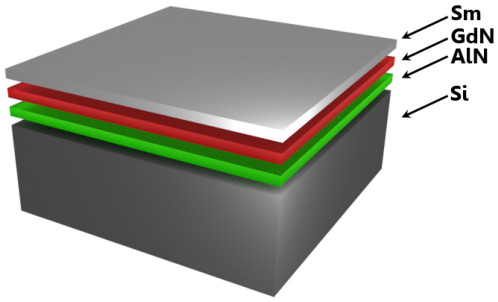

Figure 5.3: Schematics representing the thin film heterostructures grown in this thesis. The layers are offset for clarity.

Sample	GdN	Sm
A314	100	100
A372	100	100
A464	100	100
A517	100	0
A519	100	100
A520	100	300
R024	0	100

Table 5.1: Samples grown in this thesis, indicating both the GdN and Sm cap thicknesses in nm.

This chapter is written as follows: first, section 5.2 will review in detail the growth and characterisation of the capping layer. Section 5.3 will focus on the thermal desorption of the Sm cap without exposure to air. Section 5.4 discusses similar experiments except after a brief exposure of the samples to air. Finally, section 5.5 will summarize and discuss the results. The growth, RHEED and XRD characterisation were performed conjointly with J. Chan, a PhD candidate at VUW [178]. A patent on the concept of a removable capping layer on RENs has been filed [278].

5.2 Epitaxial Sm growth

5.2.1 Stability of GdN

It is important to test the thermal stability of the as-grown GdN. Undesired effects may occur through annealing, such as recrystallisation or nitrogen vacancies formation as observed on e.g. GaN [279–281]. A preliminary experiment consisting of heating an as-grown GdN layer was performed, and RHEED patterns were recorded before and after the annealing procedure, for a period of 50 minutes at an estimated temperature of 650°C. The RHEED patterns before and after annealing are shown in Fig. 5.4(a) and Fig. 5.4(b) respectively. The two RHEED patterns are identical (see chapter 2 for more details concerning the RHEED theory, set-up and published GdN results), and no degradation of the sample as a consequence of the annealing is evidenced.

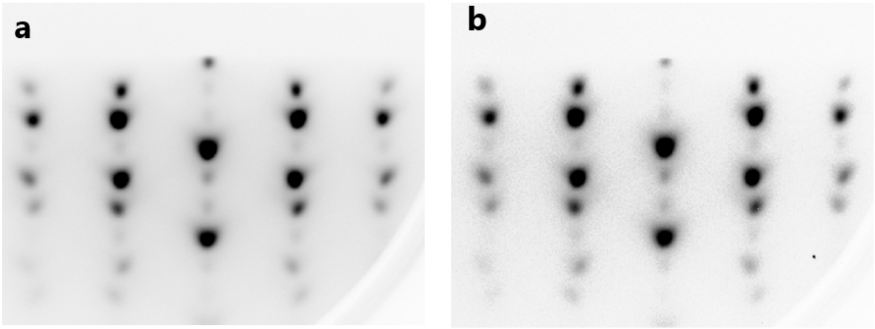

Figure 5.4: RHEED pattern recorded (a) before and (b) after annealing at $T = 650°C$ in UHV conditions ($P = 6 \times 10^{-9}$ mbar), along the GdN $\langle 1\bar{1}0 \rangle$ direction.

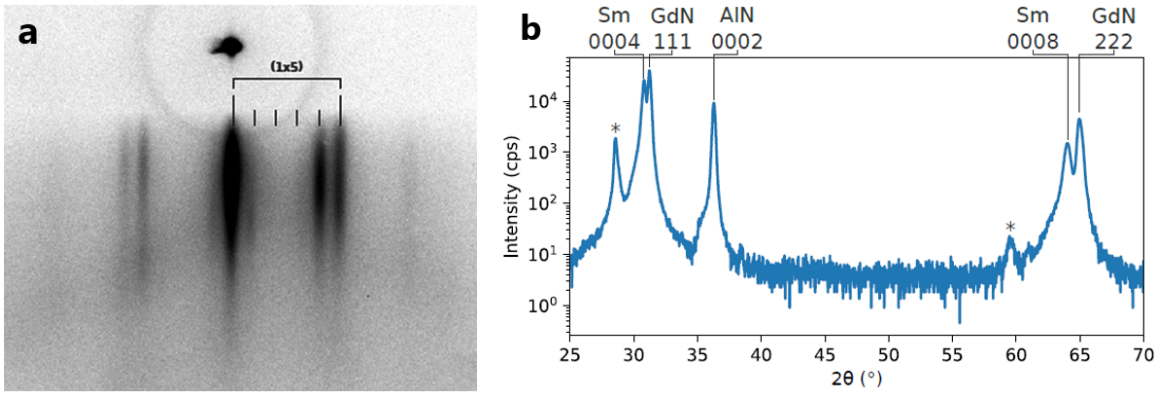

Figure 5.5: (a) RHEED pattern of a (0001)-textured Sm capping layer after deposition on GdN(111), recorded along the Sm $\langle 11\bar{2}0 \rangle$ direction. The satellite streaks related to the (5×5) reconstruction are indicated. (b) XRD pattern ($\theta - 2\theta$) of a Sm-capped epitaxial GdN thin film grown on AlN(0001). The stars indicate Si substrate peaks.

5.2.2 Capping layer growth

The Sm cap is grown in the same deposition chamber, directly on the GdN(111) surface after the REN deposition (or simply on the AlN(0001) buffer layer for the 'cap-only' samples). Sm is evaporated from high-purity (5N) solid pellets in a Knudsen cell and the sample is kept at room temperature during deposition as it is preferable to avoid premature desorption of the cap. The deposition rate, measured previously from cross-sectional SEM on calibration samples (not shown), is maintained at around 150 nm/h.

Fig. 5.5(a) shows the RHEED pattern of the surface after deposition of ~100 nm-thick Sm on a GdN layer. The streaks are continuous, suggesting a long range crystalline order, a 2D 'layer-by-layer' growth and a low roughness. Satellite streaks are observed and correspond to a (5×5) reconstruction [282, 283].

Fig. 5.5(b) is a $\theta-2\theta$ XRD pattern obtained on a 100 nm-thick Sm cap deposited on a GdN layer. Besides Si (indicated with $*$) and AlN, the sample consists of only (111)-oriented GdN and (0001)-oriented Sm. XRD $\phi-\theta$ scans of the same heterostructure (not shown) exhibit a 6-fold symmetry. Assymetric ϕ scans along the Sm $[10\bar{1}x]$ direction, compared to the GdN [022] direction [178] reveal that the Sm is dhcp (ABAC/ABAC...) in agreement with previously reported epitaxial growth of Sm(0001) on Nd [282] and thermally treated bulk Sm [277]. It is therefore possible to rule out the existence of its other known phase, the rhombohedral 'Sm-like' (stacking following ABABCBCAC/ABA...) [277]. The epitaxial relationships of the layers are:

$$\text{Sm}(0001) \parallel \text{GdN}(111) \parallel \text{AlN}(0001) \tag{5.2}$$

$$\text{Sm}\langle 11\bar{2}0\rangle \parallel \text{GdN}\langle 1\bar{1}0\rangle \parallel \text{AlN}\langle 11\bar{2}0\rangle \tag{5.3}$$

5.2.3 Capping layer morphology

The surface morphology of the samples was investigated through atomic force microscopy (AFM) at UC in UHV in non-contact mode. The samples had then been exposed to air before imaging. Figure 5.6 shows topography images of several samples, after an exposure to ambient atmosphere for a few minutes to a few hours.

Sm/GdN Fig. 5.6(a) is an AFM image of A464, consisting of a 100 nm-thick cap of Sm grown on 100 nm-thick GdN. The surface can be described by flat terraces of about ~300 nm-wide, separated by trenches up to ~60 nm deep (covering ~10% of the surface area). The terraces are nearly atomically flat, as the root-mean square roughness (RMSR) measured on the terraces is smaller than 1 nm. The trench depth is however comparable to the Sm layer thickness, indicating that further measurements are required to test whether the cap protects the underlying GdN layer from oxidation. Figure 5.6(b) shows an AFM image of A519, grown under nominally identical conditions as A464 in Fig. 5.6(a). The surface shows areas up to 1×1 μm^2 that are very smooth (RMSR < 1.0 nm). Pits, with depths up to ~30 nm are present across the surface (~3% of the surface area, density $\sim2\times10^8$ cm^{-2}). Close inspection of the

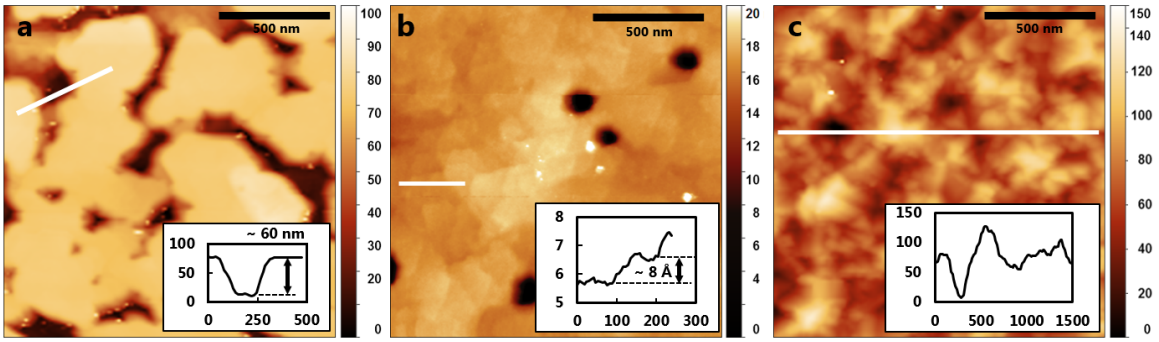

Figure 5.6: Non-contact AFM images of (a) A464, (b) A519 and (c) R024. For all three samples, the Sm capping layer is ~100 nm-thick. The z-scales are indicated on the images. In (a,b) the cap is deposited on ~100 nm-thick GdN, and in (c) directly on the AlN/Si template. The images are recorded in UHV after outgassing the samples for 1 hour above 100°C. The insets correspond to the line profiles shown in white in the respective images. The axes units are in nm.

flat surface reveals the presence of terraces with a step height of about 8 Å, corresponding to two to four atomic planes of (0001)-textured Sm (see inset in Fig. 5.2(b)).Generally, the morphology of Sm/GdN is typical of a 2D 'layer-by-layer' growth, in agreement with the RHEED pattern of Sm shown in Fig. 5.5(a). Such 'mosaic' morphology is reminiscent of AlN(0001) and GaN(0001) thin films grown by plasma-induced MBE and metal-organic chemical vapour deposition, explained in terms of coalescence [284]. The morphology differences between A464 and A519 (mainly pit shapes and density) are not fully understood, and it is hypothesised that subtle differences in the growth conditions are causing this, despite using identical growth chamber and maintaining growth conditions as consistent as possible (UHV conditions, substrate temperature, Sm growth rate and thickness). A possible reason for the different pit structure and density could be originating from differences in surface quality of the AlN/Si templates used as substrates.

Sm/AlN Fig. 5.6(c) is an AFM image of a 100 nm-thick cap of Sm grown this time directly on the AlN/Si template. Here, the morphology differs strongly from the Sm/GdN samples (Fig. 5.6(a,b)). The surface is much rougher (RMSR = 19 nm, as opposed to ~5 nm for the Sm/GdN samples). The inset in Fig. 5.6(c) shows the line profile (white line in the image), suggesting a peak-to-peak amplitude of about 120 nm). The surface of the Sm/AlN samples does not show flat terraces.

Comparison The morphology differences between Sm/GdN versus Sm/AlN samples is now discussed. First, the sample R024 shown in Fig. 5.6(c) is grown in a different chamber (Riber) than the two samples A464 and A519 (Thermionics) displayed in Fig. 5.6(a,b). Despite our efforts to keep the deposition conditions as consistent as possible, morphology variations are likely to emerge from many factors related to the differences between the two UHV systems (distance and angle of the Sm evaporator with respect to the substrate holder, base pressure, growth temperature, flux, purity of the sources, etc.). Rigorously identical growth conditions would however likely cause structural differences between Sm/AlN and Sm/GdN. Interfacial energies $\gamma_{\mathrm{Sm/AlN}}$ and $\gamma_{\mathrm{Sm/GdN}}$ are expected to differ, and it is known that γ can have a profound impact on the growth mode [285]. AlN and GdN are also likely to not have the same dislocation density, affecting the relaxation process and stress in the film [286]. The lattice mismatch δ between Sm and AlN is significantly larger ($\delta_{\mathrm{Sm/AlN}} = +12.6$ %) than for the Sm/GdN interface ($\delta_{\mathrm{Sm/GdN}} = +1.1$ %), likely to impact the stress experienced by the growth of the first few monolayers of Sm. Dislocation density is often correlated with the lattice mismatch, e.g. for SiGe epilayers on Si substrates [287], however the correlation is not universal [288].

5.2.4 Electrical characterisation

The temperature-dependent resistivity of a Sm/GdN heterostructure was measured ex-situ and is shown in Fig. 5.7(a). The measurement, performed using a 4-point probe station with contacts on the Sm surface of the heterostructure, reflects the low resistivity of the Sm layer and is not affected by the GdN and the AlN/Si template. At room temperature, the Sm resistivity is $R_{\mathrm{Sm}} = 48\mu\Omega\cdot$cm, in good agreement with the literature [274]. The resistivity linearly decreases while lowering the temperature to about $T\sim$100 K, where a knee is observed, from which the resistivity decreases more rapidly. This is consistent with previously reported temperature-dependent resistivity of Sm [289], where the anomaly at $T = 106$ K is linked with an antiferromagnetic transition [290].

Samarium thin films oxidize in air, forming Sm_2O_3, at the rate of ~1 nm per day [275]. Sm_2O_3 grown by reactive sputtering has a resistivity of the order $R_{Sm_2O_3}\sim 1\times 10^7\ \Omega\cdot$cm [291], immensely larger than metallic Sm as shown in Fig. 5.7(a). The 11 orders of magnitude dif-

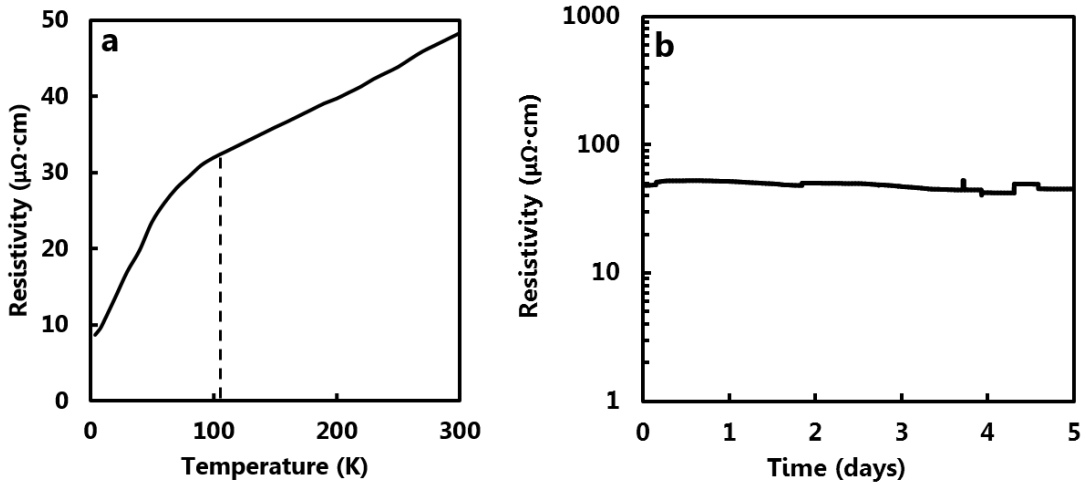

Figure 5.7: (a) Temperature-dependent resistivity of the Sm/GdN heterostructure. The dash line indicates the reported anomaly temperature of Sm [289]. (b) Time-dependent resistivity over a period of 5 days.

ference between the two is used to evaluate the oxidation rate of epitaxial Sm(0001) samples. The time-dependent resistivity of a Sm film was then measured immediately after growth, for a period of 5 days in ambient conditions. Again, a 4-point probe method is used in order to minimize the effect of contact resistance and the results are shown in Fig. 5.7(b). For the considered duration, no significant variation was observed. Besides several jumps in the data attributed to mechanical perturbations, the resistivity of the sample is very stable $R = 48 \pm 6\ \mu\Omega \cdot \text{cm}$. The low and constant resistivity of the sample over time is a good indication that the Sm layer does not degrade too rapidly and can therefore be used as a passivating layer.

5.2.5 Magnetic characterisation

The magnetisation of a Sm-capped GdN sample was also investigated, to verify the capacity of the Sm cap to shield the underlying GdN layer from ambient degradation. Figure 5.8(a) is the normalised temperature-dependent field-cooled magnetisation of a typical Sm/GdN sample under an applied field of $H = 25$ Oe. The magnetisation M is null above $T = \sim 70$ K and rises monotonically as the temperature is decreased down to 5 K. Figure 5.8(b) shows the field-dependent magnetisation of the same Sm/GdN sample realised at low temperatures. The magnetic moment saturation is $M_{\text{sat}} \sim 7\mu_B/\text{Gd}^{3+}$ and the sample shows a low coercivity

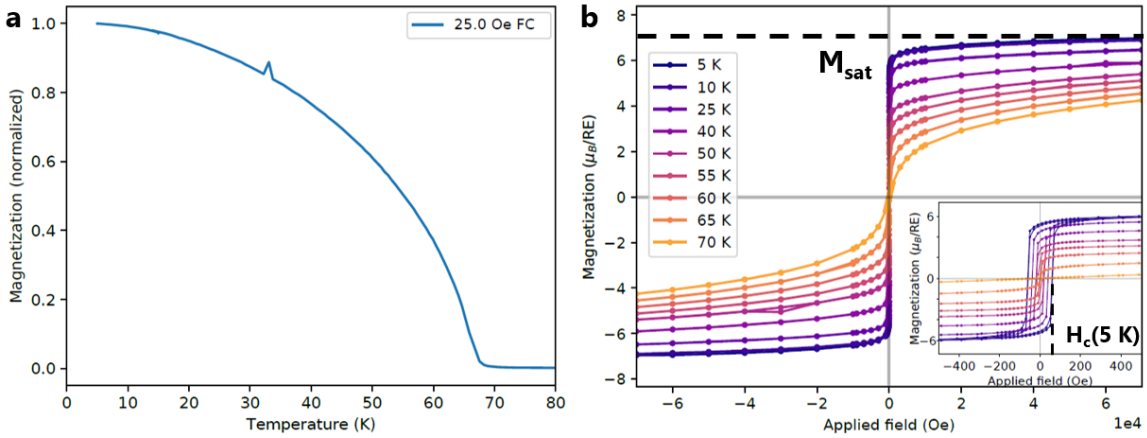

Figure 5.8: (a) Temperature-dependent field-cooled normalised magnetisation of a ~100 nm GdN capped with ~100 nm Sm, using an applied field of 25 Oe. (b) Field-dependent magnetisation of the same sample at different temperatures. The inset in (b) is a zoom of the hysteresis close to zero field.

of H~60 Oe at $T = 5$ K (see inset for magnification near zero field).

The measured $M(T)$ and $M(H)$ are in very good agreement with previous magnetic measurements of GdN [55, 70], reporting a Curie temperature of $T_C = 70$ K, which agree with the onset of magnetisation in Fig. 5.8(a). The results indicate that the capping layer (1) prevents the oxidation of GdN and (2) does not interfere significantly with the magnetic behaviour of the underlying REN.

5.3 In-situ sublimation

The decapping method consists of heating the sample in UHV, in order to sublimate the Sm cap. In this section, the method is tested in-situ, i.e. immediately after growth to avoid potential reaction of the Sm with air. For ex-situ tests (after brief exposure to air), refer to section 5.4.

5.3.1 During sublimation

Fig. 5.9(a) shows the RHEED pattern at the start of the decapping procedure. The (5×5) surface reconstruction characteristic of Sm(0001) is evidenced by the presence of satellite streaks in agreement with previously on Sm/Nd heterostructures [282]. The plot shows the intensity profile extracted from the image where the streak spacing in indicated in pixel units. Figure

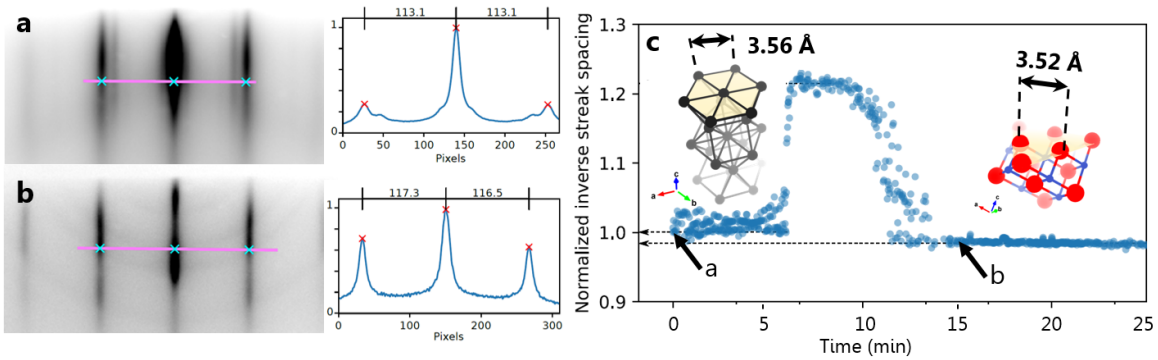

Figure 5.9: (a) RHEED pattern of the Sm(0001) along the $\langle 11\bar{2}0 \rangle$ direction before applied heat ($t = 0$ min). (b) RHEED pattern after 15 min of applied heat (T~650°C). The intensity profiles in (a) and (b) correspond to the purple lines in the RHEED images, the streak-spacing is indicated (c) Time evolution of the normalised inverse streak spacing during the decapping. The indicated arrows 'a' and 'b' correspond to the RHEED patterns in (a) and (b). Ball-and-stick models of dchp Sm [277] and fcc GdN [292] are indicated in (c), with the Sm(0001) and GdN(111) planes indicated in yellow. The in-plane lattice constants of the bulk materials are indicated.

5.9(b) shows the RHEED pattern after 15 min of heating. The surface reconstruction is no longer visible. As evidenced by the line in the right of the RHEED pattern, the streak spacing is slightly larger than before sublimation, suggesting a reduction of the lattice constant.

The reciprocal lattice observed in the RHEED images can be used to evaluate the lattice constant, inversely proportional to the streak spacing (for more details on RHEED, see chapter 2). The inverse of the streak spacing is then systematically calculated for all the images and normalised to the initial inverse streak spacing. The time evolution is shown in Fig. 5.9(c). During the first ~6 minutes of the heating, the surface lattice constant does not vary significantly. Strikingly, from t~6 min, the surface undergoes a phase transition for a few minutes during sublimation, as observed by the change in lattice spacing (~+22 % of the initial Sm lattice parameter). Sm top-surface is known to have a mixed valency where the first atomic layer is divalent while the bulk is trivalent [283, 293] and STM measurements of Sm(0001) have shown a 22% increase in the interatomic distance [294]. The reason for the transition here is not understood, yet the striking similarity with the observed mismatch of +22 % may indicate a temperature-induced valence transition. After t~10 minutes, the lattice constant drops by 2 % with respect to the initial in-plane lattice parameter of Sm(0001), corresponding to 3.49 Å if the considered initial value is that of the bulk Sm [295] lattice

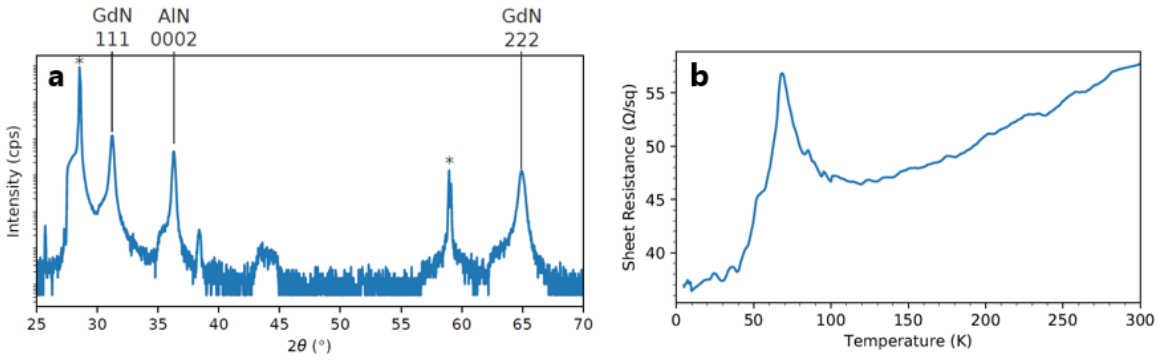

Figure 5.10: (a) XRD $\theta - 2\theta$ scan of the decapped Sm/GdN sample, recapped with a polycrystalline AlN layer. The Si peaks are indicated with $*$. (b) Temperature-dependent sheet resistance of the sample, measured with a 4-point probe method.

parameter.

The final value of the in-plane lattice parameter is in agreement with the expected atomic spacing of bulk GdN considering the (111) plane (3.52 Å [292], see ball-and-stick models of Sm and GdN in Fig. 5.9(c)), indicating removal of the Sm cap. The RHEED pattern however differs slightly from as-grown GdN, (shown in Fig. 5.4). Instead of the expected RHEED spots, the diffraction pattern is streaky, suggesting a smoother GdN surface [206]. The origin of the smoothing is unknown.

5.3.2 Post-sublimation characterisation

The sample was subsequently capped with a polycrystalline layer of AlN in order to allow ex-situ characterisation without degradation of the REN. AlN capping layers were previously reported to successfully passivate GdN [54, 58, 59].

XRD Fig. 5.10(a) shows the XRD $\theta - 2\theta$ pattern of the recapped sample. As expected, the peaks associated with the Si substrate (indicated with a $*$) and the epitaxial AlN buffer layer are still present. The Sm(0002) peak is no longer visible (compare with the XRD pattern of a Sm/GdN sample in Fig. 5.5(b)) indicating that most of the crystalline Sm was effectively sublimated. The peaks associated with GdN(111) are still present, and no difference with respect to as-grown Sm-capped GdN is observed. Importantly, no other crystalline phase is detected (e.g. recrystallised GdN).

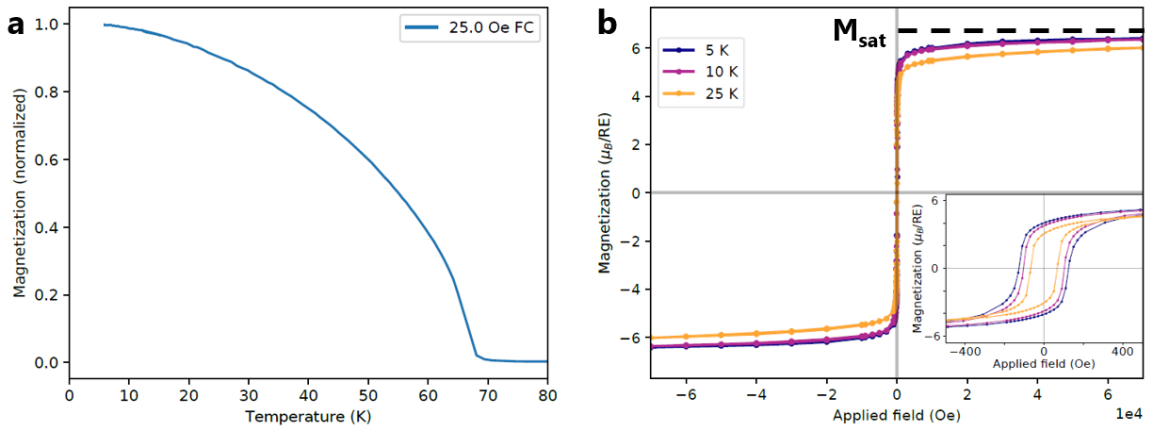

Figure 5.11: (a) Time-dependent magnetisation (field-cooled curve) of the decapped Sm/GdN sample, recapped with a polycrystalline AlN layer. (b) Field-dependent magnetisation of the sample at different temperatures. The inset is a magnification around the origin.

Electrical characterisation The transport properties of the recapped GdN were also tested using a 4-point probe method. The AlN capping layer has a high resistivity allowing for characterisation of the underlying GdN layer. Figure 5.10(b) shows the sheet resistance of the sample as a function of temperature. The anomaly at $T = 67$ K is typical of transport measurement of GdN layers due to the ferromagnetic transition and magnetic scattering [56, 70, 88].

Magnetic properties For further characterisation, magnetisation measurement of the decapped GdN (protected with the AlN layer) were also tested. Figure 5.11(a) displays the normalised temperature-dependent magnetisation of the sample. The magnetisation follows the same trend as the Sm-capped GdN sample shown in Fig. 5.8(a). The Curie temperature, estimated from the temperature-dependent magnetisation, is $T_C = 67$ K, in agreement with reported GdN [55, 56, 70, 88] and with the above electrical characterisation in Fig. 5.10(b). Figure 5.11(b) shows the field-dependent magnetisation of the sample. The dependence is characteristic of a ferromagnetic behaviour where the magnetisation saturates $M_{\text{sat}} \sim 6.5 \mu_B/\text{Gd}^{3+}$. The coercive field at $T = 5$ K is ~130 Oe. These properties are comparable to those obtained from the Sm-capped GdN shown in Fig. 5.8.

Discussion The post-sublimation measurements on the decapped GdN sample (passivated with AlN) suggest that the Sm cap is removable. The XRD, resistivity and magnetisation

measurements are in very good agreement with reported previously GdN studies, indicating that (1) most of the Sm cap has effectively been sublimated (or a knee at T~106 K would be observed, as previously shown in Fig. 5.7) and (2) the GdN layer was not significantly impacted by the decapping procedure. It is worth emphasizing that these techniques are mostly sensitive to the bulk properties.

5.4 Ex-situ sublimation

The in-situ decapping appears to be effective at removing the entire Sm capping layer, and is not detrimental for the underlying GdN as shown through RHEED, XRD, electrical and magnetic measurements. However it is essential to study the sublimation of the Sm cap after exposure to air in order to test the effectiveness of the cap desorption after transport in ambient conditions. The tested sample (A372) is now a ~100 nm-thick Sm grown on ~100 nm-thick GdN (grown under nominally identical conditions as previously), and exposed to air for a few minutes. The sample is cleaved in air in six pieces and the sublimation systematically studied. The cleaved pieces are loaded individually in the UHV chamber after exposure to air, then sublimated separately at a different temperature for a constant time of 30 mins. After each thermal treatment, the samples are characterised by RHEED and subsequently taken out of the UHV chamber for XRD measurement.

5.4.1 RHEED

Fig. 5.12(a) shows the RHEED pattern of A372 after exposure to air and degassed for about 30 minutes at T~200°C to remove of the main physisorbed contaminants (e.g. water). The diffraction pattern appears extremely diffuse, as opposed to its streaky counterpart, obtained immediately after growth (see Fig. 5.5(a)). The diffuse RHEED pattern indicates significant degradation of the top surface, likely through oxidation of the Sm surface. The lack of sharpness in the diffraction pattern indicates the amorphous nature of the oxide [206]. Air-exposed samples are then systematically loaded in the UHV chamber, heated to varying temperatures for 30 mins, during which RHEED patterns are recorded along the direction corresponding to the initial Sm $\langle 11\bar{2}0 \rangle$.

At moderate temperatures, the Sm capping layer is not expected to be entirely sublimated

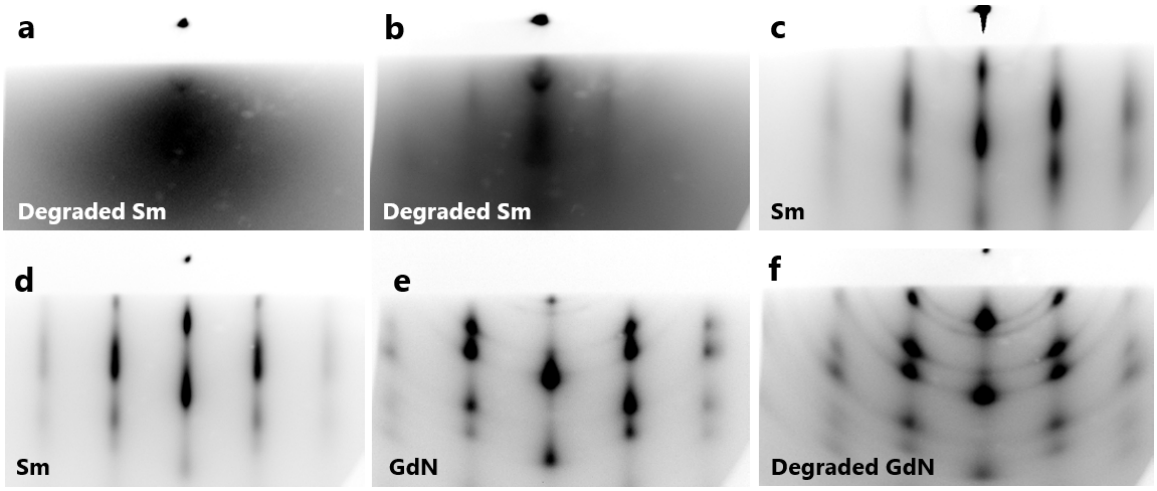

Figure 5.12: RHEED patterns of A372 (Sm/GdN) after exposure to air. (a) Untreated, (b) T~400°C, (c) T~500°C, (d) T~600°C, (e) T~620°C, (f) T~650°C. In (b-f) the samples were heated for 30 mins at the indicated temperature.

over a period of 30 mins (see estimated desorption rate in Fig. 5.2). However the Sm diffraction pattern is partially recovered as shown in Fig. 5.12(b) for a temperature of ~400°C. This is an indication that some of the oxide layer has been thermally desorbed, however the surface is rougher than the pristine, as-grown Sm.

At higher temperatures (T~500 – 600°C) a streaky RHEED pattern is visible as shown in Fig. 5.12(c,d), indicating that the Sm layer is mostly recovered. The pattern is no longer diffuse and comparable to a clean Sm(0001) surface, as previously shown in Fig. 5.5. However the satellite streaks that were visible on the pristine Sm(0001) surface corresponding to a (5×5) reconstruction are no longer observed for a reason that is not understood.

At even higher temperatures (T~620 – 650°C, see Fig. 5.12(e) and (f)), the diffraction spots are in good agreement with the as-grown GdN(111) surface (see Fig. 5.4) which is a good indication of the Sm sublimation. However polycrystalline arcs appear in the RHEED patterns in particular for T~650°C, indicating a substantial degradation of the GdN surface. The RHEED pattern shown in Fig. 5.12(f) and in Fig. 5.9(c) both correspond to the same temperature treatment, to the exception that previously the sample was not in contact with air. This is a clear indication that the degradation of the top surface of Sm caused by the exposure to air (attributed to oxidation) has an impact on the quality of the GdN surface upon sublimation of the Sm layer. Further investigation is required to address this degradation issue.

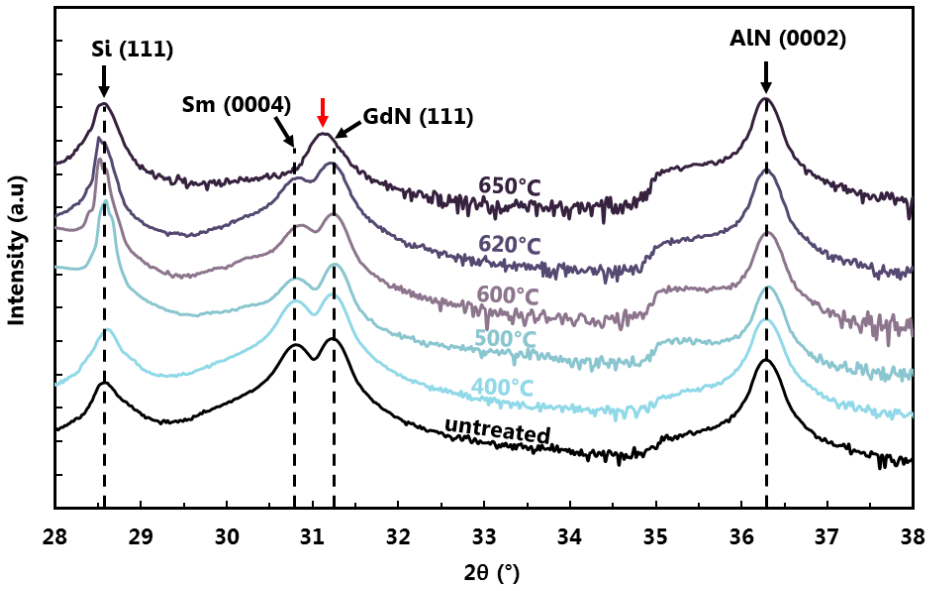

Figure 5.13: XRD $\theta - 2\theta$ patterns of air-exposed Sm-capped GdN samples with varying heat treatments, indicated above each curve. The known Bragg peaks are identified. An unexpected phase is observed for 650° (red arrow). The curves are displayed on a log scale and offset for clarity.

5.4.2 XRD

The samples were removed from the UHV chamber with no further capping layer deposition, and XRD patterns were recorded shortly (~1 h after exposure to air). Figure 5.13(a) shows the XRD $\theta - 2\theta$ patterns of A372 for each thermal treatment. The untreated sample (black) serves as a reference. All samples show clear Si(111) and AlN(0002) reflections from the substrate, in agreement with the as-grown Sm/GdN samples, shown in Fig. 5.5(b).

Up to 620°C No significant difference can be observed in the sample composition for all temperature treatments below T~620°C (see Fig. 5.13(a)). The Sm(0004) reflection is always present ($2\theta = 30.82°$). Using Bragg law (eq. 2.7), one finds $d_{(0004)} = 2.90$ Å, in very good agreement with the literature (for dchp Sm bulk the value is $d_{(0004)} = 2.905$ Å [277]). GdN(111) remains unchanged at $2\theta = 31.23°$, i.e. $d_{(111)} = 2.86$ Å, close to bulk GdN (2.88 Å [292]).

Above 620°C The XRD pattern after the 620°C-treatment evidences the presence of Sm, which is in disagreement with the RHEED in Fig. 5.12(e) where a GdN-like pattern was evidenced. After $T = 650$°C, no clear GdN(111) or Sm(0004) reflections are visible but rather

appear 'merged', forming an unexpected phase. The measured angle is $2\theta = 31.13°$, i.e. $d_{(hkl)} = 2.87$ Å.

Discussion For any treatment at a temperature below $T \leq 620°C$, the samples show a strong peak corresponding to Sm(0004). For the highest considered sublimation temperature ($T = 650°C$) an unexpected phase is observed instead of GdN and Sm. The exact nature of this crystalline phase is unknown. Because the Bragg angle is between that of the expected GdN and Sm, alloy $Gd_{1-x}Sm_xN_y$ could be hypothesised. The decapping experiments of the air-exposed Sm/GdN samples are not entirely successful, and the following morphological and compositional study focuses on further characterisation of the Sm/GdN samples decapped via thermal desorption.

5.4.3 AFM

A systematic ex-situ non-contact AFM study was performed in UHV at UC, in order to further understand the sublimation of Sm after exposure to air. A similar sample (A314) was used here (~100 nm Sm cap on a ~100 nm GdN). The sample was exposed to air for a few hours during transport and cleaved in several pieces for this study. Each piece is heated up for an hour at the following temperatures 50°C (treated as a reference), 200°C, 300°C, 400°C and 500°C. The results of the study are shown in Fig. 5.14. The temperatures are increasing with the row number, and the magnification are column-wise consistent (Widths are 2.5 μm, 500 nm and 250 nm from left to right). The vertical scales of the AFM images are chosen to show the details observed on the terraces, and are column-wise consistent as well. The pits were chosen to be excluded from the colour scale, thus appearing black (see colour scales next to the images).

Baseline and low temperatures Fig. 5.14(a) shows a large-scale AFM image of the sample after initial degassing at 50°C for an hour (to get rid of the main adsorbed contaminants). The morphology is comparable to that of other Sm/GdN samples shown in Fig. 5.6, where the surface is characterised with flat terraces, scattered with pits or measured depth up to 30 nm (see line profile extracted from the white line in Fig. 5.14(b)). Occasionally, ~15 nm-high particulates with widths up to ~500 nm (e.g. on the left-hand side and bottom of Fig.

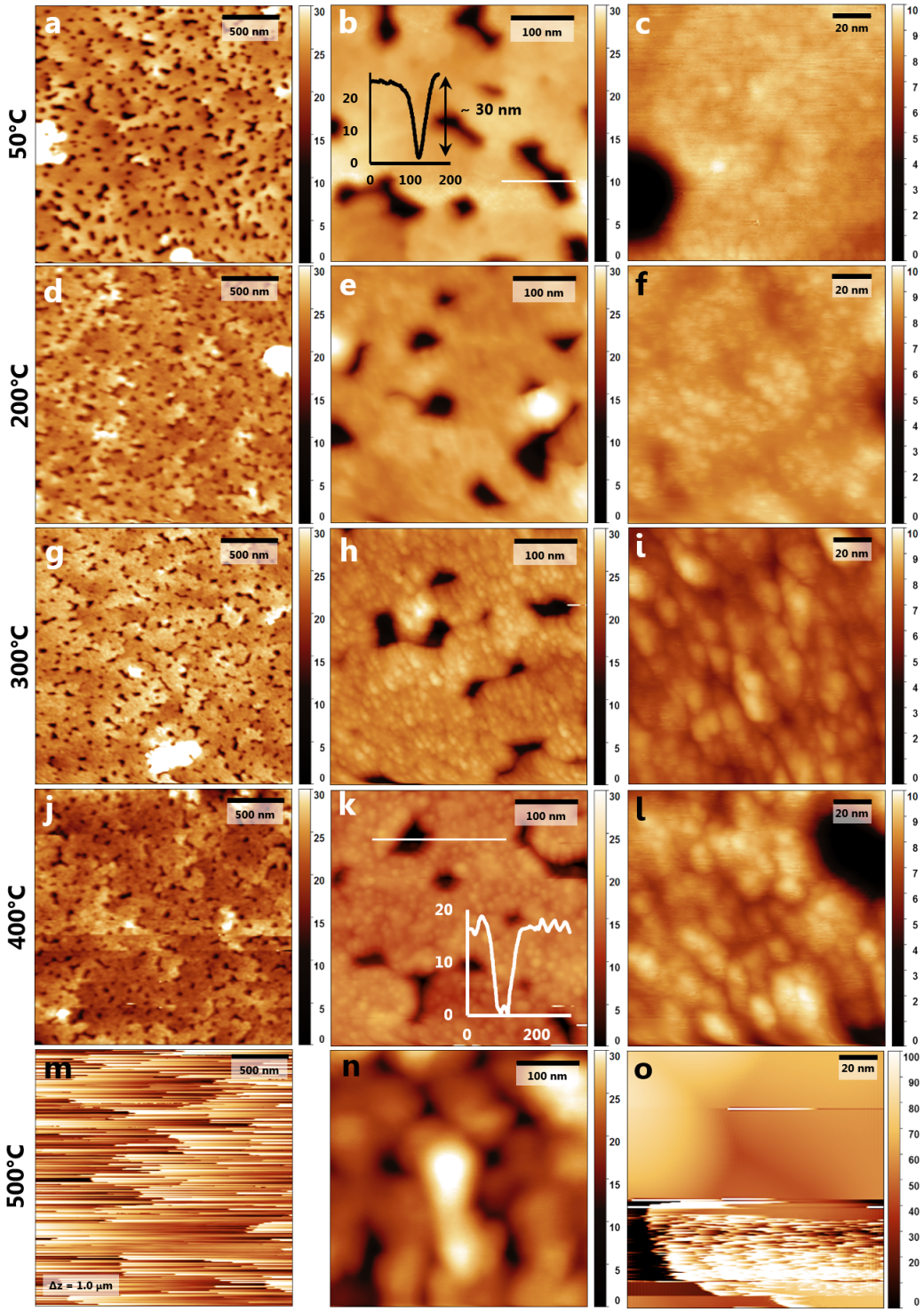

Figure 5.14: Non-contact AFM images of A314 (Sm/GdN) after heat treatment in UHV conditions: (a-c) 50°C, (d-f) 200°C, (g-i) 300°C, (j-l) 400°C, (m-o) 500°C. All samples are heated for an hour and subsequently imaged at room temperature in the same chamber. The image sizes are column-wise consistent (2.5 μm, 500 nm and 150 nm from left to right). The vertical scales are kept constant for a given scale and enhance the contrast, to the exception of (m-o). The line profiles in (b) and (k) are obtained from the white lines. All scales are in nm.

5.14(a)) are present on the surface, at an estimated density of 10^8 cm^{-2}. These features, clearly distinct from the rest of the cap morphology, are hypothesised as being Sm_xO_y grains. The roughness measured on the large resolution image is RMSR ~3 nm. Higher-resolution images (Fig. 5.14(b) and (c)) show near atomically flat terraces (RMSR ~0.3 nm) and are evidences ~10 nm wide features with heights smaller than 1 nm. Figure 5.14(d-f) shows the surface morphology of the sample after a $T = 200$°C treatment. There is no evidence of a structural change in comparison with the baseline in Fig. 5.14(a-c). The pits (density, width and depth) measured from large scale images, as well as the terrace roughness and feature size observed on higher resolution images are similar.

Intermediate temperatures Fig. 5.14(g-i) show AFM images of A314 obtained after heating for 1 hour at $T = 300$°C. No obvious change is observed at the large scale. However, higher magnification images in Fig. 5.14(h,i) indicate the presence of significantly rougher terraces (RMSR ~1 nm, i.e. three-fold increase from the untreated sample), as the surface appears less regular and flat. The heat-induced features on the terraces can be as high as 3 nm and have a characteristic width of ~30 nm. The measured pit depth, density and width remain unchanged with respect to the baseline. The AFM images in Fig. 5.14(j-l) are obtained after a $T = 400$°C treatment and there are non substantial differences with Fig. 5.14(g-i).

High temperatures Fig. 5.14(m-o) are AFM images obtained after a $T = 500$°C treatment. This time, the imaging is virtually impossible as the tip-sample junction becomes very rapidly unstable. Despite lengthy experimental efforts (attempts on various areas of the sample, trials with different tips, scanning speed and set-points), the obtained images at large scale (as shown in Fig. 5.14(m)) appear consistently streaked along the fast scanning direction. Rarely, it is possible to find areas as large as $\sim 500 \times 500$ nm^2 which can be imaged in streak-free conditions (Fig. 5.14(n)), however in this case the AFM image always appears significantly blurred, in turn making higher-resolution imaging impossible (Fig. 5.14(o)). The reason for blurred appearance is thought to arise from contamination of the AFM tip apex. It is hypothesised that at elevated temperatures, loosely-bound particulates are present on the surface. Higher temperatures ($T = 600$°C and 650°C) have been tried, but it was not possible to obtain better quality images than these in Fig. 5.14.

5.4.4 SEM

The AFM study did not allow to understand the sample morphology for thermal treatments above $T = 500°C$. For this reason the samples (heated for 1 h) were investigated with scanning electron microscopy (SEM).

GdN sample First, the reference sample (A517) consisting of an uncapped GdN sample is imaged via SEM, shown in Fig. 5.15(a). The GdN surface was exposed to air (which is presumed to decompose rapidly to Gd_2O_3 [67]). The sample serves as a test morphology for the decapping experiments; in case of ideal sublimation of the cap, the post-sublimation sample morphology after exposure to air should be very similar. Overall the surface of air-exposed GdN is nearly featureless, with the exception of very large blisters (the blister present in the image has a diameter of ~2 μm) that emerge upon electron beam focusing. This is typical of insulating materials [296].

Untreated and intermediate temperatures Fig. 5.15(b) shows an SEM image of untreated A314. The image agrees with the AFM image shown in Fig. 5.14(a). The inset in Fig. 5.15(b) shows A314 on a large scale (×5000) after a heating to $T = 300°C$ for an hour in UHV conditions. While the presence of the trenches/pits is still visible, the morphology of the sample is significantly affected by the heat treatment. The surface is indeed strongly bulged in several places, with a typical blister diameter of a few μm. Interestingly, the large-scale AFM image corresponding to the same heat-treatment in Fig. 5.14(g) does not show equivalent large-scale morphology. The bulging is therefore attributed to the reaction of the sublimated sample to air or due to the SEM imaging. Figure 5.15(d) shows a different sample, after heating to $T = 400°C$. The morphology is significantly different from the untreated and 300°C-treated samples. The pits are still visible (darker zones), except this time correspond to the space between clearer particulates (light grey) that are nearly broken down and separated. The large-scale AFM image in Fig. 5.14(j) corresponding to the same heat-treatment did not show significant morphological differences with the untreated sample in Fig. 5.14(a), which is an indication that the air transport after sublimation is responsible for the most part of the altered morphology shown in the SEM images.

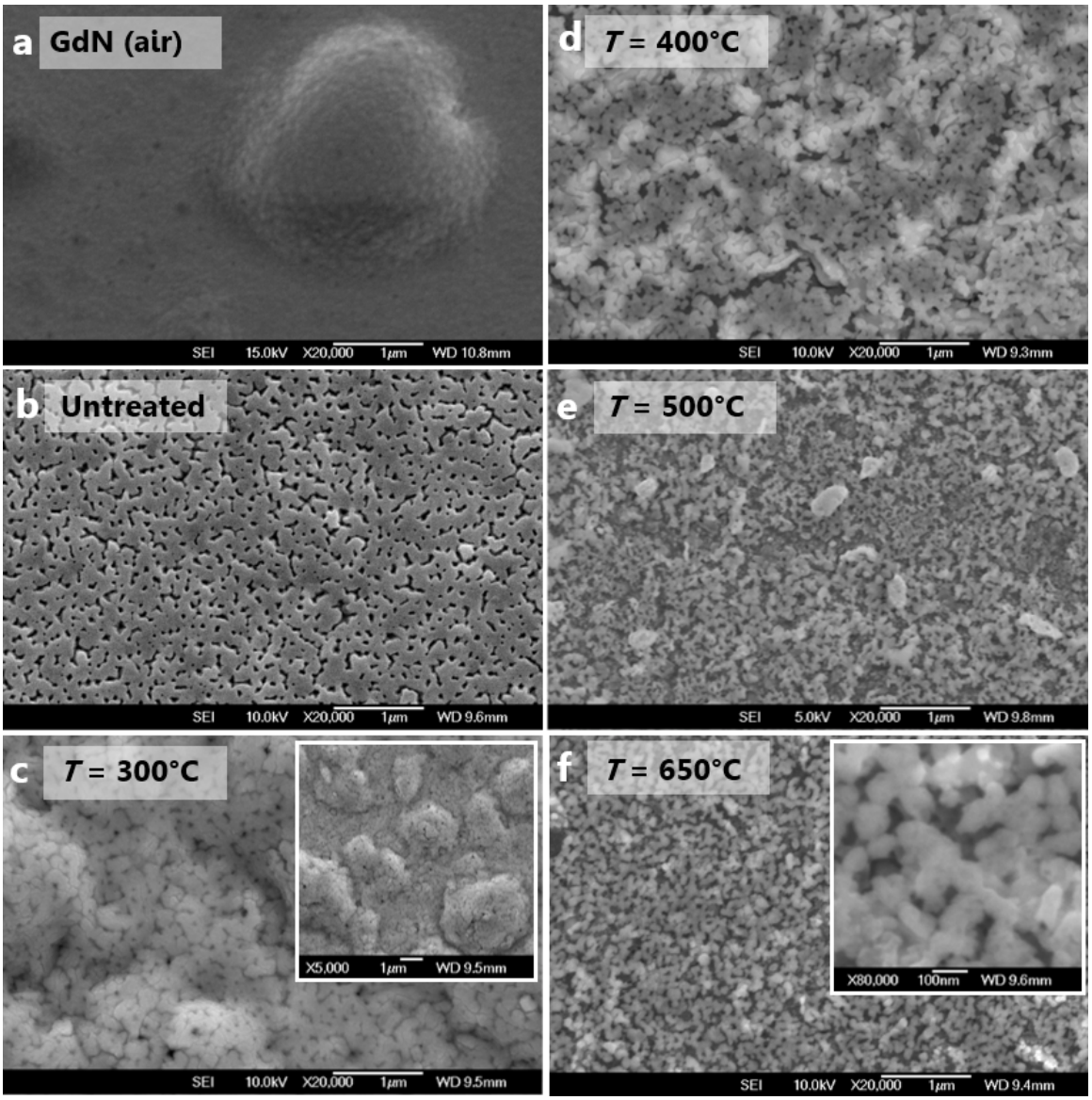

Figure 5.15: SEM images (E = 10 keV) of untreated GdN (a) and air-exposed A314 (a-f) after (b) no treatment, (c) T = 300°C, (d) T = 400°C, (e) T = 500°C and (f) T = 650°C. Each sample was heated for one hour in UHV (with the exception of the uncapped GdN and the untreated sample). All samples were exposed to air between treatment and SEM imaging, leading to possible oxidation of the GdN layer. All magnifications are kept identical (×20000), to the exception of the insets in (c) (×5000) and (f) (×80000).

High temperatures Fig. 5.15(d) shows an SEM image of a piece of A314 previously heated to $T = 500°C$. Again, the morphology differs from lower temperature treatments. This time, particulates (with diameters varying from ~100 nm to about ~1 μm) seem completely separated, or clustered together, forming a discontinuous film. Heating to a higher temperature ($T = 650°$C) yields similar morphologies, as shown in Fig. 5.15(e). The inset in Fig. 5.15(e) shows a higher resolution image of the same zone, clearly resolving the particulates (light grey).

5.4.5 EDS

Energy dispersive X-ray spectroscopy (EDS) was undertaken to evaluate the elemental composition of the sample before and after sublimation. As discussed in chapter 2, the penetration depth of the X-rays is in the order of a few hundreds of nanometres, so the technique is likely to be sensitive to the several layers of the heterostructure. EDS spectra are obtained with $E = 15$ keV electrons. See chapter 2 for more details on EDS. The inset in Fig. 5.16(a) shows the entire EDS spectra of the untreated sample (black), after heating to $T = 650°$C (red) and of a pure GdN sample A517 (blue). Two groups of peaks are present, in the $0-2$ keV range and in the $5-8$ keV range.

Low-energy EDS First the EDS spectrum of the untreated sample (black line) in the low-energy range is considered in Fig. 5.16(a). The $\mathrm{Si}_{\mathrm{K}\alpha}$ peak dominates the EDS spectrum, which is a confirmation that the penetration depth is at least of the order of ~300 nm. C, N, O and Al are also visible, although it is known that the low sensitivity of the technique to light elements prohibits quantitative analysis [202]. Al and N are expected to be present in the sample due to the presence of the AlN buffer layer. The detection of C and O is also not surprising given that the samples have been transported in air and the adsorbed contaminants are most likely light molecules e.g. H_2O, CO_2, O_2, etc. Two intense Sm peaks ($\mathrm{Sm}_{\mathrm{M}\zeta}$ and $\mathrm{Sm}_{\mathrm{M}\alpha}$) and one weaker ($\mathrm{Sm}_{\mathrm{M}\gamma}$) peaks are visible. The Gd signal is barely visible. After sublimation at $T = 650°$C (red line), the Sm peaks are strongly attenuated. The Gd peaks ($\mathrm{Gd}_{\mathrm{M}\zeta}$ and $\mathrm{Gd}_{\mathrm{M}\gamma}$) are now visible. The spectrum of A517 (air-exposed GdN) obtained under the same conditions is shown in blue and serves as a reference spectrum. The compar-

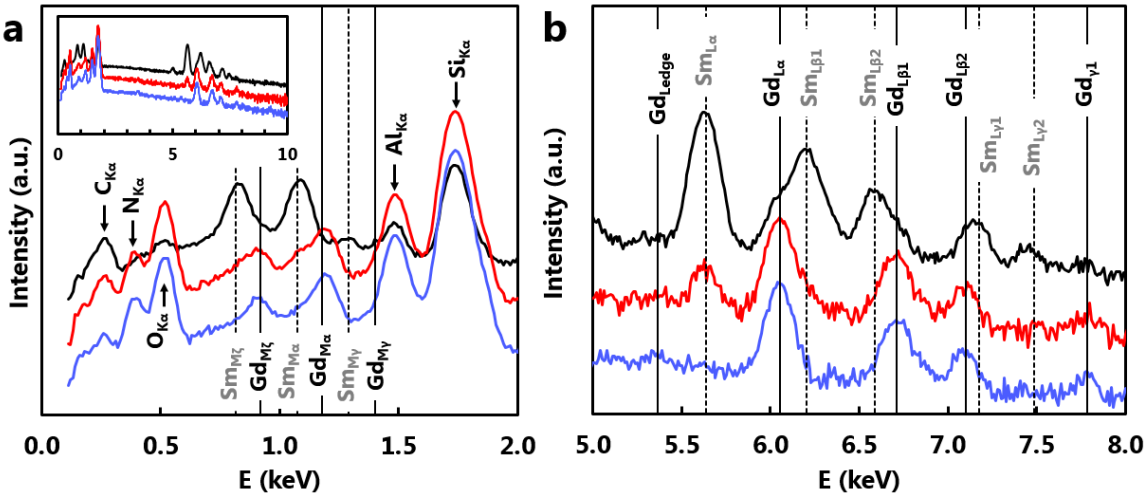

Figure 5.16: EDS spectra (E = 15 keV) of air-exposed A314, untreated (black line) and after T = 650°C (red line). The intensities are in log-scale, and the curves are offset for clarity. A spectrum obtained on air-exposed pure GdN sample (A517) is also displayed for comparison (blue line). The two panels are (a) 0 to 2 keV, (b) 5 to 8 keV. Inset in (a) shows the entire spectra. The energy levels of all the present elements are indicated. Sm and Gd X-ray energies [297] are highlighted respectively with dashed and solid vertical lines.

ison with the uncapped GdN sample (blue) permits to evaluate the cap sublimation on the treated sample (only T = 650°C is shown). The weak shoulder at the $\mathrm{Sm}_{\mathrm{M}\alpha}$ in the sublimated sample (red curve) is an indication that there is a detectable level of Sm after the decapping procedure, attributed to the presence of $\mathrm{Sm}_x\mathrm{O}_y$ particulates present on the surface.

High-energy EDS Fig. 5.16(b) shows the same spectra shown in Fig. 5.16(a) displayed over a higher-energy range (5 – 8 keV). Only Gd and Sm peaks are present in this observed range and do not overlap significantly, which simplifies the analysis. For the untreated sample (black line), both $\mathrm{Sm}_{\mathrm{L}\alpha}$ and $\mathrm{Gd}_{\mathrm{L}\alpha}$ peaks are observed. The EDS spectrum of A517 (blue) clearly resolves four Gd peaks, clearly distinct from the Sm peaks. The EDS spectrum obtained on the 650°C sublimated sample (red) shows a drastically reduced $\mathrm{Sm}_{\mathrm{L}\alpha}$ intensity comparatively to the untreated sample (relative reduction of ~95%), indicating incomplete Sm removal. The rest is attributed to the presence of $\mathrm{Sm}_x\mathrm{O}_y$ particulates that are remaining on the surface after heating to high-temperature (T > 500°C). Interestingly, the Gd peaks intensities are very similar to the GdN sample which indicates that the GdN layer did not sublimate at this temperature, in agreement with the GdN stability study shown in Fig. 5.4.

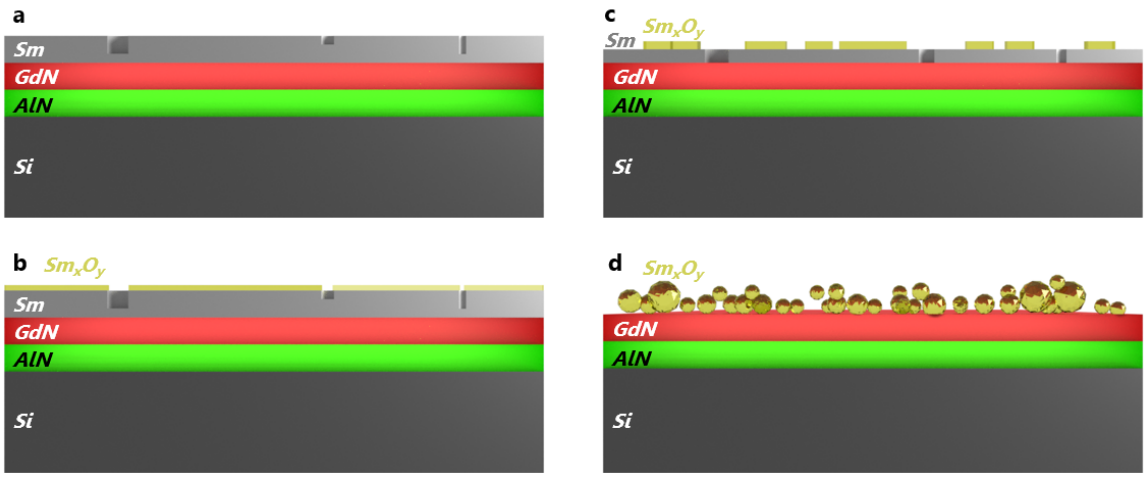

Figure 5.17: Schematic cross-section model of the air-exposed Sm/GdN heterostructures after sublimation. (a) After growth in UHV, (b) during exposure to ambient air, (c) after partial sublimation, (d) after total sublimation. The discontinuities in the Sm layer represent the pits or trenches.

5.5 Summary and discussion

The recovery of the GdN(111) surface could be achieved via sublimation on the Sm-capped samples that were not initially exposed to air. The XRD, RHEED, electric and magnetic measurements on a $T = 650°C$-treated sample are a strong evidence for the entire removal of the cap. The data also suggests that the GdN bulk properties were not impacted significantly by the procedure.

To verify whether a successful decapping procedure could be achieved in a different UHV chamber, the heating treatment was tested after transportation of the samples in atmosphere. The Sm surface after exposure to air was significantly degraded by the presence of a contamination layer (likely Sm_xO_y) as indicated by RHEED. Heating to $T = 650°C$ could not yield a clean GdN surface. Instead, RHEED and XRD indicated a degradation of the GdN surface, and SEM images evidenced the presence of a discontinuous film covering the whole sample. The particulates present on the surface were detrimental for the tip stability and AFM could not image correctly the surface. EDS measurements also detected the presence of Sm after heating to $T = 650°C$.

Heating treatments were also tested below $T = 650°C$, however XRD data evidenced metallic Sm for all temperatures considered. AFM was however possible below $T = 500°C$

and a roughening of the flat terraces was observed with increasing temperatures. It seems clear that the oxide present on the Sm (reported fusion temperature of $T_f = 2296°C$ [272]) is refractory and can not be desorbed at the tested temperatures but rather forms particulates.

It is clear that it is the exposure of the Sm/GdN sample to air that prevents successful decapping. Figure 5.17 shows a cartoon model of the layers heated to elevated temperatures. Figure 5.17(a) is a cross-section of the heterostructure in UHV immediately after growth. The Sm layer is smooth and pits/trenches are present. In Fig. 5.17(b), the heterostructure is exposed to air and the oxide Sm_xO_y layer is formed on the top-surface of the cap. During decapping in Fig. 5.17(c), the top-surface roughens and the metallic Sm is being sublimated. In Fig. 5.17(d), the entire Sm cap is evaporated, however the Sm_xO_y prevents the surface characterisation of GdN. The oxidation of the Sm layer has to be overcome in order to achieve a successful decapping.

Chapter 6

Capping layer removal with sputtering

The recovery of the GdN surface after heating is prevented by the presence of debris attributed to refractory Sm_xO_y, initially formed on the Sm surface during exposure to air. In chapter 5 it was shown that the oxide could not be thermally desorbed successfully for the temperatures considered. A refinement of the procedure is discussed in this chapter. The Sm surface is first sputtered with argon ions to remove the oxide layer before subsequent thermal desorption of the metallic Sm cap.

6.1 Principle

Sputtering is a technique used to remove material including oxides and other impurities from the surface of metals, in general as part of repeated sputtering/annealing cycles [298]. Argon ion (Ar^+) bombardment has been used on polycrystalline Sm for surface cleaning [299], however the sputtering parameters (beam energy E, current density J and time Δt) were not specified. In a different work, other RE surfaces (Y, Gd, Pr and Ho single crystals) have been sputtered with an energy of $E = 2-4$ keV and current density of $5-20$ $\mu A \cdot cm^{-2}$ for cleaning purposes [300]. In the absence of previous literature, "an energy of approximately 1 keV, a current density of a few $\mu A/cm^2$ and ambient temperature" are generally recommended [298].

Ion bombardment may lead to ion implantation, which can drastically alter the electronical properties of the substrate material [301]. Such effects can be ignored here, since implanted Ar ions in the Sm will be released upon sublimation of the capping layer.

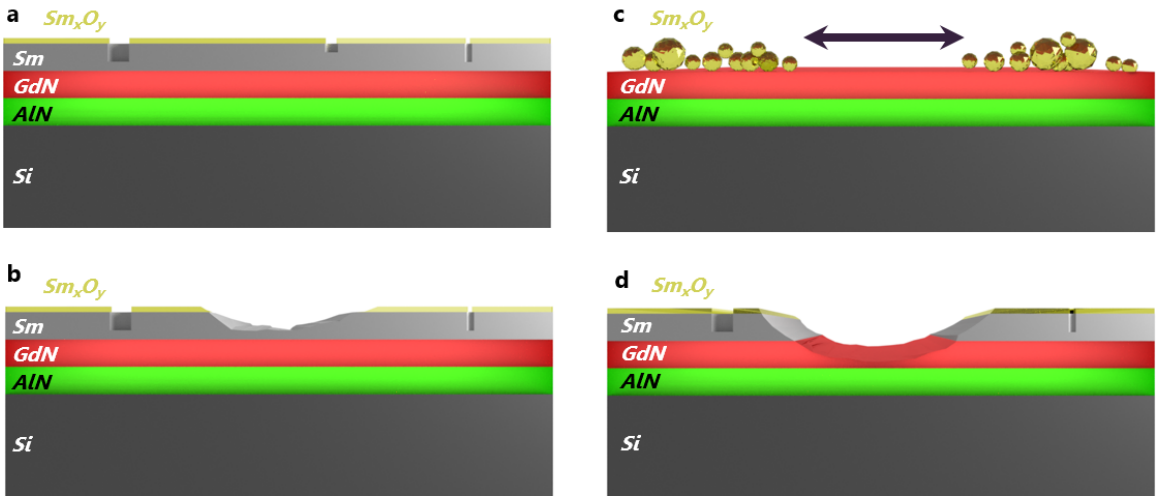

Figure 6.1: Schematic cross-section model of the air-exposed Sm/GdN heterostructure after sputtering. (a) Initial air-exposed sample, (b) after optimal sputtering, (c) optimal sputtering after sublimation of the Sm cap, where the zone indicated by the arrow is crust-free and (d) after excessive sputtering.

The aim here is to add a sputtering step in the decapping procedure to purify the Sm cap surface prior to its thermal desorption. This method has previously been applied to capping layer removal on Se-capped Bi_2Se_3 crystals [268]. Degradation of the Bi_2Se_3 after heating was observed and attributed to initial contamination of the Se surface. Including an ion bombardment step before thermal desorption successfully recovered the Bi_2Se_3 layer.

The principle of the improved decapping method is explained for Sm/GdN samples here. Figure 6.1(a) shows the sample's cross-section schematics after exposure to ambient air. The Sm_xO_y layer (thickness of a few nanometres [275]) is present at the surface. Figure 6.1(b) shows the same sample after optimal sputtering where Δz is smaller than the Sm thickness and larger than that of the oxide layer. Figure 6.1(c) shows the sputtered heterostructure after subsequent sublimation, where the debris-free area is indicated, enabling surface-sensitive measurements of GdN. Finally Fig. 6.1(d) represents the cross-section of a sample that is excessively sputtered, where Δz is larger than the Sm thickness, consequently sputtering partially the GdN surface. The aim of the ion bombardment is then to sputter approximately ~10 nm of the top surface of Sm including the Sm_xO_y layer, avoiding the two extreme scenarios of insufficient and excessive sputtering.

This chapter discusses the experimental results obtained on sputtered Sm-capped AlN

and Sm-capped GdN layers, as follows. First, an estimate of the optimum beam energy E and sputtering current I is obtained from the Sm/AlN samples using AFM, SEM and EDS in section 6.2. Secondly, section 6.3 is a time-dependent sputtering study on the Sm/GdN samples for a chosen beam energy and sputtering current. The focus here is on morphology and composition characterisation, both immediately after sputtering and after desorption of the cap. Finally, the results are critically discussed and summarised in section 6.5. Future possible work is also detailed.

6.2 Beam energy and current estimate

A sputtering rate of ~1 $\text{nm}\cdot\text{min}^{-1}$ would be a reasonable target in order to control the sputtered thickness (expected sputtering times of the order of ~10 min, which can later be fine-tuned if necessary). The sputtering rate can be estimated with equation 2.2 shown in chapter 2. Here, we use the bulk dhcp Sm atomic density of $\rho = 3.1 \times 10^{21}$ cm^{-3} [277]. Typical reported sputtering yields Y in the literature for E~1 keV are in the range $0.4 - 20$ ejected atoms per incident ion [182]. Using a current density of $J = 1$ $\mu\text{A}\cdot\text{cm}^{-2}$, one finds $0.48 < \frac{dz}{dt} < 24$ $\text{nm}\cdot\text{min}^{-1}$ (for $0.4 < Y < 20$). The target of $\frac{dz}{dt}$~1 $\text{nm}\cdot\text{min}^{-1}$ is contained in this estimate bracket, $J = 1$ $\mu\text{A}\cdot\text{cm}^{-2}$ is then a good starting value. The estimated sputtered area is of the order of ~1 cm^2 (for more details on the sputtering principle and set-up refer to chapter 2)

6.2.1 Initial sputtering

Three cleaved pieces of the same Sm/AlN sample (R024) were sputtered at various energies E and currents I at a constant Ar pressure (P~1.1×10^{-5} mbar), incident angle ($\theta = 45°$) and sputtering time ($\Delta t_{Ar^+} = 15$ min). After equilibration of the Ar pressure, the energy was raised to the desired value (the measured current I could not be independently controlled). After bombardment, the sample morphology was characterised by AFM in non-contact mode (in UHV conditions) and SEM (after exposure to air for ~10 min). Elemental composition of the samples was evaluated via EDS.

Untreated Figure 6.2(a) shows the AFM image of the untreated sample. The RMSR, obtained from the AFM image is 19 nm. The SEM image of the same sample, shown in the inset of Fig. 6.2(a) is in agreement with the AFM image. The EDS spectrum is shown in Fig. 6.3. The Si peak is strongly visible, and Al is present from the AlN buffer layer. Distinct Sm levels ($Sm_{M\zeta}$, $Sm_{M\alpha}$ and $Sm_{M\gamma}$) are visible.

1 keV The energy was set to $E = 1.0$ keV. The measured current was then $I = 4.5$ μA. The AFM image obtained after sputtering is shown in Fig. 6.2(b) and the inset shows the SEM image of the sample. No difference with the untreated sample (Fig. 6.2(a)) is evidenced. The RMSR is unchanged (19 nm). The EDS spectrum of the sample is shown in Fig. 6.3 and does not differ to that of the untreated sample, indicating that the sputtering procedure did not remove a substantial amount of Sm, i.e. the sputtering rate in these conditions is too small ($\frac{dz}{dt} \ll 1$ nm$\cdot$min^{-1})

3 keV The beam energy was set to $E = 3.2$ keV, leading to a larger sputtering current of $I = 15.1$ μA. The AFM image recorded after sputtering is shown in Fig. 6.2(c). Clearly, the surface morphology is now significantly modified, and the RMSR is much larger (= 60 nm, as opposed to 19 nm for the untreated sample). Increased roughness is commonly observed on sputtered surfaces [182, 302, 303] but largely depends on the incident ion species, its energy, angle of incidence θ and on the target structure [304]. The inset shows an SEM image obtained on the same sample. The morphology is characterised with a certain directionality, as if comprised of structured 'scales' where flat, tilted areas are stacked next to one another. The streaks in AFM image are artefacts caused by unstable tip-sample junction, likely at the sharp edges of the tilted areas. This uneven morphology is typical of sputtered layers with incident ions angle away from the normal incidence, where contaminants with a lower sputter yield are present [182]. The impurities shadowing the incident ions are almost certainly remaining Sm_xO_y particulates. The EDS spectrum after the 3.2 keV treatment is comparable to the previous spectra, with the exception of a significantly reduced intensity ($Si_{K\alpha}$ counts ratio is 1:24 with respect to the untreated sample) leading to a smaller signal-to-noise ratio (SNR). Previous work [305] attributed the intensity decrease in rougher surfaces measured by EDS to surface features shadowing the emitted photons, especially for the low-energy X-rays.

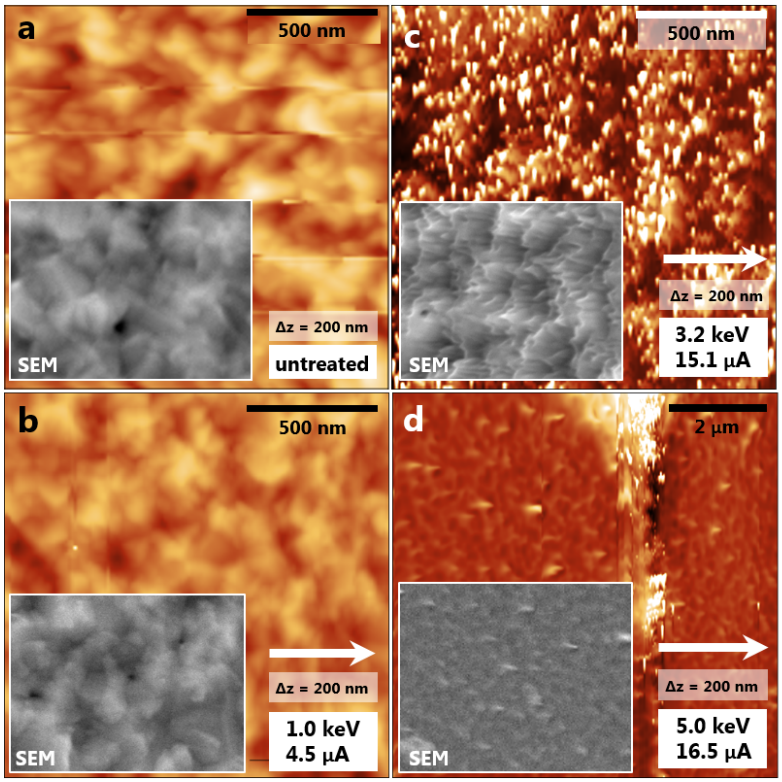

Figure 6.2: Morphology of sputtered R024. AFM images of (a) Untreated sample, (b) after sputtering with 1.0 keV, $I = 4.5$ μA, (c) after sputtering with 3.2 keV, $I = 15.1$ μA and (d) after sputtering with 5.0 keV, $I = 16.5$ μA. The insets are SEM images on the same lateral scale ($V = 15$ kV). The white arrows indicate the argon bombardment direction. The AFM z-scales are indicated.

5 keV Lastly, a higher energy was tested. On setting the value of $E = 5.0$ keV, the current rose to $I = 16.5$ μA. Figure 6.2(d) shows the AFM after $\Delta t_{Ar^+} = 15$ min of bombardment. The morphology is different from the untreated and previous ($E = 3.2$ keV) treatment. The surface is significantly less rough this time (RMSR is 9 nm). The surface shows the presence of cones (up to ~100 nm high) observed previously on various materials including Mo-Cu [306] and GaN [182]. The cone formation is attributed to the presence of impurities locally increasing the bond energy [182] and therefore decreasing the sputtering yield Y. The SEM image (in the inset of Fig. 6.2(d)) is in agreement with the AFM image. Neither Sm nor Al are visible via EDS (see Fig. 6.3) indicating that the sputtering rate is too large and rids the entire Sm cap as well as the AlN buffer layer for a bombardment of 15 minutes ($\Delta z > 200$ nm). The layer imaged by SEM and AFM is therefore the Si wafer, where sputtering-induced cones have also been previously observed [307]. The sputtering rate obtained for $E = 5$ keV and

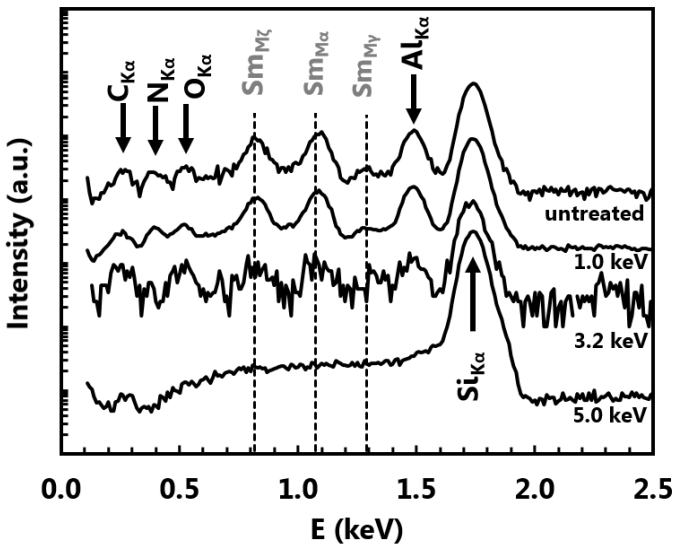

Figure 6.3: EDS spectra (V = 15 kV) of R024 (Sm/AlN) after various sputtering treatments for Δt_{Ar^+} = 15 min. The spectra are offset for clarity. All peaks are identified, dashed lines indicate the Sm X-ray emission lines.

I = 16.5 μA is too large ($\frac{dz}{dt} > 10$ nm$\cdot$min^{-1}).

6.2.2 Summary

The morphology and composition of R024 (Sm-capped AlN) was investigated via AFM, SEM and EDS and appeared to be strongly dependent on the beam energy E and current I for a constant exposure time of Δt_{Ar^+} = 15 min. It was found that sputtering using E = 1.0 keV (and I = 4.5 μA) was not enough to lead to a change in terms of morphology and composition, i.e. insufficient sputtering ($\Delta z < 10$ nm). The higher energy of E = 5.0 keV (I = 16.5 μA) led to removal of the entire Sm and AlN layers, and partially sputtered the Si wafer ($\Delta z >$ 200 nm) . The intermediate energy E = 3.2 keV (I = 15.1 μA) test led to a significant change in morphology while not sputtering the whole Sm layer. A value close to E = 3.2 keV and sputtering current near I = 15 μA was therefore used in all subsequent experiments.

6.3 Dependence on sputtering time

The ball-park estimates from the above study of sputtering on Sm/AlN samples suggested that an Ar^+ bombardment using an energy of about E~3.2 keV, a current near I~15 μA for about 15 minutes leads to acceptable sputtering, i.e. partial removal of the Sm layer. A study

Sample	I (μA)	Δt_{Ar^+} (min)	T_{sub} / Δt_{sub}
A519-0	-	-	-
A519-5	15.4 ± 0.5	5	-
A519-6	14.4 ± 0.5	10	-
A519-7	14.1 ± 0.6	20	-
A519-11	-	-	528°C / 14h
A519-8	14.6 ± 0.6	5	534°C / 15h
A519-12	15.1 ± 0.4	10	540°C / 15h
A519-10	14.7 ± 0.4	20	538°C / 18h
A520-0	-	-	-
A520-1	13.5 ± 0.5	5	-
A520-2	13.5 ± 0.5	10	-
A520-3	14.5 ± 0.5	20	-
A520-9	15.2 ± 0.4	30	-
A520-7	-	-	535°C / 13h
A520-4	14.8 ± 1.0	5	538°C / 15h
A520-5	14.9 ± 0.2	10	532°C / 16h
A520-6	15.4 ± 0.2	20	525°C / 19h
A520-8	13.4 ± 1.0	30	539°C / 14h

Table 6.1: Sample names, sputtering currents and times, as well as the sublimation parameters (when applicable). The samples A519 and A520 consist of a 100 nm-thick GdN capped respectively with 100 nm and 300 nm thick Sm. All samples are sputtered with a constant beam energy $E = 3.2$ keV.

was then conducted to determine the optimum bombardment time for removal of the Sm layer by sublimation. The samples were characterised after sputtering, both before and after thermal treatment via AFM, SEM and EDS.

The sputtering of Sm/GdN samples was first tested on thin Sm caps (~100 nm, A519) grown under identical experimental conditions than for the other Sm/GdN samples studied in chapter 5. In case of a very narrow time window for which the sputtering (1) removes an acceptable amount of Sm_xO_y and (2) does not removes the entire metallic Sm cap, it is desirable to try the sputtering/thermal desorption experiments on thicker Sm caps. Another sample was therefore grown under identical growth conditions but consisting of a thick Sm cap (~300 nm, A520) was then tested.

Table 6.1 gathers the sputter current (always near $I = 15.0$ μA) and duration for each sample studied. When applicable, the sublimation temperature and times are also indicated. This section is organised as follows. First in section 6.3.1 the thin Sm cap samples (A519) are sputtered for different times and their morphology and composition discussed. The ex-

periments are reproduced in 6.3.2 this time including the thermal desorption step in the procedure. Secondly, thick Sm samples (A520) are investigated using the same method, focusing on sputtered surfaces in section 6.3.3 and on thermally desorbed samples in section 6.3.4.

6.3.1 Sputtering of thin Sm layers (A519)

Untreated sample Figure 6.4(a) shows an SEM image of the untreated sample, and Fig. 6.4(b) and (c) show AFM images. The surface of A519 is characterised by flat terraces, occasionally pitted, in agreement with other samples previously shown in Fig. 5.6(b) in chapter 5. The RMSR is 1.5 nm (< 1.0 nm if excluding the pits). Larger features, sticking out of the terraces, occasionally present on the surface (on top of the SEM image) are attributed to Sm_xO_y. The AFM image displayed in Fig. 6.4(c) evidences atomic terraces with step heights of ~8 Å as evidenced by the line profile (see inset of Fig. 6.4(c)). It is estimated that each step corresponds to 3 atomic planes of the Sm dhcp structure (see the Sm dhcp model in Fig. 5.2). Figure 6.5(a) shows the EDS of the untreated A519, and is very similar to A314 (compare with Fig. 5.16). Both Sm and Gd levels are visible.

5 minutes sputtering Figure 6.4(d) shows an SEM image of the sample after sputtering for $\Delta t_{Ar^+} = 5$ min. The surface is no longer flat, but rather craters are present everywhere across the surface. Very similar sputter-induced craters have previously been observed on Ag(001) [302] and Pt(111) [303] for similar sputtering current densities, energy and times. A large feature (~50 nm high) is present on the surface (indicated with an asterisk). The presence of streaks near the object that it leads to tip instabilities. Figure 6.4(f) indicates a crater diameter of about ~100 nm and a depth of ~3 nm (see inset for profile obtained from the white arrow). The roughness (excluding pits) is about twice larger (RMSR = 2 nm). Small features (height of about 1 nm) are scattered across the surface. These features are identified as Sm structural defects or debris from sputtering (density $\sim 3 \times 10^8$ cm^2). The shape of the EDS spectrum of the sputtered sample, shown in Fig. 6.5(a), does not differ substantially from that of the untreated sample. A reduction of $Sm_{L\alpha}$ intensity (with respect to $Gd_{L\alpha}$) is however observed as shown in Fig. 6.5(b), indicating partial sputtering of the Sm cap.

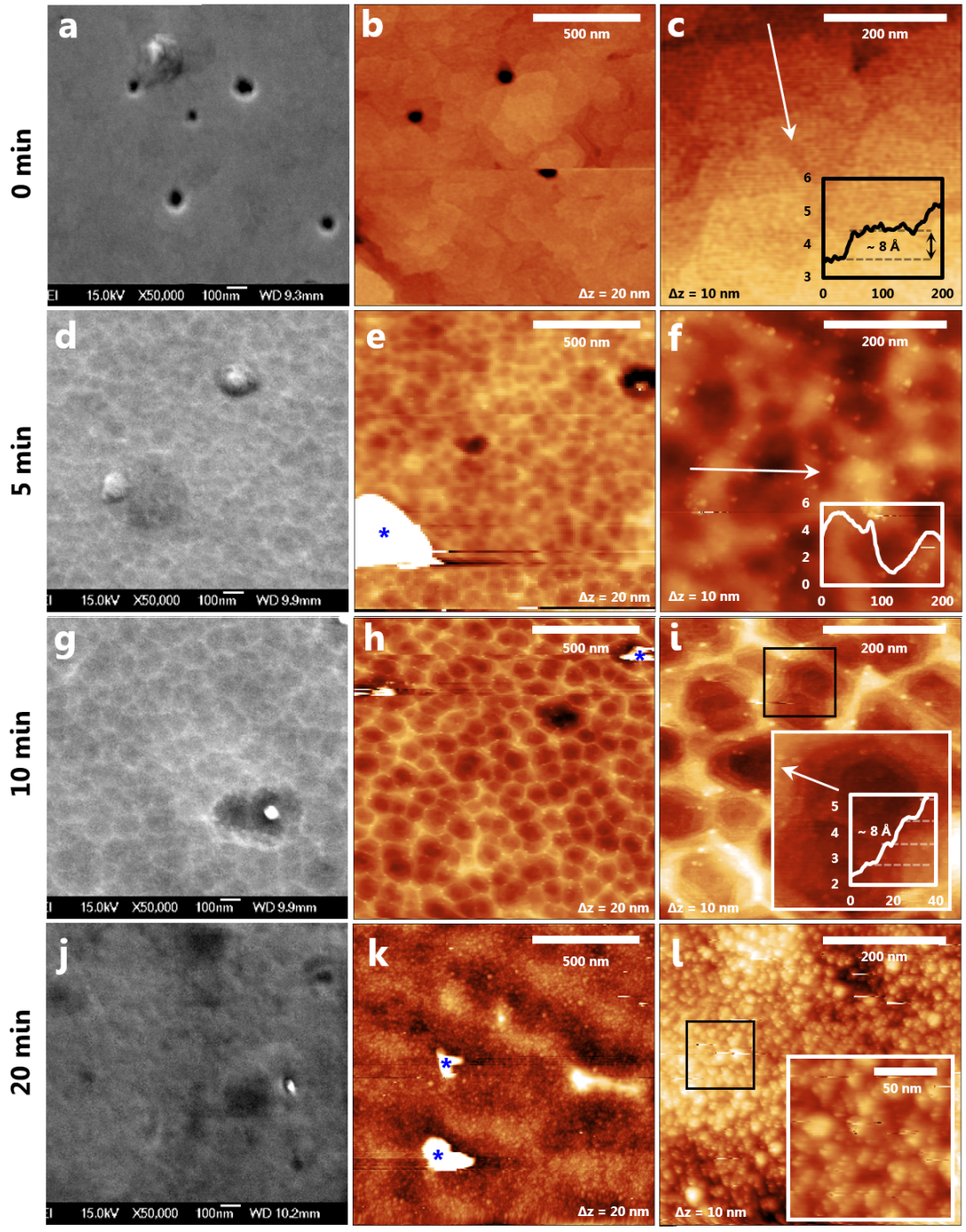

Figure 6.4: Effect of sputtering time on Sm-capped GdN (A519), using $E = 3.2$ kV Ar ions and $I \sim 15$ μA. (a-c) Untreated sample, (d-f) $\Delta t_{Ar^+} = 5$ min, (g-i) $\Delta t_{Ar^+} = 10$ min, (j-l) $\Delta t_{Ar^+} = 20$ min. The panels in the first column (a,d,g,j) are SEM images (mag. ×50000, $V = 15$ kV), others are AFM images (z-scales indicated on the images). Plots (axis in nm) in (c), (f), (i) are line profiles extracted from the white arrows. Inset in (i) is a higher resolution of the region in the black square. SEM images and the first column of AFM images are to scale. Note: these samples are *not* sublimated. The blue asterisks indicate minor instabilities caused by remaining particulates.

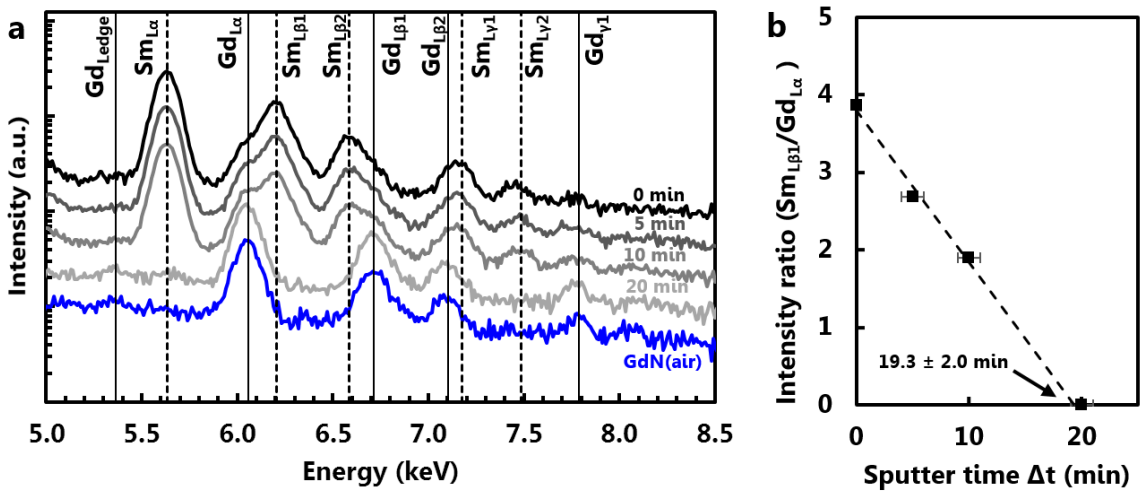

Figure 6.5: (a) EDS (V = 15 kV) of sputtered Sm-capped GdN (A519) using an ion energy E = 3.2 keV (sputtering current I~15 μA) displayed on a log-scale. The sputtering time Δt_{Ar^+} is indicated on each curve. The spectrum of A517, uncapped GdN (exposed to air) is also displayed as a reference. The spectra are offset for clarity. The energy levels of Gd and Sm are indicated respectively with solid and dashed lines. (b) $Sm_{L\beta_1}/Gd_{L\alpha}$ intensity ratio of as a function of the sputter time Δt_{Ar^+} displayed with a linear fit.

10 minutes sputtering Figure 6.4(g) shows an SEM image of a sample after sputtering for Δt_{Ar^+} = 10 min. No significant morphology differences are observed in comparison with 5 min sputtering (Fig. 6.4(a)). The white particulate present in the SEM image is observed in a slightly deeper crater and is thought to correspond to a pit in the untreated sample. The AFM image in Fig. 6.4(h) is in agreement with the SEM image. Figure 6.4(i) is a higher magnification AFM image of the sputter-induced craters. The black rectangle is expanded in the inset and the extracted profile (arrow) indicates a step-height of about ~8 Å, in agreement with the atomic steps of the as-grown sample. The crater step-edges tend to have hexagonal contours in agreement with the hexagonal structure of Sm. STM studies of Xe^+ bombarded Pt(111) surfaces [303] and Ne^+ bombarded Ag(001) surfaces [302] also report craters shapes in agreement with the crystalline structures (respectively hexagonal and cubic symmetries). The EDS spectrum of the sample shown in Fig. 6.3(a) is still comparable to the untreated sample, but a further decrease in the Sm intensity (~50 %) is clearly evidenced as shown in Fig. 6.5(b).

20 minutes sputtering Finally, a piece of A519 was sputtered for Δt_{Ar^+} = 20 min. The SEM and AFM images in Figs. 6.4(j) and (k) show a rather flat surface (RMSR ~2 nm), and

no craters are observed. Some features, causing minor tip instabilities (indicated with an asterisk) are attributed to remaining Sm_xO_y. The higher resolution AFM image in Fig. 6.4(l) and the inset (expanded from the black box) reveals finer details of the microstructure where grains tend to have triangular shapes, although this might be the result of a multiple tip. The grain size here is ~20 nm in width and about ~5 nm in height. The EDS Fig. 6.5 shows no trace of Sm, indicative of excessive sputtering ($\Delta z > 100$ nm). The surface is therefore that of a sputtered GdN(111) surface.

Morphology discussion The morphology and composition of A519 are both strongly impacted by sputtering, which was also observed on Sm/AlN samples in section 6.2. The main morphological feature associated with sputtering of Sm is the presence of shallow craters (depth of the order of 10 nm) about 100 nm wide. When the AFM tip is sharp enough, atomic steps can be resolved in agreement with dhcp Sm(0001) crystalline structure. Similar sputtering-induced morphologies were observed previously on metals [302, 303] which is a good indication that Sm_xO_y has effectively been removed with the Ar^+ bombardment. However such craters were not observed on Sm/AlN sample (in section 6.2), despite using similar beam energy, time and sputtering current - such discrepancy could be the consequence of intrinsic morphology differences between A519 and R024 (see chapter 5), known to strongly impact the post-sputtering morphology [182].

Composition discussion The Sm/Gd intensity ratio decreases linearly with sputtering duration as shown in Fig. 6.5(b). Assuming that the EDS signal is proportional to the number of Sm atoms, one can determine a rough estimate of the sputtering rate. The linear fit in Fig. 6.5 suggests a sputter rate of $\frac{dz}{dt} = 5.2 \pm 1.1$ nm/min. An alternate, more direct measurement of the sputter rate could be performed using a profilometer to measure the depth of the sputter cavity on each sample. A bombardment of $\Delta t_{Ar^+} = 20$ min sputters the entire cap thickness in the chosen experimental conditions as shown by EDS and therefore corresponds to excessive sputtering. Despite being partially bombarded, the surface morphology of GdN was in good agreement with published [56] STM images of GdN(111) (see Fig. 1.7 in section 1.4.1 or discussion in section 6.4).

6.3.2 Sublimation of thin Sm layers (A519)

The samples were subsequently thermally treated after sputtering in order to sublimate the remaining metallic Sm. Refer to Table 6.1 for the exact sputtering current, sublimation temperature and times for each sample in this study.

The bulk Sm desorption rate (see Fig. 5.2 in section 5.1) at $T = 520°C$ is of the order of ~0.3 nm/s, i.e. to sublimate 100 nm of Sm, a heating time of $\Delta t_{sub} = 5$ min should be sufficient for full desorption. To maximize Sm desorption, the samples were heated to $T > 520°C$ for $\Delta t_{sub} > 12$ h after sputtering.

Unsputtered From the previous study (see section 5.3), it is known that the native oxide of Sm (Sm_xO_y) hampers the recovery of a clean, accessible GdN(111) surface. Although it is expected that heating an unsputtered sample will not successfully remove the cap, A519 was heated to $T = 528°C$ for 14 h. Figure 6.6(a) shows the SEM image after heating. The morphology after treatment is characterised with the presence of a discontinuous film appearing white in the SEM image (occupying about ~80 % of the surface) covering a darker phase (thought to be GdN or oxidised GdN). The AFM images in Figs. 6.6(b) and (c) are intensely streaky as a consequence of a highly unstable tip-sample junction. Multiple attempts using various set-points, scanning speeds and tips could not yield streak-free imaging conditions.

The EDS spectrum is shown in Fig. 6.7(a). Compared to the untreated sample (spectra also shown in the same figure), the Sm intensity decreased substantially (about −85% for $Sm_{L\alpha}$), but is not zero. The SEM, AFM and EDS measurements are in very good agreement with the experiment on A314 in section 5.4. The presence of Sm in the heated sample is attributed to Sm_xO_y that could not be desorbed in these experimental conditions.

5 minutes sputtering Figure 6.6(d) shows an SEM image of A519 after 5 min sputtering treatment followed by heating ($T_{sub} = 534°C$, $\Delta t_{sub} = 15$ h). The surface is comparable to the unsputtered and heated sample described above, although it differs in relative proportions of Sm_xO_y, now covering ~50% of the surface. Figure 6.6(e) is an AFM image of the sample. Despite the significant improvement from the unsputtered and heated sample, tip instabilities occur and imaging is still difficult. The higher resolution AFM image in Fig.

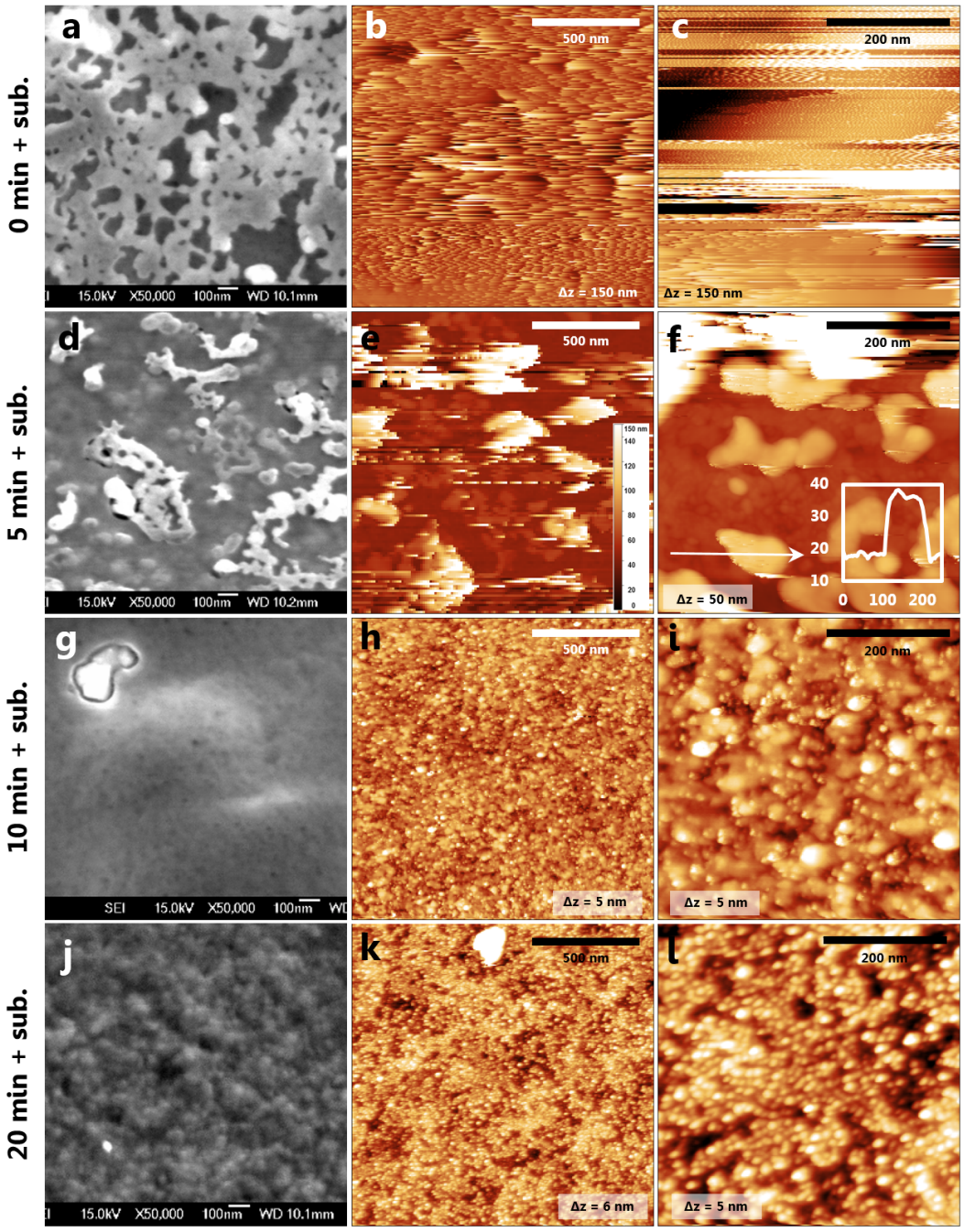

Figure 6.6: Effect of sputtering time (using $E = 3.2$ kV Ar ions and $I \sim 15$ μA) on Sm-capped GdN (A519) subsequently heated ($T \sim 530$°C for $\Delta t_{\text{sub}} > 12$ h). (a-c) Unsputtered sample, (d-f) $\Delta t_{\text{Ar}^+} = 5$ min, (g-i) $\Delta t_{\text{Ar}^+} = 10$ min, (j-l) $\Delta t_{\text{Ar}^+} = 20$ min. The panels in the first column (a,d,g,j) are SEM images (mag. $\times 50000$, $V = 15$ kV), others are AFM images (z-scales indicated on the images). SEM images and the first column of AFM images are to scale. The inset in (f) is a line profile extracted from the white arrow (axes unit in nm).

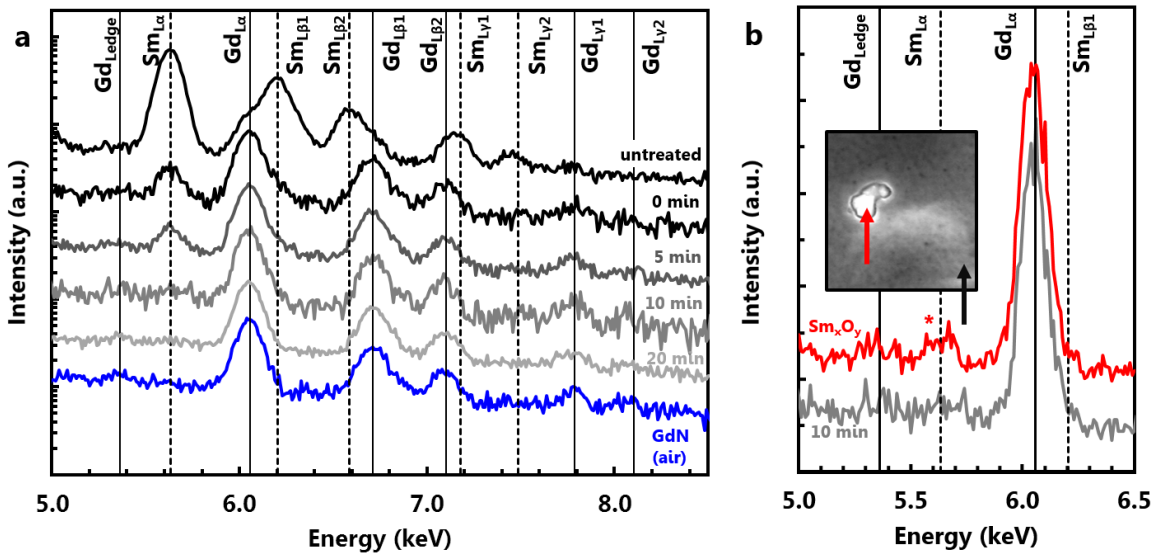

Figure 6.7: (a) EDS (V = 15 kV) of sputtered (E = 3.2 keV, I~15 μA) and heated (T~530°, Δt_{sub}12 h) A519 (Sm-capped GdN). The sputtering time Δt_{Ar^+} is indicated on each curve. The spectrum of A517, uncapped GdN (exposed to air) is also displayed as a reference. (b) EDS (linear scale) spectra of 10 min-sputtered and sublimated sample obtained from focusing the electron beam on the dark areas (grey curve, see black arrow in inset) and on the large white grains (see red arrow in inset) indicated in the inset SEM image. In (a) and (b), the spectra are offset for clarity. The energy levels of Gd and Sm are indicated respectively with solid and dashed lines.

6.6(f) reveals the two phases present on the surface. Particulates present on the surface are observed, and the inset shows a line profile across the particulate indicating a height of about ~20 nm-high. These particulates are identified as Sm_xO_y only partially sputtered here. Also, between the oxide grains a very flat surface is observed and identified as GdN. Qualitatively, the EDS shown in Fig. 6.7 does differ not from the unsputtered/sublimated sample. A decrease of the $Sm_{L\alpha}$ intensity is however observed (reduced by about 20% with respect to the unsputtered and sublimated sample), indicating partial removal of the oxide. The sputtering step for 5 min prior to thermal desorption of the Sm layer clearly improves the decapping technique. However the presence of remaining Sm_xO_y on the surface suggests that a longer bombardment time is required for optimal sputtering.

10 minutes sputtering A519 was sputtered for 10 min and subsequently heated to thermally desorb the metallic Sm. The SEM image of the sample is shown in Fig. 6.6(g). The surface is very homogeneous, flat, and blisters with beam exposure. The SEM image is also

strikingly similar to the SEM image of the (air-exposed) GdN sample shown in Fig. 5.15(f). See section 6.4 for a more detailed comparison with GdN. The AFM images in Figs. 6.6(h) and (i) acquired in UHV also exhibit a very flat surface (The RMSR is 0.8 nm for both images). The surface is granular with feature sizes ranging from ~5 to ~50 nm and heights up to ~5 nm. The EDS shown in Fig. 6.7(a) does not indicate the presence of Sm which confirms that sputtering removes the Sm_xO_y layer.

Rarely, large grains appearing white in the SEM images are observed, as shown in Fig. 6.6(g). Larger scale SEM indicates that regions that are free of those can be as wide as 5×5 μm^2. EDS was also acquired by focusing the beam on a similar grain (beam cross section $\sim 1 \times 1$ μm^2) and the data is shown in red in Fig. 6.7(b). It indicates a non-zero Sm concentration (at the $Sm_{L\alpha}$ energy shown with an asterisk) meaning that the grains are possibly Sm_xO_y. Sputtering for 10 min prior to thermally desorb the Sm allows to obtain very clean GdN surfaces, only rarely scattered with oxide grains.

20 minutes sputtering Earlier sputtering experiments in section 6.3.1 indicated an excessive sputtering for 20 min of bombardment ($\Delta z > 100$ nm), sputtering partially the GdN layer. A piece of A519 was nonetheless sputtered for 20 min and then heated for thermal desorption of the rest of Sm. The SEM image is shown in Fig. 6.6(j). The surface appears homogeneous and is in general agreement with air-exposed GdN (see Fig. 5.15). The AFM image in Fig. 6.6(k) shows a flat and homogeneous surface with a RMSR of 1.2 nm. Higher resolution AFM image in Fig. 6.6(l) indicates a granular surface comprised of ~10 nm wide features of about $1-2$ nm high. Generally the morphology is comparable to 20 min-sputtered (excessive sputtering) and 10 min-sputtered and heated A519. The EDS shown in Fig. 6.7(a) does not show the presence of Sm as expected (the sputtering removed the entire cap before heating).

Summary Sputtering the Sm cap partially prior to sublimation clearly improves the decapping method discussed in chapter 5. Both composition and surface morphology after sublimation strongly depend on the initial bombardment duration. When the samples were not initially sputtered, EDS measurement suggested the presence of Sm (~15 % of the initial intensity), corresponding to undesired Sm_xO_y covering the sample, also observed via

SEM (strongly perturbing AFM measurements). Minimal sputtering (Δt_{Ar^+} = 5 min using E = 3.2 keV and I ~15 μA) before thermal treatment further reduced the amount of Sm after heating (~10 % of the initial intensity) and decreased the oxide coverage. AFM of the underlying surface was also enabled thanks to partial oxide sputtering. The optimum sputtering duration for removing the Sm_xO_y in this experiment is around Δt_{Ar^+} = 10 min. After sublimation, sizeable areas (up to 5×5 μm^2) are free of Sm_xO_y grains and a very smooth GdN surface were recovered. The observed grains are typically ~5 to ~50 nm wide and ~5 nm high, in relative agreement with previously published STM study of 20 and 50 nm-thick GdN(111) layer [56] (more details in section 6.4).

6.3.3 Sputtering of thick Sm layer (A520)

The sputtering is optimal for A519 for a relatively narrow duration range (only Δt_{Ar^+} = 10 min removed the Sm_xO_y without sputtering the GdN layer), therefore the sputtering of thicker Sm caps was investigated. The same systematic study was undertaken on A520 with the following aims: (i) reproduce the cap removal results obtained from A519 in the previous section ('thin' Sm capping layer) on a different sample, (ii) improve the understanding of Sm sputtering (both in terms of morphology and rate) and (iii) obtain AFM imaging of the recovered GdN layer with finer resolution. The results of the sputtering experiments, similar in many ways to those observed on the thin Sm layers (A519), and are therefore presented more briefly below.

Morphology Figure 6.8(a) shows an SEM image of the untreated A520 sample. The surface looks very similar to that of other Sm/GdN samples studied in this thesis (A314, A464, A519), where flat terraces are scattered with pits. AFM images are shown in Figs. 6.8(b) and (c), and show atomically layered terraces also observed on A519 (step height of ~8 Å). The pits (not visible in the present scales to increase the contrast of the terraces) were characterised with AFM and measured as deep as ~40 nm. Due to possible tip convolution, this number is possibly underestimated (for more details on imaging artefacts, see [193]). Figure 6.8(d) shows the sample after sputtering during 5 min (in the usual sputtering conditions) and indicate sputter-induced craters. The pits are still visible (slightly deeper crater) and of-

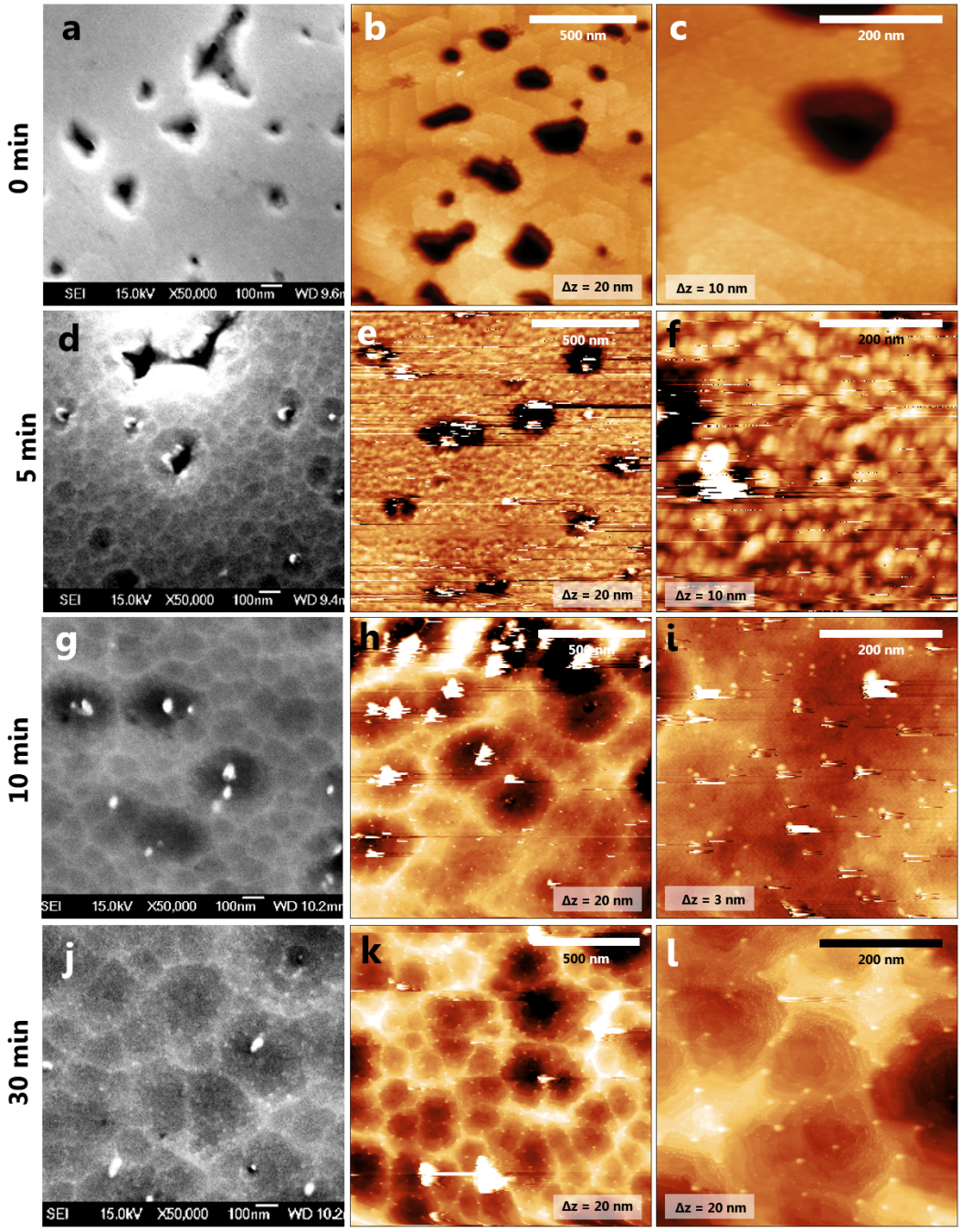

Figure 6.8: Effect of sputtering time on Sm-capped GdN (A520), using $E = 3.2$ kV Ar ions and $I \sim 15$ μA. (a-c) Untreated sample, (d-f) $\Delta t_{Ar^+} = 5$ min, (g-i) $\Delta t_{Ar^+} = 10$ min, (j-l) $\Delta t_{Ar^+} = 30$ min. The panels in the first column (a,d,g,j) are SEM images (mag. ×50000, $V = 15$ kV), others are AFM images (z-scales indicated on the images). SEM images and the first column of AFM images are to scale. Note: these samples are *not* heated. Note that $\Delta t_{Ar^+} = 20$ min has been tested and the resulting SEM/AFM images are very consistent with the 10 min- and 30 min-sputtered samples.

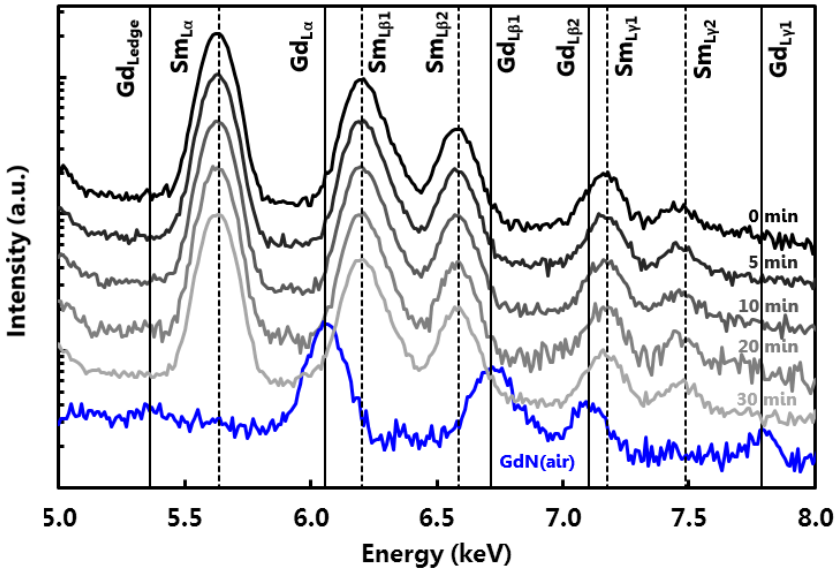

Figure 6.9: EDS (V = 15 kV) of sputtered Sm-capped GdN (A520) using an ion energy E = 3.2 keV (sputtering current I~15 μA). The sputtering time Δt_{Ar^+} is indicated on each curve. The spectrum of A517, uncapped GdN (exposed to air) is also displayed as a reference. The spectra are offset for clarity. The energy levels of Gd and Sm are indicated respectively with solid and dashed lines.

ten host a particulate (appearing white in the SEM images). The AFM images in Figs. 6.8(e) and (f) agree with the SEM image, yet here the craters are not clearly resolved, the AFM tip having likely picked up a Sm_xO_y particulate. Figure 6.8(g) shows an SEM image of a sample sputtered for 10 min. The surface is still characterised with craters and remaining particulates are observed in deeper depressions. The AFM image in Fig. 6.8(h) is in agreement with the SEM image. Figure 6.8(i) is a higher resolution AFM image of the bottom of a crater. Scattered features attributed to Sm structural defects or sputtered debris, are visible in the high-resolution AFM images as observed on A519 previously (see Fig. 6.4). Since A520 was grown with a thicker Sm cap, the sample was also sputtered for 30 min. The SEM (Fig. 6.8(j)) and AFM images (Figs. 6.8(k) and (l)) indicate a morphology comparable with the previous samples, sputtered for shorter durations. The craters also show atomic terraces. Note that a sample was also sputtered for Δt_{Ar^+} = 20 min (not displayed), however no difference in terms of morphology with the other sputtering durations were evidenced.

Composition The EDS of the sputtered A520 samples are shown in Fig. 6.9. No significant difference is observed, for all sputtering times. Notably, the Gd peaks are not visible.

The possible reason for this is because the thicker Sm (300 nm) prevents penetration of the electrons in the underlying layers. As opposed to the study on A519 samples (Fig. 6.5), the sputtering rate can not be estimated here. Longer Ar^+ exposure (not tested) should lead to a decrease of the Sm intensity.

Discussion and summary The surface morphology of A520 (300 nm-thick Sm capping layer on 100 nm-thick GdN) is very similar to A519 (100 nm-thick Sm on 100 nm-thick GdN) after sputtering. Craters and occasional grains are observed in the pits, correspond to remaining Sm_xO_y particulates. This can be explained the material surrounding the pit shadowing the bottom from the ion beam. High resolution AFM imaging indicated the presence of features of only ~1 nm high, thought to correspond to defects in the Sm crystalline structure or to sputtered debris. The only clear difference with A519 here is the effect of long sputtering times (more than 20 min). While thin Sm caps are sputtered entirely in ~20 min, it is not the case for the thicker layers, simply because of the larger amount of material. For a sputtering rate of $\frac{dz}{dt} = 5.2 \pm 1.1$ nm$\cdot$min^{-1} (as estimated for A519), a duration of ~60 min would be required to sputter the entire cap. The EDS signal was independent of the sputtering duration, because the electrons have a limited penetration depth of about $d_{15\text{keV}}$~100 nm in Sm (see chapter 2 for more details) therefore preventing the observation of Gd.

6.3.4 Sublimation of thick Sm layers (A520)

The sputtered A520 samples were then heated for $T_{\text{sub}} > 520°C$ for $\Delta t_{\text{sub}} > 12$ h. The surface morphology and elemental composition of the samples are discussed here for the various initial sputtering times. Again, due to general similarities with the previous A519 sample, the results are shown more briefly below.

Morphology Figure 6.10(a) is an SEM image of the unsputtered sample after thermal treatment. Granular Sm_xO_y covers the surface (white in the SEM image) of the sample as observed on the other samples (see sections 5.4 and 6.3.2). The AFM image in Fig. 6.10(b) is consequently very streaky. The AFM image in Fig. 6.10(c) shows the underlying layer which was this time possible to image, thanks to the absence of Sm_xO_y in this particular area. The

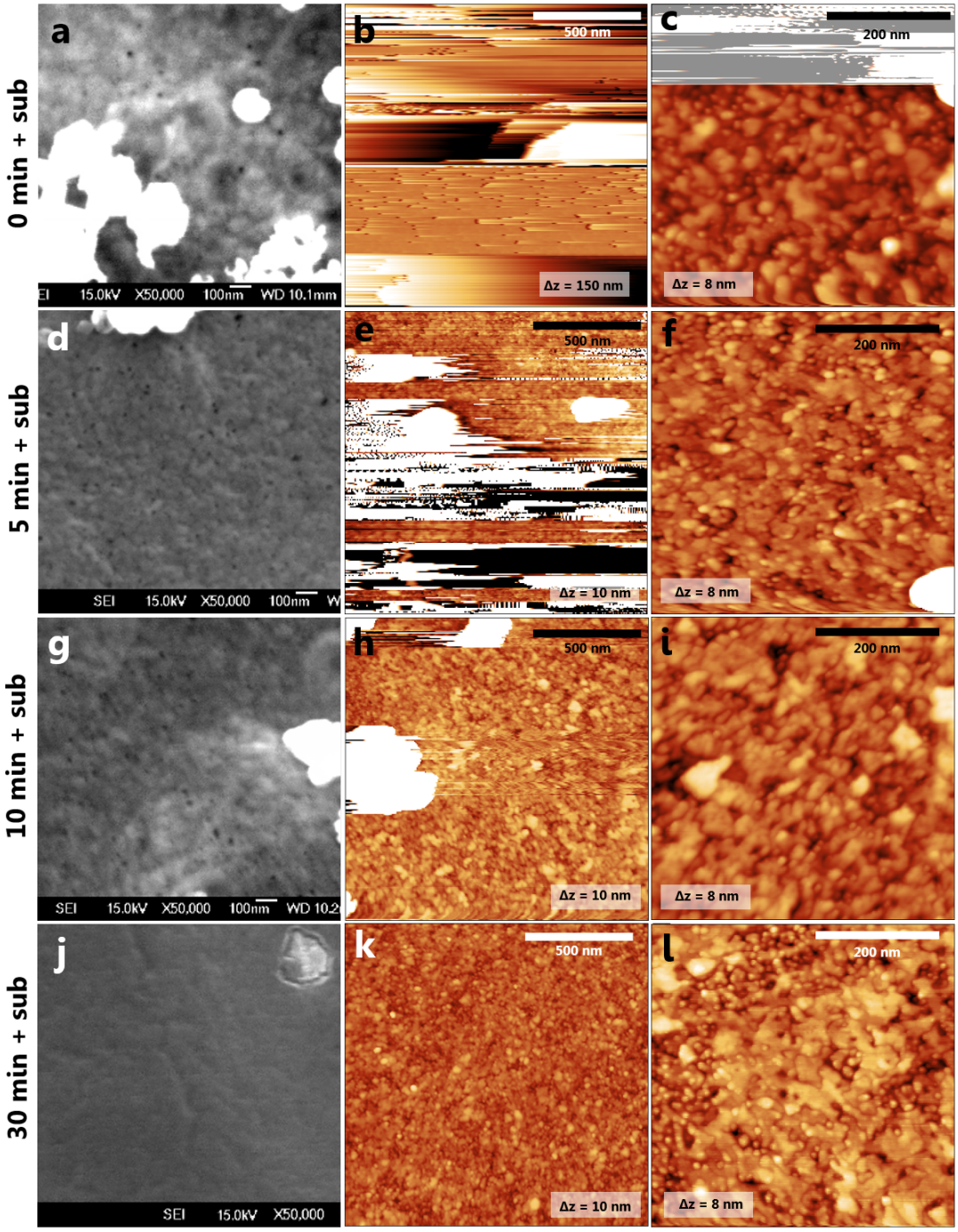

Figure 6.10: Effect of sputtering time (using $E = 3.2$ kV Ar ions and $I \sim 15$ μA) on Sm-capped GdN (A520) subsequently heated ($T \sim 530$°C for $\Delta t_{\text{sub}} > 12$ h). (a-c) Unsputtered sample, (d-f) $\Delta t_{\text{Ar}^+} = 5$ min, (g-i) $\Delta t_{\text{Ar}^+} = 10$ min, (j-l) $\Delta t_{\text{Ar}^+} = 30$ min. The panels in the first column (a,d,g,j) are SEM images (mag. ×50000, $V = 15$ kV), others are AFM images (z-scales indicated on the images). SEM images and the first column of AFM images are to scale. Note that $\Delta t_{\text{Ar}^+} = 20$ min has been tested and the resulting SEM/AFM images are very consistent with the 10 min- and 30 min-sputtered samples.

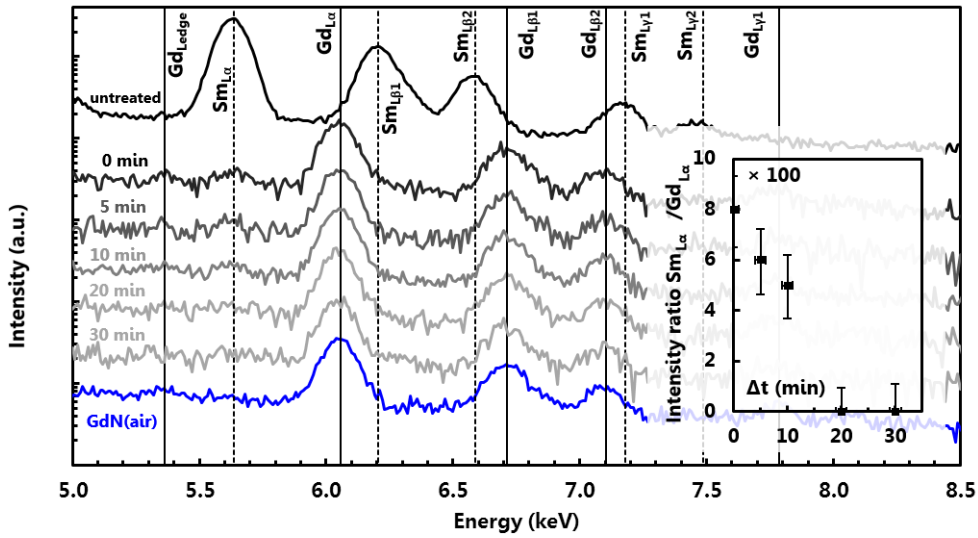

Figure 6.11: EDS (V = 15 kV) of sputtered/heated Sm-capped GdN (A520) using an ion energy E = 3.2 keV (sputtering current I~15 μA) displayed on a log-scale. The sputtering time Δt_{Ar^+} is indicated on each curve. The spectrum of A517, uncapped GdN (exposed to air) is also displayed as a reference. The spectra are offset for clarity. The energy levels of Gd and Sm are indicated respectively with solid and dashed lines. Inset: intensity ratio $Sm_{L\alpha}/Gd_{L\alpha}$ as a function of the sputtering duration.

surface is very flat (RMSR of 0.8 nm), and is in very good agreement with the morphology of the 10 min sputtered/thermally treated A519 shown in Fig. 6.6(i). The samples sputtered for 5, 10 min and 30 min here do not show obvious differences. The corresponding SEM images shown in Figs. 6.10(d) (g) and (j) show significantly less oxide than the unsputtered/heated sample in (a). Focussed SEM electron beam leads to blistering of the darker layer, as it was observed for air-exposed GdN (see Fig. 5.15). The AFM images in Figs. 6.10(e,f), (h,i) and (k,l) and the corresponding SEM images agree. Scanning as wide as ~1.5×1.5 nm^2 without instabilities is now possible for the 30 min-sputtered/thermally treated sample (Fig. 6.8(k)). High resolution AFM imaging in Fig. 6.10(f), (i) and (l) reveal the microstructure of the decapped GdN and is discussed in detail in section 6.4. A sample was sputtered for 20 min and thermally treated (not shown) and does not differ the samples sputtered initially for 10 min and 30 min.

Composition The EDS spectra of all the sputtered/heated samples are shown in Fig. 6.11. The EDS of the untreated sample is also displayed. A very weak $Sm_{L\alpha}$ intensity after heating is observed for the samples sputtered for $\Delta t_{Ar^+} \leq 10$ min, due to the presence of Sm_xO_y, not

entirely removed. Longer sputtering times (20 and 30 min) do not indicate the presence of Sm, suggesting complete removal of both the metallic cap and the Sm_xO_y layer. No difference with bare GdN (exposed to air) can be observed by means of EDS. With the exception of the untreated sample where most of the Sm is metallic, the detected Sm intensity in all the displayed spectra here arises from Sm_xO_y. The intensity of $Sm_{L\alpha}$ normalised to that of $Gd_{L\alpha}$ is displayed in the inset as a function of the argon bombardment time. While for A519 a sputtering of 10 mins was sufficient for Sm_xO_y removal, it appears to take longer for A520. This can be explained by the presence of a slightly thicker oxide in A520.

6.4 Characterisation of the decapped samples

6.4.1 GdN morphology

The morphology of the recovered GdN samples is now discussed and compared with the only previously published STM image [56]. Figure 6.12 shows the STM image from the literature (in Fig. 6.12(a)) corresponding to a 50 nm-thick GdN(111) oriented layer grown on AlN(0001)/Si templates. Figure 6.12 also shows several AFM images obtained from the decapped samples (containing no Sm as shown by EDS), obtained using the detailed procedure presented earlier in section 6.3.

Excess sputtering and unheated Figure 6.12(b) is an AFM image of A519 sputtered for 20 minutes and *not* heated. As a result of sputtering, no Sm was observed in the sample indicating a possible bombardment of the underlying GdN layer as discussed in section 6.3.1. The morphology is however very comparable to the published [56] STM image of GdN(111) reproduced in Fig. 6.12(d). Note the dashed square in the AFM image in Fig. 6.12(a) is of the same size of the STM image in Fig. 6.12(d), indicated for comparison purpose. The RMSR in the two images are similar, 0.9 nm for the sputtered Sm/GdN sample in Fig. 6.12(a) and 2.2 nm for the as-grown GdN [56].

Optimum sputtering Figure 6.12(c) shows an AFM image obtained on A519 after 10 min sputtering and thermal desorption. It is the only example of the thin Sm capped sample (A519) that (1) was not excessively sputtered and (2) did not evidence the presence of Sm

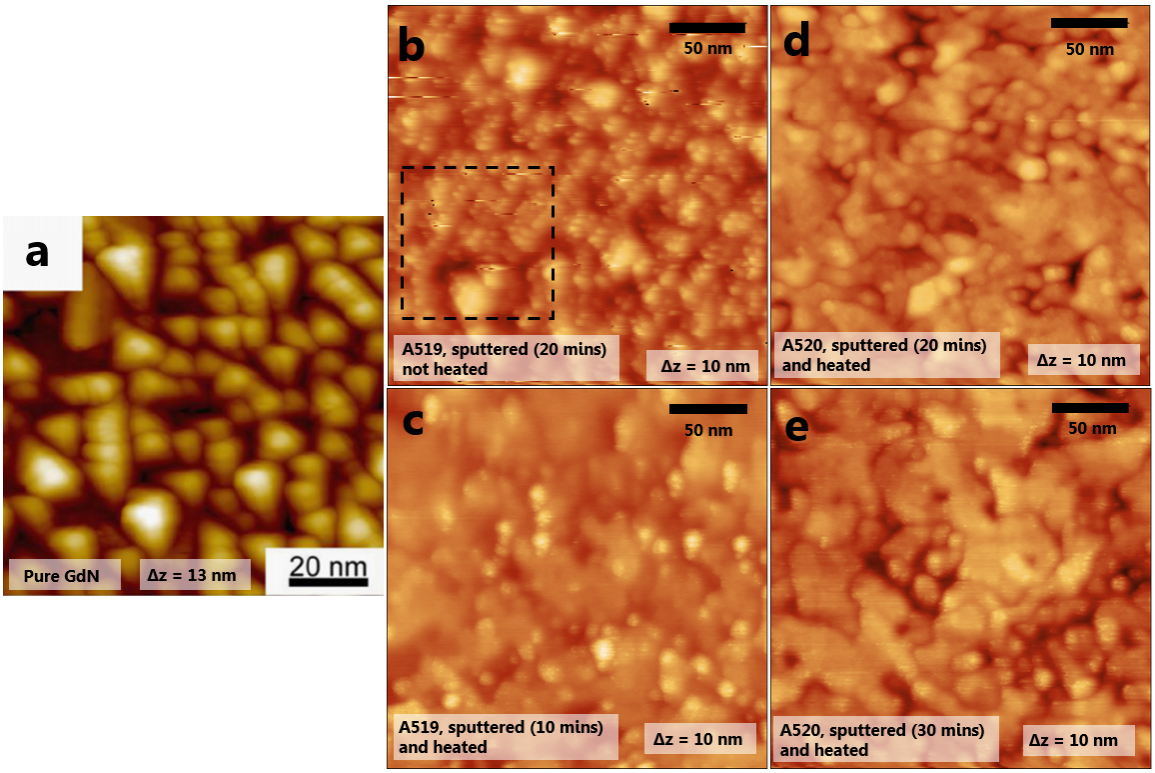

Figure 6.12: (a) STM image (V = +2.0 V, I = 0.1 nA) of a 50 nm-thick GdN, from [56]. AFM images of (b) decapped A519 (sputtered for 20 mins, not heated), (c) decapped A519 (sputtered for 10 min, heated), (d) decapped A520 (sputtered for 20 min, heated) and (e) decapped A520 (sputtered for 30 min, heated). Note the scale difference in (a). The STM image in (a) and the dashed square in (b) are the same size, displayed for comparison purpose.

after heat treatment. The surface is very flat (RMSR is 0.7 nm) but the relatively blunt tip hinders finer characterisation. Generally it is in good agreement with the other AFM images. Figs. 6.12(d) and Fig. 6.12(e) correspond to A520 sputtered for respectively 20 and 30 minutes, and subsequently thermally treated. The two images are the result of a sharper tip than in Figs. 6.12(b) and (c). The morphology of both samples can be described with a very flat surface (RMSR is 0.8 nm in the two images) and agree well with the sputtered/heated A519 sample shown in Fig. 6.12. The grains are up to ~50 nm wide, and some of them appear more or less merged or coalesced and have arbitrary shapes. Smaller grains (~10 nm-wide, density ~ 10^9 cm^{-2}) appearing more circular are also visible in the image. The reason for such morphology is unknown. It is possible to hypothesize that the circular grains are the result of dislocations emerging on the GdN surface, as observed for other nitrides at comparable densities [308, 309]. Higher resolution AFM imaging would be required for further

investigation regarding these morphological features.

Discussion The recovered GdN thin films in our experiments are reproducible and comparable to the unique STM image of GdN in the literature. The RMS roughness is also ~1 nm and the samples share a similar grain width (~10 nm) and height (~10 nm). However, side-by-side comparison of the decapped samples with the STM image in Fig. 6.12(d) indicate some differences, in particular due to the presence of the flat grains appearing merged or coalesced. A few hypotheses can be made that potentially explain the difference between the published GdN image with the decapped samples in this thesis:

- (i) **Different experimental conditions** The growth conditions of A519 and A520 for GdN were maintained as similar as possible and grown only a day apart in the same system minimizing possible structural differences. Despite using generally similar growth conditions and substrate, the sample from the literature in Fig. 6.12(a) was grown in different vacuum chamber. Moreover it was reported to be 50 nm-thick [56] which is two times thinner than in A519 and A520. The GdN layers in A519 and A520 were essentially annealed for $\Delta t > 12$ h at $T > 520$°C (which was not the case for the sample in Fig. 6.12(a)) and despite the absence of structural variation of GdN(111) upon thermal treatment (see study in section 5.2.1), the effect of the thermal treatment in real-space is unknown.

- (ii) **Remaining oxide** The ion bombardment step removes most of the Sm_xO_y as proven by SEM but may not be 100% effective, leaving behind trace amounts of oxide particulates below the detection level of EDS. The Sm_xO_y particles if sputtered insufficiently were always found to hindering AFM imaging as discussed previously, which in the 'successfully' decapped samples in Fig. 6.12 was not observed. It is possible that the potential remaining particulates of Sm_xO_y in decapped samples have a much smaller size and adhere more to the GdN layer than in inappropriately treated samples. Ruling these out would require measurements with higher sensitivity to oxygen (e.g. XPS).

- (iiI) **Remaining metallic Sm** The EDS detection limit is of the order of ~0.1 – 1.0 wt% [202, 204] i.e a remaining 0.1 – 1.0 Å equivalent thickness of Sm is possible, assuming

a probed depth in the range of ~100 nm. Upon heating at elevated temperatures, it is be expected that the Sm thin films fully sublimate, but it is unclear if it is the case of atomic clusters that can have a higher sublimation temperature due to quantum size effects [310]. This scenario is highly hypothetical and would require high sensitivity measurements to prove that Sm is still existing on the decapped samples in a nanoscale form.

- (iv) **Alloying of the GdN layer with metallic Sm** Intermixing of Sm below the EDS detection level with GdN during the cap desorption step can not be completely excluded. Such alloying could be accompanied by a change in morphology of the GdN surface.

- (v) **Metallisation of GdN**. Lastly, it is known that N_2 desorbs off the first few nanometres of the RENs when heated in UHV [68]. Considering an ideal decapping by sputtering/sublimation, the GdN top surface in our decapping experiments is likely to be depleted of nitrogen due to the heat treatment.

These hypotheses can not be tested further using the present AFM images and EDS data. The morphological differences discussed here are most likely from subtle changes in the growth conditions and treatment of the samples. Further experiments are required to characterize the recovered GdN, and are discussed in section 6.5.

6.4.2 Raman spectroscopy

To characterize the surface of the decapped samples, Raman spectroscopy (in air) was briefly investigated at VUW at the Raman lab. The basic experimental set-up is discussed in chapter 2. Figure 6.13 shows the Raman spectra (obtained with λ = 514 nm) of several samples including untreated A519, 0, 5 and 10 min-sputtered/heated A519, A517 (uncapped GdN, exposed in air) and a Si wafer.

The surface of the untreated Sm/GdN sample does not show the presence of phonon modes using conventional Raman spectrometry due to the very limited penetration depth of visible light, like most metals [312]. No peaks associated to Sm_xO_y are observed. A silicon wafer was tested for reference (light blue). All the peaks correspond to well-known phonon modes previously observed on Si [313]. The Raman spectrum of the air-exposed GdN sample is

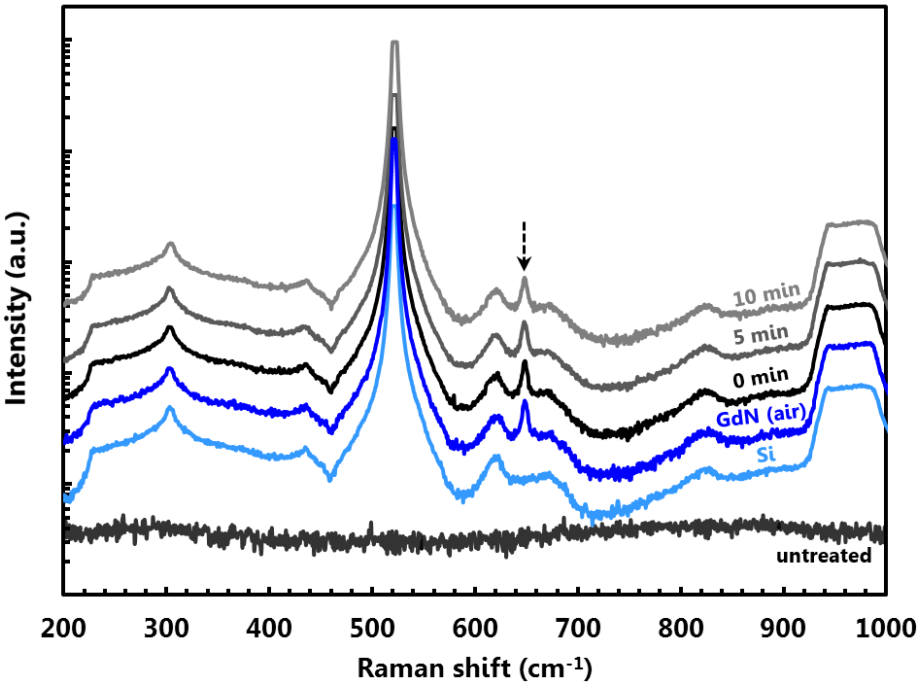

Figure 6.13: Raman spectra ($\lambda = 514$ nm) of A519 (0 min, 5 min, 10 min sputtered and heated, as well as untreated), A517 (GdN exposed to air), and Si wafer. The dashed arrow indicates AlN (E_2) phonon mode [311]. The spectra (displayed on a log-scale) are offset for clarity. No extra feature is identified on the treated samples with respect to the air-exposed GdN sample.

identical to Si, except for a the peak at σ~648 cm^{-1} (dashed arrow), corresponding to a previously reported AlN phonon mode [311, 313]. No GdN [314] nor Gd_2O_3 [315] peaks are observed. Regardless of the treated sample that is considered (unsputtered/sublimated or sputtered/sublimated) the Raman spectra are identical to that of the oxidised GdN sample, only the AlN and Si substrate peaks can be observed.

The Raman scattering experiments here do not evidence any phase in the treated sample, beyond the AlN/Si substrate. Further analysis (see section 6.5) using more sensitive techniques will be required to characterize the surface of the decapped samples.

6.5 Conclusion and outlook

6.5.1 Summary

The Sm cap removal of air-transported epitaxial Sm/GdN samples was achieved through argon sputtering and thermal desorption, using both AFM (in UHV) and SEM (after transfer in air) for morphology characterisation, and EDS (after transfer in air) for elemental composi-

tion analysis. It was found that using $E \sim 3.2$ keV and $I \sim 15$ μA led to an acceptable sputtering for a Sm/AlN sample.

A study was then performed on Sm/GdN samples (A519 and A520, consisting of a 100 nm and 300 nm-thick Sm cap respectively, grown on a 100 nm-thick GdN) wherein the sputtering energy and currents were kept identical throughout the experiments ($E = 3.2$ keV, $I \sim 15$ μA, chosen in agreement with initial testing) and systematically varying the bombardment duration ($\Delta t_{Ar^+} = 0$, 5, 10, 20 min, plus 30 min for A520) before sublimation. The sputtering rate was measured as $\frac{dz}{dt} = 5.2 \pm 1.1$ nm/min. The morphology and elemental composition were characterised both before and after heating ($T > 520$°C for $\Delta t > 12$ h). From AFM, SEM and EDS analyses, it was shown that a Sm_xO_y discontinuous or granular film covers most of the heated Sm/GdN samples if initially insufficiently sputtered, typically for $\Delta t_{Ar^+} \leq 5$ min. The oxide particulates also prevent AFM investigations because they are loosely bound and adhere to AFM tips creating instabilities or significant decrease of sharpness. For longer sputtering times ($\Delta t_{Ar^+} = 10$ min for A519 and $\Delta t_{Ar^+} = 20$ and 30 min for A520), the heated samples show very large areas (up to $\sim 5 \times 5$ μm^2) that are free of Sm_xO_y as evidenced by SEM and EDS. The absence of oxide enables AFM characterisation of the uncovered GdN layer.

The uncovered GdN surfaces are typically very flat (RMSR below 1 nm) and agree with the literature. However further experiment need to address the purity, the crystalline structure, and stoichiometry of the recovered GdN.

It is clear that the sputtering procedure is beneficial for obtaining large areas free of Sm and Sm_xO_y, thought to correspond to GdN. The technique presented here is therefore a significant improvement in contrast to the method reported in chapter 5 using only a thermal treatment to desorb the Sm from the samples. The reported cap removal technique of Bi_2Se_3 (using a Se cap [268]) is therefore also valid for Sm-capped GdN samples.

6.5.2 Future work

Further testing is required to assess the purity, stoichiometry and crystalline quality of the recovered GdN. Comparison with uncapped, unoxidised GdN grown in similar conditions would be ideal to address the properties of the recovered GdN layer. Also, testing this capping/decapping technique on other RENs e.g. Sm/SmN or Sm/DyN samples could also gener-

alize the technique for other RENs, and open up new avenues for REN surface characterisations.

For future Sm/GdN decapping experiments, the decapping procedure should be performed in the experimental conditions developed in this thesis. It is however important to note that the history of the sample plays a crucial role, as it is expected that the oxidation kinetics are a function of exposure time, humidity, and temperature in particular during the transport phase of the Sm-capped GdN sample. The crystalline quality of Sm may also play an important role in the oxidation rate. In the case of Sm/GdN samples exposed to air for a significantly longer time (e.g. 10 days), sputtering times should be longer to remove an appropriate quantity of Sm_xO_y. The Sm cap thickness must be designed accordingly.

A series of experiments can be undertaken to characterize the decapped samples. The recovered GdN layer must be investigated with surface-sensitive techniques in UHV to test the electronic properties:

- STM experiments and in particular scanning tunneling spectroscopy (STS) should be carried on the recovered GdN layers. The obtained results should be compared to experimental optical measurements [316] and ab-initio calculations of the band structure of bulk GdN [71, 80, 90]. The absence of literature on the electronic structure of the GdN(111) surface (both theoretical and experimental investigations are inexistent to the best of of knowledge) could be addressed with the support of future theoretical work (e.g. DFT calculations of a relaxed GdN layer). The observation of the energy band-gap closing below the Curie temperature (T_C~70 K) [71] would be a major landmark in GdN research. STM and STS have been very briefly tested at room temperature on the decapped samples, however the images and $I(V)$ curves were not reproducible, which was attributed to contaminated STM tips.

- X-ray photoelectron spectrometry (XPS) has a significantly higher surface sensitivity than EDS, typically probing ~$2-5$ nm below the surface [317]. XPS yields the electronic energy spectrum of the present superficial elements. Comparing an as-grown GdN spectrum with that of a decapped Sm/GdN sample using XPS could potentially verify whether Sm-Sm, Sm-O, Sm-Gd or Sm-N bonds are evidenced within the system at the expected energies. Such experiment would require a combined system where

GdN growth, argon sputtering, and XPS analysis are all available without breaking the vacuum.

- Angle-resolved X-ray photoelectron spectroscopy (ARPES) can image the electronic band-structure of a sample below the Fermi level, as it is possible for a variety of materials [113, 318, 319]. ARPES data of GdN could verify the validity of the electronic structure calculations published earlier [71, 80, 90]. Comparing as-grown GdN and decapped Sm/GdN samples would provide a robust testing for the validity of the decapping method.

To conclude, the decapping method developed here enables ex-situ surface sensitive techniques of GdN. Future work should focus on testing whether or not the GdN properties are impacted during the procedure beyond general morphology and elemental composition. If the GdN appears to be unaltered, the decapping method presented in this thesis could pave the way for further ex-situ surface characterisation of GdN and other RENs.

Chapter 7

Preliminary study of gadolinium nitridation

This chapter focuses on room temperature nitridation of Gd thin films. The impetus for obtaining a GdN surface via an alternative method (other than conventional REN deposition by PVD in N_2 atmosphere) was stimulated by the challenges discussed in the previous chapter using the Sm cap desorption technique to recover a pristine GdN surface. In this chapter, preliminary tests are reported on the nitridation of pure Gd thin films, both in UHV immediately after Gd deposition and after exposure of the Gd films to air. This introductory work was conducted at VUW in conjunction with J. Chan, another PhD candidate.

This chapter is written as follows. First, section 7.1 reviews the principle nitridation of RE materials. The nitridation growth model is also presented. Secondly, section 7.2, the growth of Gd thin films on AlN/Si templates via MBE is presented . Thirdly, the N_2 exposure of a Gd surface is examined in UHV in section 7.3. In section 7.4, nitridation is attempted on previously air-exposed Gd layers. The structural characterisation via XRD is then performed in section 7.5. Finally, the results are summarised and future nitridation experiments are suggested in section 7.6.

7.1 Principle

7.1.1 Catalytic breakdown of N_2

As reviewed in chapters 1 and 2, REN deposition using molecular beam epitaxy (MBE) techniques consists of the evaporation of pure solid RE at low flux (~0.1 Å/s) under a nitro-

gen atmosphere. Various nitrogen sources have been reported, including nitrogen plasma [57, 58, 60, 61, 78, 84, 88, 320, 321], ammonia (NH_3) [70, 166] or molecular nitrogen (N_2) [54, 56, 57, 81, 314]. Most of the RE elements can form a REN in a N_2 amosphere (e.g. GdN [54, 56, 57], SmN [57, 81], DyN, ErN and LuN [314]), yet it is not the case for EuN [57, 61, 78, 320, 321] and YbN [77]. It is worth noting that a numerical diffusion model has been investigated on bulk Gd crystals [322], however this is not in our direct interest because it focuses on bulk properties at the millimetre scale. The nitridation of RE polycrystalline thin films has been investigated very recently via XRD and time-dependent conductance measurements [68], however no direct surface-sensitive technique has been used to study this phenomenon so far.

The crystal structure of RENs, fcc for the most part [50] means that each RE atom is coordinated with 6 nitrogen atoms, and vice versa. This implies dissociation of N_2 during growth (there is no N−N bond in a REN crystal), and REN formation is observed even at room temperature [50]. A priori, the separation of N_2 by pure RE elements at room temperature is surprising, and despite some effort to understand the RE-N bonding formation [323] no theoretical investigation has yet been fully successful to explain why this reaction occurs although the oxidation number and atomic volume have been suggested [68]. It is unclear if the catalyst is a single RE atom, cluster, surface or even defect. It is important to note that N_2 reduction is a common topic in catalysis research [324], and transition-metal mononitrides, e.g. ZrN and NbN (also crystallizing in fcc rocksalt structures) are under investigation [325, 326].

Novel pathways for dissociation of N_2 may have significant technological consequences as the highly energy-consuming Haber-Bosch process [327] is today the standard industrial technique used for NH_3 production, accountable for more than 1 % of the world's energy consumption [328]. Reducing the cost of N_2 fixation (the Haber-Bosch process requires temperatures of about 400°C and pressures of about 200 bar [329]) is therefore highly desirable. The use of a RE layer as a catalyst for NH_3 production has recently been patented [69].

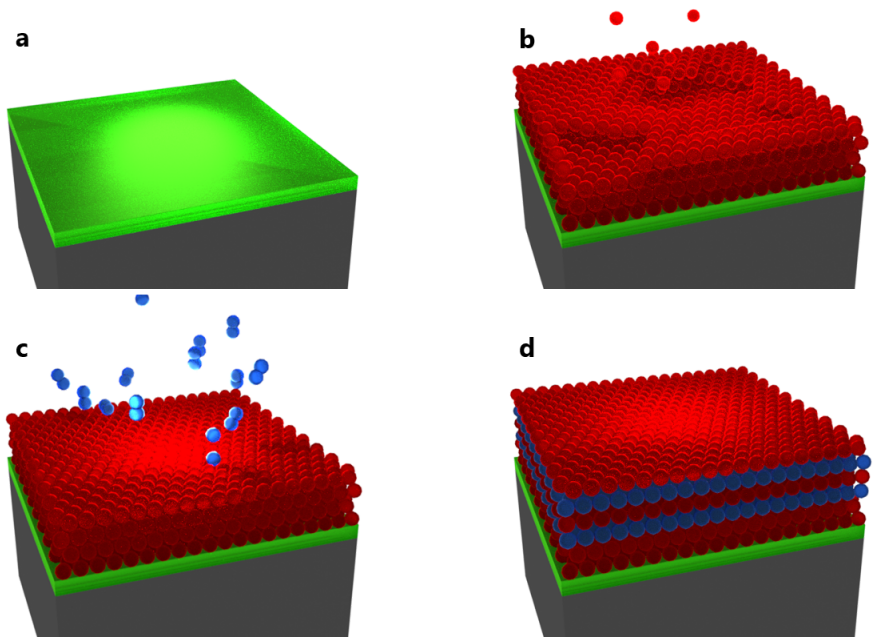

Figure 7.1: Nitridation schematics: (a) AlN template before RE deposition, (b) during RE(0001) deposition, (c) during N_2 exposure of the RE layer, and (d) completed REN(111) layer. Grey: Si, green: AlN, red: RE, blue: N/N_2. These hypothetical models are idealised and not to scale.

7.1.2 Nitridation

In this chapter, nitridation tests are undertaken in order to obtain GdN by exposing a Gd film to molecular N_2. The principle of the nitridation is detailed as follows. First, the commercially available AlN/Si templates are loaded in the UHV chamber. Figure 7.1(a) is a cartoon of the AlN/Si substrate. The substrates in this chapter are identical to those used for sample growth in chapters 5 and 6. The Gd(0001) layer is then deposited by MBE, as shown in 7.1(b). In Fig. 7.1(c), molecular nitrogen is introduced into the growth chamber, reacting with the RE layer, forming a GdN(111) layer as displayed in Fig. 7.1(d). This hypothetical growth model is tested in this chapter, both with and without initial exposure of the Gd layer to ambient air.

In this chapter, the N_2-exposed Gd layer is labelled as GdN_x, where $x = 0$ for inactive nitridation and $x = 1$ for complete nitridation. After exposure to N_2, the samples are passivated with an Al capping layer to avoid reaction of the GdN_x layer with air.

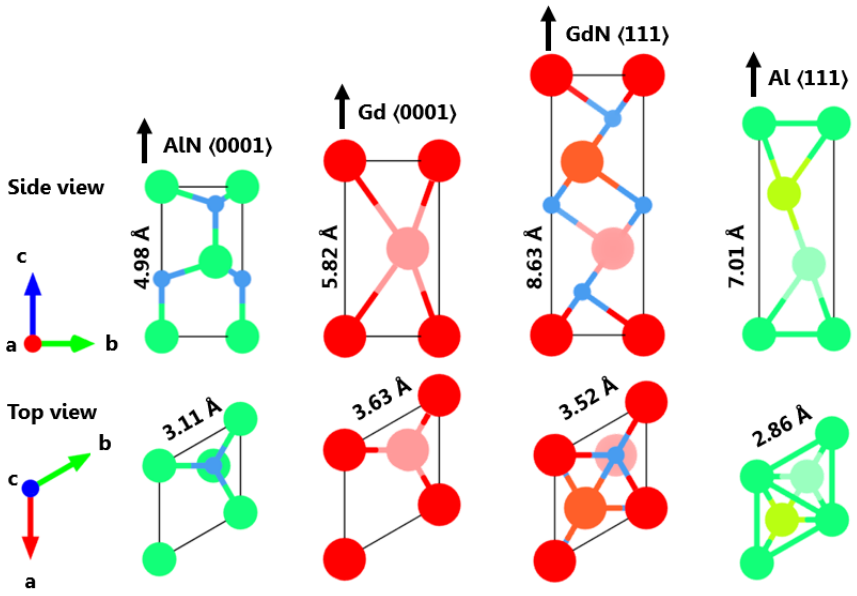

Figure 7.2: Bulk crystal structures of wurtzite AlN, hcp Gd, fcc GdN and fcc Al. The lattice parameters of the corresponding models are indicated. Green: Al, blue: N and red/pink/orange: Gd. The structures are to scale with one another. Only AlN and Gd are represented in their primitive unit-cells, GdN and Al are chosen to be displayed in hexagonal form. The c-axis is the preferential growth direction.

7.1.3 Crystal structures

Fig. 7.2 shows the bulk structure of the crystals of interest in this chapter, and literature lattice constants are indicated next to the models. The samples are grown on AlN(0001) [330] where the c axis is perpendicular to the (0001) plane. Bulk Gd crystallizes in hexagonal close-packed [271]. The stacking along the c axis is ABAB...etc. as shown on the figure. GdN [292] crystallizes in fcc 'rocksalt' structure. Here GdN is displayed in hexagonal form, where the c axis is perpendicular to the (111) planes. The Gd stacking along GdN⟨111⟩ direction is ABCABC... etc. The bulk structure of Al is also fcc [331] and here too it is chosen to be displayed along its preferential ⟨111⟩ axis (parallel to c).

7.1.4 Aim of this chapter

This study has multiple aims: (i) understand the growth of Gd(0001) on AlN, (see section 7.2) (ii) study the effect of N_2 exposure immediately after Gd deposition (see section 7.3), (iii) test the effect of N_2 exposure on air-exposed Gd samples (see section 7.6). In particular, if nitridation of Gd is possible after exposure to air, this would enable REN fabrication at

Sample	Gd (nm)	Δt_{air} (min)	Δt_{N2} (min)	P_{N2} (mbar)	Template
A412	10	-	-	-	AlN/Si
A415	10	-	-	-	AlN/Si
A416	10	-	-	-	AlN/Si
A413	10	0	40	1.1×10^{-4}	AlN/Si
A418	10	0	40	2.0×10^{-4}	AlN/Si
A414	10	480	40	1.1×10^{-4}	A412
A426	10	5*	60	1.1×10^{-4}	A416

Table 7.1: Samples grown for the nitridation experiments. The Gd thickness, intermediate exposure to air Δt_{air}, nitrogen pressure P_{N2} and exposure times Δt_{N2} are indicated. Also, the templates are indicated. All the samples are kept at room temperature during N_2 exposure, except A426 (T_{N2}~700°C).∗ A426 was also stored in a vacuum-sealed bag for 10 days before exposure to N_2, 5 min corresponds to the exposure to ambient air.

UC by exposing to N_2 Gd thin films previously grown at VUW. The study is at this stage preliminary, aiming for a general understanding of the nitridation process, paving the way for further experiments.

The grown samples are tabulated in Table 7.1. Three types of samples are grown here. A412, A415 and A416 consist of a 10 nm-thick Gd layer grown on AlN. A413 and A418 are nominally identical Gd samples that are immediately exposed to N_2 and then capped with Al. Finally, A414 and A426 are Gd samples that are exposed to N_2 after different air exposure times, and subsequently capped with Al.

The RHEED patterns during Gd growth, nitridation and Al capping are systematically recorded and analysed to determine the relative in-plane lattice constant, technique previously used in chapter 5. The streak spacing s is proportional to the inverse of the in-plane lattice constant a^* [206] as discussed in more details in chapter 2. The inverse of the streak spacing $\frac{1}{s}$ is normalised by its initial value s_0 such that $a(t) = \frac{s_0}{s(t)}$. To clarify, a^* is therefore the absolute in-plane lattice constant (in Å) and a the in-plane lattice constant relative to the substrate (unit-less). For the nitridation, it is equivalent to consider $a_{\text{Gd}} = 1$ and the evolution of a indicates the evolution of the GdN_x lattice constant. The lattice mismatch is often discussed in this chapter, where $\delta = a - 1$ (in %). Further structural characterisation via XRD is performed after sample growth. The reflection peaks are fitted with Gaussian functions. For more details on the experimental set-up and elements of theory, refer to chapter 2.

The extracted quantities from the RHEED experiments, i.e. in-plane mismatch δ for

Gd/AlN and GdN_x/Gd (and corresponding absolute in-plane lattice mismatch a^*) are given in Table 7.2 at the end of section 7.4. The XRD peak positions 2θ, full-width at half-maximum β and peak areas for Gd(0002) and GdN_x(111) are given in Table 7.3 in section 7.5.

7.2 Growth of Gd on AlN

Bulk Gd is a ferromagnet (T_C = 293 K [271]) and heterostructures comprised of Gd thin films have previously been demonstrated, e.g. Gd/W [332]. While bulk Gd crystallizes in hcp structure [271] (see Fig. 7.2), Gd thin films grown on Ta/Si(100) have been reported to consist of a mixture of hcp and fcc phases, depending on the growth temperature, thickness and buffer layer [333]. Here, we focus on the growth of a very thin Gd layer (nominal thickness of 10 nm) on AlN(0001), which to the best of our knowledge, has never been reported. The RHEED data presented here was obtained during the growth of A415, but these results were identical in other samples.

Fig. 7.3(a) (top) shows the RHEED pattern at room temperature of the AlN(0001) template, recorded along the AlN $\langle 11\bar{2}0\rangle$ direction after outgassing for 1 h at about T~200°C in UHV. The streaky diffraction pattern confirms the high quality of the AlN/Si substrate (commercially available, EasyGaN [179]). The Gd evaporator is set to have a flux of ~0.1 Å/s, measured with a quartz micro-balance located near the sample holder. The sample is kept at room temperature during deposition. The Gd shutter is opened (t = 0) and a few seconds after the RHEED pattern changes to become more diffuse as shown in Fig. 7.3(b) (middle). The streak spacing then decreases significantly. After about t~1 min, the RHEED pattern stabilizes and shows clear streaks, characteristic of a 2D 'layer-by-layer' growth as shown in the RHEED after growth in Fig. 7.3(a) (bottom). The growth was stopped when the micro balance indicated a deposited thickness of 10 nm (~4 min).

The time-evolution of the normalised inverse streak spacing a is shown in Fig. 7.3(b). For the first few seconds near t = 0, the streak spacing is constant. A change in the lattice constant can be observed from t = 30 s, i.e. after deposition of ~3 Å (~1 atomic plane) of Gd. The in-plane lattice parameter first overshoots to a value about 20% larger than that of AlN, and decreases as the growth is taking place. The value of a stabilizes after 2 minutes and indicates a Gd/AlN mismatch of $\delta = 16.4 \pm 0.4\%$. The mismatch corresponds to

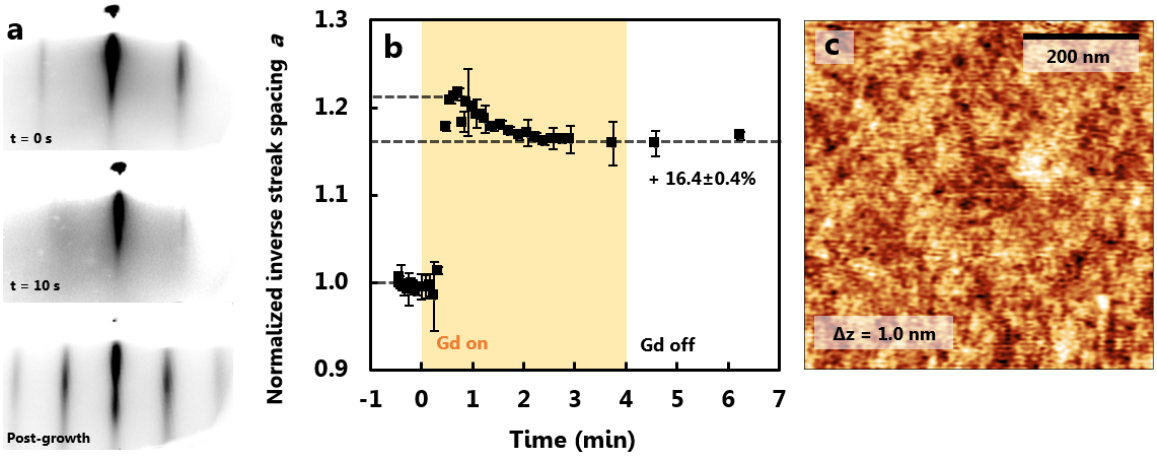

Figure 7.3: Growth of Gd/AlN. (a) RHEED patterns along the AlN$\langle 11\bar{2}0\rangle$ direction during Gd deposition of A415 for $t = 0$ s (Gd shutter opens), $t = 10$ s, and after the growth is finished. (b) Normalised inverse streak spacing of A415 as a function of time. The yellow zone corresponds to the growth duration. (c) AFM in air (tapping mode) of A412. The z-scale (corresponding to the maximum topographic amplitude) is indicated.

$a^*_{\mathrm{Gd}} = 3.62\pm0.02$ Å, in very good agreement with bulk hcp Gd [334] ($a^*_{\mathrm{Gd-bulk}} = 3.636$ Å, [334]).

RHEED patterns are recorded immediately after growth at different sample rotations (not shown) and indicate that the surface atoms possess a 6-fold rotational symmetry. The atomic arrangements of the top monolayer of fcc(111) and hcp(0001) structures are identical, only the stacking along the c-axis differs (respectively ABCABC... and ABAB...). Typically, distinction of the two structures via RHEED is possible in the presence of finite islands, where the faceted edges induce different RHEED diffraction spots (as reported for Co fcc/hcp thin films [335]). However, in this case the streaky nature of the RHEED patterns can not allow distinction between fcc and hcp. See section 7.5 for further structural characterisation of the Gd thin films.

A412 (grown under nominally identical conditions) was imaged shortly after deposition (the sample was in ambient air for less than an hour) with AFM (clean room, VUW) in order to characterize its surface morphology. The tapping-mode AFM image is shown in Fig. 7.3(c). The measured roughness is RMS ~0.2 nm indicative of a nearly atomically-flat surface. The features on the image are likely the result of adsorption of air-borne contaminants (H_2O, O_2, ...) on the Gd surface. The very flat morphology of the samples is in agreement with the high-quality layer-by-layer epitaxial growth of GdN evidenced via RHEED experiments.

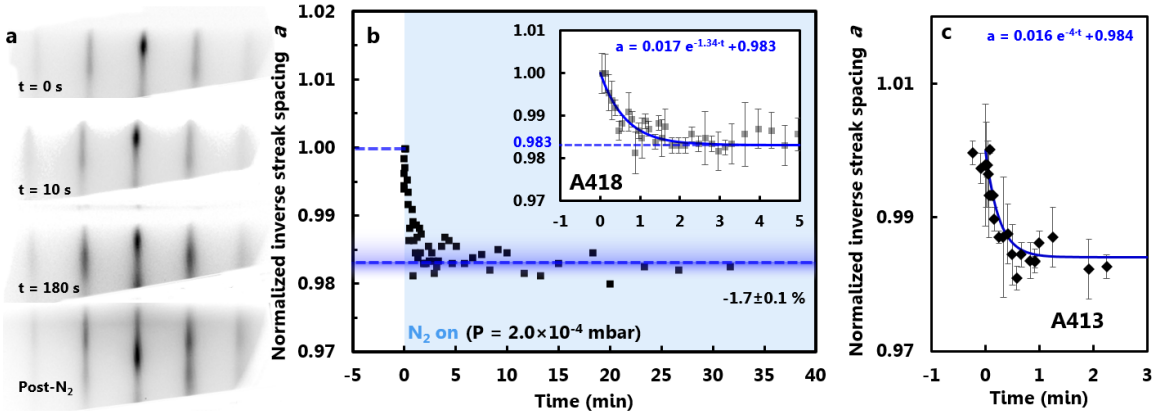

Figure 7.4: Nitridation of Gd(0001). (a) RHEED patterns of A418 along the AlN $\langle 11\bar{2}0 \rangle$ direction during (t = 0, 10, 180 s) and after exposure to N_2. (b) Normalised inverse streak spacing a during N_2 exposure. The dashed line indicates the final value and the blue area the exposure time. Initial and final values are indicated with a dashed line. The inset shows the same data, except on a linear-log scale evidencing an exponential law. The exponential model (blue solid line) parameters are indicated. (c) Normalised inverse streak spacing a during N_2 exposure of A413. The parameters of the exponential model (blue line) are indicated.

7.3 Nitridation results

7.3.1 N_2 exposure

We now focus on the exposure to N_2 of the Gd layer. In this section we only consider nitridation attempts without exposure of Gd to air. The Gd layer (nominal thickness 10 nm) was grown in identical conditions to those described previously in section 7.2. RHEED patterns are recorded during the nitrogen exposure.

Immediately after the Gd deposition, the N_2 pressure was set to $P = 2.0 \times 10^{-4}$ mbar and maintained constant for $\Delta t_{N2} = 40$ min. Figure 7.4(a) shows the RHEED patterns recorded along the initial AlN $\langle 11\bar{2}0 \rangle$ direction (the sample was not rotated). During N_2 exposure, the RHEED pattern did not qualitatively change (it remained streaky) and no obvious spacing variation was observed. However, analysis of the RHEED patterns (using J. Chan's software [178]) shows that a small increase in the streak spacing is occurring during N_2 exposure. Figure 7.4(b) shows the normalised inverse streak spacing a. Shortly after the opening of the N_2 valve, a decreases to ~0.983.

Because the decay at the early stage of nitrogen exposure is relatively fast the same plot is magnified in the inset (with the uncertainties). The in-plane lattice parameter decreases

quickly and is stable after about t~2 min. Despite a significant scatter and uncertainty in the data, an exponentially decaying model fits the evolution of the normalised inverse streak spacing relatively well (blue solid line). The associated time constant is $\tau \sim 1.3 \pm 0.4$ min^{-1}. The in-plane lattice constant of the nitrided Gd(0001), compressed by -1.7 ± 0.1 % with respect to that of epitaxial Gd(0001) thin film (i.e. $a^*_{\mathrm{GdNx}} = 3.59 \pm 0.06$ Å) is reached after about t~2 min of N_2 exposure. RHEED patterns are obtained at various sample rotation angles (not shown) revealing a 6-fold symmetry of the top surface, in agreement with both bulk Gd(0001) and GdN(111) (see ball-and-stick models of the structures in Fig. 7.2).

A413 is exposed to N_2 following the same procedure, except $P_{N2} = 1.1 \times 10^{-4}$ mbar. The RHEED patterns of A413 are qualitatively similar to those of A418 (not shown) and the evolution of the normalised inverse streak spacing is displayed in Fig. 7.4(c). The in-plane lattice parameter is also decreasing exponentially upon N_2 exposure and fitting yields $a = 0.016 \times \exp(-4 \cdot t) + 0.984$, in good agreement with A418 where the final value for A413 a is $a = 0.984$ or $\delta = -1.6 \pm 0.2$ % (i.e. $a^*_{\mathrm{GdNx}} = 3.55 \pm 0.03$ Å). The decay is faster during A413 than for A418, however due to the large scatter and uncertainty in the data, it is not possible to establish clear kinetic comparison, beyond that the in-plane lattice spacing is stable after a few minutes of N_2 exposure. Only the final value of the streak-spacing, indicating whether or not nitridation occurred, is discussed.

Assuming an ideal nitridation of bulk Gd(0001) to GdN(111), the observed lattice constant would reduce from 3.636 Å [334] for Gd to 3.517 Å [292] for GdN, i.e. by $\delta_{\mathrm{bulk}} = -2.7$ %. Here, the experimentally observed mismatches of $\delta = -1.7 \pm 0.1$ % for A418 and $\delta = -1.6 \pm 0.02$ for A413 are in acceptable agreement. Deviation from ideal bulk nitridation may be related to the strain experienced by the thin films or incomplete yield where $x < 1$.

7.3.2 Al capping

The GdN_x layers were then passivated to avoid potential reaction with air. Al is chosen due to availability in the chamber, and is preferable over Gd for further structural characterisation (thus avoiding confusion with potential remaining Gd in the heterostructure). Its paramagnetic properties are also convenient for further magnetic characterisation of the samples. The aimed thickness for the Al cap is ~20 nm, at a growth rate (measured with a quartz

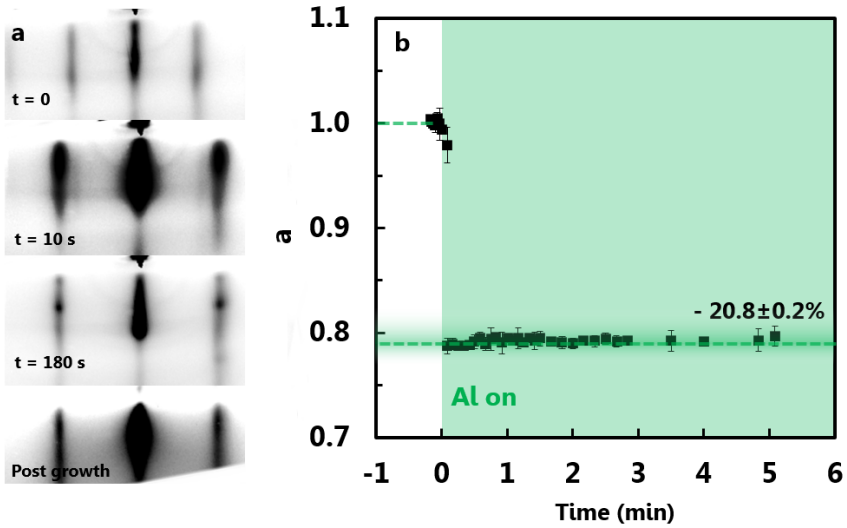

Figure 7.5: Al capping of GdN_x. (a) RHEED patterns along the AlN $\langle 11\bar{2}0 \rangle$ direction during (t = 0, 10, 180 s) and after Al growth (A418 sample) (b) Normalised inverse streak spacing during Al deposition. The dashed line indicates the final value and the green area the Al growth. Initial and final values are indicated with a dashed line.

micro-balance located near the substrate) of ~0.1 Å/s, leading to a deposition time of about 30 minutes. The sample was maintained at room temperature during Al capping for all the samples.

Al deposition was performed after shutting the N_2 valve, when the base pressure is recovered (~1×10^{-7} mbar). Figure 7.5(a) shows the RHEED pattern before, during and after the Al deposition on GdN_x. The transition from GdN_x to Al is clear and the lattice parameter relaxes immediately, as expected for a strongly-mismatched epilayer [287]. The streaky nature of the RHEED pattern of Al during the growth is suggesting a high quality, 2D 'layer-by-layer' growth mode. Figure 7.5(b) shows the normalised inverse streak spacing (normalised to the averaged value before $t = 0$) as a function of time. The transition from the GdN_x is relatively sharp, no intermediate phase or surface reconstruction are evidenced during Al growth. The lattice mismatch measured by RHEED is $\delta = -20.8 \pm 0.2\%$. The RHEED patterns are observed after rotation of the sample (not shown) revealing a 6-fold rotational symmetry along the growth axis.

The in-plane lattice parameter is measured to be $a^*_{\mathrm{Al}} = 2.85 \pm 0.03$ Å, and the rotational symmetry of the streaky RHEED pattern are in very good agreement with bulk fcc Al(111) (inter-atomic distance $a^*_{\mathrm{Al-bulk}} = 2.863$ Å [331]). Overall, the RHEED study of the Al deposi-

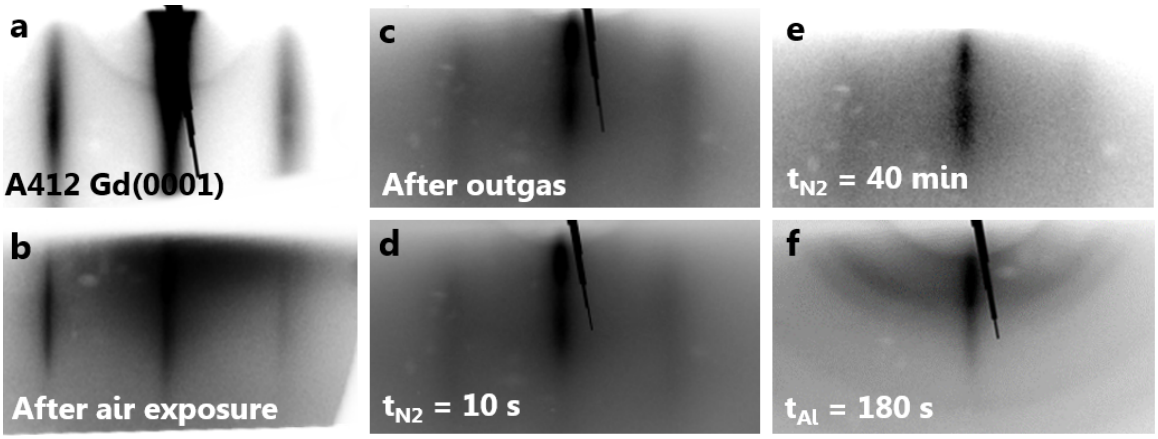

Figure 7.6: N_2 exposure of Gd after 8 h in air. RHEED patterns along the AlN $\langle 11\bar{2}0 \rangle$ direction, (a) A412 after growth, (b) after air-exposure, (c) after heating to T~450°C for 30 min, (d) during N_2 exposure, (e) after N_2 exposure and (f) after Al capping.

tion on the nitrided Gd(0001) surface suggests a high quality epitaxial growth of Al(111).

After capping, the samples are taken out of the vacuum chamber and their XRD patterns are obtained (see section 7.5). Magnetic characterisation of the samples is planned, and at the time of writing, no measurement have yet been undertaken.

7.4 Nitridation of air-exposed Gd layers

The aim of this section is to test whether GdN films could be prepared by first growing Gd(0001) thin films in the UHV lab at VUW and then transported to UC for nitridation in a different chamber. Two air exposure procedures were investigated: A412 was left for 8 h in air, and A416 was stored for 10 days in a vacuum-sealed bag, at an estimated pressure of 1 mbar. The RHEED patterns after exposure to air, after outgassing and during exposure to N_2 are discussed here. Because it is not the main focus of this study, the Al capping deposition will only be briefly discussed.

7.4.1 After 8 h in air

Gd surface after air exposure A412 (~10 nm Gd(0001) grown on AlN/Si) was loaded in the UHV after 8 h of exposure in ambient conditions of temperature (T~295 K) and atmospheric pressure. Figure 7.6(b) shows the RHEED pattern along the AlN $\langle 11\bar{2}0 \rangle$ direction of the sample immediately after insertion in the UHV chamber after exposure. For comparison,

the RHEED pattern obtained immediately after grown is shown in Fig. 7.6(a). The pattern (obtained at room temperature) has become very diffuse, indicating a degradation of the Gd surface, likely through oxide layer formation [336]. Although it is unlikely to succeed (as discussed for Sm_xO_y desorption on Sm layer in chapters 5 and 6), the sample is heated to get rid of the oxide layer. The cleaning procedure for this sample here consists of heating to T~450°C for 30 min. Fig. 7.6(c) shows the RHEED pattern after thermal treatment. The pattern is still diffuse, no clear improvement is evidenced. In fact, the streaks appear slightly more blurred. The diffraction pattern is not quite comparable to the Gd(0001) obtained immediately after growth, the cleaning procedure is then considered unsatisfactory.

Nitridation attempt The sample is exposed to N_2, in similar conditions to that of A413 in section 7.3 ($P_{N2} = 1.1 \times 10^{-4}$ mbar, $\Delta t_{N2} = 40$ min at room temperature). It is not expected to work given the degraded/oxidised surface of the Gd thin film, but nitridation is nonetheless attempted. Figure 7.6(d) shows the diffraction pattern after $t = 10$ s of exposure to N_2, no significant change is observed. Figure 7.6(e) is the RHEED pattern after $t = 40$ min, the first-order streaks almost entirely vanished. The extreme diffusivity of the pattern hinders a clear streak-spacing estimation, which increases significantly the measurement uncertainty. The time-dependent normalised inverse streak spacing (not shown) indicates $a = 1.02 \pm 0.2$, averaged from $t > 2$ min. The absence of clear variation of in-plane lattice constant ($a^*_{\mathrm{GdNx}} = 3.78 \pm 0.12$ Å). It is likely that the nitridation reaction is prevented by the presence of the oxide layer prevents nitridation.

Capping The layer was then capped with Al in the same growth conditions as previously. The RHEED pattern after deposition is shown in Fig. 7.6(f). The presence of arcs indicates a significant degree of polycrystallinity, likely due to the poor surface quality of the interface before Al deposition. The sample was then taken out of the vacuum chamber and characterised via XRD (see section 7.5). Note that the sample was relabelled to A414 to avoid confusion with A412 (Gd/AlN which was also characterised via XRD).

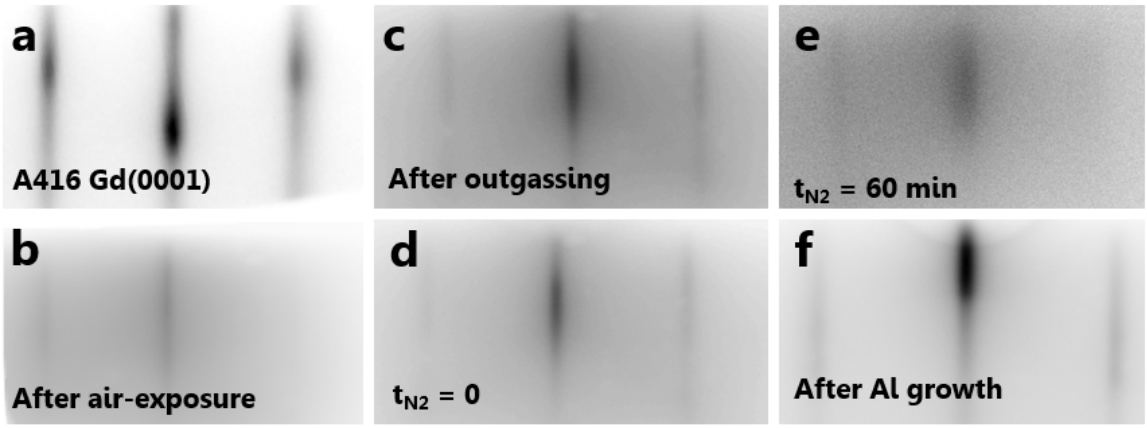

Figure 7.7: RHEED patterns along the AlN $\langle 11\bar{2}0 \rangle$ direction, (a) immediately after Gd deposition, (b) after exposure to air for $\Delta t_{\text{air}} = 5$ min, (b) after outgassing at T~700°C for 4.5 h, (d) at the start of the N_2 exposure, (e) after N_2 exposure and (f) after Al deposition.

7.4.2 After 10 days in low vacuum

Gd surface A416 (Gd/AlN) was loaded in the UHV chamber after storage for 10 days in a vacuum-sealed bag (imitating transport of a Gd thin film). The sample was estimated to be in contact with ambient air for ~5 min. Figure 7.7(a) and (b) shows the RHEED patterns before and after air-exposure. Again, the RHEED pattern was very diffuse due to oxidation and adsorption of other contaminants in a similar fashion to A412 (Fig. 7.6). An outgassing procedure was undertaken, this time at a higher temperature and for a longer time (T = 700°C for ~4.5 h) than for A414. The RHEED pattern after outgassing treatment shows some contrast and streak sharpness improvement, but it is still diffuse.

Nitridation attempt The exposure to N_2 was undertaken, this time for a slightly longer time ($\Delta t_{N2} = 60$ min) at an elevated substrate temperature of T_{N2}~700°C. The reason for using an increased thermal energy and exposure time is to maximize the likelihood of nitridation. Figure 7.7(d) and (e) show the RHEED pattern respectively before N_2 exposure and after 60 min. A loss of contrast and sharpness was observed, in agreement with previous N_2 exposure of A412/A414. Again, due to the diffusivity of the pattern, it is very challenging to estimate the streak-spacing. The evolution of the normalised inverse streak spacing a (not shown) is relatively scattered and no trend can be made. Averaging of the data after $t = 2$ min suggests a final in-plane lattice mismatch of $\delta = 0.0 \pm 1.3$ % after N_2 exposure, indicating no

Layer	Gd		GdN_x	
Sample	δ (%)	a^* (Å)	δ (%)	a^* (Å)
Bulk	+16.8	3.636 [334]	−3.3	3.517 [292]
A412	19 ± 2	3.70 ± 0.06	-	-
A415	16.4 ± 0.4	3.62 ± 0.01	-	-
A416	16.5 ± 0.4	3.62 ± 0.01	-	-
A413	17.2 ± 1.3	3.65 ± 0.04	-1.6 ± 0.5	3.59 ± 0.06
A418	16.2 ± 0.8	3.61 ± 0.02	-1.7 ± 0.1	3.55 ± 0.03
A414	*cf* A412	*cf* A412	$+2 \pm 2$	3.78 ± 0.12
A426	*cf* A416	*cf* A416	$+1.1 \pm 1.3$	3.66 ± 0.05

Table 7.2: RHEED analysis summary for all samples. The mismatch δ is given as well as the corresponding in-plane lattice parameter a^* for Gd and GdN_x.

variation of the in-plane lattice parameter ($a^*_{GdNx} = a^*_{Gd} = 3.66 \pm 0.05$ Å). It is almost certain that the nitridation did not occur (x~0).

Capping An Al cap is deposited in the same growth conditions as previously. Surprisingly, the deposition of Al follows this time a 2D 'layer-by-layer' growth mode indicated by a streaky RHEED pattern, as shown in Fig. 7.7(f). The lattice mismatch of Al/GdN_x is measured to $\delta = -7.0 \pm 0.5$ %, i.e. $a^*_{Al} = 3.41 \pm 0.07$ Å. This is in complete disagreement with both bulk Al structure ($a^*_{Al-bulk} = 2.863$ Å, i.e. +20 % expansion of the lattice constant) and previous Al deposition on A413 and A418 where the structure agreed with bulk Al (see section 7.3.2) The sample was then relabelled A426 to avoid confusion with A416 (Gd only). The sample is then taken out of the vacuum chamber for XRD characterisation.

7.5 X-Ray Diffraction

XRD ($\theta - 2\theta$) patterns were recorded in order to characterize the structural properties of the samples beyond the surface lattice parameters and surface symmetry given by RHEED. Figure 7.8(a) shows the XRD patterns of the samples discussed previously, except A415 (Gd/AlN) which was not measured. As expected, the Si(111) and AlN(0002) reflections from the template are visible in every sample. The capped samples also show the Al(222) reflection. The differences between these patterns are mostly noticeable in the region near 2θ~31°, where both Gd(0002) and GdN(111) are to be expected, and near 2θ~38.5° where the Al(222) reflection is visible. The key parameters extracted from the XRD patterns (after alignment with

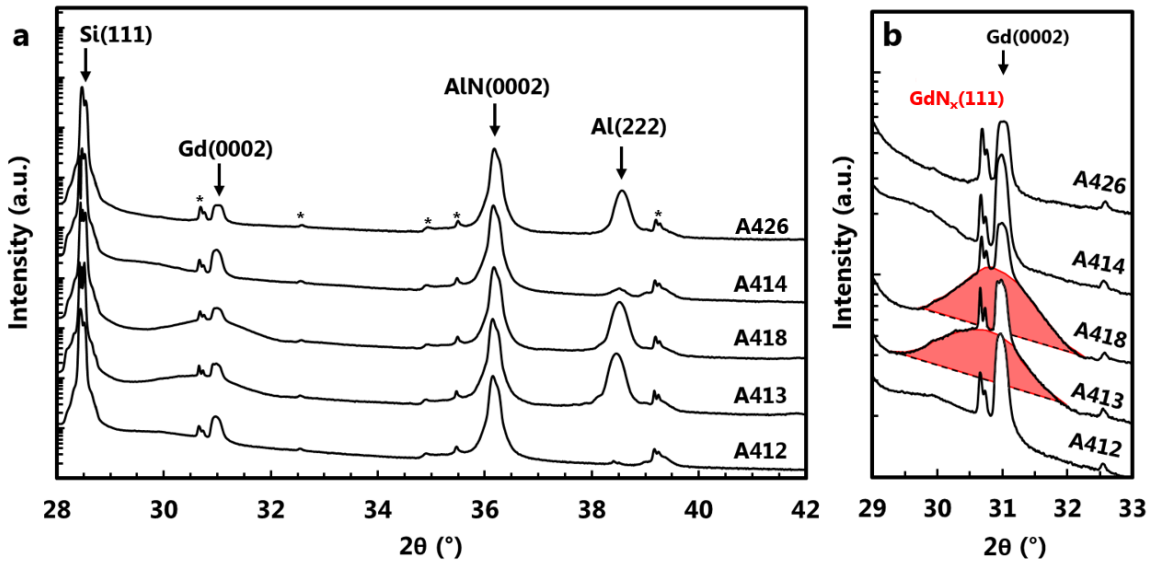

Figure 7.8: (a) XRD ($\theta - 2\theta$) of A412 (Gd/AlN), A413 ($P_{N2} = 1.1 \times 10^{-4}$ mbar, $\Delta t_{N2} = 40$ min), A418 ($P_{N2} = 2.0 \times 10^{-4}$ mbar, $\Delta t_{N2} = 40$ min), A414 (Gd exposed for 8 h in air, $P_{N2} = 1.1 \times 10^{-4}$ mbar, $\Delta t_{N2} = 40$ min) and A426 (Gd exposed for 5 min in air, $P_{N2} = 1.1 \times 10^{-4}$ mbar, $\Delta t_{N2} = 60$ min at 700°C). Asterisks indicate polychromaticity-induced reflections. (b) Magnification near $2\theta = 31°$, the hypothetical $GdN_x(111)$ reflections are highlighted in red when applicable.

Si(111), see chapter 2 for more details) are given in Table 7.3. Due to the undesired polychromaticity of the X-ray source, several weak sharp peaks can be observed in the diffraction patterns (indicated with asterisks) corresponding to Bragg reflections of Si(111) and AlN(0002) for other wavelengths than Cu_{K_α}. These reflections are therefore simply discarded.

Gd(0002) Fig. 7.8(b) magnifies the XRD patterns near $2\theta = 31°$. The Gd(0002) reflection is visible for all samples at $2\theta = 31.00 \pm 0.02°$. As discussed in section 2.2.5, the evaluation of the out-of-plane lattice constant of the crystals from XRD patterns uses Bragg law (equation 2.7). The value of $d_{(0002)} = 2.88$ Å is found for all samples, in close agreement with the bulk value of Gd (2.911 Å). Previously published Gd thin films grown on Si(100) [333] report hcp Gd(0002) at 2θ~30.8° and fcc Gd(111) at 2θ~29.1°. The XRD data here is therefore a strong indication of the presence of hcp Gd(0001) as opposed to fcc Gd(111). Further measurements (e.g. transmission electron microscopy) could further confirm the structural properties of Gd in real-space.

Peak	Gd	(0002)		GdN_x	(111)	
Sample	2θ (°)	β (°)	Area	2θ (°)	β (°)	Area
A412	30.99	0.20	106.6	-	-	-
A413	30.98	0.17	62.2	30.65	1.33	244.4
A418	30.99	0.20	59.7	30.90	1.13	242.8
A414	30.99	0.17	97.9	-	-	-
A425	31.00	0.19	79.4	-	-	-
A426	31.02	0.20	41.6	-	-	-

Table 7.3: Parameters extracted of Gd(0002) and GdN_x(111) using Gaussian fitting with linear background (peak position 2θ, full width at half-maximum β and area) from the XRD patterns for the different samples.

GdN_x(111) The XRD patterns of the samples nitrided with an observed decrease of the in-plane lattice constant (A413 and A418) contain a wide bulge at respectively $2\theta = 30.65°$ and 30.90° as observed clearly in Fig. 7.8 (b). Using eq. (2.7) one finds $d_{hkl} = 2.92$ Å and 2.89 Å, in good agreement with d_{111} of bulk GdN(111) (2.875 Å). The breadth of the peak here indicates a small coherence length within the crystallites [207]. Unfortunately, it is difficult to make an estimate of the crystallite size as the common standard of the Scherrer equation [207] is only applicable for powder samples or nano-crystalline bulk materials [337]. The reflection associated with GdN_x is not observed in other samples (A414 and A426) where RHEED did not evidence a change in the in-plane lattice parameter.

7.6 Discussion and conclusion

Gd(0001) thin films were successfully grown for the first time on AlN substrates. RHEED and XRD indicate a lattice constant in very close agreement with the bulk value of hcp Gd. The Gd layers were then either kept in UHV (A413 and A418) for immediate N_2 exposure, or exposed to air (A412 and A416) prior to nitridation attempts. The N_2 exposure of Gd(0001) thin films was investigated using RHEED and XRD.

A relative increase of the RHEED streak spacing was observed during N_2 exposure of the samples unexposed to air (A413 and A418) at room temperature, in agreement with a Gd(0001) surface incorporating nitrogen to form GdN_x. Interestingly, the in-plane lattice constant tends to decrease exponentially from the Gd value to a value close to bulk GdN(111). Caution is however required as the streak spacing is relatively scattered and shows some

discrepancy during N_2 exposure. Repeated measurements using an improved RHEED fitting algorithm could potentially address the N_2 dissociation and diffusion into a RE surface with more acuity (e.g. nitridation kinetics and perhaps the stoichiometry). The XRD patterns of the two samples suggest the formation of a new phase at a Bragg angle $2\theta = 30.8 \pm 0.2°$ in good agreement with bulk GdN(111). The relatively large width of the reflection attributed to GdN_x(111) suggests a small coherent length of the nitrided Gd crystals, however further tests should be undertaken for grain-size estimation (e.g. AFM and STM). This confirms the catalytic behaviour of Gd(0001) layers at room temperature to dissociate the otherwise very robust N_2 bond.

The exposure to air of the Gd(0001) thin films inevitably led to surface degradation as evidenced with the significant loss of contrast in the RHEED images, both after 8 h in air and 10 days in a vacuum sealed bag. The degradation of the Gd surface is attributed to oxidation, reported previously for Gd(0001) exposed to O_2 in UHV [336]. Both thermal treatments (450°C for 30 min and 700°C for 4.5 h) were not satisfactory to clean adequately the Gd thin films from the oxide, as the RHEED patterns did not show a clear improvement. The XRD and RHEED patterns of these samples did not evidence the formation of a crystalline N_2 induced phase. The catalytic breakdown behaviour of N_2 observed on pristine Gd(0001) (without exposure to air) is likely inactivated by the presence of a degraded Gd surface.

The Al capping layer is in agreement with the fcc bulk structure for the samples that indicated nitridation of the Gd layer (A413 and A418). However, results diverge for the samples initially exposed to air despite maintaining consistent Al deposition conditions. A degraded/polycrystalline surface was observed for the sample exposed to air initially for 8 h (A414). The sample that was stored in a vacuum sealed bag for 10 days showed the formation of a higher-quality Al structure with an expanded in-plane lattice (about +20 % with respect to bulk via RHEED). Further work will be required to elucidate whether or not it correspond to a different phase of Al.

The coexistence of Gd(0002) and GdN_x(111) reflections in A413 and A418 indicate that both RE and REN phases are present within the samples. The nitridation reaction is therefore only partial: not all the Gd layer has reacted with N_2 to form GdN, suggesting that the room temperature nitridation is partial. Furthermore, the present data does not allow the

determination of the stoichiometry x within the GdN_x phase. The type of stacking in the GdN_x is also unclear, bulk GdN(111) is fcc where the Gd layers follow ABCABC stacking (see the GdN structure in Fig. 7.2) which implies a stacking reconfiguration of the Gd(0001) layer upon N_2 exposure (hcp Gd(0001) planes follow ABAB stacking, see Fig. 7.2). This effect could be further investigated using other structural characterisation methods (e.g. XRD ϕ scans or TEM) and possibly predicted through DFT calculations.

Finally, a proof relying on other methods beyond structural characterisation techniques is required in order to indisputably confirm the presence of GdN in the N_2 exposed samples. GdN thin films are known for their ferromagnetic properties below T_C~70 K [56], and magnetisation measurements (underway) using SQUID should clarify this. Electrical characterisation (e.g. temperature dependent resistivity) of GdN_x should also allow the distinction between metallic Gd from semiconducting GdN. In case of a ferromagnetic transition, the value of the Curie temperature T_C may allow to estimate the stoichiometry x, known to raise up to T_c~200 K for N-deficient GdN [55]. Electrical measurements would however require an insulating cap (e.g. GaN or AlN) instead of a metallic one (Al) for horizontal configurations (e.g. van der Pauw).

To conclude, nitridation of Gd thin films was performed in UHV. The nitridation was only be possible without exposing the precursor Gd layer in air. Experimental realisation of a GdN layer at UC will not be enabled via nitridation of a Gd layer grown in the UHV lab at VUW due to the degradation the film would undergo during transport. A way to enable the nitridation of a Gd layer in a separate chamber may be through sputtering and annealing cycles in order to obtain a clean Gd(0001) surface as reported previously [299]. However it is not guaranteed that this technique would lead to a 'good-enough' Gd surface for nitridation. Using a removable capping layer (see chapters 5 and 6) is currently the most viable solution for ex-situ surface characterisation of GdN.

Chapter 8

Conclusion, outlook and further work

This conclusions chapter aims to give a conceptual overview of the work undertaken in this thesis. The general ideas are summarised, and their potential benefit to the fields of topotronics and spintronics are discussed. The detailed results and discussions of the methods developed in this thesis have been addressed in their respective chapters. Two different classes of materials were investigated in this thesis, the group-V 2D materials (in the context of VDWHs) and RENs. For this reason the conclusion is naturally separated in two sections below.

8.1 Topotronics and moiré patterns

Topology in 2D systems has attracted enormous attention in the condensed-matter physics community over the last few years. Materials including Bi and Sb are particularly investigated due to their non-trivial topologies. Their various 2D allotropes may be combined into nanostructured VDWHs and are expected to play an important role in future dissipation-less devices. To that effect we investigated with STM a variety of 2D Bi and Sb crystals grown on graphite and MoS_2. We set out to explore the moiré patterns (MPs) because of their potential to control the topology and electronic band-structure in other systems studied previously.

Ball-and-stick approach We first explored a simple superposition model based on ball and stick models. MPs were observed by STM in five VDWHs (α-Sb/α-Bi, β-Sb/α-Bi, MBi/α-Bi, α-Bi/HOPG and α-Bi/MoS_2) and were successfully modelled in terms of geometry (period

and angles). Only very small corrections of the lattice parameters (within experimental uncertainties) were necessary to obtain very good agreement with the STM observations. The simulations, previously demonstrated for hexagonal layers, were shown to be valid for other symmetries (rectangular/rectangular and mixed symmetry). When it was possible (rectangular/rectangular cases) the simulations were compared and agreed with Hermann's model.

General model The ball-and-stick approach is successful for modeling the MPs in all the VDWHs investigated, however the manual procedure that it requires is a bit cumbersome. For this reason a more general model based on reciprocal lattices was developed. The model views MP wave-vectors as a difference of reciprocal vectors; meaning for example that the MP period is large when the two vectors are close in the reciprocal space. The method was first tested on the widely studied case of twisted bilayer graphene. To show that it can be applied to other 2D materials and symmetries, it was tested against the five experimentally observed cases of this thesis and the agreement with experiments and the VESTA simulations was confirmed (also with Hermann's method when possible). Finally it was shown that the general model could be summarised in a simple compact analytical formula for the period and angle of any given MP emerging from any kind of 2D superposition. Understanding the MPs in the reciprocal space also gives an insight into their origin. Importantly, in all the systems studied here the rotation angle between the layers was observed at the value that generates a maximum of a MP period, presumable because this minimises strain between the two lattices. Whether this result applies more generally needs to be tested in a wider variety of systems. So far almost all the experimentally reported 2D materials in the literature crystallize into either hexagonal or rectangular symmetries, and thus the general model can potentially be applied to all VDWHs.

Prospects It is worth noting than since the start of this work, the condensed-matter physics field has seen the number of publications on MPs explode with huge interest in the community (including the demonstration of the many exotic phases of the twisted bilayer graphene) and it is possible that other examples of VDWHs will host a variety of new physics in which the MPs will play a crucial role. Testing the various MP models on other 2D systems would be necessary in the future, including group-V 2D materials but also others that include large

lattice mismatches, exotic symmetries and surface reconstructions. The general model is expected to benefit the field of the VDWHs both because it can model and interpret the MPs observed via STM experiments, but also because it could be used for prediction of MPs in arbitrary combinations of 2D materials. The periods and angles of the MPs in systems that are not yet realised can be predicted as well as the expected rotation angle in the VDWH pair. The obtained MP 'superlattice' dimensions could be integrated into DFT calculation schemes to predict the band structure of complex VDWHs.

8.2 Spintronics and RENs

Future spin information processing devices will rely on the development of intrinsic ferromagnetic semiconductors, among which the RENs are a promising family of materials. However, very little is known in terms of their surface properties. To that effect this thesis presents a technique that enables ex-situ surface-sensitive characterisation. A novel technique to achieve GdN thin films was also investigated, which involves the nitridation of a pure Gd layer.

Removable capping layer for GdN Epitaxial thin films of Sm acting as removable passivating layers were grown onto GdN thin films. Their effectiveness to protect the underlying GdN from degradation in ambient atmosphere was initially demonstrated. The thermal desorption of the cap without initial exposure to air was successfully achieved, and the properties of the recovered GdN layer were unchanged after decapping. However, when the Sm was exposed to air, the decapping procedure was not fully successful due to the formation of a Sm oxide layer. Debris, present on the surface of the sample after heat treatment, prevented AFM measurements. We proposed and developed an alternative method by introducing an argon ion sputtering step, prior to thermal desorption. The method was tested systematically, firstly by varying the beam energy and sputter current, and secondly by varying the sputtering time. The method was successful and the recovered underlying GdN was shown to be debris- and Sm-free for areas as large as 5×5 μm^2.

Capping layer prospects The removable capping layer method using a sequential sputtering/thermal desorption procedure has been shown to be very promising. As shown in this thesis, the technique enables AFM measurements of GdN for relatively large regions, opening avenues for further surface-sensitive measurements. Extending the technique to other members of the RENs is also a high priority, in the context of the broad REN research. Future experimental surface investigations will also possibly tell whether or not RENs possess topologically non-trivial properties, which have been suggested for LaN and GdN. Experiments such as ARPES and STM could possibly infer this, and these measurements would be a significant milestone in REN research.

Nitridation of Gd An alternative method to grow GdN was also investigated in this thesis. The procedure involved the exposure of an epitaxial Gd layer to molecular N_2 in a UHV environment. It was shown that GdN was effectively formed at room temperature with a N_2 pressure as low as 10^{-4} mbar. The procedure was also tested on Gd layers pre-exposed to air, but the oxide layer on the Gd surface appeared to prevent the nitridation reaction.

Gd nitridation outlook The nitridation of Gd, if confirmed by forthcoming measurements (magnetic and electrical characterisation mainly), may have significant scientific and technological potential. First, the growth of GdN at room temperature and at very low N_2 pressures is a simple and highly promising technique for the investigation of RENs in the future. One can also expect that nitridation might be a method for fabricating REN spintronic devices. Secondly, the possibility of reacting N_2 with Gd to form GdN indicates that the pure RE surface breaks down the nitrogen molecule at room temperature and low pressures, which could impact the nitrogen chemical industry, and in particular ammonia production [68, 69].

Bibliography

[1] R. P. Feynman. There's Plenty of Room at the Bottom. *Engineering and Science*, 5:22, 1960. http://calteches.library.caltech.edu/1976/.

[2] L. Xiu. Time Moore: Exploiting Moore's law from the perspective of time. *IEEE Solid-State Circuits Mag.*, 11:39, 2019. https://doi.org/10.1109/MSSC.2018.2882285.

[3] Taiwan Semiconductor Manufacturing Company Ltd. TSMC Breaks Ground on Fab 18 in Southern Taiwan Science Park. Retrieved from website 09/04/2019, 2018. https://www.tsmc.com/tsmcdotcom/PRListingNewsAction.do?action=detail&language=E&newsid=THGOHITHTH.

[4] E. Sperling. Quantum Effects At 7/5nm And Beyond. Retrieved from website 09/04/2019, 2018. https://semiengineering.com/quantum-effects-at-7-5nm/.

[5] M. M. Waldrop. The chips are down for Moore's law. *Nature*, 530:144, 2016. https://doi.org/10.1038/530144a.

[6] International Energy Agency. Digitalization and Energy. Retrieved from website 11/04/2019, 2017. https://www.iea.org/digital/.

[7] R. Danilak. Why Energy Is A Big And Rapidly Growing Problem For Data Centers. Retrieved from website 10/04/2019, 2017. https://www.forbes.com/sites/forbestechcouncil/2017/12/15/why-energy-is-a-big-and-rapidly-growing-problem-for-data-centers/#4b33a2835a30.

[8] N. Jones. How to stop data centres from gobbling up the world's electricity. *Nature*, 561:163, 2018. https://doi.org/10.1038/d41586-018-06610-y.

[9] A. W. Harrow and A. Montanaro. Quantum computational supremacy. *Nature*, 549:203, 2017. https://doi.org/10.1038/nature23458.

[10] John Preskill. Quantum Computing in the NISQ era and beyond. *Quantum*, 2:79, 2018. https://doi.org/10.22331/q-2018-08-06-79.

[11] S. J. Devitt. Performing quantum computing experiments in the cloud. *Phys. Rev. A*, 94:032329, 2016. https://doi.org/10.1103/PhysRevA.94.032329.

[12] V Kose. *Superconducting quantum electronics*. 1989. https://doi.org/10.1007/978-3-642-95592-1.

[13] M. H. Devoret and R. J. Schoelkopf. Superconducting Circuits for Quantum Information: An Outlook. *Science*, 339:1169, 2013. https://doi.org/10.1126/science.1231930.

[14] Y. Makhlin, G. Schön, and A. Shnirman. Quantum-state engineering with Josephson-junction devices. *Rev. Mod. Phys.*, 73:357, 2001. https://doi.org/10.1103/RevModPhys.73.357.

[15] C. Mead. Neuromorphic electronic systems. *Proc. IEEE*, 78:1629, 1990. https://doi.org/10.1109/5.58356.

[16] P. A. Merolla, J. V. Arthur, R. Alvarez-Icaza, A. S. Cassidy, J. Sawada, F. Akopyan, B. L. Jackson, N. Imam, C. Guo, Y. Nakamura, B. Brezzo, I. Vo, S. K. Esser, R. Appuswamy, B. Taba, A. Amir, M. D. Flickner, W. P. Risk, R. Manohar, and D. S. Modha. A million spiking-neuron integrated circuit with a scalable communication network and interface . *Science*, 345:668, 2014. https://doi.org/10.1126/science.1254642.

[17] G. Indiveri, B. Linares-Barranco, T. J. Hamilton, A. van Schaik, R. Etienne-Cummings, T. Delbruck, S.-C. Liu, P. Dudek, P. Häfliger, S. Renaud, J. Schemmel, G. Cauwenberghs, J. Arthur, K. Hynna, F. Folowosele, S. Saighi, T. Serrano-Gotarredona, J. Wijekoon, Y. Wang, and K. Boahen. Neuromorphic silicon neuron circuits. *Front. Neurosci.*, 5:73, 2011. https://doi.org/10.3389/fnins.2011.00073.

[18] C. Joachim, J. K. Gimzewski, and A. Aviram. Electronics using hybrid-molecular and mono-molecular devices. *Nature*, 408:541, 2000. https://doi.org/10.1038/35046000.

[19] A. Aviram and M. A. Ratner. Molecular Rectifiers. *Chem. Phys. Lett.*, 29:277, 1974. https://doi.org/10.1016/0009-2614(74)85031-1.

[20] H. Jeong, D. Kim, D. Xiang, and T. Lee. High-Yield Functional Molecular Electronic Devices. *ACS Nano*, 11:6511, 2017. https://doi.org/10.1021/acsnano.7b02967.

[21] M. Fuechsle, J. A. Miwa, S. Mahapatra, H. Ryu, S. Lee, O. Warschkow, L. C. L. Hollenberg, G. Klimeck, and M. Y. Simmons. A single-atom transistor. *Nat. Nanotech.*, 7:242, 2012. https://doi.org/10.1038/nnano.2012.21.

[22] F. Xie, A. Peukert, T. Bender, C. Obermair, F. Wertz, P. Schmieder, and T. Schimmel. Quasi-Solid-State Single-Atom Transistors. *Adv. Mater.*, 30:1801225, 2018. https://doi.org/10.1002/adma.201801225.

[23] G. P. Lansbergen. Transistors arrive at the atomic limit. *Nat. Nanotech.*, 7:209, 2012. https://doi.org/10.1038/nnano.2012.23.

[24] C. Chappert, A. Fert, and F. Nguyen Van Dau. The emergence of spin electronics in data storage. *Nat. Mater.*, 6:813, 2007. https://www.nature.com/articles/nmat2024.

[25] X.-L. Qi. The Quantum spin Hall effect and topological insulators. *Phys. Today*, 63:33, 2010. https://doi.org/10.1063/1.3293411.

[26] A. Fert. Nobel Lecture: Origin, development, and future of spintronics. *Rev. Mod. Phys.*, 80:1517, 2008. https://doi.org/10.1103/RevModPhys.80.1517.

[27] S. A. Wolf, D. D. Awschalom, R. A. Buhrman, J. M. Daughton, S. von Molnár, M. L. Roukes, A. Y. Chtchelkanova, and D. M. Treger. Spintronics: A Spin-Based Electronics Vision for the Future. *Science*, 294:1488, 2001. https://doi.org/10.1126/science.1065389.

[28] K. Michaeli, V. Varade, R. Naaman, and D. H. Waldeck. A new approach towards spintronics-spintronics with no magnets. *J. Phys.: Condens. Matter*, 29:103002, 2017. https://doi.org/10.1088/1361-648X/aa54a4.

[29] V. V. Kruglyak, S. O. Demokritov, and D. Grundler. Magnonics. *J. Phys. D: Appl. Phys.*, 43:264001, 2010. https://doi.org/10.1088/0022-3727/43/26/264001.

[30] A. Fert, V. Cros, and J. Sampaio. Skyrmions on the track. *Nat. Nanotechnol.*, 8:152, 2013. https://doi.org/10.1038/nnano.2013.29.

[31] C. Kittel. *Introduction To Solid State Physics, 8th Edition: Chapter 2, Wave Diffraction and the Reciprocal Lattice*. John Wiley & Sons, Inc, 1986. https://books.google.co.nz/books?id=JrPvAAAAMAAJ.

[32] M. N. Baibich, J. M. Broto, A. Fert, F. Nguyen Van Dau, F. Petroff, P. Eitenne, G. Creuzet, A. Friederich, and J. Chazelas. Giant Magnetoresistance of (001)Fe/(001)Cr Magnetic Superlattices. *Phys. Rev. Lett.*, 61:2472, 1988. https://doi.org/10.1103/PhysRevLett.61.2472.

[33] S. Parkin. Spin-polarized current in spin valves and magnetic tunnel junctions. *MRS Bulletin*, 31:389, 2006. https://doi.org/10.1557/mrs2006.99.

[34] J. Fabian, A. Matos-Abiague, C. Ertler, P. Stano, and I. Zutic. Semiconductor Spintronics. *Acta Phys. Slovaca*, 57:565, 2007. https://doi.org/10.2478/v10155-010-0086-8.

[35] Y. Ohno, D. K. Young, B. Beschoten, F. Matsukura, H. Ohno, and D. D. Awschalom. Electrical spin injection in a ferromagnetic semiconductor heterostructure. *Nature*, 402:790, 1999. https://doi.org/10.1038/45509.

[36] T. Valet and A. Fert. Theory of the perpendicular magnetoresistance in magnetic multilayers. *Phys. Rev. B*, 48:7099, 1993. https://doi.org/10.1103/PhysRevB.48.7099.

[37] G. Schmidt, D. Ferrand, L. W. Molenkamp, A. T. Filip, and B. J. van Wees. Fundamental obstacle for electrical spin injection from a ferromagnetic metal into a diffusive semiconductor. *Phys. Rev. B*, 62:R4790(R), 2000. https://doi.org/10.1103/PhysRevB.62.R4790.

[38] P. Chuang, S.-C. Ho, L. W. Smith, F. Sfigakis, M. Pepper, C.-H. Chen, J.-C. Fan, J. P. Griffiths, I. Farrer, H. E. Beere, G. A. C. Jones, D. A. Ritchie, and T.-M. Chen. All-electric all-semiconductor spin field-effect transistors. *Nat. Nanotechnol.*, 10:35, 2015. https://doi.org/10.1038/nnano.2014.296.

[39] A. Slachter, F. L. Bakker, J-P. Adam, and B. J. van Wees. Thermally driven spin injection from a ferromagnet into a non-magnetic metal. *Nat. Phys.*, 6:879, 2010. https://doi.org/10.1038/nphys1767.

[40] A. Oiwa, Y. Mitsumori, R. Moria, T. Slupinski, and H. Munekata. Effect of Optical Spin Injection on Ferromagnetically Coupled Mn Spins in the III-V Magnetic Alloy Semiconductor (Ga,Mn)As. *Phys. Rev. Lett.*, 88:137202, 2002. https://doi.org/10.1103/PhysRevLett.88.137202.

[41] S. Datta and B. Das. Electronic analog of the electro-optic modulator. *Appl. Phys. Lett.*, 56:665, 1990. https://doi.org/10.1063/1.102730.

[42] S. Datta. How we proposed the spin transistor. *Nat. Electron.*, 1:604, 2018. https://doi.org/10.1038/s41928-018-0163-4.

[43] J. Linder and J. W. A. Robinson. Superconducting spintronics. *Nat. Phys.*, 11:307, 2015. https://doi.org/10.1038/nphys3242.

[44] H. Ohno. (Ga,Mn)As: A new diluted magnetic semiconductor based on GaAs. *Appl. Phys. Lett.*, 69:363, 1996. https://doi.org/10.1063/1.118061.

[45] T. Dietl, H. Ohno, F. Matsukura, J. Cibert, and D. Ferrand. Zener Model Description of Ferromagnetism in Zinc-Blende Magnetic Semiconductors. *Science*, 287:1019, 2000. https://doi.org/10.1126/science.287.5455.1019.

[46] K. Y. Wand, R. P. Campion, K. W. Edmonds, M. Sawicki, T. Dietl, C. T. Foxon, and B. L. Gallagher. Magnetism in (Ga,Mn)As Thin Films With T C Up To 173K. *AIP Proc.*, 772:333, 2005. https://doi.org/10.1063/1.1994124.

[47] T. Dietl and H. Ohno. Dilute ferromagnetic semiconductors: Physics and spintronic structures. *Rev. Mod. Phys.*, 86:187, 2014. https://doi.org/10.1103/RevModPhys.86.187.

[48] F. Matsukura and H. Ohno. *Nanomagnetism and Spintronics: Chapter 7, III-V-Based Ferromagnetic Semiconductors*, volume 4. Elsevier B. V., 2009. https://doi.org/10.1016/B978-0-444-53114-8.00007-8.

[49] K. H. Lee, S. Bao, L. Zhang, D. Kohen, E. Fitzgerald, and C. S. Tan. Integration of GaAs, GaN and Si-CMOS on a common 200 mm Si substrate through multilayer transfer process. *Appl. Phys. Exp.*, 9:086501, 2016. https://doi.org/10.7567/APEX.9.086501.

[50] F. Natali, B. J. Ruck, N. O. V. Plank, H. J. Trodahl, S. Granville, C. Meyer, and W. R. L. Lambrecht. Rare-earth mononitrides. *Prog. Mater. Sci.*, 58:1316, 2013. https://doi.org/10.1016/j.pmatsci.2013.06.002.

[51] A. Schmehl, V. Vaithyanathan, A. Herrnberger, S. Thiel, C. Richter, M. Liberati, T. Heeg, M. Röckerath, L. F. Kourkoutis, S. Mühlbauer, P. Böni, D. A. Muller, Y. Barash, J. Schubert, Y. Idzerda, J. Mannhart, and D. G. Schlom. Epitaxial integration of the highly spin-polarized ferromagnetic semiconductor EuO with silicon and GaN. *Nat. Mater.*, 6:882, 2007. https://doi.org/10.1038/nmat2012.

[52] S. Van Houten. Magnetic interaction in EuS, EuSe, and EuTe. *Phys. Lett.*, 2:215, 1962. https://doi.org/10.1016/0031-9163(62)90231-7.

[53] J. Nakai, S. Kunii, and E. Hirahara. Antiferromangetic Resonance of Europium Telluride. *J. Phys. Soc. Jpn*, 34:917, 1973. https://doi.org/10.1143/JPSJ.34.917.

[54] F. Natali, N. O. V. Plank, J. Galipaud, B. J. Ruck, H. J. Trodahl, F. Semond, S. Sorieul, and L. Hirsch. Epitaxial growth of GdN on silicon substrate using an AlN buffer layer. *J. Cryst. Growth*, 312:3583, 2010. http://doi.org/10.1016/j.jcrysgro.2010.09.030.

[55] N. O. V. Plank, F. Natali, J. Galipaud, J. H. Richter, M. Simpson, H. J. Trodahl, and B. J. Ruck. Enhanced Curie temperature in N-deficient GdN. *Appl. Phys. Lett.*, 98:112503, 2011. https://doi.org/10.1063/1.3566996,.

[56] F. Natali, S. Vézian, S. Granville, B. Damilano, H. J. Trodahl, E.-M. Anton, H. Warring, F. Semond, Y. Cordier, S. V. Chong, and B. J. Ruck. Molecular beam epitaxy of ferromagnetic epitaxial GdN thin films. *J. Cryst. Growth*, 404:146, 2014. https://doi.org/10.1016/j.jcrysgro.2014.07.010.

[57] F. Natali, B. Ludbrook, J. Galipaud, N. Plank, S. Granville, A. Preston, B. Le Do, J. Richter, I. Farrell, R. Reeves, S. Durbin, J. Trodahl, and B. Ruck. Epitaxial growth and properties of GdN, EuN and SmN thin films. *Phys. Status Solidi C*, 9:605–608, 2011. http://doi.org/10.1002/pssc.201100363.

[58] H. Yoshitomi, S. Kitayama, T. Kia, O. Wada, M. Fujisawa, H. Ohta, and T. Sakurai. Optical and magnetic properties in epitaxial GdN thin films. *Phys. Rev. B*, 83:155202, 2011. http://doi.org/10.1103/PhysRevB.83.155202.

[59] T.-Y Lee, D. Gall, C.-S Shin, N. Hellgren, I. Petrov, and J. E. Greene. Growth and physical properties of epitaxial CeN layers on MgO(001). *J. Appl. Phys.*, 94:921, 2003. http://doi.org/10.1063/1.1579113.

[60] J. W. Gerlach, J. Mennig, and B. Rauschenbach. Epitaxial gadolinium nitride thin films. *Appl. Phys. Lett.*, 90:061919, 2007. http://doi.org/10.1063/1.2472538.

[61] J. H. Richter, B. J. Ruck, M. Simpson, F. Natali, N. O. V. Plank, M. Azeem, H. J. Trodahl, A. R. H. Preston, B. Chen, J. McNulty, K. E. Smith, A. Tadich, B. Cowie, A. Svane, M. van Schilfgaarde, and W. R. L. Lambrecht. Electronic structure of EuN: Growth, spectroscopy, and theory. *Phys. Rev. B*, 84:235120, 2011. https://doi.org/10.1103/PhysRevB.84.235120.

[62] S. Vézian, B. Damilano, F. Natali, M. Al Khalfioui, and J. Massies. AlN interlayer to improve the epitaxial growth of SmN on GaN (0001). *J. Cryst. Growth*, 450:22, 2016. https://doi.org/10.1016/j.jcrysgro.2016.06.006.

[63] J. R. Chan, S. Vézian, J. Trodahl, M. Al Khalfioui, B. Damilano, and F. Natali. Temperature-Induced Four-Fold-on-Six-Fold Symmetric Heteroepitaxy, Rocksalt SmN on Hexagonal AlN. *Cryst. Growth Des.*, 16:6454, 2016. http://doi.org/10.1021/acs.cgd.6b01133.

[64] S. Sanna, C. Dues, W. G. Schmidt, F. Timmer, J. Wollschläger, M. Franz, S. Appelfeller, and M. Dähme. Rare-earth silicide thin films on the Si(111) surface. *Phys. Rev. B*, 93:195407, 2016. https://doi.org/10.1103/PhysRevB.93.195407.

[65] F. Timmer, R. Oelke, C. Dues, W. G. Schmidt, M. Franz, S. Appelfeller, M. Dähne, and J. Wollschläger. Strain-induced quasi-one-dimensional rare-earth silicide structures on Si(111). *Phys. Rev. B*, 94:205431, 2016. https://doi.org/10.1103/PhysRevB.94.205431.

[66] S. Cwik, S. M. J. Beer, S. Hoffmann, M. Krasnopolski, D. Rogalla, H.-W. Becker, D. Peeters, A. Ney, and A. Devi. Integrating AlN with GdN Thin Films in an in Situ CVD Process: Influence on the Oxidation and Crystallinity of GdN. *ACS Appl. Mater. Interf.*, 9:27036, 2017. https://doi.org/10.1021/acsami.7b08221.

[67] T. B. Thiede, M. Krasnopolski, A. P. Milanov, T. de los Arcos, A. Ney, H.-W. Becker, D. Rogalla, J. Winter, A. Devi, and R. A. Fischer. Evaluation of Homoleptic Guanidinate and Amidinate Complexes of Gadolinium and Dysprosium for MOCVD of Rare-Earth Nitride Thin Films. *Chem. Mater.*, 23:1430, 2011. http://doi.org/10.1021/cm102840v.

[68] F. Ullstad, G. Bioletti, J. R. Chan, A. Proust, C. Bodin, B. J. Ruck, J. Trodahl, and F. Natali. Breaking Molecular Nitrogen under Mild Conditions with an Atomically Clean Lanthanide Surface. *ACS Omega*, 4:5950, 2019. https://doi.org/10.1021/acsomega.9b00293.

[69] F. Natali, B. J. Ruck, and H. J. Trodahl. Ammonia production method and apparatus for ammonia production. European Patent Application Number EP17179326.8.

[70] F. Natali, B. J. Ruck, H. J. Trodahl, D. Le Binh, S. Vezian, B. Damilano, Y. Cordier, F. Semond, and C. Meyer. Role of magnetic polarons in ferromagnetic GdN. *Phys. Rev. B*, 87:035202, 2013. https://doi.org/10.1103/PhysRevB.87.035202.

[71] H.J. Trodahl, A. R. H. Preston, J. Zhong, B. J. Ruck, N. M., Strickland, C. Mitra, and W. R. L. Lambrecht. Ferromagnetic redshift of the optical gap in GdN. *Phys. Rev. B*, 76:085211, 2007. https://doi.org/10.1103/PhysRevB.76.085211.

[72] P. Larson, W. R. L. Lambrecht, A. Chantis, and M. van Schilfgaarde. Electronic structure of rare-earth nitrides using the LSDA+U approach: Importance of allowing 4f orbitals to break the cubic crystal symmetry. *Phys. Rev. B*, 75:045114, 2007. https://doi.org/10.1103/PhysRevB.75.045114.

[73] F. Hulliger. Magnetic properties of the rare earth pnictides. *J. Magn. Magn. Mater*, 8:183, 1978. https://doi.org/10.1016/0304-8853(78)90121-X.

[74] E.-M. Anton, J. F. McNulty, B. J. Ruck, M. Suzuki, M. Mizumaki, V. N. Antonov, J. W. Quilty, N. Strickland, and H. J. Trodahl. NdN: An intrinsic ferromagnetic semiconductor. *Phys. Rev. B*, 93:064431, 2016. https://doi.org/10.1103/PhysRevB.93.064431.

[75] C. Meyer, B. J. Ruck, J. Zhong, S. Granville, A. R. H. Preston, G. V. M. Williams, and H. J. Trodahl. Near-zero-moment ferromagnetism in the semiconductor SmN. *Phys. Rev. B*, 78:174406, 2008. http://doi.org/10.1103/PhysRevB.78.174406.

[76] D. L. Cortie, J. D. Brown, S. Brück, T. Saerbeck, J. P. Evans, H. Fritzche, X. L. Wang, J. E. Downes, and F. Klose. Intrinsic reduction of the ordered $4f$ magnetic moments in semiconducting rare-earth nitride thin films: DyN, ErN, and HoN. *Phys. Rev. B*, 89:064424, 2014. https://doi.org/10.1103/PhysRevB.89.064424.

[77] H. Warring, B. J. Ruck, J. F. McNulty, E.-M. Anton, S. Granville, A. Koo, B. Cowie, and H. J. Trodahl. YbN: An intrinsic semiconductor with antiferromagnetic exchange. *Phys. Rev. B*, 90:245206, 2014. https://doi.org/10.1103/PhysRevB.90.245206.

[78] D. Le Binh, B. J. Ruck, F. Natali, H. Warring, H. J. Trodahl, E.-M. Anton, C. Meyer, L. Ranno, F. Wilhelm, and A. Rogalev. Europium Nitride: A Novel Diluted Magnetic Semiconductor. *Phys. Rev. Lett.*, 111:167206, 2013. https://doi.org/10.1103/PhysRevLett.111.167206.

[79] P. Wachter and E. Kaldis. Magnetic interaction and carrier concentration in GdN and $GdN_{1-x}O_x$. *Solid State Commun.*, 34:241, 1980. https://doi.org/10.1016/0038-1098(80)90401-9.

[80] P. Larson and W. R. L. Lambrecht. Electronic structure and magnetism of europium chalcogenides in comparison with gadolinium nitride. *J. Phys.: Condens. Matter*, 18:11333, 2006. https://doi.org/10.1088/0953-8984/18/49/024.

[81] E.-M. Anton, B. J. Ruck, C. Meyer, F. Natali, H. Warring, F. Wilhelm, A. Rogalev, V. N. Antonov, and H. J. Trodahl. Spin/orbit moment imbalance in the near-zero moment ferromagnetic semiconductor SmN. *Phys. Rev. B*, 87:134414, 2013. https://doi.org/10.1103/PhysRevB.87.134414.

[82] R. Vidyasagar, T. Kita, T. Sakurai, T. Shimokawa, and H. Ohta. Ferromagnetic resonance features of degenerate GdN semiconductor. *Phys. Lett. A*, 381:1905, 2017. https://doi.org/10.1016/j.physleta.2017.03.031.

[83] M. Azeem, B. J. Ruck, B. D. Le, H. Warring, H. J. Trodahl, N. M. Strickland, A. Koo, V. Goian, and S. Kambda. Optical response of DyN. *J. Appl. Phys.*, 113:203509, 2013. https://doi.org/10.1063/1.4807647.

[84] R. Vidyasagar, S. Kitayama, H. Yoshitomi, T. Kita, T. Sakurai, and H. Ohta. Tuning optical and ferromagnetic properties of thin GdN films by nitrogen-vacancy centers. *Eur. Phys. J. B*, 86:52, 2013. https://doi.org/10.1140/epjb/e2012-30566-3.

[85] R. Vidyasagar, T. Kita, T. Sakurai, and H. Ohta. Electronic transitions in GdN band structure. *J. Appl. Phys.*, 115:203717, 2014. https://doi.org/10.1063/1.4880398.

[86] C.-M. Lee, H. Warring, S. Vézian, B. Damilano, S. Granville, M. Al Khalfioui, Y. Cordier, H. J. Trodahl, B. J. Ruck, and F. Natali. Highly resistive epitaxial Mg-doped GdN thin films. *Appl. Phys. Lett.*, 106:022401, 2015. https://doi.org/10.1063/1.4905598.

[87] C.-M. Lee, J. Schacht, H. Warring, H. J. Trodahl, B. J. Ruck, S. Vézian, N. Gaston, and F. Natali. Experimental and *ab initio* study of Mg doping in the intrinsic ferromagnetic semiconductor GdN. *J. Appl. Phys.*, 123:115106, 2018. https://doi.org/10.1063/1.5020081.

[88] B. M. Ludbrook, I. L. Farrell, M. Kuebel, B. J. Ruck, A. R. H. Preston, H. J. Trodahl, L. Ranno, R. J. Reeves, and S. M. Durbin. Growth and properties of epitaxial GdN. *J. Appl. Phys.*, 106:063910, 2009. https://doi.org/10.1063/1.3211290.

[89] E.-M. Anton, S. Granville, A. Engel, S. V. Chong, M. Governale, U. Zülicke, A. G. Moghaddam, H. J. Trodahl, F. Natali, S. Vézian, and B. J. Ruck. Superconductivity in the ferromagnetic semiconductor samarium nitride. *Phys. Rev. B*, 94:024106, 2016. http://doi.org/10.1103/PhysRevB.94.024106.

[90] A. R. H. Preston, B. J. Ruck, W. R. L. Lambrecht, L. F. J. Piper, J. E. Downes, K. E. Smith, and H. J. Trodahl. Electronic band structure information of GdN extracted from x-ray absorption and emission spectroscopy. *Appl. Phys. Lett.*, 96:032101, 2010. https://doi.org/10.1063/1.3291057.

[91] M. Zeng, C. Fang, G. Chang, Y.-A. Chen, T. Hsieh, A. Bansil, H. Lin, and L. Fu. Topological semimetals and topological insulators in rare earth monopnictides. *arXiv*, 1504.03492, 2015. https://arxiv.org/abs/1504.03492.

[92] Z. Li, J. Kim, N. Kioussis, S.-Y. Ning, H. Su, T. Iitaka, T. Tohyama, X. Yang, and J.-X. Zhang. GdN thin film: Chern insulating state on square lattice. *Phys. Rev. B*, 92:201303(R), 2015. https://doi.org/10.1103/PhysRevB.92.201303.

[93] J. Kim, H.-S. Kim, and D. Vanderbilt. Nearly triple nodal point topological phase in half-metallic GdN. *Phys. Rev. B*, 98:155122, 2018. https://doi.org/10.1103/PhysRevB.98.155122.

[94] F. Natali, J. Trodahl, S. Vézian, A. Traverson, B. Damilano, and B. Ruck. Epitaxial GdN/SmN-based superlattices grown by molecular beam epitaxy. *MRS Advances*, 2:189, 2017. https://doi.org/10.1557/adv.2017.147.

[95] H. Warring, H. J. Trodahl, N. O. V. Plank, F. Natali, S. Granville, and B. J. Ruck. Magnetic Tunnel Junctions Incorporating a Near-Zero-Moment Ferromagnetic Semiconductor. *Phys. Rev. Applied*, 6:044002, 2016. https://doi.org/10.1103/PhysRevApplied.6.044002.

[96] K. Senapati, M. G. Blamire, and Z. H. Barber. Spin-filter Josephson junctions. *Nat. Mater.*, 10:849, 2011. http://doi.org/10.1038/nmat3116.

[97] K. Senapati. Superconducting and normal state tunneling in NbN-GdN-NbN junctions. *AIP Conf. Proceed.*, 1512:1316, 2016. https://doi.org/10.1063/1.4791542.

[98] A. Kandala, A. Richardella, D. W. Rench, D. M. Zhang, T. C. Flanagan, and N. Samarth. Growth and Characterization of Hybrid Insulating Ferromagnet-Topological Insulator Heterostructure Devices. *Appl. Phys. Lett.*, 103:202409, 2013. http://doi.org/10.1063/1.4831987.

[99] L. Fu and C. L. Kane. Topological insulators with inversion symmetry. *Phys. Rev. B*, 76:045302, 2007. http://doi.org/10.1103/PhysRevB.76.045302.

[100] M. Z. Hasan and C. L. Kane. Colloquium: Topological insulators. *Rev. Mod. Phys.*, 82:3045, 2010. https://doi.org/10.1103/RevModPhys.82.3045.

[101] X.-L. Qi and S.-C. Zhang. Topological insulators and superconductors. *Rev. Mod. Phys.*, 83:1057, 2011. https://doi.org/10.1103/RevModPhys.83.1057.

[102] K. v. Klitzing, G. Dorda, and M. Pepper. New Method for High-Accuracy Determination of the Fine-Structure Constant Based on Quantized Hall Resistance. *Phys. Rev. Lett.*, 45:494, 1980. https://doi.org/10.1103/PhysRevLett.45.494.

[103] D. C. Tsui, H. L. Stormer, and A. C. Gossard. Two-Dimensional Magnetotransport in the Extreme Quantum Limit. *Phys. Rev. Lett.*, 48:1559, 1982. https://doi.org/10.1103/PhysRevLett.48.1559.

[104] J. Sinova, S. O. Valenzuela, J. Wunderlich, C. H. Back, and T. Jungwirth. Spin Hall effects. *Rev. Mod. Phys.*, 87:1213, 2015. https://doi.org/10.1103/RevModPhys.87.1213.

[105] C. L. Kane. *Contemporary Concepts of Condensed Matter Science: Topological insulators. Part 1, "Theoretical Foundations"*, volume 6. Elsevier B. V., 2013. http://doi.org/10.1016/B978-0-444-63314-9.00001-9.

[106] C. L. Kane and E. J. Mele. Quantum Spin Hall Effect in Graphene. *Phys. Rev. Lett.*, 95:226801, 2005. http://doi.org/10.1103/PhysRevLett.95.226801.

[107] C. L. Kane and E. J. Mele. Z_2 Topological Order and the Quantum Spin Hall Effect. *Phys. Rev. Lett.*, 95:146802, 2005. https://doi.org/10.1103/PhysRevLett.95.146802.

[108] D. J. Thouless, M. Kohmoto, M. P. Nightingale, and M. den Nijs. Quantized Hall Conductance in a Two-Dimensional Periodic Potential. *Phys. Rev. Lett.*, 49:405, 1982. https://doi.org/10.1103/PhysRevLett.49.405.

[109] X.-G. Wen. Topological orders and edge excitations in fractional quantum Hall states. *Adv. Phys.*, 44:405, 1995. http://doi.org/10.1080/00018739500101566.

[110] X. Peng, A. Copple, and Q. Wei. Edge effects on the electronic properties of phosphorene nanoribbons. *J. Appl. Phys.*, 116:144301, 2014. https://doi.org/10.1063/1.4897461.

[111] D. Hsieh, D. Qian, L. Wray, Y. Xia, Y. S. Hor, R. J. Cava, and M. Z. Hasan. A topological Dirac insulator in a quantum spin Hall phase. *Nature*, 452:970, 2008. http://doi.org/10.1038/nature06843.

[112] Y. Xia, D. Qian, D. Hsieh, L. Wray, A. Pal, H. Lin, A. Bansil, D. Grauer, Y. S. Hor, R. J. Cava, and M. Z. Hasan. Observation of a large-gap topological-insulator class with a single Dirac cone on the surface. *Nat. Phys.*, 5:398, 2009. https://doi.org/10.1038/nphys1274.

[113] Y. L. Chen et al. Experimental Realization of a Three-Dimensional Topological Insulator, Bi_2Te_3. *Science*, 325:178, 2009. https://doi.org/10.1126/science.1173034.

[114] S. Ito, B. Feng, M. Arita, A. Takayama, R.-Y. Liu, T. Someya, W.-C. Chen, T. Iimori, H. Namatame, M. Taniguchi, C.-M. Cheng, S.-J. Tang, F. Komori, K. Kobayashi, T.-C. Chiang, and I. Matsuda. Proving Nontrivial Topology of Pure Bismuth by Quantum Confinement. *Phys. Rev. Lett.*, 117:236402, Dec 2016. https://doi.org/10.1103/PhysRevLett.117.236402.

[115] F.Schindler, Z. Wang, M. G. Vergniory, A. Murani A. M. Cook, S. Sengupta, A. Y. Kasumov, R. Deblock, S. Jeon, I. Drozdov, H. Bouchiat, S. Guéron, A. Yazdani, B. A. Bernevig, and Titus Neupert. Higher-order topology in bismuth. *Nat. Phys.*, 14:918, 2018. https://doi.org/10.1038/s41567-018-0224-7.

[116] D. Hsieh, Y. Xia, L. Wray, D. Qian, A. Pal, J. H. Dil, J. Osterwalder, F. Meier, G. Bihlmayer, C. L. Kane, Y. S. Hor, R. J. Cava, and M. Z. Hasan. Observation of Unconventional Quantum Spin Textures in Topological Insulators. *Science*, 323:919, 2009. https://doi.org/10.1126/science.1167733.

[117] M. König, S. Wiedmann, C. Brüne, A. Roth, H. Buhmann, L. W. Molenkamp, X.-L. Qi, and S.-C. Zhang. Quantum Spin Hall Insulator State in HgTe Quantum Wells. *Science*, 318:766, 2007. https://doi.org/10.1126/science.1148047.

[118] B. A. Bernevig, T. L. Hughes, and S.-C. Zhang. Quantum Spin Hall Effect and Topological Phase Transition in HgTe Quantum Wells. *Science*, 314:1757, 2006. https://doi.org/10.1126/science.1133734.

[119] I. Knez, R.-R. Du, and G. Sullivan. Evidence for Helical Edge Modes in Inverted InAs/GaSb Quantum Wells. *Phys. Rev. Lett.*, 107:136603, 2011. https://doi.org/10.1103/PhysRevLett.107.136603.

[120] X. Wang, C. Xu, H. Hu, P. Wang, G. Bian, W. Tan, S. A. Brown, and T.-C. Chiang. Topological phase stability and transformation of bismuthene. *Europhys. Lett.*, 119:27002, 2017. https://doi.org/10.1209/0295-5075/119/27002.

[121] G. Bian, T. Miller, and T.-C. Chiang. Passage from Spin-Polarized Surface States to Unpolarized Quantum Well States in Topologically Nontrivial Sb Films. *Phys. Rev. Lett.*, 107:036802, 2011. https://doi.org/10.1103/PhysRevLett.107.036802.

[122] P.-F. Zhang, Z. Liu, W. Duan, F. Liu, and J. Wu. Topological and electronic transitions in a Sb(111) nanofilm: The interplay between quantum confinement and surface effect. *Phys. Rev. B*, 85:201410, May 2012. https://doi.org/10.1103/PhysRevB.85.201410.

[123] K. S. Novoselov, A. K. Geim, S. V. Morozov, D. Jiang, Y. Zhang, S. V. Dubonos, I. V. Grigorieva, and A. A. Firsov. Electric Field Effect in Atomically Thin Carbon Films. *Science*, 306:666, 2004. https://doi.org/10.1126/science.1102896.

[124] B Lalmi, H. Oughaddou, H. Enriquez, A. Kara, S. Vizzini, B. Ealet, and B. Aufray. Epitaxial growth of a silicene sheet. *Appl. Phys. Lett.*, 97:223109, 2010. http://doi.org/10.1063/1.3524215.

[125] M. E. Dávila, L. Xian , S. Cahangirov , A. Rubio , and G. Le Lay. Germanene: a novel two-dimensional germanium allotrope akin to graphene and silicene. *New J. Phys.*, 16:095002, 2014. http://doi.org/10.1088/1367-2630/16/9/095002.

[126] F.-F. Zhu, W.-J. Chen, Y. Xu, C.-L. Gao, D.-D. Guan, C.-H. Liu, D. Qian, S.-C. Zhang, and J.-F. Jia. Epitaxial growth of two-dimensional stanene. *Nat. Mater.*, 14:1020, 2015. https://doi.org/10.1038/nmat4384.

[127] K. Watanabe, T Taniguchi, and H. Kanda. Direct-bandgap properties and evidence for ultraviolet lasing of hexagonal boron nitride single crystal. *Nat. Mater.*, 3:404, 2004. https://doi.org/10.1038/nmat1134.

[128] Kin Fai Mak, Changgu Lee, James Hone, Jie Shan, and Tony F. Heinz. Atomically Thin MoS_2: A New Direct-Gap Semiconductor. *Phys. Rev. Lett.*, 105:136805, Sep 2010. https://doi.org/10.1103/PhysRevLett.105.136805.

[129] B. Hunt, J. D. Sanchez-Yamagishi, A. F. Young, M. Yankowitz, B. J. LeRoy, K. Watanabe, T. Taniguchi, P. Moon, M. Koshino, P Jarillo-Herrero, and R. C Ashoori. Massive Dirac Fermions and Hofstadter Butter-

fly in a van der Waals Heterostructure. *Science*, 340:1427, 2013. https://doi.org/10.1126/science.1237240.

[130] A. K. Geim and I. V. Grigorieva. Van der Waals heterostructures. *Nature*, 499:419, 2013. https://doi.org/10.1038/nature12385.

[131] A. J. Mannix, B. Kiraly, M. Hersam, and N. P. Guisinger. Synthesis and chemistry of elemental 2D materials. *Nat. Rev. Chem.*, 1:0014, 2017. https://doi.org/10.1038/s41570-016-0014.

[132] K. S. Novoselov, A. Mishchenko, A. Carvalho, and A. H. Castro Neto. 2D materials and van der Waals heterostructures. *Science*, 353, 2016. https://doi.org/10.1126/science.aac9439.

[133] F. D. M. Haldane. Landau Levels: Condensed-Matter Realization of the "Parity Anomaly". *Phys. Rev. Lett.*, 61:2015, 1988. https://doi.org/10.1103/PhysRevLett.61.2015.

[134] M. Gmitra, S. Konschuh, C. Ertler, C. Ambrosch-Draxl, and J. Fabian. Band-structure topologies of graphene: Spin-orbit coupling effects from first principles. *Phys. Rev. B*, 80:235431, 2009. https://doi.org/10.1103/PhysRevB.80.235431.

[135] Z.-Y. Jia, Y.-H. Song, X.-B. Li, K. Ran, P. Lu, H.-J. Zheng, X.-Y. Zhu, Z.-Q. Shi, J. Sun, J. Wen, D. Xing, and S.-C. Li. Direct visualization of a two-dimensional topological insulator in the single-layer $1T'-WTe_2$. *Phys. Rev. B*, 96:041108(R), 2017. https://doi.org/10.1103/PhysRevB.96.041108.

[136] L. Kou, Y. Ma, B. Yan, X. Tan, C. Chen, and S. C. Smith. Encapsulated Silicene: A Robust Large-Gap Topological Insulator. *ACS Appl. Mater. Interfaces*, 7:19226, 2015. https://doi.org/10.1021/acsami.5b05063.

[137] F. Matusalem, D. S. Koda, F. Bechstedt, M. Marques, and L. K. Teles. Deposition of topological silicene, germanene and stanene on grpahene-covered SiC substrates. *Sci. Rep.*, 7:15700, 2017. https://www.nature.com/articles/s41598-017-15610-3.

[138] J. Deng, B. Xia, X. Ma, H. Chen, H. Shan, X. Zhai, B. Li, A. Zhao, Y. Xu, W. Duan, S.-C. Zhang, B. Wang, and J. G. Hou. Epitaxial growth of ultraflat stanene with topological band inversion. *Nat. Mater.*, 17:1081, 2018. https://doi.org/10.1038/s41563-018-0203.

[139] S. Tang, C. Zhang, and D. Wong et al. Quantum spin Hall state in monolayer 1T'-WTe_2. *Nat. Phys.*, 13:683, 2017. https://doi.org/10.1038/nphys4174.

[140] Y. Lu, W. Xu, M. Zeng, G. Yao, L. Shen, M. Yang, Z. Luo, F. Pan, K. Wu, T. Das, P. He, J. Jiang, J. Martin, Y.-P. Feng, H. Lin, and X.-S. Wang. Topological Properties Determined by Atomic Buckling in Self-Assembled Ultrathin Bi(110). *Nano Lett.*, 15:80, 2015. http://doi.org/10.1021/nl502997v.

[141] S. Murakami. Quantum Spin Hall Effect and Enhanced Magnetic Response by Spin-Orbit Coupling. *Phys. Rev. Lett.*, 97:236805, 2006. https://doi.org/10.1103/PhysRevLett.97.236805.

[142] S. Murakami. Phase transition between the quantum spin Hall and insulator phases in 3D: emergence of a topological gapless phase. *New J. Phys.*, 9:356, 2007. https://doi.org/10.1088/1367-2630/9/9/356.

[143] X. Wang, G. Bian, C. Xu, P. Wang, H. Hu, S. A. Brown, and T.-C. Chiang. Topological phases in double layers of bismuthene and antimonene. *Nanotechnology*, 28:395706, 2017. https://doi.org/10.1088/1361-6528/aa825f.

[144] S. A. Scott, M. V. Kral, and S. A. Brown. A crystallographic orientation transition and early stage growth characteristics of thin Bi films on HOPG. *Surf. Sci.*, 587:175, 2005. http://doi.org/10.1016/j.susc.2005.05.013.

[145] D. N. McCarthy, D. Robertson, P. J. Kowalczyk, and S. A. Brown. The effects of annealing and growth temperature on the morphologies of Bi nanostructures on HOPG. *Surf. Sci.*, 604:1273, 2010. https://doi.org/10.1016/j.susc.2010.04.013.

[146] P. J. Kowalczyk, O. Mahapatra, D. N. McCarthy, W. Kozlowski, Z. Klusek, and S. A. Brown. STM and XPS investigations of bismuth islands on HOPG. *Surf. Sci.*, 605:659, 2011. http://doi.org/10.1016/j.susc.2010.12.032.

[147] P. J. Kowalczyk, D. Belic, O. Mahapatra, S. A. Brown, E. S. Kadantsev, T. K. Woo, B. Ingham, and W. Kozlowski. Anisotropic oxidation of bismuth nanostructures: Evidence for a thin film allotrope of bismuth. *Appl. Phys. Lett.*, 100:151904, 2012. http://doi.org/10.1063/1.3701166.

[148] P. J. Kowalczyk, D. Belić, O. Mahapatra, and S. A. Brown. Grain boundaries between bismuth nanocrystals. *Acta Mater.*, 60:674, 2012. http://doi.org/10.1016/j.actamat.2011.09.041.

[149] P. J. Kowalczyk, O. Mahapatra, S. A. Brown, G. Bian, X. Wang, and T.-C. Chian. Electronic Size Effects in Three-Dimensional Nanostructures. *Nano Lett.*, 13:43, 2013. http://doi.org/10.1021/nl3033119.

[150] P. J. Kowalczyk, O. Mahapatra, S. A. Brown, G. Bian, and T.-C. Chiang. STM driven modification of bismuth nanostructures. *Surf. Sci.*, 621:140, 2014. http://doi.org/10.1016/j.susc.2013.11.007.

[151] P. J. Kowalczyk, O. Mahapatra, D. Belić, S. A. Brown, G. Bian, and T.-C. Chiang. Origin of the moiré pattern in thin Bi films deposited on HOPG. *Phys. Rev. B*, 91:045434, 2015. http://doi.org/10.1103/PhysRevB.91.045434.

[152] M. Zhao. Strain-driven band inversion and topological aspects in Antimonene. *Sci. Rep.*, 5:16108, 2015. https://www.nature.com/articles/srep16108.

[153] T. Märkl, P. J. Kowalczyk, M. Le Ster, I. V. Mahajan, H. Pirie, Z. Ahmed, G. Bian, X. Wang, T.-C. Chiang, and S. A. Brown. Engineering multiple topological phases in nanoscale Van der Waals heterostructures: realisation of α-antimonene. *2D Mater.*, 5:011002, 2018. https://doi.org/10.1088/2053-1583/aa8d8e.

[154] I. Mahajan. *STM studies of $Bi_{1-x}Sb_x$ topological nanostructures*. PhD thesis, University of Canterbury, 2017.

[155] H. Fang, C. Battaglia, C. Carraro, S. Nemsak, B. Ozdol, J. S. Kang, H. A. Bechtel, S. B. Desai, F. Kronast, A. A. Unal, G. Conti, C. Conlon, G. K. Palsson, M. C. Martin, A. M. Minor, C. S. Fadley, E. Yablonovitch, R. Maboudian, and A. Javey. Strong interlayer coupling in van der Waals heterostructures built from single-layer chalcogenides. *Proc. Natl. Acad. Sci.*, 111:6198, 2014. https://doi.org/10.1073/pnas.1405435111.

[156] Y. Liu, N. O. Weiss, X. Duan, H.-C. Cheng, Y. Huang, and X. Duan. Van der Waals heterostructures and devices. *Nat. Rev. Mater.*, 1:16042, 2016. http://doi.org/10.1038/natrevmats.2016.42.

[157] C. R. Dean, L. Wang, P. Maher, C. Forsythe, F. Ghahari, Y. Gao, J. Katoch, M. Ishigami, P. Moon, M. Koshino, T. Tanigushi, K. Watanabe, K. L. Shepard, J. Hone, and P. Kim. Hofstadter's butterfly and the fractal quantum Hall effect in moiré superlattices. *Nature*, 497:598–602, 2013. http://doi.org/10.1038/nature12186.

[158] Q. Tong, H. Yu, Q. Zhu, Y. Wang, X. Xu, and W. Yao. Topological mosaics in moiré superlattices of van der Waals heterobilayers. *Nat. Phys.*, 13:356, 2016. http://doi.org/10.1038/nphys3968.

[159] G. Li, A. Luican, J. M. B. Lopes dos Santos, A. H. Castro Neto, J. Kong A. Reina, and E. Y. Andrei. Observation of Van Hove singularities in twisted graphene layers. *Nat. Phys.*, 6:109–113, 2009. https://doi.org/10.1038/nphys1463.

[160] L. A. Ponomarenko, R. V. Gorbachev, G. L. Yu, D. C. Elias, R. Jalil, A. A. Patel, A. Mishchenko, A. S. Mayorov, C. R. Woods, J. R. Wallbank, M. Mucha-Kruczynski, B. A. Piot, M. Potemski, I. V. Grigorieva, K. S. Novoselov, F. Guinea, V. I. Fal'ko, and A. K. Geim. Cloning of Dirac fermions in graphene superlattices. *Nature*, 497:594, 2013. https://doi.org/10.1038/nature12187.

[161] Y. Cao, V. Fatemi, S. Fang, K. Watanabe, T. Taniguchi, E. Kaxiras, and P. Jarillo-Herrero. Unconventional superconductivity in magic-angle graphene superlattices. *Nature*, 556:43, 2018. https://doi.org/10.1038/nature26160.

[162] J. C. W. Song and N. M. Gabor. Electron quantum metamaterials in van der Waals heterostructures. *Nat. Nanotechnol.*, 13:986, 2018. https://doi.org/10.1038/s41565-018-0294-9.

[163] B. Bhushan. *Scanning Probe Microscopy in Nanoscience and Nanotechnology*, volume 2. Springer, Berlin, Heidelberg, 2010. https://doi.org/10.1007/978-3-642-10497-8.

[164] J. R. Brewer, Z. Gernhart, H.-Y. Liu, , and C. L. Cheung. Growth of [100]-Textured Gadolinium Nitride Films by CVD. *Chem. Vap. Deposition*, 16:216, 2010. https://doi.org/10.1002/cvde.201004288.

[165] Z. Fang, P. A. Williams, R. Odedra, H. Jeon, and R. J. Potter. Gadolinium nitride films deposited using a PEALD based process. *J. Cryst. Growth*, 338:111, 2012. https://doi.org/10.1016/j.jcrysgro.2011.10.049.

[166] M. A. Scarpulla, C. S. Gallinat, S. Mack, J. S. Speck, and A. C. Gossard. GdN (111) heteroepitaxy on GaN (0001) by N_2 plasma and NH_3 molecular beam epitaxy. *J. Cryst. Growth*, 311:1239, 2009. https://doi.org/10.1016/j.jcrysgro.2008.12.050.

[167] T. Sun J, H, Huang, S.-L. Wong, H.-J. Gao, Y.-P. Feng, and A. Thye Shen Wee. Energy-Gap opening in a Bi(110) Nanoribbon Induced by Edge Reconstruction. *Phys. Rev. Lett.*, 109:246804, 2012. http://doi.org/10.1103/PhysRevLett.109.246804.

[168] P. Hofmann. The surfaces of bismuth: Structural and electronic proerties. *Prog. Surf. Sci.*, 18:191, 2006. http://doi.org/10.1016/j.progsurf.2006.03.001.

[169] O. Mahapatra. *A scanning probe microscopy (SPM) study of Bi(110) nanostructures on highly oriented pyrolytic graphite (HOPG)*. PhD thesis, University of Canterbury, 2013.

[170] Y. Ren, Z. Qiao, and Q. Niu. Topological phases in two-dimensional materials: a review. *Rep. Prog. Phys.*, 79:066501, 2016. https://doi.org/10.1088/0034-4885/79/6/066501.

[171] S. Scott. *Self-assembly of Sb and Bi nanostructure on graphite*. PhD thesis.

[172] P. Ares, F. Aguilar-Galindo, D. Rodríguez-San-Miguel, D. A. Aldave, S. Díaz-Tendero, M. Alcamí, F. Martín, J. Gómez-Herrero, and F. Zamora. Mechanical Isolation of Highly Stable Antimonene under Ambient Conditions. *Adv. Mater.*, 28:6332, 2016. http://doi.org/10.102/adma.201602128.

[173] X. Wu, Y. Shao, H. Liu, Z. Feng, Y.-L. Wang, J.-T. Sun, C. Liu, J.-O. Wang, Z.-L. Liu, Y.-Q. Wang, S.-X. Du, Y.-G. Shi, K. Ibrahim, and H.-J. Gao. Epitaxial growth and air-stability of Monolayer Antimonene on $PdTe_2$. *Adv. Mater.*, 1605407:14345, 2017. https://doi.org/10.1002/adma.201605407.

[174] K. Hermann. Periodic overlayers and moiré patterns: theoretical studies of geometric properties. *J. Phys.: Condens. Matter*, 24:314210, 2012. https://doi.org/10.1088/0953-8984/24/31/314210.

[175] Scienta Omicron, Scanning Probe Microscopy - VT SPM. Retrieved from website, May 2019. https://www.scientaomicron.com/en/products/variable-temperature-spm/variants.

[176] SPI supplies - HOPG substrates. Retrieved from website, May 2019. https://www.2spi.com/category/hopg/.

[177] L. A. Walsh and C. L. Hinkle. van der Waals epitaxy: 2D materials and topological insulators. *Appl. Mater. Today*, 9:504, 2017. https://doi.org/10.1016/j.apmt.2017.09.010.

[178] Jay Chan. *Growth and Structural Properties of Rare Earth Nitride Thin Films*. PhD thesis, Victoria University of Wellington, 2018.

[179] EasyGaN. Retrieved from website, March 2019. https://www.easy-gan.com/aln-on-si-template.

[180] Omicron VT-AFM user manual, 2009.

[181] Argon Zero Grade from BOC supply. Retrieved from website, May 2019. https://www.boc.co.nz/shop/en/nz/gases/argon-gas/argon-zero-grade.

[182] V. S. Smentkowski. Trends in sputtering. *Prog. Surf. Sci.*, 64:1, 2000. https://doi.org/10.1016/S0079-6816(99)00021-0.

[183] G. Binnig, H. Rohrer, Ch. Gerber, , and E. Weibel. Tunneling through a controllable vacuum gap. *Appl. Phys. Lett.*, 40:178, 1982. https://doi.org/10.1063/1.92999.

[184] G. Binnig, H. Rohrer, Ch. Gerber, , and E. Weibel. Surface studies by Scanning Tunneling Microscopy. *Phys. Rev. Lett.*, 49:57, 1982. https://doi.org/10.1103/PhysRevLett.49.57.

[185] G. Binnig and H. Rohrer. Scanning Tunneling Microscopy. *Surf. Sci.*, 126:236, 1983. https://doi.org/10.1016/0039-6028(83)90716-1.

[186] Nobel Prize in Physics. Press Release, October 1986. https://www.nobelprize.org/nobel_prizes/physics/laureates/1986/press.html.

[187] H.-J. Güntherodt and R. Wiesendanger. *Scanning Tunneling Microscopy I: General Principle and Applications to Clean and Adsorbate-Covered Surfaces*, volume 20. Springer-Verlag Berlin Heidelberg, 1992. https://doi.org/10.1007/978-3-642-97343-7.

[188] R. Wiesendanger and H.-J. Güntherodt. *Scanning Tunneling Microscopy III: Theory of STM and Related Scanning Probe Methods*, volume 29. Springer-Verlag Berlin Heidelberg, 1996. https://doi.org/10.1007/978-3-642-80118-1.

[189] H. A. Kramers. Wellenmechanik und halbzahlige Quantisierung. *Z. Phys.*, 39:828, 1926. https://doi.org/10.1007/BF01451751.

[190] J. Bardeen. Tunnelling from a Many-Particle Point of View. *Phys. Rev. Lett.*, 6:57, 1961. https://doi.org/10.1103/PhysRevLett.6.57.

[191] J. Tersoff and D. R. Hamann. Theory of the scanning tunneling microscope. *Phys. Rev. B*, 31:805, 1985. https://doi.org/10.1103/PhysRevB.31.805.

[192] R. J. Hamers. Atomic-Resolution Surface Spectroscopy with the Scanning Tunneling Microscope. *Annu. Rev. Phys. Chem.*, 40:531, 1989. https://doi.org/10.1146/annurev.pc.40.100189.002531.

[193] U. D. Schwarz, H. Haefke, P. Reimann, and H.-J. Güntherodt. Tip artefacts in scanning force microscopy. *J. Microsc.*, 173:183, 1994. https://doi.org/10.1111/j.1365-2818.1994.tb03441.x.

[194] Gwyddion - Free SPM data analysis software. Retrieved from website, May 2019. https://gwyddion.net/.

[195] E. O. Brigham. *The fast Fourier transform and its applications*. Prentice-Hall. New York, USA., 2002.

[196] G. Binnig, C. F. Quate, and Ch. Gerber. Atomic Force Microscope. *Phys. Rev. Lett.*, 56:930, 1986. http://doi.org/10.1103/PhysRevLett.56.930.

[197] F. J. Giessibl. Advances in atomic force microscopy. *Rev. Mod. Phys.*, 75:949, 2003. https://doi.org/10.1103/RevModPhys.75.949.

[198] F. J. Giessibl. Forces and frequency shifts in atomic-resolution dynamic-force microscopy. *Phys. Rev. B*, 56:16010, 1997. https://doi.org/10.1103/PhysRevB.56.16010.

[199] J. E. Sader and S. P. Jarvis. Accurate formulas for interaction force and energy in frequency modulation force spectroscopy. *Appl. Phys. Lett.*, 84:1801, 2004. https://doi.org/10.1063/1.1667267.

[200] Nanosensors SSS-NCL Probes. Retrieved from website, May 2019. https://www.nanosensors.com/SuperSharpSilicon-Non-Contact-Tapping-Mode-Long-Cantilever-afm-tip-SSS-NCL.

[201] Nanosurf NaioAFM. Retrieved from website, May 2019. https://www.nanosurf.com/en/products/naioafm-the-leading-compact-afm.

[202] J. I. Goldstein, D. E. Newbury, D. C. Joy, C. E. Lyman, P. Echlin, E. Lifshin, L. Sawyer, and J. R. Michael. *Scanning Electron Microscopy and X-Ray Microanalysis, Third Edition*. Springer US, 2003. https://doi.org/10.1007/978-1-4615-0215-9.

[203] JEOL website. Retrieved from website, May 2019. https://www.jeol.co.jp/en/products/list_sem.html.

[204] Thermo Scientific. *Energy-Dispersive X-Ray Microanalysis: An introduction*. https://tools.thermofisher.com/content/sfs/brochures/D17000~.pdf.

[205] K. Oura, M. Katayama, A. V. Zotov, V. G. Lifshits, and A. A. Saranin. *Surface Analysis I. Diffraction Methods. In: Surface Science, Advanced Texts in Physics.* Springer, Berlin, Heidelberg, 2003.

[206] S. Hasegawa. *Characterization of Materials, Chapter "Reflection High-Energy Electron Diffraction", Second edition.* John Wiley and Sons, Ltd., 2012. https://doi.org/10.1002/0471266965.com139.

[207] B. D. Cullity. *Elements of X-Ray Diffraction: Second edition*. Addison-Wesley Publishing Company, Inc., 1978.

[208] Y. Waseda and E. Matsubara K. Shinoda. *X-Ray Diffraction Crystallography: Introduction, Examples and Solved Problems*. Springer-Verlag Berlin Heidelberg, 2011. https://doi.org/10.1007/978-3-642-16635-8.

[209] H. A. Szymanski. *Raman Spectroscopy: Theory and Practice*. Springer US, 1967. https://doi.org/10.1007/978-1-4684-3024-0.

[210] U. A. Jayasooriya, D. L. Andrews R. D. Jenkins, and A. A. Demidov. *An Introduction to Laser Spectroscopy: Introduction to Raman Spectroscopy*. Springer, Boston, MA, 2002.

[211] H. Weinstock. *SQUID Sensors: Fundamentals, Fabrication and Applications*. 1996. https://doi.org/10.1007/978-94-011-5674-5.

[212] G. Oster and Y. Nishijima. Moiré Patterns. *Scientific American*, 208:5, 1963. https://www.jstor.org/stable/24936147.

[213] K. Momma and F. Izumi. VESTA 3 for three-dimensional visualization of crystal, volumetric and morphology data. *J. Appl. Crystallogr.*, 44:1272–1276, 2011. http://doi.org/10.1107/S0021889811038970.

[214] M. Yankowitz, J. Xue, D. Cormode, J. D. Sanchez-Yamagishi, K. Watanabe, T. Taniguchi, P. Jarillo-Herrero, P. Jacquod, and B. J. LeRoy. Emergence of superlattice Dirac points in graphene on hexagonal boron nitride. *Nat. Phys.*, 8:382–386, 2012. https://doi.org/10.1038/nphys2272.

[215] J. R. Wallbank, M. Mucha-Kruczyński, X. Chen, and V. I. Fal'ko. Moiré superlattice effects in graphene/boron-nitride van der Waals heterostructures. *Ann. Phys. (Berlin)*, 527:359–376, 2015. http://doi.org/10.1002/andp.201400204.

[216] Y. Liao, W. Cao, J. W. Connell, Z. Chen, and Y. Li. Evolution of Moiré Profiles from van der Waals Superstructures of Boron Nitride Nanosheets. *Sci. Rep.*, 6:26084, 2016. https://doi.org/10.1038/srep26084.

[217] T. Mitsuishi, H. Nagasaki, and R. Uyeda. A New Type of Interference Fringes Observed in Electronmicrograph of Crystalline Substance. *Proc. Jap. Acad.*, 27:86, 1951. https://www.jstage.jst.go.jp/article/pjab1945/27/2/27_2_86/_pdf.

[218] D. W. Pashley, J. W. Menter, and G. A. Bassett. Observations of dislocations in metals by means of moiré patterns on electron micrographs. *Nature*, 179:4563, 1957. https://doi.org/10.1038/179752a0.

[219] G. A. Geach and R. Phillips. Moiré patterns in Transmission Electron Micrographs of Sub-Boundaries of Aluminium. *Nature*, 179:4573, 1957. https://doi.org/10.1038/1791293a0.

[220] A. Keller and A. O'Connor. Study of single crystals and their associations in polymers. *Disc. Faraday Soc.*, 25:141, 1958. https://doi.org/10.1039/DF9582500114.

[221] V. F. Holland. Dislocation Arrays in Polymer Single Crystals. *J. Appl. Phys.*, 35:1351, 1964. https://doi.org/10.1063/1.1713619.

[222] V. F. Holland. Dislocations in Polyethylene Single Crystals. *J. Appl. Phys.*, 35:3235, 1964. https://doi.org/10.1063/1.1713204.

[223] G. A. Bassett, J. W. Menter, and D. W. Pashley. Moiré patterns on electron micrographs, and their application to the study of dislocations in metals. *Proc. Royal Soc. Lond. A*, 246:1246, 1958. https://doi.org/10.1098/rspa.1958.0144.

[224] K. Abe, M. Niinomi, and M. Takayanagi. Study of structural changes of polyethylene single crystals during annealing by means of moire pattern technique. *J. Macromol. Sci. B*, 4:87, 1970. https://doi.org/10.1080/00222347008212475.

[225] T. R. Albrecht, H. A. Mizes, J. Nogami, S.-I Park, and C. F. Quate. Observation of tilt boundaries in graphite by scanning tunneling microscopy and associated multiple tip effects. *Phys. Rev. Lett.*, 52:362, 1988. https://doi.org/10.1063/1.99465.

[226] M. Kuwabara, D. R. Clarke, and D. A. Smith. Anomalous superperiodicity in scanning tunneling microscope images of graphite. *Appl. Phys. Lett.*, 56:2396, 1990. https://doi.org/10.1063/1.102906.

[227] B. Nysten, J.-C. Roux, S. Flandrois, C. Daulan, and H. Saadaoui. AFM and STM studies of the carbonization and graphitization of polyimide films. *Phys. Rev. B*, 48:12527, 1993. https://doi.org/10.1103/PhysRevB.48.12527.

[228] Z. Y. Rong and P. Kuiper. Electronic effects in scanning tunneling microscope: Moiré pattern on a graphite surface. *Phys. Rev. B*, 48:17427, 1993. https://doi.org/10.1103/PhysRevB.48.17427.

[229] J. C. Patrin, Y. Z. Li, M. Chander, and J. H. Weaver. Sb and Bi on GaAs(110): Substrate-stabilized overlayer structures studied with scanning tunneling microscopy. *Phys. Rev. B*, 46:10221, Oct 1992. http://doi.org/10.1103/PhysRevB.46.10221.

[230] U. Müller, D. Carnal, H. Siegenthaler, E. Schmidt, W. J. Lorenz, W. Obretenov, U. Schmidt, G. Staikov, and E. Budevski. Superstructures of Pb monolayers electrochemically deposited on Ag(111). *Phys. Rev. B*, 46:12899(R), 1992. https://doi.org/10.1103/PhysRevB.46.12899.

[231] G. L. Yu, R. V. Gorbachev, J. S. Tu, A. V. Kretinin, Y. Cao, R. Jalil, F. Withers, L. A. Ponomarenko, B. A. Piot, M. Potemski, D. C. Elias, X. Chen, K. Watanabe, T. Tanguchi, I. V. Grigorieva, K. S. Novoselov, V. I. Fal'ko, A. K. Geim, and A Mishchenko. Hierarchy of Hofstadter states and replica quantum Hall ferromagnetism in graphene superlattices. *Nat. Phys.*, 10:525, 2014. https://doi.org/10.1038/nphys2979.

[232] R. Decker, Y. Wang, V. W. Brar, W. Regan, H.-Z. Tsai, Q. Wu, W. Gannett, A. Zettl, , and M. F. Crommie. Local Electronic Properties of Graphene on a BN Substrate via Scanning Tunneling Microscopy. *Nano Lett.*, 11:2291–2295, 2011. https://doi.org/10.1021/nl2005115.

[233] D. R. Hofstadter. Energy levels and wave functions of Bloch electrons in rational and irrational magnetic fields. *Phys. Rev. B*, 14:2239, 1976. https://doi.org/10.1103/PhysRevB.14.2239.

[234] F. Varchon, P. Mallet, L. Magaud, and J.-Y. Veuillen. Rotational disorder in few-layer graphene films on 6H-SiC(000$\bar{1}$): A scanning tunneling microscopy study. *Phys. Rev. B*, 77:165415, 2007. http://doi.org/10.1103/PhysRevB.77.165415.

[235] H. S. Wong and C. Durkan. Unraveling the rotational disorder of graphene layers in graphite. *Phys. Rev. B*, 81:045403, 2010. http://doi.org/10.1103/PhysRevB.81.045403.

[236] F. Joucken, F. Frising, and R. Sporken. Fourier transform analysis of STM images of multilayer graphene moiré patterns. *Carbon*, 83:48, 2015. https://doi.org/10.1016/j.carbon.2014.11.030.

[237] J. M. Martin, C. Donnet, Th. Le Mogne, and Th. Epicier. Superlubricity of molybdenum disulphide. *Phys. Rev. B*, 48:10583(R), 1993. https://doi.org/10.1103/PhysRevB.48.10583.

[238] D. A. Cosma, J. R. Wallbank, V. Cheianov, and V. I. Fal'ko. Moiré pattern as a magnifying glass for strain and dislocations in van der Waals heterostructures. *Faraday Discuss.*, 173:137, 2014. http://doi.org/10.1039/C4FD00146J.

[239] P. J. Kowalczyk, O. Mahapatra, M. Le Ster, S. A. Brown, G. Bian, X. Wang, and T.-C. Chiang. Single atomic layer allotrope of bismuth with rectangular symmetry. *Phys. Rev. B*, 96:205434, 2017. http://doi.org/10.1103/PhysRevB.96.205434.

[240] M. Wada, S. Murakami, F. Freimuth, and G. Bihlmayer. Localized edge states in two-dimensional topological insulators: Ultrathin Bi films. *Phys. Rev. B*, 83:121310(R), Mar 2011. https://doi.org/10.1103/PhysRevB.83.121310.

[241] S. K. Gupta, Y. Sonvane, G. Wang, and R. Pandey. Size and edge roughness effects on thermal conductivity of pristine antimonene allotropes. *Chem. Phys. Lett.*, 641:169, 2015. http://doi.org/10.1016/j.cplett.2015.10.072.

[242] J. Ji, X. Song, J. Liu, Z. Yan, C. Huo, S. Zhang, M. Su, L. Liao, W. Wang, Z. Ni, Y. Hao, and H. Zeng. Two-dimensional antimonene single crystals grown by van der Waals epitaxy. *Nat. Commun.*, 7:13352, 2016. http://doi.org/10.1038/ncomms13352.

[243] O. Üzengi Aktürk, V. Ongun Özçelik, and S. Ciraci. Single-layer crystalline phases of antimony: Antimonenes. *Phys. Rev. B*, 91:235446, Jun 2015. http://doi.org/10.1103/PhysRevB.91.235446.

[244] G. Wang, R. Pandey, and S. P. Karna. Atomically Thin Group V Elemental films: Theoretical Investigations of Antimonene Allotropes. *ACS Appl. Mater. Inter.*, 7:11490, 2015. http://doi.org/10.1021/acsami.5b02441.

[245] S. Zhang, M. Xie, Z. Yan F. Li, Y. Li, E. Kan, W. Liu, Z. Chen, and H. Zeng. Semiconducting Group 15 Monolayers: A Broad Range of Band Gaps and High Carrier Mobilities. *Angewandte Chemie Int. Ed.*, 55:1666, 2016. http://doi.org/10.1002/anie.201507568.

[246] Y. Xu, B. Peng, H. Zhang, H. Shao, R. Zhang, and H. Zhu. First-principle calculations of optical properties of monolayer arsenene and antimonene allotropes. *Ann. Phys. (Berlin)*, 529:1600152, 2017. https://doi.org/10.1002/andp.201600152.

[247] K. Zhao, Y.-F. Lv, S.-H. Ji, X. Ma, X. Chen, and Q.-K. Xue. Scanning tunneling microscopy studies of topological insulators. *J. Phys.: Condens. Matter*, 26(39):394003, 2014. https://doi.org/10.1088/0953-8984/26/39/394003.

[248] P. Moon and M. Koshino. Optical properties of the Hofstadter butterfly in the moiré superlattice. *Phys. Rev. B*, 88:241412(R), 2013. https://doi.org/10.1103/PhysRevB.88.241412.

[249] X. Zhang and H. Luo. Scanning tunneling spectroscopy studies of angle-dependent van Hove singularities on twisted graphite surface layer. *App. Phys. Lett*, 103:231602, 2013. https://doi.org/10.1063/1.4839419.

[250] I. Amidror and R. D. Hersch. Analysis of the Superposition of Periodic Layers and Their Moiré Effects through the Algebraic Structure of Their Fourier Spectrum. *J. Math. Imaging Vis.*, 8:99, 1998. https://doi.org/10.1023/A:1008248527004.

[251] G. Lebanon and A. M. Bruckstein. Variational approach to moiré pattern synthesis. *J. Opt. Soc. Am. A*, 6:1371, 2001. https://doi.org/10.1364/JOSAA.18.001371.

[252] I. Amidror and R. D. Hersch. The role of Fourier theory and of modulation in the prediction of visible moiré effects. *J. Mod. Opt.*, 56:1103, 2009. https://doi.org/10.1080/09500340902994140.

[253] P. Zeller and S. Günther. What are the possible moiré patterns of graphene on hexagonally packed surfaces? Universal solution for hexagonal coincidence lattices, derived by a geometric construction. *New J. Phys.*, 16:083028, 2014. https://doi.org/10.1088/1367-2630/16/8/083028.

[254] M. M. van Wijk, A. Schuring, M. I. Katsnelson, and A. Fasolino. Relaxation of moiré patterns for slightly misaligned identical lattices: graphene on graphite. *2D Mater.*, 2:034010, 2015. https://doi.org/10.1088/2053-1583/2/3/034010.

[255] K. B. Howell. *Principles of Fourier Analysis: Chapter IV, Generalized Functions and Fourier Transforms*. Chapman & Hall/CRC, 2001. .

[256] S. J. Ahn, P. Moon, T.-H Kim, H.-W. Kim, H.-C. Shin, E. H. Kim, H. W. Cha, S.-J. Kahng, P. Kim, M. Koshino, Y.-W. Son, C.-W. Yang, and J. R. Ahn. Dirac electrons in a dodecagonal graphene quasicrystal. *Science*, 2018. https://doi.org/10.1126/science.aar8412.

[257] W Yao, E Wang, C Bao, Y Zhang, K Zhang, K Bao, C.-K. Chan, C Chen, J. Avila, M. C. Asensio, J. Zhu, and S. Zhou. Quasicrystalline 30° twisted bilayer graphene as an incommensurate superlattice with strong interlayer coupling. *Proc. Natl. Acad. Sci.*, 115:6928, 2018. https://doi.org/10.1073/pnas.1720865115.

[258] L. Zou, H. C. Po, A. Vishwanath, and T. Senthil. Band structure of twisted bilayer graphene: Emergent symmetries, commensurate approximants, and Wannier obstructions. *Phys. Rev. B*, 98:085435, 2018. https://doi.org/10.1103/PhysRevB.98.085435.

[259] S. Granville, B. J. Ruck, A. Koo, D. J. Pringle, F. Kuchler, A. R. H. Preston, D. H. Housden, N. Lund, A. Bittar, G. V. M. Williams, and H. J. Trodahl. Semiconducting ground state of GdN thin films. *Phys. Rev. B*, 73:235335, 2006. http://doi.org/10.1103/PhysRevB.73.235335.

[260] F. Leuenberger, A. Parge, W. Felsch, K. Fauth, and M. Hessler. GdN thin films: Bulk and local electronic and magnetic properties. *Phys. Rev. B*, 72:9, 2005. http://doi.org/10.1103/PhysRevB.72.014427.

[261] K. Senapati, T. Fix, M. E. Vickers, M. G. Blamire, and Z. H. Barber. Structural evolution and competing magnetic orders in polycrystalline GdN films. *Phys. Rev. B*, 83:014403, 2011. http://doi.org/10.1103/PhysRevB.83.014403.

[262] B.-J. Schäfer, A. Förster, M. Londschien, A. Tulke, K. Werner, M. Kamp, H. Heinecke, M. Weyers, H. Lüth, and P. Balk. Arsenic passivation of MOMBE grown GaAs surfaces. *Surf. Sci.*, 204:485, 1988. https://doi.org/10.1016/0039-6028(88)90228-2.

[263] U. Resch, N. Esser, Y.S. Raptis, W. Richter, J. Wasserfall, A. Förster, and D.I. Westwood. Arsenic passivation of MBE grown GaAs(100): structural and electronic properties of the decapped surfaces. *Surf. Sci.*, 269:797, 1992. https://doi.org/10.1016/0039-6028(92)91351-B.

[264] K. Knorr, M. Pristovsek, U. Resch-Esser, N. Esser, M. Zorn, and Z. Richter. In situ surface passivation of III-V semiconductors in MOVPE by amorphous As and P layers. *J. Cryst. Growth*, 170:230, 1997. https://doi.org/10.1016/S0022-0248(96)00629-X.

[265] R. Hunger, T. Schulmeyer, A. Klein, W. Jaegermann, K. Sakurai, A. Yamada, P. Fons, K. Matsubara, and S. Niki. An option for the surface science on Cu chalcopyrites: the selenium capping and decapping process. *Surf. Sci.*, 557:263, 2004. https://doi.org/10.1016/j.susc.2004.03.055.

[266] D. Drews, A. Schneider, D. R. T Zahn, D. Wolffframm, and D. A. Evans. Raman monitoring of selenium decapping and subsequent antimony deposition on MBE-grown ZnSe(100). *App. Surf. Sci.*, 104:485, 1996. https://doi.org/10.1016/S0169-4332(96)00191-2.

[267] K. Virwani, S. E. Harrison, A. Pushp, T. Topuria, E. Delenia, P. Rice, A. Kellock, L. Collis-McIntyre, J. Harris, T. Hesjedal, and S. Parkin. Controlled removal of amorphous Se capping layer from a topological insulator. *Appl. Phys. Lett.*, 105:241605, 2014. http://doi.org/10.1063/1.4904803.

[268] J. Dai, W. Wang, M. Brahlek, N. Koirala, M. Salehi, S. Oh, and W. Wu. Restoring pristine Bi_2Se_3 surfaces with an effective Se decapping process. *Nano Research*, 8:1222, 2014. http://doi.org/10.1007/s12274-014-0607-8.

[269] D. M. Zhernokletov, H. Dong, B. Brennan, J. Kim, R. M. Wallace, M. Yakimov, V. Tokranov, and S. Oktyabrsky. Investigation of arsenic and antimony capping layers, and half cycle reactions during atomic layer deposition of Al_2O_3 on GaSb(100). *J. Vac. Sci. Technol. A*, 31:060602, 2013. https://doi.org/10.1116/1.4817496.

[270] X. Wallart, S. Godey, Y Douvry, and L. Desplanque. Comparative Sb and As segregation at the InP on GaAsSb interface. *Appl. Phys. Lett.*, 93:123119, 2008. https://doi.org/10.1063/1.2991299.

[271] D. R. Lide. *CRC Handbook of Chemistry and Physics*, volume 4. CRC Press., Boca Raton, Florida, 2003. https://books.google.co.nz/books/about/CRC_Handbook_of_Chemistry_and_Physics_85.html?id=WDll8hA006AC&redir_esc=y.

[272] C. B. Alcock, V. P. Itkin, and M. K. Horrigan. Vapour Pressure Equations for the Metallic Elements: 298-2500K. *Canadian Metallurgical Quarterly*, 23:309, 1984. http://10.1179/cmq.1984.23.3.309.

[273] N. D Greene and F. G. Hodge. Oxidation Characteristics of the Lanthanide Metals. *Corrosion*, 22:206, 1966. https://doi.org/10.5006/0010-9312-22.7.206.

[274] P. Patnaik. *Handbook of Inorganic Chemicals*. McGraw-Hill Companies Inc., 2003.

[275] A. K. Burnham and G. T. Jameson. Oxidation kinetics for thin rare-earth metal films. *J. Vac. Sci. Technol. A*, 5:1713, 1987. http://doi.org/10.1116/1.574515.

[276] Kurt W. Kolasinski. *Surface Science: Foundation of Catalysis and Nanoscience, Third Edition*. John Wiley & Sons, Ltd, 2012. https://doi.org/10.1002/9781119941798.

[277] N. L. Shi and D. Fort. Preparation of samarium in the double hexagonal close packed form. *JLCM*, 113:L21, 1985. https://doi.org/10.1016/0022-5088(85)90294-2.

[278] F. Natali, J. Chan, H. J. Trodahl, and B. J. Ruck. Rare Earth Nitride Structures and Devices and Method for Removing a Passivating Capping. US Patent number 16202663.7.

[279] Y.-M. Le Vaillant, S. Ciur, A. Andenet, O. Briot, B. Gil, R. L. Aulombard, R. Bisaro, J. Olivier, O. Durand, and J.-Y. Duboz. Dependence of the Residual Strain in GaN on the AlN Buffer Layer Annealing Parameters. *MRS Proc.*, 468:173, 1997. https://doi.org/10.1557/PROC-468-173.

[280] F. Grandjean, J. Massies, and F. Semond. GaN evaporation in molecular-beam epitaxy environment. *Appl. Phys. Lett.*, 74:1854, 1999. https://doi.org/10.1063/1.123691.

[281] S. Fernández, G. Koblmüller, E. Calleja, and J. S. Speck. In situ GaN decomposition analysis by quadrupole mass spectrometry and reflection high-energy electron diffraction. *J. Appl. Phys.*, 104:033541, 2008. https://doi.org/10.1063/1.2968442.

[282] C. Dufour, K. Dusmesnil, S. Soriano, D. Pierre, Ch. Senet, and Ph. Mangin. Epitaxial growth of dhcp samarium: single crystal films and Sm/Nd superlattices. *J. Cryst. Growth*, 234:447, 2002. https://doi.org/10.1016/S0022-0248(01)01719-5.

[283] A. Stenborg, J. N Andersen, O. Björneholm, A. Nilsson, and N. Mårtensson. Valence-transition-induced 5×5 surface reconstruction of Sm(0001). *Phys. Rev. Lett.*, 63:187, 1989. https://doi.org/10.1103/PhysRevLett.63.187.

[284] V. Lebedev, K. Tonisch, F. Niebelschütz, V. Cimalla, D. Cengher, Ch. Mauder I. Cimalla, S. Hauguth, O. Ambacher, F. M. Morales, J. G. Lozano, and D. González. Coalescence aspects of III-nitride epitaxy. *J. Appl. Phys.*, 101:054906, 2007. https://doi.org/10.1063/1.2464195.

[285] J. A. Venables. *Introduction to Surface and Thin Film Processes*. Cambridge University Press, 2003.

[286] S. Raghavan, X. Weng, E. Dickey, and J. M. Redwing. Effect of AlN interlayers on growth stress in GaN layers deposited on (111) Si. *Appl. Phys. Lett.*, 87:142101, 2005. https://doi.org/10.1063/1.2081128.

[287] A. Fischer, H. Kühne, and H. Richter. New Approach in Equilibrium Theory for Strained Layer Relaxation. *Phys. Rev. Lett.*, 73:2712, 1994. https://doi.org/10.1103/PhysRevLett.73.2712.

[288] K. Tamamura, K. Akimoto, and Y. Mori. Dislocation density of lattice mismatched epitaxial layers. *J. Cryst. Growth*, 94:821, 1989. https://doi.org/10.1016/0022-0248(89)90114-0.

[289] J. K Alstad, R. V. Colvin, S. Legvold, and F. H. Spedding. Electrical Resistivity of Lanthanum, Praseodymium, Neodymium, and Samarium. *Phys. Rev.*, 121:1637, 1961. https://doi.org/10.1103/PhysRev.121.1637.

[290] C. R. Johnson, G. M Tsoi, and Y. K Vohra. Magnetic transition temperatures follow crystallographic symmetry in samarium under high-pressures and low-temperatures. *J. Phys.: Condens. Matter*, 29:065801, 2017. https://doi.org/10.1088/1361-648X/29/6/065801.

[291] S. Kaya, E. Yilmaz, H. Karacali, A. O. Cetinkaya, and A. Aktag. Samarium oxide thin films deposited by reactive sputtering: Effects of sputtering power and substrate temperature on microstructure, morphology and electrical properties. *Mater. Sci. Semicond. Process.*, 33:42, 2015. https://doi.org/10.1016/j.mssp.2015.01.035.

[292] D. X. Li, Y. Haga, H. Shida, T. Suzuki, Y. S. Kwon, and G. Kido. Magnetic properties of stoichiometric Gd monopnictides. *J. Phys.: Condens. Matter*, 9:10777, 1997. https://doi.org/10.1088/0953-8984/9/48/019.

[293] G. K. Wertheim and G. Crecelius. Divalent Surface State on Metallic Samarium. *Phys. Rev. Lett.*, 40:813, 1978. https://doi.org/10.1103/PhysRevLett.40.813.

[294] E. Lundgren, J. N. Andersen, R. Nyholm, X. Torrelles, J. Rius, A. Delin, A. Grechnev, O. Eriksson, C. Konvicka, M. Schmid, and P. Varga. Geometry of the Valence Transition Induced Surface Reconstruction of Sm(0001). *Phys. Rev. Lett.*, 88:136102, 2002. https://doi.org/10.1103/PhysRevLett.88.136102.

[295] F. H. Ellinger and W. H. Zachariasen. The Crystal Structure of Samarium Metal and of Samarium Monoxide. *J. Am. Chem. Soc.*, 75:5650, 1953. https://doi.org/10.1021/ja01118a052.

[296] K. Kersten. Sample degradation during SEM analysis: what causes it and how to slow down the process. ThermoFisher Scientific website. Accessed 2019-01-19, 2018. http://blog.phenom-world.com/sample-degradation-scanning-electron-microscope-sem.

[297] A. Bearden and A. F. Burr. Reevaluation of X-Ray Atomic Energy Levels. *Rev. Mod. Phys.*, 39:125, 1967. https://doi.org/10.1103/RevModPhys.39.125.

[298] R. G. Musket, W. McLean, C. A. Colmenares, D. M. Makowiecki, and W. J. Siekhaus. Preparation of Atomically Clean Surfaces of Selected Elements: A Review. *App. Surf. Sci.*, 10:143, 1982. https://doi.org/10.1016/0378-5963(82)90142-8.

[299] W. Färber and P. Braun. Oxygen Exposure of Sm, Gd and Tb studied by Auger Electron Spectroscopy. *Surf. Sci.*, 41:195, 1974. https://doi.org/10.1016/0039-6028(74)90303-3.

[300] R. I. R. Blyth, R. Cosso, S. S. Dhesi, K. Newstead, A. M. Begley, R. G. Jordan, and S. D. Barrett. Surface structure of rare earth metals. *Surf. Sci.*, 251/252:722–726, 1990. https://doi.org/10.1016/0039-6028(91)91086-D.

[301] J. F. Gibbons. Ion implantation in semiconductors - Part I: Range distribution theory and experiments. *Proc. IEEE*, 56:295, 1968. https://doi.org/10.1109/PROC.1968.6273.

[302] U. Valbusa, C. Boragno, and F. Buatier de Mongeot. Nanostructuring surfaces by ion sputtering. *J. Phys.: Condens. Matter*, 14:8153, 2002. https://doi.org/10.1088/0953-8984/14/35/301.

[303] M. Kalff, G. Comsa, and M. Thomas. Temperature dependent morphological evolution of Pt(111) by ion erosion: destabilization, phase coexistence and coarsening. *Surf. Sci.*, 486:103, 2001. https://doi.org/10.1016/S0039-6028(01)01015-9.

[304] M. Küstner, W. Eckstein, V. Dose, and J. Roth. The influence of surface roughness on the angular dependence of the sputter yield. *Nucl. Instrum. Methods Phys. Res. B*, 145:320, 1998. https://doi.org/10.1016/S0168-583X(98)00399-1.

[305] T. Rönnhult, B. Brox, and G. Fritze. The influence of Surface Topography on the X-ray Intensity in Electron Microprobe Analysis (EDS/WDS). *Scanning*, 9:81, 1987. https://doi.org/10.1002/sca.4950090205.

[306] G. K. Wenhner and D. J. Hajicek. Cone Formation on Metal Targets during Sputtering. *J. Appl. Phys.*, 42:1145, 1971. https://doi.org/10.1063/1.1660158.

[307] Y. Fujimoto, M. Nozu, and F. Okuyama. Geometry and structure of sputter-induced cones on nickel-seeded silicon. *J. Appl. Phys*, 77:2725, 1995. https://doi.org/10.1063/1.359569.

[308] B. Heying, E. J. Tarsa, C. R. Elsass, P. Fini, S. P. DenBaars, and J. S. Speck. Dislocation mediated surface morphology of GaN. *J. Appl. Phys.*, 85:6470, 1999. https://doi.org/10.1063/1.370150.

[309] C. D. Lee, Y. Dong, R. M. Feenstra, J. E. Northrup, and J. Neugebauer. Reconstructions of the AlN(0001) surface. *Phys. Rev. B*, 68:205317, 2003. https://doi.org/PhysRevB.68.205317.

[310] N. Gaston. Cluster melting: new, limiting and liminal phenomena. *Adv. Phys. X*, 3:1401487, 2018. https://doi.org/10.1080/23746149.2017.1401487.

[311] M. Kuball. Raman spectroscopy of GaN, AlGaN and AlN for process and growth monitoring/control. *Surf. Interface Anal.*, 31:987, 2001. https://doi.org/10.1002/sia.1134.

[312] A. F. Goncharov and V. V. Struzhkin. Raman spectroscopy of metals, high-temperature superconductors and related materials under high pressure. *J. Raman Spectrosc.*, 34:532, 2003. https://doi.org/10.1002/jrs.1030.

[313] H. Hobert, H. H. Dunken, J. Meinschien, and H. Stafast. Infrared and Raman spectroscopic investigation of thin films of AlN and SiC on Si substrates. *Vib. Spectrosc.*, 19:205, 1999. https://doi.org/10.1016/S0924-2031(98)00076-9.

[314] S. Granville, C. Meyer, A. R. H. Preston, B. M. Ludbrook, B. J. Ruck, H. J. Trodahl, T. R. Paudel, and W. R. L Lambrecht. Vibrational properties of rare-earth nitrides: Raman spectra and theory. *Phys. Rev. B*, 79:054301, 2009. https://doi.org/10.1103/PhysRevB.79.054301.

[315] N. D. Sharma, J. Singh, A. Vijay, K. Samanta, S. Dogra, and A. K. Bandyopadhyay. Pressure-Induced Structural Transition Trends in Nanocrystalline Rare-Earth Sesquioxides: A Raman Investigation. *J. Phys. Chem. C*, 120:11679, 2016. https://doi.org/10.1021/acs.jpcc.6b02104.

[316] M. Azeem. *Optical Properties of Rare Earth Nitrides*. PhD thesis, Victoria University of Wellington, 2013.

[317] S. Oswald. X-Ray Photoelectron Spectroscopy in Analysis of Surfaces. *Encyclopedia of Analytical Chemistry*, 2013. https://doi.org/10.1002/9780470027318.a2517.pub2.

[318] A. Damascelli, Z. Hussain, and Z.-X. Shen. Angle-resolved photoemission studies of the cuprate superconductors. *Rev. Mod. Phys.*, 75:473, 2003. https://doi.org/10.1103/RevModPhys.75.473.

[319] M. Arita, K. Shimada, Y. Takeda, M. Nakatake, H. Namatame, M. Taniguchi, H. Negishi, T. Oguchi, T. Saitoh, A. Fujimori, and T. Kanomata. Angle-resolved photoemission study of the strongly correlated semiconductor FeSi. *Phys. Rev. B*, 77:205117, 2008. https://doi.org/10.1103/PhysRevB.77.205117.

[320] K. Shimomoto, J. Ohta, T.Fujii, R.Ohba, A.Kobayashi, M.Oshima, and H.Fujioka. Epitaxial growth of InN films on lattice-matched EuN buffer layers. *J. Cryst. Growth*, 311:4483, 2009. https://doi.org/10.1016/j.jcrysgro.2009.08.020.

[321] B. J. Ruck, H. J. Trodahl, J. H. Richter, J. C. Cezar, F. Wilhelm, A. Rogalev, V. N. Antonov, B. Do Le, and C. Meyer. Magnetic state of EuN: X-ray magnetic circular dichroism at the Eu $M_{4,5}$ and $L_{2,3}$ absorption edges. *Phys. Rev. B*, 83:174404, 2011. https://doi.org/10.1103/PhysRevB.83.174404.

[322] A. N. Chetyrbotskii, I. S. Tereshina, and V. A. Chetyrbotskii. A Numerical Model of Nitriding of a Gadolinium Specimen and Its Further Destruction during Storage. *Prot. Met. Phys. Chem.*, 54:308, 2018. https://doi.org/10.1134/S207020511802003X.

[323] R.-N. Zhao, R. Chen, S. Sun, Y.-J. Zhang, and Y.-H. Yuan. Geometries, electronic and magnetic properties of dinitrogen adsorbed on lanthanide element LnN_2 (Ln = La-Lu) systems: A density functional investigation. *J. Mol. Struct.*, 1141:600, 2017. https://doi.org/10.1016/j.molstruc.2017.04.013.

[324] Y. Roux, C. Duboc, and M. Gennari. Molecular Catalysts for N2 Reduction: State of the Art, Mechanism, and Challenges. *Chem. Phys. Chem.*, 18:2606–2617, 2017. https://doi.org/10.1002/cphc.201700665,.

[325] Y. Abghoui, A. L. Garden, V. F. Hlynsson, S. Björgvinsdóttir, H. Ólafdóttir, and E. Skúlason. Enabling electrochemical reduction of nitrogen to ammonia at ambient conditions through rational catalyst design. *Phys. Chem. Chem. Phys.*, 17:4909, 2015. https://doi.org/10.1039/C4CP04838E.

[326] Y. Abghoui, A. L. Garden, J. G. Howalt, T. Vegge, and E. Skúlason. Electroreduction of N_2 to Ammonia at Ambient Conditions on Mononitrides of Zr, Nb, Cr, and V: A DFT Guide for Experiments. *ACS Catal.*, 6:635, 2016. https://doi.org/10.1021/acscatal.5b01918.

[327] M. Kitano, Y. Inoue, Y. Yamazaki, F. Hayashi, S. Kanbara, S. Matsuishi, T. Yokoyama, S.-W. Kim, M. Hara, and H. Hosono. Ammonia synthesis using a stable electride as an electron donor and reversible hydrogen store. *Nat. Chem.*, 4:934, 2012. https://doi.org/10.1038/nchem.1476.

[328] N. Notman. Haber-Bosch power consumption slashed. Chemistry World, Retrieved from website on 5/03/2019, 2012. https://www.chemistryworld.com/news/haber-bosch-power-consumption-slashed/5544.article.

[329] G. Ertl. Primary steps in catalytic synthesis of ammonia. *J. Vac. Sci. Technol. A*, 1:1247, 1983. https://doi.org/10.116/1.572299.

[330] Y. Goldberg. *Properties of Advanced Semiconductor Materials GaN, AlN, InN, BN, SiC, SiGe*. John Wiley and Sons Inc., New York, 2001.

[331] G. E. Totten and D. S. MacKenzie. *Handbook of Aluminium. Vol. 1: Physical Metallurgy and Processes, Volume 1*. CRC Press, 2003.

[332] C. W. Miller, D. V. Williams, N. S. Bingham, and H. Srikanth. Magnetocaloric effect in Gd/W thin film heterostructures. *J. Appl. Phys.*, 107:09A903, 2010. https://doi.org/10.1063/1.3335515.

[333] T. P. Bertelli, E. C. Passamani, C. Larica, V. P. Nascimento, A. Y. Takeuchi, and M. S. Pessoa. Ferromagnetic properties of fcc Gd thin films. *J. Appl. Phys.*, 117:203904, 2015. https://doi.org/10.1063/1.4921813.

[334] F. H. Spedding, A. H. Daane, and K. W. Herrmann. The Crystal Structures and Lattice Parameters of High-Purity Scandium, Yttrium and the Rare Earth Metals. *Acta Cryst.*, 9:559, 1956. https://doi.org/10.1107/S0365110X5600156X.

[335] M. Ohtake, O. Yabuhara, Y. Nukaga, and M. Futamoto. Preparation of Co(0001)$_{hcp}$ and (111)$_{fcc}$ Films on Single-Crystal Oxide Substrates. *J. Phys.: Conf. Ser.*, 303:012016, 2011. https://doi.org/10.1088/1742-6596/303/1/012016.

[336] C. Schüßler-Langeheine, R. Meier, H. Ott, Z. Hu, C. Mazumdar, A. Y. Grigoriev, G. Kaindl, and E. Weschke. Magnetically ordered surface oxide on Gd(0001). *Phys. Rev. B*, 60:3449, 1999. https://doi.org/10.1103/PhysRevB.60.3449.

[337] U. Holzwarth and N. Gibson. The Scherrer equation versus the 'Debye-Scherrer equation'. *Nat. Nanotechnol.*, 6:534, 2011. https://doi.org/10.1038/nnano.2011.145.